Faculteit Wetenschappen

Departement Bio-ingenieurswetenschappen

Foto(-elektro)katalytische luchtzuivering en roetafbraak met gelijktijdige energieherwinning

Proefschrift voorgelegd tot het behalen van de graad van doctor in de Bio-ingenieurswetenschappen aan de Universiteit Antwerpen te verdedigen door

Myrthe Van Hal

Promotoren:
Prof. dr. Silvia Lenaerts
Prof. dr. ir. Sammy Verbruggen

Antwerpen, 2021

Faculty of Science

Department of Bioscience Engineering

Photo(electro)catalytic air purification and soot degradation with simultaneous energy recovery

Thesis submitted to obtain the doctorate degree in Bioscience Engineering at the University of Antwerp by

Myrthe Van Hal

Members of the jury:

Prof. dr. P. Cool	(chair) University of Antwerp
Prof. dr. S. Lenaerts	(promotor) University of Antwerp
Prof. dr. ir. S. Verbruggen	(promotor) University of Antwerp
Prof. dr. K. De Wael	University of Antwerp
Prof. dr. ir. J. Martens	KU Leuven
Prof. dr. P. Van Der Voort	University of Ghent
Prof. dr. M. Koper	Leiden University

Antwerp, 2021

Samenvatting

De huidige samenleving krijgt in toenemende mate te maken met een brede waaier aan prangende milieuproblemen. Een van de belangrijkste problemen is luchtvervuiling. In deze thesis zal voornamelijk gefocust worden op de afbraak van vluchtige organische stoffen (VOCs) en fijn stof, meer specifiek roet. Naast luchtvervuiling is ook het gebruik van fossiele brandstoffen een belangrijk aspect in de wereldwijde milieuproblematiek. In deze thesis wordt een foto-elektrochemische (PEC) cel toegepast om gelijktijdig lucht te zuiveren en duurzame energie op te wekken. Fotokatalyse wordt toegepast aan de foto-anode van een foto-elektrochemische cel en drijft het luchtzuiveringsproces, terwijl de energie vervat in de afgebroken verbindingen (deels) wordt herwonnen aan de kathode, als H_2 gas of als elektriciteit. De eerste twee experimentele hoofdstukken focussen op een gasfase PEC cel die werkt zonder de aanleg van een externe spanning, met als doel de afbraak van VOCs. Hierbij werden zowel TiO_2- als WO_3-gebaseerde fotokatalysatoren bestudeerd. In de twee volgende hoofdstukken werd de capaciteit van deze TiO_2- en WO_3-gebaseerde fotokatalysatoren voor het fotokatalytisch afbreken van roet bestudeerd. In het laatste experimentele hoofdstuk werden de resultaten uit de vorige hoofdstukken gecombineerd, strevend naar een efficiënte, zonlicht gedreven en roet degraderende PEC cel die afvalgassen omzet in energie.

Daar waar reeds uitgebreid onderzoek werd verricht naar het gebruik van PEC cellen in de context van afvalwaterzuivering, is het toepassen van de PEC technologie in gasfase een relatief nieuw onderzoeksdomein. Het eerste experimentele hoofdstuk dient als *proof of concept* voor een gasfase PEC cel die simultaan lucht zuivert en energie produceert onder de vorm van H_2 gas, zonder de aanleg van een externe spanning. In gasfase werden ongeveer 30% hogere fotostromen behaald dan in vloeistoffase, wat veelbelovend is voor het toepassen van de PEC cel als luchtzuiveringstechnologie. Er werd een toename in fotostroomproductie waargenomen wanneer de methanolconcentratie steeg. De invloed van O_2 werd vervolgens bestudeerd. Wanneer de PEC cel gespoeld werd met lucht in plaats van puur N_2 gas werd een *trade-off* waargenomen, met een kleine daling (8%) in fotostroomproductie aan de ene

kant en een meer complete mineralisatie van methanol naar CO_2 aan de andere kant. Deze resultaten ondersteunen opnieuw de toepasbaarheid van de PEC cel voor luchtzuiveringsdoeleinden. Infraroodspectroscopie toonde de aanwezigheid van methylformiaat en dimethylether aan onder aerobe omstandigheden. In het laatste deel van dit hoofdstuk werd de PEC cel toegepast op ethanol- en azijnzuurdampen. Volgende volgorde in fotostroom-productie werd bekomen: methanol $>$ ethanol $>$ azijnzuur.

In het tweede experimentele hoofdstuk van deze thesis werd een goedkope PEC cel ontworpen, met als doel de omzetting van afvalgas naar elektriciteit. PEC cellen die afval en polluenten afbreken aan de anode met als doel de productie van elektriciteit aan de (aerobe) kathode worden fotobrandstofcellen (PFCs) genoemd. De werking van vijf TiO_2- en WO_3-gebaseerde fotokatalysatoren als fotoanode van een gasfase PFC werd bestudeerd in dit hoofdstuk. Inzicht in de belangrijkste materiaaleigenschappen voor gasfase werking van een PFC werd verworven door vergelijking met rechtstreekse fotokatalytische experimenten. Hoewel de TiO_2-gebaseerde fotokatalysatoren de hoogste rechtstreekse fotokatalytische VOCs afbraak behaalden, functioneerden de WO_3-gebaseerde fotokatalysatoren duidelijk beter als fotoanodes in de gasfase PFC. De kleine actieve oppervlakte van de WO_3-gebaseerde fotokatalysatoren limiteerde hun rechtstreekse fotokatalytische activiteit, maar bleek veel minder belangrijk voor een goede werking als foto-anode. De hoge elektronenmobiliteit van WO_3 aan de andere kant maakte dit een zeer geschikt materiaal voor toepassing in gasfase fotobrandstofcellen. Bovendien kan WO_3 gebruik maken van een groter deel van het zonlichtspectrum als gevolg van de zichtbaar licht activiteit van dit materiaal, wat dit een veelbelovend materiaal maakt voor toepassing in een zonlicht gedreven fotobrandstofcel. In het laatste deel van dit hoofdstuk werd het bereik van de studie uitgebreid naar andere afvalgassen en polluenten. Volgende volgorde van fotostroomproductie werd waargenomen: ammoniak $>$ etheen $>$ methaan.

Aangezien hoge fijn stof, en dus roet, concentraties een wereldwijd probleem vormen, is het vermogen van een foto-anode om om te gaan met afgezet roet cruciaal voor de stabiele en lange termijn werking van een PFC. Eerst werd een bestaande optische roetdetectiemethode, gekend voor zijn lage kost en tijds-

efficiëntie, verbeterd en gevalideerd. In de originele foto-analyse methode werd een drempelwaarde voor L* (helderheidsas van de CIELab kleurruimte) gebruikt om elke pixel te categoriseren als ofwel volledig vuil of volledig proper. Door in plaats daarvan de verschuiving van de meest voorkomende L* waarde te gebruiken als maat voor de roetafbraak in elke pixel, werd een meer realistische en accurate methode bekomen. Bovendien liet deze aanpassing toe om verschillende gradaties van vervuiling apart op te volgen. Deze optische methode werd aangevuld met een *in situ* Fourier-transform infrarood (FTIR) reactor, die het mogelijk maakte om zowel gasvormige als geadsorbeerde reactieproducten op te volgen tijdens fotokatalytische roetafbraak. De gepresenteerde methode werd gevalideerd door toepassing op TiO_2- en ZnO-gebaseerde fotokatalysatoren. Commercieel TiO_2 (P25) was de snelste in het afbreken van roet. Bij alle bestudeerde fotokatalysatoren werd de vorming van formiaat-gerelateerde verbindingen ($CHOO^-_{(ad)}$) vastgesteld.

In het volgende hoofdstuk werd de gepresenteerde roetdetectiemethodologie toegepast om de roetoxidatiecapaciteit te bepalen van de eerder bestudeerde foto-anodes onder een reeks verschillende lichtbronnen. Wanneer de optische foto-analyse methode werd toegepast op de (groen-gelig gekleurde) WO_3-gebaseerde fotokatalysatoren bleek de intrinsieke kleur van deze materialen accurate detectie van roetafbraak te verhinderen. Een extra dataverwerkingsstap werd toegevoegd, waardoor het toepassingsgebied van de methode werd uitgebreid naar gekleurde fotokatalysatoren. Bij het toepassen van de verder verbeterde detectiemethode kon worden aangetoond dat onder UV licht TiO_2-gebaseerde fotokatalysatoren beter presteren dan WO_3-gebaseerde fotokatalysatoren. Onder zichtbaar licht daarentegen werd het beste resultaat behaald met de in het labo gesynthetiseerde WO_3. Onder artificieel daglicht waren twee van de drie bestudeerde TiO_2-gebaseerde fotokatalysatoren beter dan de twee bestudeerde WO_3-gebaseerde fotokatalysatoren. Fotokatalytische roetafbraak kon worden waargenomen voor alle bestudeerde fotokatalysatoren onder de laag-intense daglicht lamp, wat het potentieel van fotokatalyse als energie-efficiënte roetdegradatietechnologie benadrukt. De bestudeerde WO_3-gebaseerde fotokatalysatoren vertoonden veruit de hoogste selectiviteit voor het volledig mineraliseren van roet naar CO_2.

In het laatste deel van deze thesis werden de resultaten van de voorgaande hoofdstukken gecombineerd, strevend naar een efficiënte, zonlicht gedreven en roet degraderende PFC die afvalgassen afbreekt en omzet in elektriciteit. Hiervoor werd de best presterende TiO_2-gebaseerde fotokatalysator (*i.e.* P25) gecombineerd met de best presterende WO_3-gebaseerde fotokatalysator (*i.e.* WO_3 gesynthetiseerd volgens een protocol van Martínez-de la Cruz *et al.*). De combinatie van een vier keer minder beladen P25 laag (0.4 mg cm^{-2}) bovenop een standaard WO_3 laag (1.6 mg cm^{-2}) bleek '*the best of both worlds*', aangezien deze configuratie de hoge roetoxidatiecapaciteit van P25 kon combineren met de uitstekende foto-anode eigenschappen en zichtbaar licht activiteit van WO_3. In het laatste experimentele gedeelte werd de in ons labo ontwikkelde PFC buiten toegepast. Autonome werking kon worden aangetoond, wat wijst op het potentieel van een autonome fotobrandstofcel die elektriciteit genereert enkel gebruik makend van zonlicht en buitenlucht. Ik ben hoopvol dat deze thesis kan dienen als belangrijke eerste stap richting ontwikkeling – en uiteindelijk toepassing – van een robuuste, efficiënte en zonlicht gedreven fotobrandstofcel, die afvalgassen afbreekt en omzet in elektriciteit.

Abstract

Today's society is increasingly challenged by a range of urgent environmental problems. Air pollution is one of these pressing topics. This thesis will mainly focus on the degradation of volatile organic compounds (VOCs) and particulate matter (PM) - more specifically soot. A second globally urging topic is the quest for sustainable energy production. In this thesis a photoelectrochemical (PEC) cell will be used to simultaneously target both air pollution and sustainable energy production using a single device. Photocatalysis is used at the anode of the PEC cell to drive the air purification process, while the energy contained in the degraded compounds is (partially) recovered at the cathode, either as H_2 or electricity. The first two experimental chapters focus on the proof of concept of such an unbiased all-gas phase PEC cell targeting VOC degradation, using both TiO_2- and WO_3-based photocatalysts. In the two following experimental chapters the photocatalytic soot oxidation capacity of these TiO_2- and WO_3-based photocatalysts was studied. In the final experimental chapter the previously obtained results were combined striving towards an efficient, sunlight-driven and soot-degrading waste gas-to-energy PEC cell.

While PEC cells have been widely studied in the context of waste water treatment, gas phase PEC cell operation is a very recent research area. The first experimental chapter provides a proof of concept of an unbiased all-gas phase PEC cell, simultaneously purifying contaminated air and recovering energy (as H_2 gas). When methanol vapour was introduced in a gas flow, circa 30% higher photocurrents were obtained than in liquid phase, evidencing the potential of the PEC technology for waste gas abatement. Higher photocurrents were obtained when the methanol content of the photoanode feed increased. Next, the influence of O_2 was studied. A trade-off was observed when working with air instead of pure N_2 as the carrier gas, resulting in a small drop in generated photocurrent (8%) on one hand, but a more complete mineralization of methanol towards CO_2 on the other hand. These results again support the applicability of the PEC cell for air purification purposes. Infrared spectroscopy evidenced the presence of methyl formate and dimethyl ether as intermediates under aerobic conditions. A final case study was performed, operating the PEC

cell with ethanol and acetic acid vapours, resulting in the following order of photocurrent generation: methanol > ethanol > acetic acid.

In the second experimental part of this thesis a low-cost PEC cell was designed, serving as waste gas-to-electricity PEC device. PEC cells using waste and pollutants at the anode (= 'fuel'), while generating electricity at the (aerobic) cathode, are called photofuel cells (PFCs). The performance of five either TiO_2- or WO_3-based photocatalysts as photoanodes of an all-gas phase PFC was studied in this chapter. By comparing direct photocatalytic and photoelectrochemical gas phase experiments, insight was gained into the key material properties driving gas phase PFC operation. While the TiO_2-based photocatalysts resulted in the highest direct photocatalytic VOC degradation, they were outperformed by the WO_3-based photocatalysts in the gas phase PFC device. Where the low surface area of the WO_3-based photocatalysts largely hindered their direct photocatalytic performance, this property was of lesser importance in the gas phase PFC. The high electron mobility of WO_3 on the other hand, makes it a very promising photoanode material for use in an all-gas phase PFC. In addition, the visible light activity of WO_3 allows it to use a larger fraction of the (freely available) sunlight, making WO_3 an interesting material for sunlight-driven PFC operation. In a final case study the scope was broadened, operating the in-house engineered PFC with ammonia, ethylene and methane, obtaining the highest photocurrents with ammonia.

As high PM, and thus soot, concentrations are a worldwide problem, the ability of a photoanode to cope with soot deposits is crucial for robust and long-term operation of the PFC. First, an existing low-cost and time-efficient optical soot oxidation detection method was improved and validated. The original image analysis method used a single threshold value for L* (brightness axis of CIELab colour space), categorising each pixel as either completely fouled or clean. By using the most frequent L* value to determine the amount of soot present in each pixel a more realistic, accurate and complete method was obtained, enabling separate monitoring of different grades of soot fouling. This improved optical detection method was complemented by *in situ* Fourier transform infrared (FTIR) spectroscopy, allowing monitoring of both gaseous and adsorbed reaction products. The presented methodology was validated by application on TiO_2- and ZnO-based photocatalysts.

In the next part, the newly improved soot detection methodology was used to determine the soot oxidation capacity of the photoanodes studied in the first two experimental sections, under a range of different light sources. When applying the optical image analysis method on (yellow-greenish coloured) WO_3-based photocatalysts, the intrinsic colour of these materials hindered accurate soot detection. An additional data processing step was therefore introduced, expanding the application range of our detection method to inherently coloured photocatalysts. It could be observed that under UV light the studied TiO_2-based photocatalysts outperformed both WO_3-based photocatalysts. On the other hand, the lab-synthesized WO_3 performed best under visible light irradiation. Under artificial daylight, two out of the three TiO_2-based photocatalysts outperformed both WO_3-based photocatalysts. Photocatalytic soot degradation was observed for all studied photocatalysts under a low-intensity daylight lamp, highlighting the potential of photocatalysis as energy-efficient soot abatement technology. The studied WO_3-based photocatalysts had by far the highest specificity towards complete soot mineralisation into CO_2.

In the last part of this thesis the results of the previous chapters were combined, striving towards an efficient, sunlight-driven and soot-degrading waste gas-to-electricity PFC device. To this end, the best performing TiO_2-based photocatalyst (*i.e.* P25) was combined with the best performing WO_3-based photocatalyst (*i.e.* lab-synthesised WO_3 according to protocol of Martínez-de la Cruz *et al.*). The combination of a four times less dense layer of P25 (0.4 mg cm^{-2}) on top of standard $WO_{3\ Mart.}$ layer (1.6 mg cm^{-2}) proved to be the 'best of both worlds', combining the high soot oxidation capacity of P25 with the excellent photoanode properties and visible light activity of the lab-synthesized WO_3. Finally, the in-house engineered PFC device was applied outside under real-life conditions. Autonomous operation was demonstrated, evidencing the feasibility of an autonomous PFC device purely using sunlight and outdoor air to generate electricity. I am hopeful that this thesis serves as an important first step towards development - and eventually application - of a robust, efficient and sunlight-driven waste gas-to-electricity PFC device.

Dankwoord

Tijdens mijn doctoraat kon ik rekenen op veel mensen die mij allen op hun eigen manier bij dit doctoraat hebben geholpen en waarvoor een oprechte dankjewel op zijn plaats is.

Bedankt Silvia om mij de kans te geven om mijn doctoraat bij DuEL te starten en voor de wijze raad tijdens mijn doctoraat. Voor hulp en advies kon ik tijdens mijn doctoraat ook steeds terecht bij Sammy. Het was aangenaam te weten dat je altijd klaarstond voor een goede brainstormsessie als ik even vastzat in een kluwen van resultaten en experimenten. Bedankt hiervoor! Prof. Karolien De Wael en Rui zou ik willen bedanken voor hun hulp bij de elektrochemische kant van de experimenten. Tom T., de computerheld van DuEL, eeuwige dank voor het oplossen van al mijn computer-problemen. Zonder het werk van Gilles en zijn collega's van de mechanische werkplaats was er geen cel, en zonder cel geen doctoraat, dus ook heel hard bedankt hiervoor! De bachelor- en masterstudenten die ik heb begeleid wil ik bedanken voor hun harde werk en inzet.

During my PhD I had the pleasure to be surrounded by a group of nice colleagues. Hilde en Annelize, jullie zijn van onschatbare waarde voor iedere doctoraatsstudent! I would like to thank all my colleagues for their help and good advice, and off course for all the fun moments that we shared, going from nice chats to delicious potluckdiners and crazy dance evenings. Thank you all for contributing to these beautiful memories!

Natan, voor jou is een apart bedanking op zijn plaats. Je stond steeds klaar om mij te helpen met mijn vragen, maar ook om gewoon te luisteren als ik een klankbord nodig had. Jouw kalmte en immer goed humeur gaven mij ook tijdens het schrijven van mijn doctoraat dat extra duwtje in de rug. Bedankt voor je onvoorwaardelijke steun en alle leuke momenten samen, op en naast het werk!

Last but not least! Mijn ouders, grootouders en vrienden zou ik willen bedanken om er altijd te zijn wanneer dat nodig is, zowel tijdens mijn doctoraat als erbuiten!

Aan jullie allen, dikke merci!

Table of contents

List of figures

List of tables

Symbols and abbreviations

A	Absorbance
AEM	Anion exchange membrane
AFM	Atomic force microscopy
AOP	Advanced oxidation process
a.u.	Arbitrary units
BET	Brunauer–Emmett–Teller
c	Speed of light (3.00×10^8 m s^{-1})
CA	Chronoamperometry
CB	Conduction band
CFD	Computational fluid dynamics
CV	Cyclic voltammetry
DIA	Digital image analysis
DME	Dimethyl ether
DOC	Diesel oxidation catalyst
DPF	Diesel particulate filter
DRM	Dry reforming of methane
E	Energy
E_g	Band gap energy
e^-	Electron
EC	European Commission
EDXRF	Energy dispersive X-ray fluorescence
EPA	(United States) Environmental protection agency
EPR	Electron paramagnetic resonance

EU	European Union
F	Faraday constant (96 485.34 C mol^{-1})
FF	Fill factor
FTIR	Fourier transform infrared
FTO	Fluorine-doped tin oxide
GC	Gas chromatography
h	Planck's constant (6.63 x 10^{-34} J s)
h^+	Hole
HC	Hydrocarbons
HER	Hydrogen evolution reaction
I	Absolute photocurrent
IEA	International energy agency
I_{SC}	Short-circuit current
ITO	Indium tin oxide
J	Photocurrent density
J_{SC}	Short-circuit current density
LEZ	Low emission zone
LHV	Lower heating value
L^*_{max}	Most frequent L* value
MEA	Membrane electrode assembly
MeOH	Methanol
MF	Methyl formate
n	Number of electrons in the reaction
NECD	National emission ceilings directive
NHE	Normal hydrogen electrode
NIST	National institute of standards and technology

NMVOCs	Non-methane volatile organic compounds
NOCM	Non-oxidative coupling of methane
NO_x	Nitrogen oxides
NP_{max}	Maximal height of the concentrated soot peak
OCM	Oxidative coupling of methane
OER	Oxygen evolution reaction
$^{\bullet}OH$	Hydroxyl radical
$^{\bullet}OOH$	Hydroperoxyl radical
$O_2^{-\bullet}$	Superoxide anion
PAH	Polycyclic aromatic hydrocarbon
PC	Photocatalytic
PE	Photonic efficiency
PEC	Photoelectrochemical
PEM	Proton exchange membrane
PFC	Photofuel cell
PM	Particulate matter
$PM_{2.5}$	PM with diameter below 2.5 µm
PM_{10}	PM with diameter below 10 µm
P_{max}	Maximal electric power output
PMMA	Poly(methyl methacrylate)
Q	Total amount of photogenerated charge
RH	Relative humidity
ROS	Reactive oxygen species
Rq	Surface roughness
SBS	Sick building syndrome
SDG	Sustainable development goals

SEM	Scanning electron microscopy
SO_x	Sulphur oxides
SPR	Surface plasmon resonance
SRM	Steam reforming of methane
STH	Solar to hydrogen
TTIP	Titanium tetraisopropoxide
UNECE	United Nations Economic Commission for Europe
UNFCCC	United Nations Framework Convention on Climate Change
UV	Ultraviolet
VB	Valence band
VIS	Visible
V_m	Molar gas volume
VOC	Volatile organic compound
V_{OC}	Open-circuit voltage
WHO	World health organisation
XRD	X-ray diffraction
η	Overall efficiency
λ	Wavelength
ν	Frequency

Chapter 1

Environmental problems and the photoelectrochemical cell as potential solution

1.1 Problem statement part 1: air pollution

Air pollution is an increasingly urgent worldwide problem. According to the World Health Organisation (WHO) one out of every nine deaths worldwide can be related to air pollution (in 2012), making it the biggest environmental health risk. Annual health costs related to air pollution are estimated to account for €1.45 trillion for the European member states alone.[1] Periods of acute air pollution have increased over the past years, certainly in urban areas, consequentially resulting in an increase in associated problems (*e.g.* health problems, building fouling, decreased visibility, *etc.*). The WHO estimated that around 90% of the world population lives in places where the WHO guideline limits for air quality are exceeded.

The term air pollution covers a range of different compounds, including both primary and secondary pollutants, consisting of volatile organic compounds (VOCs), particulate matter (PM, including soot), nitrogen oxides (NO_x), ozone (O_3), *etc.*[2] The need for pure air and a healthy living environment is also clearly emphasized in the sustainable development goals (SDGs, Figure 1.1). Three SDGs express the urge for air purifying measures with as goal to: obtain a global good health and wellbeing (SDG 3), reach sustainable cities and communities (SDG 11) and combat climate change (*e.g.* soot, SDG 13).[3] This thesis focusses on soot (PM) and VOCs.

Figure 1.1. The 17 sustainable development goals (SDGs) as drafted by the United Nations.

1.1.1 VOCs

An important health concern is exposure to volatile organic compounds. VOCs are organic compounds with a boiling point up to 260°C, resulting in easy off-gassing at room temperature. Some well-known examples are: acetone,

benzene, formaldehyde, ethylene, ethanol, methanol, and xylene. Some specific VOCs (*i.e.* ethylene, methane) are discussed in more detail further on. Many have useful properties making them attractive materials for a variety of applications.[4] Common outdoor VOC sources are exhaust gases, gas stations, biogenic sources (*e.g.* plant emissions), biomass burning and industrial sources (*e.g.* combustion processes, use of solvents). Indoor sources include paints, adhesives, furnishings, clothing, cigarettes, deodorants, cleaning products, construction materials and combustion devices.[5,6]

The United States' Environmental Protection Agency (EPA) has estimated that we spend over 90% of our time indoors, while indoor VOC concentrations are known to greatly exceed outdoor concentrations (1 - 10 times, exceptionally over 100 times higher concentrations).[6,7] A syndrome that is related to high indoor VOC concentrations, mainly formaldehyde, is sick building syndrome (SBS). SBS often occurs in new or recently renovated buildings and results in symptoms such as eye irritation, a sore throat, and headache.[4,8] Other symptoms of VOC exposure are loss of coordination, nausea, dizziness, cancer and damage to liver, kidney and the central nervous system.[4] Next to direct health effects, VOCs are also known to cause photochemical smog through reaction with NO_x (Figure 1.2). When both compounds are simultaneously present and exposed to sunlight, a brown haze consisting of a variety of secondary pollutants (*e.g.* ground level ozone, peroxyacetyl nitrate) can be formed, called photochemical smog. This phenomenon occurs mainly in summer, as it is sunlight dependent, and in cities, due to higher concentrations of primary pollutants.[9] Important negative effects of photochemical smog include reduction of visibility and a range of health problems (*e.g.* respiratory problems, coughing, eye irritation).[9]

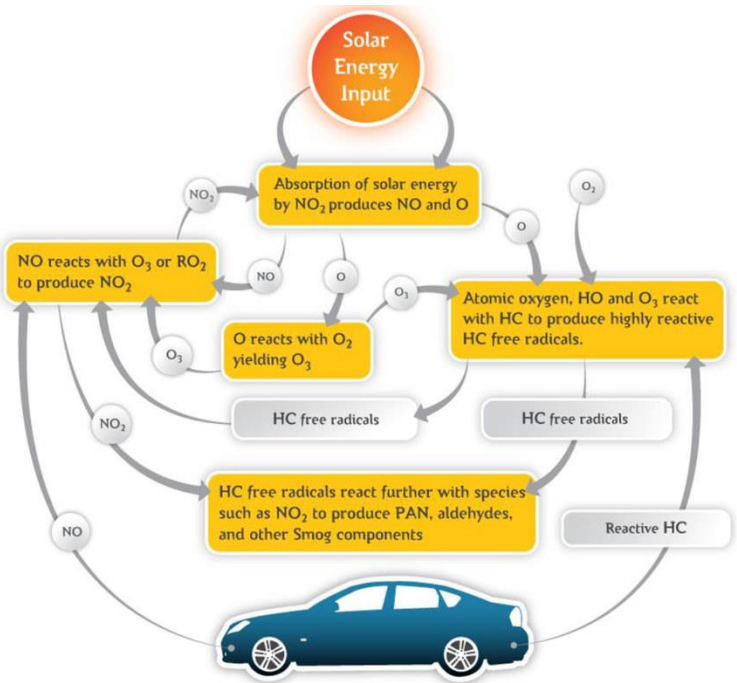

Figure 1.2. Schematical representation of photochemical smog formation. HC = hydrocarbons. Reproduced from International Journal of Sustainable Development and Planning with permission from the authors.[10] Courtesy of WIT Press.

In 2001 the European commission (EC) drafted their National emission ceilings directive (NECD), limiting concentrations of SO_2, NO_x, ammonia (NH_3) and non-methane volatile organic compounds (NMVOCs) for each member state from 2010 onwards (2001/81/EC). Additionally, regulations are in place controlling specific VOC sources including industrial solvents, the automobile industry (*e.g.* Euro-norms) and petrol storage and distribution. This thesis focusses on VOC degradation in general (using methanol as model VOC), eventually also applying the studied techniques for the degradation of three other specific waste gases/pollutants:

Ethylene

Ethylene (C_2H_4) is a VOC that regulates a broad variety of processes in plants as phytohormone, such as growth, development, and the stress response. When present in low concentrations, ethylene aids the development of colour, taste and flavour of plants, fruits and vegetables.[11] However, ethylene can also induce premature ripening, softening and senescence and can be constantly

produced through respiration after harvesting of fruits and vegetables.[11] Control of ethylene concentrations is thus an important tool used for lowering post harvesting losses of fruit and vegetables, which mainly occur during storage and transport.[11–13]

Methane

Depending on the classification, methane (CH_4) is counted as a regular VOC or given a separate classification (*vs.* NMVOCs) due to its lower boiling point, smaller size, greenhouse effect and relatively high atmospheric concentration (~1850 ppb).[14] Since the industrial revolution methane concentrations have more than doubled due to extensively increased human activities.[15] Main anthropogenic sources of methane are agriculture (*e.g.* rice cultivation, ruminant livestock), natural gas production, transport and consumption, waste decomposition and biomass burning. The most important natural methane source is wetlands.[16] Methane is a 28 times stronger greenhouse gas than CO_2 (over a 100-year time horizon) and is, after CO_2, the second largest contributor to the enhanced greenhouse effect (16%).[17] In addition, it affects both tropospheric and stratospheric chemistry, influencing levels of ozone, water vapour, hydroxyl radicals, *etc.*[15] Methane emissions are included in the Kyoto Protocol (1997) and the more recent Paris agreement (2015) that aims at limiting the global temperature increase to 1.5°C above pre-industrial levels (drafted by the United Nations framework convention on climate change (UNFCCC)).

Ammonia

The past few decades emissions of ammonia (NH_3), which is not a VOC, have been globally increasing.[18] It is formed by the breakdown and volatilisation of urea.[19] Agriculture (*e.g.* fertiliser application, manure, slurries) accounts for the largest fraction of anthropogenic ammonia emissions. Other sources of ammonia include industry, animal husbandry, fertiliser manufacturing, the automotive sector (via catalytic converters), composting, landfilling, biomass burning, and oceans and soils via volatilisation.[18,20] Due to the alkaline and reactive nature of ammonia, it has a deleterious effect when sensitive ecosystems are exposed to high concentrations. In addition, it also contributes to PM formation (secondary ammonium aerosols) and reduced visibility.[18] As

stated above, NH_3 emissions are regulated since 2010 by the European NECD (2001/81/EC).

1.1.1.1 VOC abatement: state of the art

As a broad range of health and environmental effects are related to VOC emissions, measures aiming at the reduction of VOC emissions are of great importance. To this end, VOC-free alternatives (*e.g.* water-based paints), alternative technologies resulting in reduced VOC use and air-tight storage of VOC-emitting products are crucial measures reducing the amount of VOCs emitted into the atmosphere.[21] In addition, a broad range of VOC abatement techniques exists, targeting emitted VOCs. Some commonly used methods are adsorption, scrubbers and (improved) ventilation. The disadvantage of these methods is that the VOCs are not degraded, but only relocated. These techniques can thus be used to collect VOCs at a certain location - for example useful for high VOC concentrations encountered in industry - but need to be coupled to VOC degradation techniques if effective VOC abatement is desired. Another disadvantage of the use of adsorbents is the need for regeneration.[22] Some commonly used destructive methods are biofiltration, catalytic oxidation (*e.g.* diesel oxidation catalyst (DOC) in diesel cars) and advanced oxidation processes (AOPs) such as ozonation and photocatalysis.[22,23] Biofiltration is mainly used for stationary sources, while (photo)catalytic oxidation is a suitable technology for mobile VOC sources. AOPs produce reactive oxygen species (ROS), with a crucial role for the hydroxyl radical ($^{\bullet}OH$), aiming at oxidation of pollutants. A disadvantage of traditional (thermal) catalytic oxidation is that it still largely depends on noble metals.[24] When applying ozonation it has to be kept in mind that ozone itself is harmful both for human health and the environment and in addition (harmful) by-products are often formed.[25] Photocatalysis proves to be a promising technology for VOC degradation, as it uses (sun)light to initiate the reactions, resulting in low chemical use, energy consumption and waste production.[26] However, there are still important challenges that need to be overcome before photocatalysis can be used for large-scale VOC degradation (*e.g.* increased sunlight activity, efficiency).[27] Photocatalysis will be discussed in more detail in section 1.3, together with its applications for VOC abatement. Recently, a photoelectrochemical (PEC) cell has been presented as a possible VOC abatement method, applying

photocatalysis at the anode to combine VOC oxidation with H_2 production.[28] The composition of this PEC cell and its applications for air purification will be discussed in section 1.4.

Ethylene

Reduction of post harvesting losses of fruit and vegetables can be obtained by controlled ethylene degradation. To this end, refrigeration and ventilation during transport and storage can be used, minimising the respiratory rate of the fruit and vegetables, but this is an energy-intensive process. Some other studied methods are chemical adsorbents, ozonation, photolysis, thermal catalysis, photocatalysis and the use of plant bioregulators.[12,29,30] Ozonation, UV-C light and thermal catalysis have all been found to result in reduced fruit/vegetable quality. Photocatalysis on the other hand has shown promising results for ethylene control, avoiding fruit/vegetable deterioration with low energy consumption and costs.[12,30] In addition, the first experiments evidencing biased photoelectrochemical ethylene degradation have been performed by Ye *et al*.[31,32]

Methane

As methane is an important greenhouse gas, reduction of methane emissions is crucial for controlling global climate change. To this end, a broad variety of techniques is currently studied. Methane residues are often flared off, converting methane into CO_2, and thus reducing the overall greenhouse effect, but losing the energy stored in methane. Many processes are also in place converting methane to higher hydrocarbons such as non-oxidative coupling of methane (NOCM) and oxidative coupling of methane (OCM). In addition, methane can also be used to produce syngas (CO and H_2) by dry reforming of methane (DRM) and steam reforming of methane (SRM). However, all these technologies still suffer from large limitations such as the requirement of high temperatures (NOCM, DRM and SRM), and low yield and selectivity (OCM). Recently, photocatalysis has been successfully used to achieve complete methane oxidation at room temperature by Chen *et al.* (2016).[33] In addition, selective CO production was obtained for the first time in 2018 by Li *et al.* when photoelectrochemically oxidising methane at room temperature using an external bias.[34]

Ammonia

Since agriculture is responsible for a large part of the current NH_3 emissions, changing the protein content of animal feed and altering their housing could already result in significant reductions of NH_3 emissions.[35] In addition, aerobic and anaerobic treatment of the produced waste has shown effective for NH_3 reduction, but is often not economically feasible.[35] Currently, the best available technology for reducing NH_3 emissions from livestock farming is a scrubber in which NH_3 is trapped in acid solutions made of sulfuric acid. The ammonium sulphate produced in the scrubber could then be used as fertiliser.[36] Biological scrubbers converting ammonia to N_2 are an alternative technology used in farming practice.[37] Currently, oxidation is being considered a promising method for reducing NH_3 emissions, including selective catalytic oxidation, UV-irradiation and photocatalytic oxidation.[35,38,39] Photoelectrochemical NH_3 oxidation, in addition, has been evidenced by multiple studies, but so far only aqueous ammonia streams have been targeted.[40–45]

1.1.2 Particulate matter

An aerosol is a gaseous suspension of fine solid and/or liquid particles. Particulate matter (PM) is an aerosol consisting of a broad variety of components, both organic (*e.g.* polycyclic aromatic hydrocarbons (PAHs)) and inorganic (*e.g.* nitrates, sulphates, metals) and can be divided into primary and secondary PM based on the origin.[2,46] PM can originate both from natural and anthropogenic sources. Examples of natural PM sources are sea salt, volcanic ash and imported desert sand. Anthropogenic sources of PM include incomplete combustion originating from transport, energy production, waste incineration, domestic heating, *etc.*, but also dust produced by wearing of brakes, train rails and many more.

For health purposes, PM is categorised based on the size of the suspended particles. PM_{10} represents inhalable particles with a diameter of 10 µm or less, $PM_{2.5}$ are fine inhalable particles with diameters below 2.5 µm and particles with a diameter below 100 nm are called ultrafine particles. PM has become an increasingly important air pollutant. PM concentrations are especially high in

urban environments, where they often exceed the WHO air quality annual mean target for PM_{10} and $PM_{2.5}$ (20 and 10 µg/m³, respectively, Figure 1.3).[46,47]

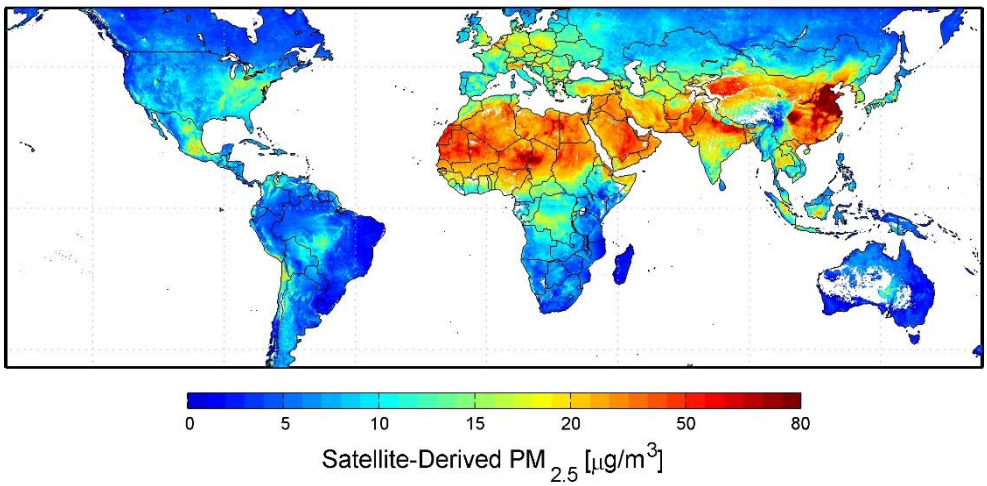

Figure 1.3. The mean annual concentration of $PM_{2.5}$ between 2001 and 2006. Reproduced from Environmental Health Perspectives with permission from the authors.[47]

The presence of PM is associated with a variety of both short- and long-term health effects.[48,49] These health effects depend on several PM properties, such as size (the smaller, the more damage), composition (*e.g.* PAHs, metals) and of course the PM concentration.[50] Some examples of health effects that are related to PM exposure are respiratory and cardiovascular diseases, preterm birth, DNA damage and low birth weight. Next to causing health effects, PM also influences the global climate. On one hand, the black carbon fraction of PM results in a decreased albedo and thus enhances climate change, while on the other hand sulphate aerosols have an overall cooling effect.[46,51] Another important consequence of PM emissions is the deterioration of buildings due to fouling, mainly caused by the black carbon fraction of PM.

Soot, or black carbon, is part of the $PM_{2.5}$ fraction and mainly consists of elemental carbon and carbon-based organic matter. It originates from incomplete combustion of hydrocarbons (*e.g.* diesel, coal, wood), and has been associated with a variety of health risk (*e.g.* respiratory, cardiovascular and chronic pulmonary diseases).[52] As mentioned, it also enhances climate change and causes rapid building deterioration.

Due to increasing PM concentrations and consequently also an increase in associated problems, regulations have been implemented to decrease PM emissions/concentrations. In 2008, the European Union (EU) drafted air quality standards for their member states, setting limit values for several common air pollutants (*e.g.* SO_2, NO_2, O_3), including guidelines for PM concentrations (2008/50/EC).[53] Besides these general restricting values, the EU has drawn up more specific regulations aiming at reducing pollutant concentrations in a variety of sectors (*e.g*. industry, shipping, energy production). As the automotive sector is a large contributor to global PM emissions,[54] the EU also implemented regulations in this sector aiming at PM reduction. For example, the Euro 1 norm obliged the installation of a diesel oxidation catalyst (DOC) in new cars since 1992. The Euro 5 norm resulted in compulsory installation of a diesel particulate filter (DPF) in all new diesel cars from 2011 onwards.[55] Black carbon is specifically targeted by the United Nations economic commission for Europe (UNECE) convention on long range transboundary air pollution.

1.1.2.1 PM/soot abatement: state of the art

Currently several measures are taken both to prevent soot emissions and to reduce soot concentrations once emitted. As a result of the regulations imposed by the EU on the automotive industry, a broad range of actions have already been taken in this sector aiming at the reduction of PM concentrations. For example, reduction of traffic volume and congestion can result in improvement of the global air quality. In this, politics, both on national and local level, have an important role and can implement a broad range of measures (*e.g.* bicycle allowance, allowance per kilometre, low emission zone (LEZ)).[56] For example, LEZs are currently being introduced in several cities, banning the oldest and most polluting cars from city centres (*e.g.* Antwerp, Brussels, London, Berlin, Stockholm).[57] However, despite the worldwide introduction of transport emission reduction measures, the decrease in traffic-related emissions is being counteracted by an increase in cars that is driven by continuing urbanisation and global population growth. For example, the EC estimated a 40% increase in passenger cars between 2005 and 2030.[58] As traffic is expected to further expand in the following decades measures reducing traffic-related emissions are indispensable. A first possible PM-reducing measure is the improvement of engine design towards more complete

combustion (*e.g.* high pressure fuel injection, optimised shape of combustion chamber).[24] In addition, since the implementation of the Euro 1 norm in Europe in 1992, a DOC has been mandatory in every new car, oxidising incompletely burned fractions towards CO_2 and H_2O.[55] More recently, the DPF has been obliged for diesel cars by the Euro 5 norm, collecting up till 99% of all PM before emission.[55] Another innovation is the catalytic oxidation of hydrocarbons (HC) and PM by simultaneous reduction of NO_x emissions.[59] Eventually, four-way catalysts, combining the control of CO, HC, PM and NO_x emissions in a single component, will probably be required to meet both the increasing stringent emission regulations and cost, weight and space limitations imposed to future (diesel) cars.[24] As the effects (*e.g.* on human health, the environment) of PM emissions are closely linked to its size distribution and composition, the effect of new technologies on these PM characteristics should always be studied before implementation.

Despite the large number of presented PM mitigation measures applied in the automotive industry, a holistic solution eliminating PM emissions is not yet available. All mentioned techniques suffer from drawbacks limiting their applicability or effect. Noble metals are required in most catalytic exhaust treatments, which have a limited availability and high cost. These catalytic techniques are in addition also often susceptible to sulphur contamination.[24,59] Political measures often bring along high costs and only result in a limited decrease in emissions. For example, in 2018 the LEZ in Brussels only resulted in a 6.4% $PM_{2.5}$ decrease.[60]

Similar measures, both aiming at reduction of PM production and degradation of formed PM, are also being introduced in many other PM-emitting sectors (*e.g.* industry, shipping, aviation, energy production). Stoves for example, a large household source of PM, can be equipped with an electrostatic precipitator, which filters the exhaust gas by deposition of ionised PM particles. In 2002, Lee and Choi demonstrated the possibility to photocatalytically degrade soot for the first time. Since then, a variety of applications of photocatalytic soot degradation have been studied, such as self-cleaning applications (*e.g.* windows, construction materials)[61,62] and low-temperature regeneration of a DPF (*e.g.* photocatalytic PM oxidation with simultaneous NO_x

reduction).[94,95] Photocatalysis will be discussed in more detail in section 1.3, together with its applications for soot abatement.

1.2 Problem statement part 2: the quest for renewable energy

1.2.1 Problems and opportunities

The need for clean air and a healthy living environment, as reflected in multiple SDGs, was discussed in section 1.1. The urge for more affordable and clean energy is also directly expressed in one of the SDGs (SDG 7, Figure 1.1) and indirectly contained in multiple SDGs targeting a healthy environment as a result of the emissions related to the current energy system.[3] In 2018 around 82% of the global energy mix still consisted of fossil fuels (Figure 1.4).[63,64] An important advantage of fossil fuels is their low cost compared to alternative energy sources. In addition, as fossil fuels are used on a large scale for over 250 years, their supporting infrastructure is completely developed. One of the major concerns regarding fossil fuel use are the related CO_2 emissions.[56] Fossil fuels are responsible for over 99% of the CO_2 emissions originating from the primary energy production,[63] resulting in 36 - 60% of the total worldwide greenhouse gas emissions.[56,64] Another important drawback of fossil fuels is their finiteness. As the International Energy Agency (IEA) estimated that the global energy demand will increase with around 28% by 2040, it is likely that fossil fuel supplies will not suffice to meet this globally increasing energy demand.[63] This will cause fossil fuel prices to increase as supply decreases and demand increases. In addition, uncertainty about the extent of the fossil fuel reserves, their (in)accessibility and their unequal distribution might cause severe market disruptions.[65] It can be concluded that the rapidly increasing energy demand combined with the unsustainability of fossil fuels demands a global shift towards sustainable energy production.

To this end, a broad range of possibilities exist, of which some are already widely known and implemented such as solar panels, wind turbines and hydropower plants. Despite their rapidly increasing implementation, renewable energy sources still only account for less than 5% of the global energy consumption, and only around 11% when including hydroelectricity

(Figure 1.4).[66] In addition to these relatively mature renewable energy technologies, extensive research is currently being performed on a widespread number of less developed renewable energy technologies. An example of such a technology is the PEC cell. A detailed explanation on the principles and composition of a PEC cell can be found in section 1.4. In brief, using a PEC cell waste streams or pollutants (either in liquid or gas phase) can be degraded, while simultaneously energy contained in these targeted molecules is partially recovered. As photocatalysis (section 1.3) is the driving force of a PEC cell, it can be operated using solely (sun)light and contaminated streams as energy input. Depending on the operating conditions, energy is recovered either under the form of the green energy carrier H_2 or as electricity (*i.e.* photofuel cell (PFC)).

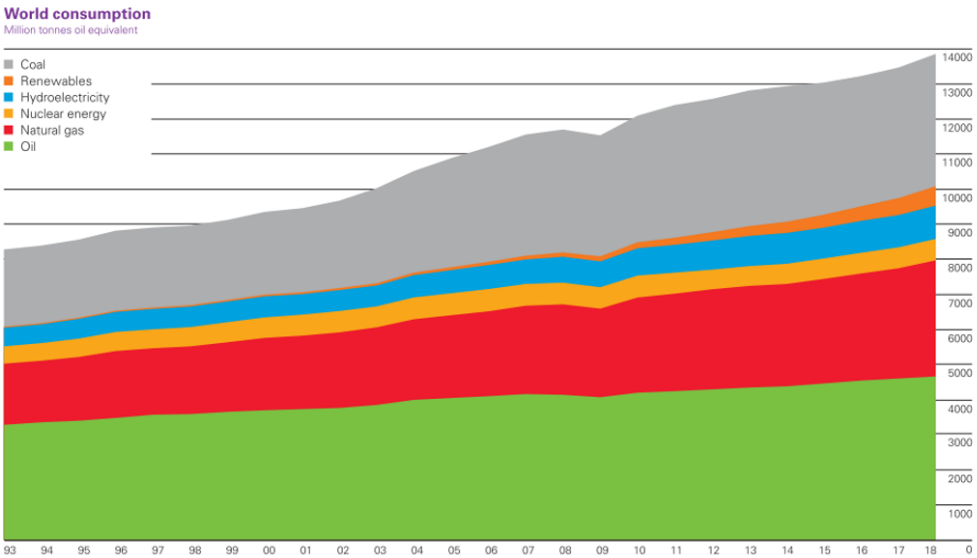

Figure 1.4. The division of global consumption quantities of different energy sources, in million tonnes of oil equivalents (Mtoe with 1 toe = 41.87 GJ). Figure obtained from Ref[66] with permission.

Nearly 40% of the global energy demand is used to generate electricity. Due to (mainly heat) losses during conversion the global electricity supply accounts for around 16% of the global energy supply. The global share of renewable electricity has been rapidly increasing with a three-fold increase over the past ten years, but with high regional differences. However, currently less than 10% of the global electricity production stems from renewable sources (excluding

nuclear energy and hydroelectricity), thus still leaving a lot of room for improvement. In view of SDG 7 - targeting affordable and clean energy – extensive research on technologies for renewable electricity production is crucial. Kaneko *et al.* (2006) already showcased conversions towards electricity up to 78% of the energy of the targeted compound in their first, non-optimised, experiments on PFCs, indicating the potential of PFCs for renewable electricity production, with simultaneous environmental sanitation.[43]

In the quest for more sustainable energy production, hydrogen as green energy carrier recently gained a lot of attention and is extensively studied.[67] In this view, (mainly water-splitting) PEC cells have also been a topic of interest. Solar to hydrogen (STH) efficiencies up to 16.1 and 26% for respectively single and dual junction PEC cells are theoretically possible based on currently existing materials.[68]

1.3 Photocatalysis

As previously mentioned, photocatalysis is a promising technology for tackling both the problems discussed in section 1.1 and 1.2. In addition, it serves as driving force for the anodic reactions in the PEC cell. Therefore, in this section photocatalysis and the current state of the art will be discussed in more detail.

In photocatalysis a semiconductor can be activated by light, hereby enabling a chemical reaction. A semiconductor is characterized by the band gap between the valence band (highest energy level still occupied by electrons at 0 K) and the conduction band (lowest energy level without electrons at 0 K). When light with a photon energy larger than the band gap energy of the photocatalyst strikes the material, electron-hole pairs are generated (Figure 1.5). As the energy content of light is related to its wavelength (Planck's law), the maximal wavelength still able to activate a photocatalyst can be determined from its band gap (Eq. 1.1):[27]

$$E = h.\nu = \frac{h.c}{\lambda} \qquad \text{(Eq. 1.1)}$$

With E being energy content, h is Planck's constant (6.63×10^{-34} J s), ν is the frequency of the incident light, c is the speed of light (3.00×10^{8} m s^{-1}) and λ is the wavelength of the incident light.

The formation of an electron-hole pair is the result of excitation of an electron (e^-) from the valence to the conduction band, leaving behind a positively charged hole (h^+) in the valence band. The formed e^- and h^+ can then react with species adsorbed on the photocatalyst surface. Species can only be reduced by a conduction band electron when the redox potential of the electron is more negative than that of the reactant. The valence band hole on its turn can only oxidise reactants when the redox potential of the hole is more positive than that of the reactant. In this way, the photogenerated electron-hole pairs can result in the degradation of organic pollutants via a chain of radical reactions. Two important radical species that are involved in these degradation reactions are hydroxyl radicals ($^{\bullet}OH$) and superoxide anions ($O_2^{-\bullet}$). These radical species can respectively be formed by oxidation of water or ^-OH species and reduction of O_2. Further reaction of $O_2^{-\bullet}$ with protons results in the formation of more ROS, such as hydrogen peroxide (H_2O_2), hydroperoxyl radicals ($^{\bullet}OOH$) and also $^{\bullet}OH$, that in their turn can also participate in the reaction chain. Eventually organic pollutants present can be completely oxidised towards CO_2 and H_2O.[27,69–71] Direct oxidation of adsorbed organic pollutants by valence band holes mainly occurs at low relative humidity or strong water-pollutant competition for adsorption sites.[27]

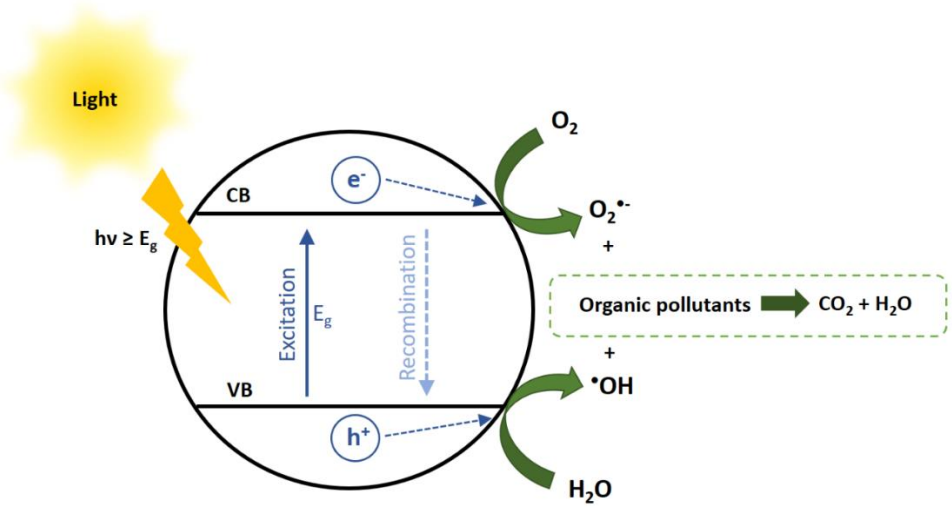

Figure 1.5. Mechanisms of photocatalysis.

Not all electron-hole pairs contribute to this radical reaction chain as it is

possible that an excited electron recombines with a valence band hole, hereby neutralizing the electron-hole pair and releasing the absorbed energy as heat or light. This recombination drastically reduces the efficiency of photocatalytic reactions and is enhanced by impurities and defects in the crystal lattice.[72,73]

1.3.1 Semiconductor

As a broad variety of semiconducting materials is available, the choice of the optimal material for a certain application is often complex. A first important characteristic of a semiconducting material is the position of the band gap, as it should allow all desired reactions to proceed. Other often considered properties are: efficiency of charge transport, the width of the band gap, chemical stability, cost, availability and toxicity.[74]

Due to good performance on most of these characteristics TiO_2 is one of the most widely studied and used photocatalysts. It has a good stability, low cost, high abundance and high photoactivity. An important limitation is its large band gap (3.0 - 3.3 eV), as this limits TiO_2 to the use of UV light ($\sim$5% of solar spectrum), resulting in a theoretical maximal STH efficiency of 2.2%. The exact band gap of TiO_2 varies and depends on its crystalline composition. TiO_2 can occur as four different polymorphs: anatase (tetragonal), rutile (tetragonal), brookite (orthorhombic) and monoclinic TiO_2.[27,69,70] Anatase (3.26 eV) and rutile (3.05 eV) are the most widely used crystal structures of TiO_2, of which anatase has the highest photoactivity and rutile is the most thermodynamically stable form.[69] Both crystal structures consist of chains of TiO_6 octahedra, but their spatial orientation differs (Figure 1.6).[27] Contradictory, in some cases a combination of both crystal structures outperforms solely anatase, for example the commercially available P25 (anatase:rutile ratio of 4:1) is a broadly used photocatalyst due to its outstanding performance in a broad range of applications such as VOC oxidation. The exact process behind this observation is not yet fully understood, but it is thought that due to the presence of both crystal structures charge carriers can be transferred between interconnecting particles of both structures, reducing charge carrier recombination.[75] For a long time TiO_2 nanoparticles were considered harmless, but this recently came under discussion as recent research (animal tests) points at potential health risks (*e.g.* immune disruption, carcinogenesis, oxidative stress) related to

exposure to TiO_2 nanoparticles.[76] In France a decree was hence signed in 2019 halting the sales of food containing the additive E171 (*i.e.* TiO_2).[77]

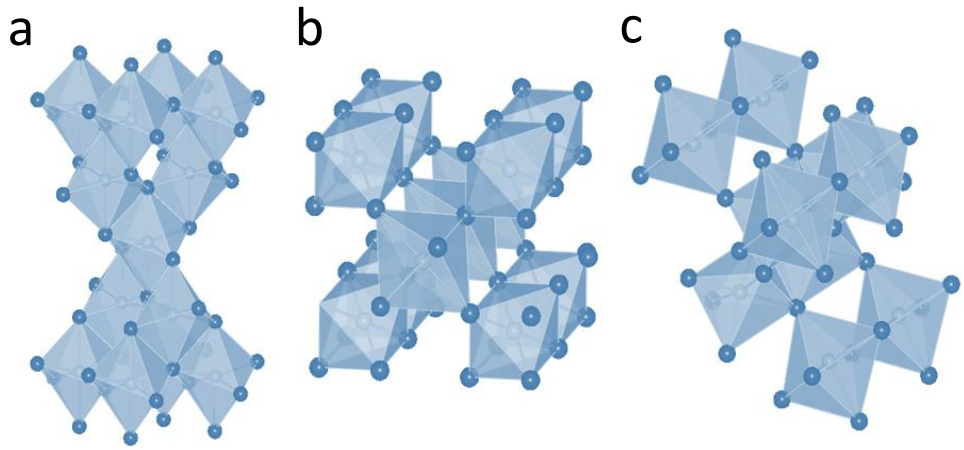

Figure 1.6. Crystal structures of a) anatase, b) rutile and c) brookite. The images were obtained using the VESTA software.

Another promising semiconductor is WO_3. As it has a band gap between 2.5 and 2.8 eV it is able to absorb visible light up to 500 nm (~ 12% of solar spectrum, theoretical STH of 4.8%).[78] The only photoactive and most stable form at room temperature is its monoclinic polymorph.[79] Many studies have looked into its photocatalytic properties since the discovery of its photoactivity in 1976, with a clear increase over the past ten years. Next to its ability to absorb visible light it has some other interesting properties such as low cost, good stability in acidic and oxidative environments and low toxicity. Currently it is deployed in a variety of applications such as dye-sensitized solar cells, photoelectrochemical water splitting and high temperature superconductivity applications.[78,80]

1.3.2 Applications: photocatalytic VOC removal

The application of photocatalysis for VOC degradation has been studied for over 30 years, making it a relative mature research field.[26,81–83] As photocatalytic coatings are able to oxidise a broad range of pollutants, including VOCs and soot, photocatalytic self-cleaning surfaces not only clean themselves but also simultaneously purify the air near the photocatalytic surface. A broad range of applications such as photocatalytic construction

materials, paints and coatings can be used to locally reduce VOC concentrations.[84] Additionally, the application of photocatalysis in indoor air purifiers has also been widely studied. Some examples are: a photocatalyst-coated filter as presented by Li *et al.* (2017)[85] and a photocatalyst-coated multi-tube reactor as studied by van Walsem *et al.* (2018).[86] The first promising results were also obtained using an all-gas phase PEC cell for VOC degradation, allowing simultaneous air purification and H_2 production, recovering part of the energy stored in the organic molecules.[87] The composition of a PEC cell and the current state of the art on photoelectrochemical VOC degradation will be discussed below (section 1.4).

1.3.3 Applications: photocatalytic soot oxidation

Lee and Choi were the first to evidence photocatalytic soot oxidation in 2002. Complete oxidation towards CO_2 of a bulk soot layer of 2 µm was obtained by TiO_2 after 30 h of UV illumination. In this study, the OH radical was assigned as main oxidant species and the necessity of O_2 for this process was stressed.[88] Multiple studies have since pointed at the importance of the mobility of the photooxidants,[88–90] evidencing direct, but also (much slower) lateral and remote photocatalytic degradation of soot.[89] As soot is immobile, the apparent activation energy for photocatalytic soot oxidation (18.7 kJ mol^{-1}) can largely be ascribed to diffusional activation of these photooxidants.[88] In 2007, Chin *et al.* hypothesised the presence of two soot degradation pathways via kinetic modelling with both direct soot oxidation to CO_2 and indirect oxidation via solid intermediates.[91]

Currently, photocatalytic soot oxidation is studied for a range of applications. As high PM and soot concentrations are globally encountered, certainly in urban environments, surface fouling is an increasing problem faced in many cities. Self-cleaning applications have therefore been widely studied, targeting amongst others buildings, windows and asphalt.[51,61,62,92,93] In addition to cleaning of the surface, air close-by the surface is purified by these applications (*e.g.* soot, VOCs, NO_x). Some of these applications have already been commercialised, for example photocatalytic TiO_2-based self-cleaning glass is currently produced by Pilkington.[61] Another well-known example is the Jubilee church in Rome (2003) which was built using photocatalytic concrete blocks

(Figure 1.7). The first photocatalytic pavement in Belgium was constructed in 2004 at the Leien in Antwerp, which was followed by projects on TiO_2-based concrete roads in Lier and Wijnegem (2011).[84] In addition, simultaneous soot oxidation and NO_x reduction proves promising, for example allowing regeneration of a diesel particulate filter.[94,95]

Figure 1.7. TiO_2-based Jubilee church in Rome. Reprinted from Ref[96] with permission. © Elsevier (2010).

Prior to large-scale application, increased knowledge on photocatalytic soot oxidation is indispensable to overcome present challenges (*e.g.* adverse effects of outdoor conditions, long term activity, selection of optimal photocatalysts). Currently, most studies focus on either self-cleaning aspects or reaction kinetics,[61,88–91,93,97–99] but literature on development and improvement of user-friendly, accurate and unambiguous detection methods is scarce.[92] The quartz crystal microbalance is a commonly used tool to quantify soot degradation by weighing, but has the disadvantage of being expensive and time-consuming. In addition, this method doesn't allow to detect intermediates or end products. Another possible soot oxidation detection method presented in 2009 is based on discolouration of the surface when soot is being degraded using a spectrophotometer.[100] In 2013 Smits *et al.* presented the digital image analysis

(DIA) as alternative method based on the discolouration of the surface. As this method solely relies on digital images it is a cheap and less time-consuming alternative, but still not allowing identification of the formed products.[92] To complement these techniques, a climate chamber coupled to Fourier transform infrared (FTIR) spectroscopy or gas chromatography (GC) is often used to provide insight into the formed end products.[96]

1.3.4 Applications: photocatalytic energy (H_2) production

As previously mentioned, when light with sufficient energy reaches the photocatalyst surface, electron-hole pairs are formed initiating a cascade of oxidation and reduction reactions. Holes can for example be used to oxidise water or organic molecules. Conduction band electrons, on the other hand, can for example be used to reduce protons formed in the oxidation reactions, resulting in H_2 production.[101] Photocatalytic hydrogen production has been known since the discovery of Fujishima and Honda (1972), evidencing light-driven water-splitting by TiO_2, resulting in the production of O_2 and H_2 (see section 1.4).[102] The first article on successful photocatalytic hydrogen production using water and organic compounds was published in 1980 using platinized TiO_2, evidencing enhanced hydrogen production efficiencies in the presence of organic molecules.[103] However, by the middle of the 1980s the enthusiasm rapidly declined as a result of the large challenges hindering efficient photocatalytic hydrogen production, and shifted towards environmental sanitation.[104] To date, the highest STH efficiency obtained with a photocatalytic system is only ~ 1%. An additional drawback is the need for a subsequent separation step as all products (*e.g.* O_2, H_2) are produced together in a single compartment.[101] This problem is overcome by separating the oxidation from the reduction reactions using a two-compartment system. The following section will describe the principle, composition and state of the art of a two-compartment PEC cell in more detail.

1.4 Photoelectrochemical cell

1.4.1 Introduction

The first studies evidencing the possibility of photoelectrochemical (PEC) water splitting were Fujishima and Honda in 1972.[102] Figure 1.8a is a schematic representation of this PEC cell concept completely operated in liquid.[105] It took till 2009 before Seger and Kamat published the first article on the concept of an all-solid PEC cell, using a solid electrolyte membrane (Nafion®) to separate the photoanode from the cathode (Figure 1.8b).[106] Although this new cell design was initially applied in aqueous phase, it also allows to work with gaseous flows, both at anode and cathode. Most current gas phase PEC cells are based on this concept.[28,80,87,107,108]

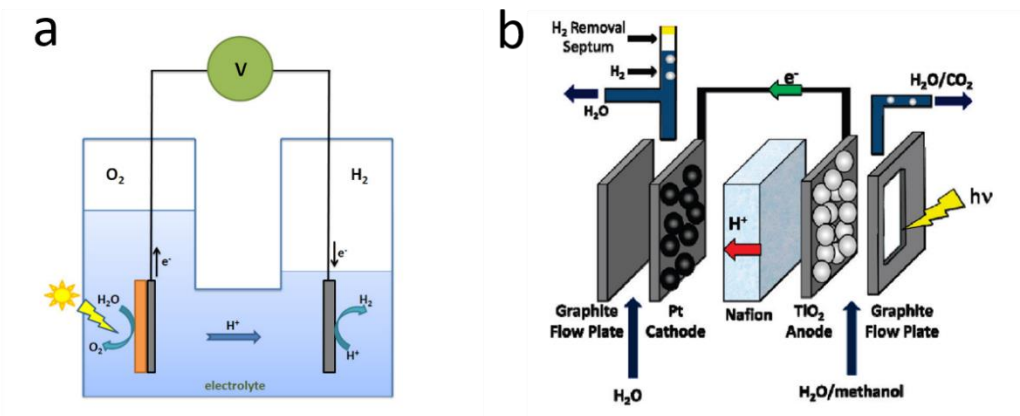

Figure 1.8. Schematical structure of PEC cell according to concept of a) Fujishima and Honda, obtained from Ref[105] with permission and b) Seger and Kamat. Reprinted with permission from Journal of Physical Chemistry C.[106] © American Chemical Society.

When illuminating the photoanode of a PEC cell, electron-hole pairs are formed. As a result, oxidation reactions take place at the photoanode, for example enabling oxidation of water (vapour), thus water-splitting, or oxidation of organic pollutants such as VOCs. Protons formed in these reactions can in this example be transported via a proton-conducting membrane (Nafion®) to the cathode, where they can react with the externally bypassed electrons. Depending on the composition of the cathode flow either the green energy carrier hydrogen gas (inert atmosphere) or water (aerobic conditions) is

produced at the cathode. Thus, part of the energy stored in the oxidised compounds (*e.g.* water, VOCs, soot) can be recovered, either as H_2 gas or electricity.[28,43,109] In this way, multiple SDGs (*e.g.* affordable and clean energy, sustainable cities and communities, climate action (methane), and good health and well-being, Figure 1.1)[3] are targeted simultaneously by a PEC cell.

The possibility to produce H_2 using a PEC cell has been known and studied extensively since 1972, however, PEC cells pursuing electricity production (thus without H_2 production) have only recently come into picture. It was only in 2006 that Kaneko *et al.* introduced the term 'photofuel cell (PFC)' for a PEC cell targeting waste degradation (= fuel) at the anode, while using an O_2-reducing cathode. A so-called PFC thus converts part of the energy of these 'fuel compounds' into electrical energy under illumination.[43] As this term is since then applied in literature as such,[43,110–116] it will also be used in this work to describe a PEC cell targeting simultaneous waste degradation and electricity production. As done in a standard fuel cell - using H_2 as fuel - the PFC thus converts a 'fuel' into electricity. As in a common PEC cell this is obtained by splitting (waste) compounds under illumination at the anode.

A second type of PEC cell is based on the famous work of O'Regan and Grätzel (1991), aiming at electricity production in their so-called dye-sensitised solar cells, which will not be further discussed here.[117] A more detailed explanation of the composition of a PEC cell will be given in the following text, after which the current state of the art will be discussed focussing on VOC and soot degradation.

1.4.2 Composition

The general composition of a PEC cell is shown in Figure 1.8. It consists of a working and a counter electrode, the anode and cathode, respectively. Depending on the application either or both can be photoactive. They are separated by an electrolyte, either an aqueous electrolyte solution (*e.g.* sodium sulphate) or a solid ion exchange membrane (*e.g.* Nafion®), such as used in an all-solid PEC cell. The anode and cathode are externally connected via an electric circuit. Often the (photo)anode consists of an n-type semiconductor (*e.g.* TiO_2) and the cathode is in most cases a noble metal (*e.g.* Pt), resulting in

an electron flow from anode to cathode.[74,109,118] In the following paragraphs a more detailed description of the different components of a PEC cell is given.

(Photo)anode

As mentioned before, in the most common configuration of a PEC cell the anode consists of an n-type semiconductor. A photocatalyst that is often used as photoanode is TiO_2 (see section 1.3.1), but many other materials are currently being studied. There are some important requirements the semiconductors must meet:[119,120]

- Suitable band edge positions for desired oxidation and reduction reactions (Figure 1.9)
- High (visible) light absorption
- Efficient charge transport through the material
- Chemically and photoelectrochemically stable
- Cheap and abundant
- Low (no) toxicity

As described in section 1.3, if the photoanode is irradiated with light containing sufficient energy to bridge the band gap of the material, electron-hole pairs are formed. The electrons (e^-) are externally transported to the cathode where they take part in reduction reactions. It is also possible that, instead, the electrons react with oxygen at the anode, resulting in formation of superoxide anions (0.08 V *vs.* NHE at pH = 0, (Eq. 1.2)), and decreasing the generated photocurrents. The valence band holes (h^+) can react with species adsorbed on the photocatalyst surface. This results in oxidation of water towards oxygen and protons (1.23 V *vs.* NHE at pH = 0, (Eq. 1.3)) and $^{\bullet}OH$ formation (2.8 V *vs.* NHE at pH = 0, (Eq. 1.4)), but it is also possible that the photogenerated holes lead to direct oxidation of other molecules adsorbed on the photocatalyst surface (*e.g.* sulphates, VOCs).[27,28,109,119] As the majority of the target molecules (*e.g.* VOCs) are often in the bulk solution and not adsorbed on the photocatalyst surface $^{\bullet}OH$ plays an important role by facilitating oxidation of these target molecules. The overall reaction of organic molecules present at the anode (at low pH values) is shown in (Eq. 1.5). The exact series of oxidation steps prior to complete mineralisation depends on the complexity of the targeted compound.[109]

$$O_2 + e^- \rightarrow O_2^{\bullet -} \quad \text{(Eq. 1.2)}$$

$$2H_2O + 4h^+ \rightarrow O_2 + 4H^+ \quad \text{(Eq. 1.3)}$$

$$H_2O + h^+ \rightarrow {}^{\bullet}OH + H^+ \quad \text{(Eq. 1.4)}$$

$$C_xH_yO_z + (2x - z)H_2O + (4x + y - 2z)h^+ \rightarrow xCO_2 + (4x + y - 2z)H^+ \quad \text{(Eq. 1.5)}$$

It is thus important that the position of the band edges of valence and conduction band allow the desired reactions to proceed. Therefore, the top of the valence band must be more positive than the redox potential of the desired oxidation reactions (*e.g.* •OH formation, VOC oxidation) and the lower boundary of the conduction band must more negative than the redox potential of the pursued reduction reaction at the cathode (*i.e.* H_2 production or O_2 reduction), as illustrated in Figure 1.9. It is important to include thermodynamic losses and overpotentials in this consideration.[119] Often a bias between anode and cathode is applied to increase the electromotive force and ensure the targeted reactions (*e.g.* chemical bias, externally applied potential).[115]

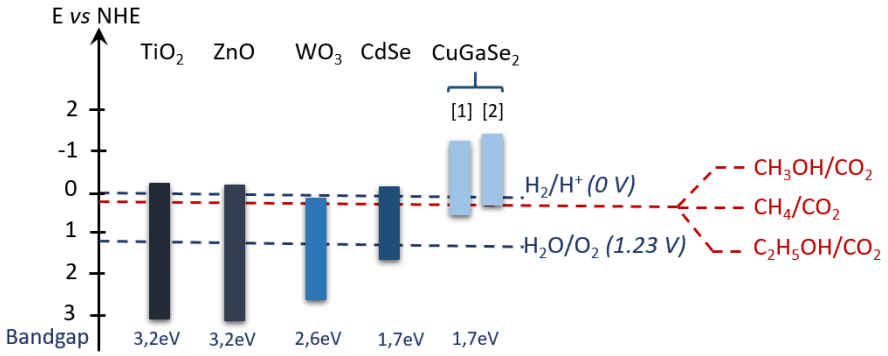

Figure 1.9. E_g values (eV) for different semiconductors at pH = 0 *vs.* NHE. Values for TiO_2, ZnO, CdSe and WO_3 were adapted from Lu *et al.* (2014), the values of $CuGaSe_2$ originate from [1] Leisch *et al.* (2006) and [2] Marsen *et al.* (2008).[119,121,122]

Many different photocatalysts are currently under attention for use as photoanode in a PEC cell. Besides the position of the band gap, the width of the band gap also plays a crucial role as it determines the minimum energy light must have to activate the photocatalyst, as explained in section 1.3. Thus, materials with a larger band gap are restricted to a smaller fraction of the solar spectrum. TiO_2 (E_g = 3.0 - 3.3 eV) for example can only use the UV fraction of

the solar spectrum (~ 5%), which is a large limitation if independent operation solely based on sunlight is pursued.[74,119] Metal oxide semiconductors (*e.g.* TiO_2, ZnO, WO_3, Fe_2O_3, $CuWO_4$, $BiVO_4$) are a first group of possible photoanode materials. The largest limitation of many of these materials, for example TiO_2 and ZnO, is their relatively large band gap (Figure 1.9) and thus low (to none) visible light absorption. In this view, small band gap materials such as metal chalcogenides (*e.g.* CdSe, $CuGaSe_2$) are currently also studied as possible photoanode materials (Figure 1.9). Some other materials that are recently under attention as possible photoanode materials are nitrides and organic materials. In addition, the sunlight activity of a photocatalyst can also be altered by a variety of currently studied processes such as doping and surface plasmon resonance (SPR).[27] Another option that is currently studied to overcome limitations related to a single material is combining different semiconductors, for example coupling a small with a large band gap material (*e.g.* CdSe-TiO_2).[74,123] To date, however, there is no semiconductor that fulfils all requirements for use in a PEC cell and further research on potential PEC photoanodes is necessary.[74,118,120]

Cathode

Photogenerated electrons formed at the photoanode that have not recombined will be externally bypassed to the cathode. Which reaction occurs at the cathode is in principle independent of the type of molecules that are present at the photoanode, but depends solely on the pH and the molecules present at the cathode. When H_2 production is targeted (0 V *vs.* NHE at pH = 0, (Eq. 1.6)), reactions at the cathode should be carried out in an inert environment (*e.g.* N_2). In this case, the externally bypassed electrons can react with protons that are formed in the series of reactions at the photoanode and transferred through the proton conducting membrane separating anode from cathode. The overall reaction in the PEC cell in that case is given by (Eq. 1.7). When on the other hand electricity production is targeted, the presence of O_2 at the cathode is required, resulting in (Eq. 1.8) at the cathode and (Eq. 1.9) when looking at the overall reaction in the PEC cell.

$$2H^+ + 2e^- \rightarrow H_2 \qquad \text{(Eq. 1.6)}$$

$$C_xH_yO_z + (2x - z)H_2O \rightarrow xCO_2 + (2x + \frac{y}{2} - z)H_2 \quad \text{(Eq. 1.7)}$$

$$2H^+ + \frac{1}{2}O_2 + 2e^- \rightarrow H_2O \quad \text{(Eq. 1.8)}$$

$$C_xH_yO_z + \left(x + \frac{y}{4} - \frac{z}{2}\right)O_2 \rightarrow xCO_2 + \frac{y}{2}H_2O \quad \text{(Eq. 1.9)}$$

In contrast to the high diversity in possible photoanode materials, the options for the cathode are limited. The most commonly used material is the electrocatalyst platinum (Pt). Many different configurations are possible, such as Pt-sheets, Pt-wires, Pt-foils or a Pt/carbon-black electrocatalyst deposited on a substrate (*e.g.* carbon paper, carbon cloth).[106,115] The high price of Pt is an important bottleneck that could hamper mass production of PEC cells in the future. Therefore, more research towards Pt-free counter electrodes is currently being performed (*e.g.* metal sulphides, mixed metals (*e.g.* NiCo, NiMo), active metal oxides (*e.g.* RuO_2, SrNbO)).[74,115,124]

Ion exchange membrane

An electrolyte is added between the anode and cathode of a PEC cell to avoid build-up of charges as it allows ions (H^+ or OH^-) to migrate between both compartments of the cell.[74] A distinction can be made between PEC cells operated in liquid and gas phase. In liquid phase, the choice of electrolyte depends on a variety of factors such as which semiconductor is used. To reduce ionic transport resistances and Nernstian potential losses due to pH gradients generally strongly acidic or basic liquid electrolytes are used. When TiO_2 is used, the most frequently used electrolytes are NaOH and KOH, thus obtaining a high pH and high OH^- concentration, and consequently efficient hole scavenging and production of $^{\bullet}OH$ radicals.[115] Another factor influencing the choice of electrolyte is the location in the PEC cell (anode/cathode). This is the case when two different electrolyte solutions are added in a two-compartment cell separated by an ion-exchange membrane (*e.g.* Nafion®). In this case, the electrolyte at the anode is often a base (*e.g.* NaOH), while the electrolyte at the cathode is often acidic (*e.g.* H_2SO_4) to promote H^+ conductivity, inducing a chemical bias.[109,115] A major advantage of this configuration is minimisation of product crossover (*e.g.* O_2, H_2, CO_2).

As shown by Seger and Kamat in 2009, an ion exchange membrane or solid electrolyte is also used in all-solid cells. An adapted configuration is used in these all-solid PEC cells with a membrane electrode assembly (MEA, Figure 1.8b) positioned in the centre of the cell consisting of anode, electrolyte and cathode. The use of a MEA has the added benefit of minimised electrolyte resistance and associated current losses due to the reduced distance between the two electrodes.[106] These solid electrolytes can be either proton exchange membranes (PEM) or anion exchange membranes (AEM).[106,125,126] Some common solid acid electrolytes are perfluorosulfonic acid, sulfonated polyether ketones, polyether sulfones and poly benzimidazoles. The most widely used solid electrolyte is a perfluorosulfonic acid membrane produced by Dupont, called Nafion® (Figure 1.10a).[74,127] When Nafion® is exposed to water, hydrated pockets form that surround the hydrophilic sulfonate groups. When sufficiently swollen, the pockets connect with each other, allowing protons to move through the membrane (Figure 1.10b).[128] Nafion® has a relatively good chemical and thermal stability, high mechanical strength, desirable proton conductivity and low gas crossover. However, its relatively high price and low lifetime spur research on alternative materials for ion exchange membranes.[74,128,129] Other materials that can be used as solid acid electrolytes are composite materials and hydrocarbon based materials. Some solid alkaline ion diaphragms are also developed (*e.g.* polymer materials, metal oxides), which are known for their high robustness, but relatively low ion conductivity and high gas crossover.[74,125,127]

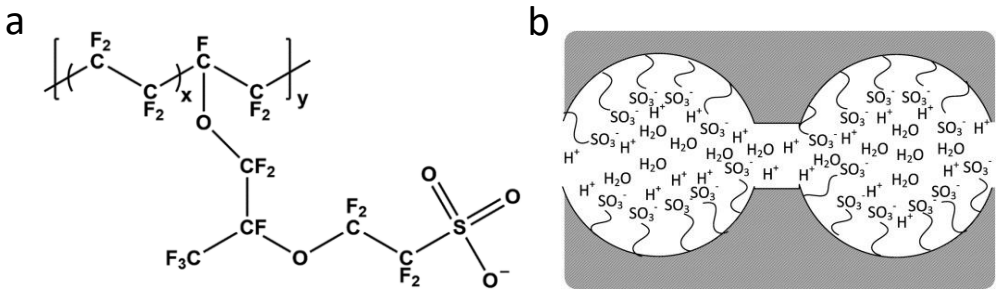

Figure 1.10. a) The structural formula of Nafion® 117 membranes, obtained from Ref[130] with permission and b) a concept of the cluster structure of Nafion® where the negative charge of SO_3^- is compensated by protons, obtained from Ref[128] with permission.

Electrode substrate and electrical circuit

Depending on the configuration of the PEC cell, the catalysts at anode and cathode can be either self-supporting (*e.g.* Pt-wires) or deposited on a substrate. When transparent substrates are required conductive oxide electrodes such as indium tin oxide (ITO) and fluorine-doped tin oxide (FTO) are often used. An important drawback of these substrates is their relatively low conductivity.[115,118] Other possible (non-transparent) substrates are metal electrodes (*e.g.* titanium) and carbon paper/cloth, the latter known for their high porosity and conductivity.[106,115]

In most cases PEC cells use external conducting wires (*e.g.* Cu, stainless steel, Pt) for electron transport between anode and cathode as they result in a high electrical conductivity and limited ionic transport distance between both electrodes.[131]

1.4.3 Applications: PEC VOC oxidation with energy recovery

Extended research has been performed on photoelectrochemical degradation of organics present in liquid phase. To this end, methanol, ethanol and glycerol are the most widely studied organics as they give high yields, are easy to photodegrade, widely available, relatively cheap and extensive literature on these molecules is available.[109] When for example applying (Eq. 1.5) for a photoanode flow containing a combination of water and methanol (either in gas or liquid phase), (Eq. 1.10) is obtained (Figure 1.11a):

$$CH_3OH + H_2O + 6h^+ \rightarrow CO_2 + 6H^+ \qquad \text{(Eq. 1.10)}$$

As mentioned above, the series of oxidation steps at the photoanode depend on the complexity of the targeted compound. A variety of intermediate species (*e.g.* formaldehyde, formic acid) can be formed before complete photoelectrochemical methanol mineralisation is obtained.[132] Up to 10-fold efficiency increases were observed when short-chain alcohols and glycerol were oxidised in a PEC cell compared to pure water-splitting PEC cell operation.[133]

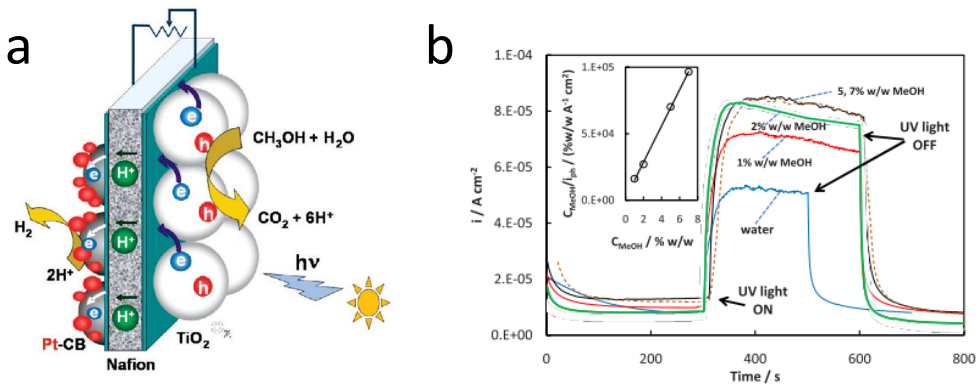

Figure 1.11. a) Operating principle of photoelectrochemical methanol oxidation using a TiO_2/ Nafion®/Pt-CB assembly. Reprinted with permission from Ref[106]. © American Chemical Society. b) CA curves when using a TiO_2/ Nafion®/stainless steel assembly held at +1.00 V vs Ag/AgCl in water-saturated and 1, 2, 5, and 7 wt% methanol solution-saturated air streams under UV-A illumination. Inset: Plot of C_{MeOH}/I_{ph} vs. C_{MeOH}, where C_{MeOH} is the methanol solution concentration (wt%) and I_{ph} is the net dark current-corrected photocurrent density (A cm^{-2}). Graph is obtained from Ref[107] with permission.

Upon introduction of either methanol, ethanol or glycerol in a photoanode flow consisting of pure water, a clear photocurrent increase is observed as shown in Figure 1.11b for methanol. As all three organics are known electron donors, enhanced hole scavenging in the presence of these compounds could possibly explain these increased photocurrents. In addition, a second phenomenon is known to contribute to this observation, namely current doubling. This phenomenon is attributed to the formation of unstable radicals when oxidising a sacrificial agent, resulting in subsequent injection of electrons into the conduction band of the photocatalyst. For methanol for example, the methoxy radical $H_3CO^{\bullet}$ can be formed as intermediate (one-hole oxidation), which can in turn inject an electron into the conduction band of the photocatalyst. In this way, one absorbed photon results in the generation of both a photogenerated and an injected electron, and thus current doubling. When a forward bias is applied, and consequently recombination is reduced, current doubling effects are more pronounced.[109] This increase in generated photocurrent upon introduction of a sacrificial (both organic and inorganic) agent, makes photoelectrochemical oxidation of these compounds even more interesting.

At the start of the 21th century, a broader range of organic molecules was studied, mainly focusing on waste materials and pollutants.[43,45,87,107,132–134] As PEC

cells prove useful for the degradation of a broad range of waste products and pollutants, they can be considered for a broad variety of environmental applications.[133] The use of PEC cells for environmental applications becomes even more interesting when considering the simultaneous energy recovery (either as electricity or H_2 production) and the possibility to operate a PEC cell solely using sunlight (and pollutants/waste). However, further research on more sunlight active photoanodes is needed to make sunlight-driven PEC cell operation a more efficient process (*e.g.* doping, plasmonic nanostructures, efficient small band gap photocatalysts).[27] Currently, extensive research is being performed on the application of PEC cells for waste water treatment.[43,45,132–134] In contrast to the broadly studied field of photoelectro-chemical waste water purification, only limited research has been performed on the application of PEC cells for air purification.[28,87,107] Although only scarcely studied, complete gas phase operation of PEC cell presents a number of advantages:[135,136]

- Able to cope with higher temperatures and pressures (enhanced kinetics)
- Reduced risk of contamination of membranes and electrodes
- Reduced complexity (*e.g.* no need for frost protection or pumping system), resulting in decreased costs and increased lifetime
- Reduced risk of corrosion
- Avoids diffusion limitations

Georgieva *et al.* (2009) were the first to showcase oxidation of organic vapours using a PEC cell, pointing at the potential of the PEC technology for air purification with simultaneous energy recovery (Figure 1.11b showing similar results from 2010). For this proof of concept they applied an external bias and targeted H_2 gas production at the cathode. A significant increase in generated photocurrent (I_{ph}) was observed when flushing the photoanode with a moist methanol vapour instead of pure water vapour. This increase in generated photocurrent upon methanol introduction was ascribed to scavenging of photogenerated holes and OH radicals by methanol.[87] Georgieva *et al.* repeated these experiments (2010) with a pure TiO_2 photoanode and additionally performed cyclic voltammetry (CV) measurements, hereby evidencing methanol oxidation over a range of applied potentials, reaching maximal

photocurrent generation at 1 V. This result was attributed to the nanoparticulate structure of the used TiO_2 photoanode.[107] Subsequently, Iwu *et al.* (2014) evidenced a positive temperature effect increasing the generated photocurrents when heating the PEC cell, which was limited to 45°C by dehydration of Nafion®.[137] As mentioned earlier, the research area of PEC cells using waste products and pollutants as fuels to generate electricity (*i.e.* photofuel cell) is still relatively new, with – to the best of our knowledge - only a single paper reporting on complete gas phase application of this system so far.[116]

1.4.4 Applications: PEC soot oxidation with energy recovery

As photocatalytic soot oxidation is still a relatively new research field ($<$ 20 years), to the best of our knowledge, photoelectrochemical soot degradation has not been studied yet.

1.5 Motivation and outline

As explained in the introduction, today's society is faced with a wide range of environmental problems. Both the quest for clean air and sustainable energy production are currently receiving worldwide attention. In section 1.4 a technology was presented – the photoelectrochemical (PEC) cell - tackling both problems simultaneously.

The goal of this thesis is to study autonomous, all-gas phase PEC cell operation simultaneously degrading air pollution (*e.g.* VOCs, soot) and producing energy (*i.e.* H_2 gas or electricity) using (sun)light.

Using light a PEC cell allows to convert part of the energy stored in the degraded (waste) compounds into energy, either as H_2 gas or electricity. The all-solid PEC cell used in this thesis is based on the concept presented by Seger and Kamat in 2009. The two-compartment cell is constructed around a membrane electrode assembly (MEA), using Nafion® as a proton exchange membrane. At the photoanode targeted molecules (*e.g.* organic pollutants) can be mineralised towards CO_2, while the protons transported through the Nafion® membrane are used at the cathode to form H_2 or water (in case only electricity production is targeted) by reaction with the externally transferred electrons. PEC cells have been widely studied and proven promising for application in liquid phase (*e.g.* energy recovering waste water treatment). Application of a PEC cell in gas phase (*e.g.* air purification) on the other hand is a more novel research area. The first promising results for biased H_2 production using an all-gas phase PEC device were obtained around ten years ago, as described in more detail in the introduction.

Most literature focusses on PEC cells targeting H_2 production by applying an external bias. In the first experimental chapter (= **Chapter 2**) a PEC cell will be operated completely in gas phase to obtain a proof of concept of an unbiased all-gas phase PEC cell, starting from the - in liquid phase - broadly used two-compartment configuration. In addition, increased insight into the operation of an all-gas phase PEC cell (*i.e.* effect of O_2, possible reaction pathways) was gathered in this chapter.

As mentioned in the introduction, PEC cells targeting H_2 production have been extensively studied (in liquid phase), while PEC cells pursuing electricity production have only recently gained attention. The production of electricity instead of H_2 gas might overcome some important bottlenecks limiting implementation of the PEC cell technology. A first important limitation is that depending on the applied photocatalysts, the redox potential of H_2 evolution often requires the application of an external bias, reducing the net energy gain of the system. Other important limitations are the lack of a broadly developed H_2 infrastructure and the very small amounts of H_2 that are produced with autonomous PEC cells. Only in 2006 Kaneko and co-workers presented the idea of a photofuel cell (PFC). This is a PEC cell degrading waste products and pollutants (= 'fuel') targeting electricity production (aerobic cathode compartment). This recently novel PEC cell concept has since been increasingly studied to target liquid wastes and pollutants, while research on gas phase PFC operation is still scarce. A low-cost waste gas-to-electricity PFC device developed in our lab will be studied in **Chapter 3** (Figure 1.12), targeting simultaneous VOC degradation and electricity generation.

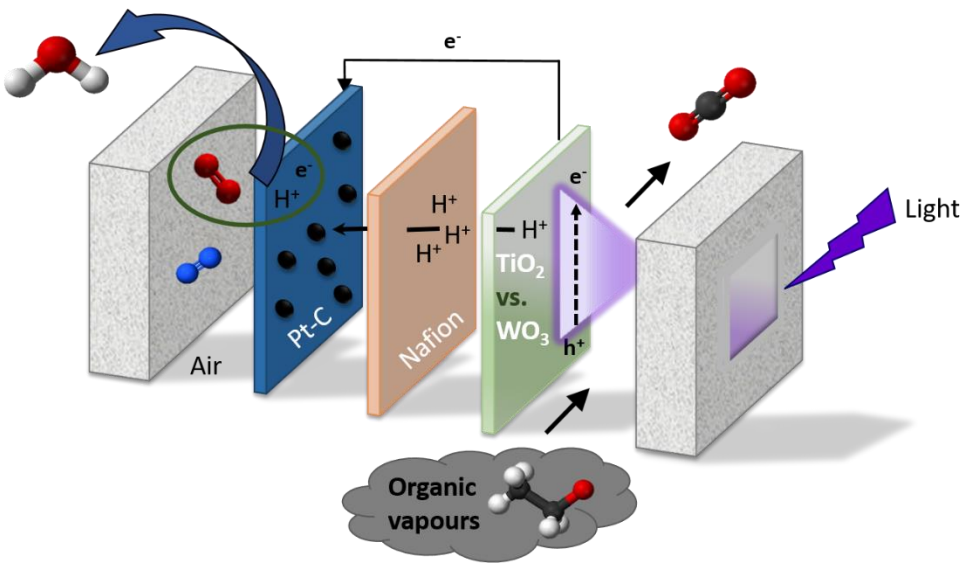

Figure 1.12. Schematical representation of PFC system as used in this thesis.

A broad variety of photoanodes can be used to this end as described in the introduction. TiO_2 is an interesting photocatalyst due to a wide range of positive characteristics such as its stability, low cost, high abundance and high

photoactivity. Therefore, a large part of the literature on photocatalysis focusses on TiO_2-based photocatalysts. An important drawback of TiO_2 is its large band gap (3.0 - 3.3 eV), limiting it to the use of UV light, while UV light only accounts for ~ 5% of the solar spectrum. When aiming at energy-efficient, and thus sunlight-driven, photocatalytic applications visible light active photocatalysts are promising candidates. A visible light active photocatalyst increasingly studied in the past ten years for a wide range of applications is WO_3 (band gap = 2.5 - 2.8 eV). It is known for its stability, low cost, low toxicity and visible light activity (< 500 nm, ~ 12% of solar spectrum). The performance of a range of TiO_2- and WO_3-based photocatalysts as photoanodes will be compared in **Chapter 3**.

The concept of an unbiased all-gas phase PEC cell simultaneously degrading VOCs and producing energy was validated and studied in more detail in the first two experimental chapters. Air pollution is a broad problem, covering a wide range of compounds including, besides VOCs, also particulate matter. An important component of PM is soot, mainly consisting of elemental carbon and carbon-based organic matter. High PM, and thus soot, concentrations are a globally encountered problem, especially troubling urban areas. This problem is described in more detail in the introduction. When aiming at real-life application of photocatalysis as an environmental sanitation process, the ability of the employed photocatalysts to cope with soot is crucial for long-term performance in soot contaminated environments. In the case of a PEC cell, continuous deposition of soot on the photoanode surface will eventually result in complete blocking of all incoming light, and thus inhibition of all photocatalytic reactions. In addition, the presence of soot might interfere with the ongoing reactions at the photoanode. Therefore, to obtain a widely applicable PEC cell, the soot oxidation capacity of the photoanode is crucial for long-term, and thus sustainable, operation of the device. To study this, a low-cost and accurate soot oxidation detection method is required. However, the limited soot oxidation detection methods present are either expensive, time-consuming and/or incomplete, as described in the introduction. Therefore, in **Chapter 4** an existing low-cost and time-efficient optical soot oxidation detection method was improved and validated, obtaining a complete and accurate soot oxidation detection methodology. In **Chapter 5**, this method was

applied on the in chapter 3 studied TiO_2- and WO_3-based photoanode materials to determine their photocatalytic soot oxidation capacity under different light sources. In doing so, the method was adapted, expanding the application range to inherently coloured (visible light active) materials. In the last experimental chapter of this thesis, **Chapter 6**, the best performing photocatalysts and photocatalyst-combinations were selected for further study, considering both their photocatalytic soot oxidation capacity and photoanode performance. The ability of these photoanodes to cope with soot deposition during PFC operation was determined. Finally, the in-house engineered PFC device was applied outdoor, targeting autonomous operation using solely sunlight and outdoor air to drive the waste gas-to-electricity PFC device.

Chapter 2

Proof of concept of an unbiased all-gas phase photoelectrochemical cell

Based on:

Sammy W. Verbruggen, **Myrthe Van Hal**, Tom Bosserez, Jan Rongé, Birger Hauchecorne, Johan A. Martens, and Silvia Lenaerts, *Harvesting hydrogen gas from air pollutants with an unbiased gas phase photoelectrochemical cell*, ChemSusChem (Inside back cover). 10 (2017), p. 1413-1418. http://doi.org/10.1002/cssc.201601806.

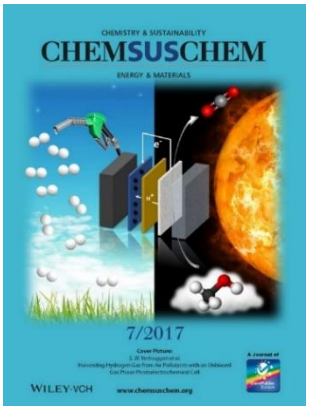

Author contributions:

M.V.H. performed the experiments and assisted with writing the paper.

S.W.V. designed the experiments and wrote the paper.

T.B. and J.R. performed the hydrogen measurement and designed the PEC cell.

B.H. assisted with writing the paper.

J.A.M. and S.L. supervised the work.

2.1 Introduction

Today's society is faced with two persistent demands: a healthy living environment and sustainable energy production, both are described in more detail in Chapter 1. In both contexts, the use of semiconductors as photocatalysts has been identified as a promising technology. Heterogeneous photocatalysis has proven to be successful in both light-driven hydrogen production through water splitting,[138,139] and for the degradation of organic pollutants in gaseous media.[27] Both applications can be targeted simultaneously in a single device: a solid and stand-alone photoelectrochemical (PEC) cell. PEC cells have been widely studied and proven promising for application in liquid phase,[45,113,132,140–142] while gas phase PEC cell operation is a relative recent research area.[80,87,107,143] In an air purifying PEC cell part of the energy stored in airborne pollutants is recovered (as H_2 gas or electricity), while mineralizing the contaminants to less harmful CO_2.

In this chapter simultaneous degradation of volatile organic compounds (VOCs) and hydrogen production is studied using an all-gas phase PEC cell. In this case, oxidation of VOCs occurs at the photoanode, while hydrogen is produced at the (dark) cathode on the opposite side of a proton-conducting solid electrolyte membrane. This concept of an all-solid PEC cell with oxidation reactions and H_2 evolution in separated compartments was first proposed by Seger and Kamat in 2009.[144] In 2014 Rongé and co-workers have successfully explored the possibility of using water vapour (ambient humid air), rather than liquid water as the anode feed based on this design.[145] In the quest for coupling air treatment with energy production in a PEC cell, available literature is scarce. Georgieva *et al.* showcased the photooxidation of organic vapours using a solid PEC cell with a different design and by applying additional external bias.[80,107,146] In addition, the actual H_2 yield was not determined. In this chapter, the absence of external bias is a crucial operating parameter for evolving towards autonomous real-life applications. Although autonomous water splitting using TiO_2 is often regarded difficult because of the overpotential involved in the reaction, it has clearly been shown to be feasible.[106] In other reports, the gas feed is generated by bubbling an inert carrier gas (*e.g.* Ar) through a gas wash bottle containing a solution of organic contaminants.[108] When considering air pollution, however, the presence of oxygen in the gas mixture should not be

neglected, as it could scavenge the photogenerated electrons at the photoanode, rendering them unavailable for H_2 evolution.[147] In this chapter we therefore investigate the effect of oxygen on the photocurrent delivered by the cell, but also its effect on the photocatalytic reaction pathway at the photoanode by online FTIR analysis of the anode gas outlet. This should lead to a better understanding and fast development of stand-alone (*i.e.*, unbiased) gas phase PEC devices for converting air pollution to energy.

2.2 Experimental

2.2.1 PEC cell

The PEC cell design and membrane electrode assembly (MEA) are described and characterized in detail by Rongé and co-workers in 2013.[147] In brief, the photoanode (0.5 mg cm^{-2} P25 TiO_2 (Evonik) on Toray paper 030 (Fuel Cell Earth)) was calcined at 450°C for 2 h and embedded in 0.015 mg cm^{-2} Nafion® (Sigma-Aldrich). Subsequently, the anode and cathode (0.09 mg cm^{-2} Pt on carbon black (Umicore) on Toray paper 030) were fixed on opposite sides of a preconditioned Nafion® 117 membrane (Quintech) by hot-pressing between two Teflon liners at 130°C for 2.5 min. The as-prepared MEA was mounted in the PEC cell by sandwiching the MEA between a graphite block (cathode side) and a transparent fused-silica plate (anode side), both with grafted serpentine flow fields (Figure 2.1).

To irradiate the cell, a Philips Cleo 25 W UVA light source was positioned at a distance of 5 cm from the fused-silica plate, resulting in an incident intensity of 4 mW cm^{-2}, which roughly corresponds to the UV content of solar radiation on earth.

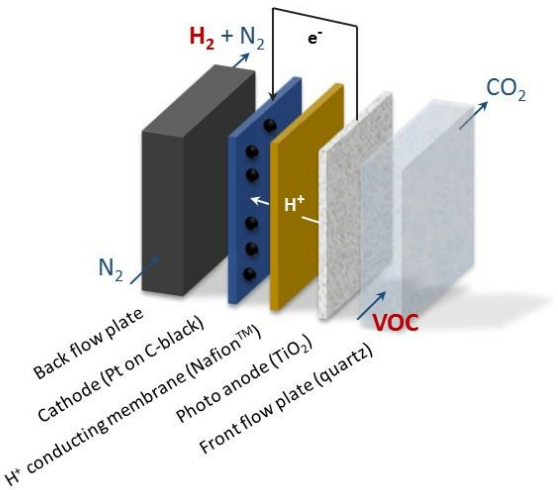

Figure 2.1. Schematic representation of the PEC cell as used in this chapter.

2.2.2 Aqueous phase experiments

Methanol (VWR Analytic, >99.8%) solutions were prepared in deionized water (< 0.5 µS cm^{-1}) with concentrations of 0, 0.1, 1 and 5 wt%. In a first set of experiments each solution was purged with pure N_2 for 1 h in order to remove all traces of O_2. The purged solution was then pumped (Thermo Scientific FH10 peristaltic pump) through the anode compartment at a pumping speed of 1.2 mL min^{-1}. After 1 h equilibration in dark conditions, a 90 s chrono-amperometric (CA) measurement was conducted under UV illumination using a potentiostat (Versastat 3, Princeton Applied Research). The generated photocurrent density was calculated by dividing the measured photocurrent by the area of the anode surface exposed to the light source (0.8 cm^2). To study the effect of oxygen present in the system, the solutions were purged with synthetic air (21% O_2, Messer) for 1 h and analysed likewise. The cathode compartment was flushed with N_2 at 50 mL min^{-1} at all times to avoid gas cap formation over the cathode.[148]

2.2.3 Gas phase experiments

Gas phase experiments were conducted in a fully automated gas test setup developed in our group.[149] To introduce methanol and/or water vapour in the gas flow, a gas wash bottle filled with either pure deionized water, or a 5 wt%

aqueous methanol solution was mounted in the setup. Carrier gas was bubbled through this vessel at a steady flow rate of 50 mL min^{-1}. The carrier gas was pure N_2 or synthetic air containing 21% O_2 (Messer) to investigate the effect of oxygen on cell performance. According to Raoult's law for partial vapour pressures in ideal gas mixtures, a maximum theoretical methanol vapour concentration of 0.15 mol m^{-3} was thus attained. The composition of the gas stream was continuously analysed online by Fourier transform infrared spectroscopy (Thermo Fisher Scientific Nicolet 380 with ZnSe windows and 2 m heated gas cell). A humidity sensor (Vaisala) was attached to the gas outlet. The cathode compartment was flushed with N_2 at 50 mL min^{-1} at all times to avoid gas cap formation over the cathode.[150] After equilibration of the outlet concentrations, long CA measurements (20 min) were conducted using the potentiostat, while simultaneously monitoring the changes in outlet gas composition by FTIR. The generated photocurrent density was calculated by dividing the measured photocurrent by the area of the anode surface exposed to the light source (0.8 cm^2).

2.2.4 H_2 evolution efficiency

The Faradaic efficiency for H_2 evolution was determined using a quantitative gas analyser (Hiden Analytical). An inert argon flow was bubbled at a rate of 25 mL min^{-1} through a 5 wt% aqueous methanol solution in MilliQ water, sent through the anode compartment and then to the detection unit. The cathode compartment was flushed with pure N_2 at 25 mL min^{-1} at all times. The gas evolution was corrected for slight fluctuations in flow rate by means of the N_2 signal. To ensure a measurable quantity of H_2 well above the detection limit of the apparatus, the cell was irradiated by a 400 W broad spectrum Xe source (200 - 750 nm, Oriel 66984, Newport) adjusted so the incident intensity was 100 mW cm^{-2}. The generated photocurrent was collected by the potentiostat. Ultimately, the Faradaic efficiency was determined as the ratio of the actual amount of H_2 collected, over the theoretical amount of H_2 that can be produced from the generated photocurrent, as calculated by the formula (Eq. 2.1):

$$Theoretical\ H_2\ (mL) = \frac{Q\ .\ V_m}{n\ .\ F} \qquad \text{(Eq. 2.1)}$$

with Q the total amount of photogenerated charge (C), V_m the molar gas volume (22400 mL mol^{-1}), n the number of e^- in the reaction (2) and F the Faraday constant (96 485.34 C mol^{-1}).

2.3 Results and discussion

2.3.1 Aqueous phase experiments

As a first short test, the cell's capacity for organic waste water remediation was studied. Methanol was selected as a model compound, as it is convenient to study and it is the best available system described in literature. Different aqueous methanol solutions were prepared with concentrations of 0, 0.1, 1 and 5 wt%. First, the solutions were purged with N_2 gas to remove all oxygen. Next, the purged solutions were pumped through the serpentine flow channels of the anode compartment at a pumping speed of 1.2 mL min^{-1}. After 1 h equilibration in dark conditions, a chronoamperometric measurement was started under UV illumination. The *I-t* plots for all four solutions are given in Figure 2.2a. It was observed that a methanol concentration of 0.1 wt% hardly influences the generated photocurrent and basically remains at the same level as pure water (around 10 µA cm^{-2}). At higher methanol content, the photocurrent density increases to a level of ca. 25 µA cm^{-2} for 1 wt% (an increase of a factor of 2.5 compared to pure H_2O) and 45 µA cm^{-2} for 5 wt% (an increase of a factor 4.5 compared to pure water). The observed increase in photocurrent is comparable to the findings of Seger and Kamat, who observed a 3-fold increase in photocurrent for a 1 wt% methanol solution compared to pure water.[151] In absolute numbers, however, the photocurrent obtained in their work is almost one order of magnitude higher, which is evident due to a larger photocatalyst loading at the anode (3 mg cm^{-2} *vs.* 0.5 mg cm^{-2}), the presence of 0.1 M H_2SO_4 as an electrolyte and a stronger irradiation source (100 mW cm^{-2} Xe source *vs.* 4 mW cm^{-2} UVA light).

Next, the influence of oxygen on the generated photocurrent was investigated. For this experiment all solutions were purged with synthetic air for 1 h, prior to each chronoamperometric measurement. The results are presented in Figure 2.2b. Fortunately, the trend of increasing photocurrent density with increasing methanol content is well retained. On the other hand, an average decrease of

40% is observed compared to the photocurrent density generated under N_2 purge. This effect is explained by electron scavenging of O_2 molecules at the photoanode with the formation of superoxide anions ($O_2^{\bullet -}$),[147] similar to the observed recombination process of photogenerated electrons with I_3^- ions at the semiconductor-electrolyte interface in dye-sensitized solar cells.[152] Nonetheless, the available photocurrent is still almost 3 times higher in the presence of organic pollution compared to pure PEC water splitting.

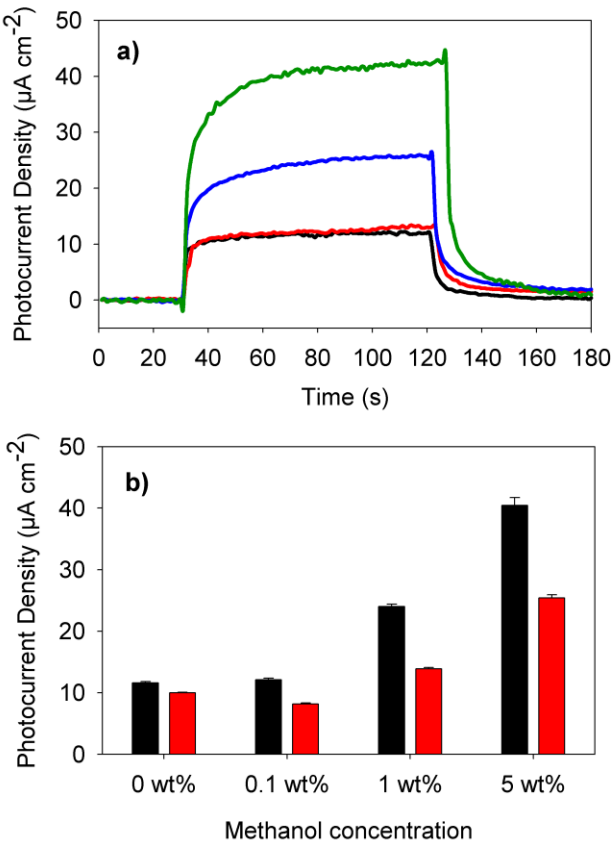

Figure 2.2. Aqueous phase experiments. a) Photocurrent density as a function of time obtained for N_2-purged aqueous solutions of methanol at concentrations of 0 wt% (black), 0.1 wt% (red), 1 wt% (blue) and 5 wt% (green) as the photoanode feed. b) Photocurrent density obtained for different aqueous methanol solutions in the absence (*i.e.* N_2-purged, black bars) and in the presence (*i.e.* purged with air, red bars) of dissolved oxygen. All experiments were performed without applying any external bias and a N_2-purged cathode.

2.3.2 Gas phase experiments

After benchmarking the cell in aqueous phase and evaluating the effect of dissolved oxygen, the PEC cell was tested for gas treatment. A gas wash bottle was filled with pure water or a 5 wt% methanol solution and mounted in a fully automated gas analysis setup.[149] A steady flow of N_2 gas was bubbled through the bottle at a constant rate of 50 mL min^{-1}. A humidity sensor (Vaisala) was connected to the gas outlet and 65% relative humidity was measured. For studying the PEC air treatment performance in realistic conditions, that is, in the presence of 21% O_2, the carrier gas was changed from N_2 to compressed air (Messer). The chronoamperometric measurements under UV illumination were performed over a time span of 20 min to enable the detection of all formed intermediates and mineralization products by infrared spectroscopy of the gas outlet (see below). The resulting *I-t* plots in the presence and absence of methanol vapour, when using an inert or an oxygenated carrier gas, are shown in Figure 2.3.

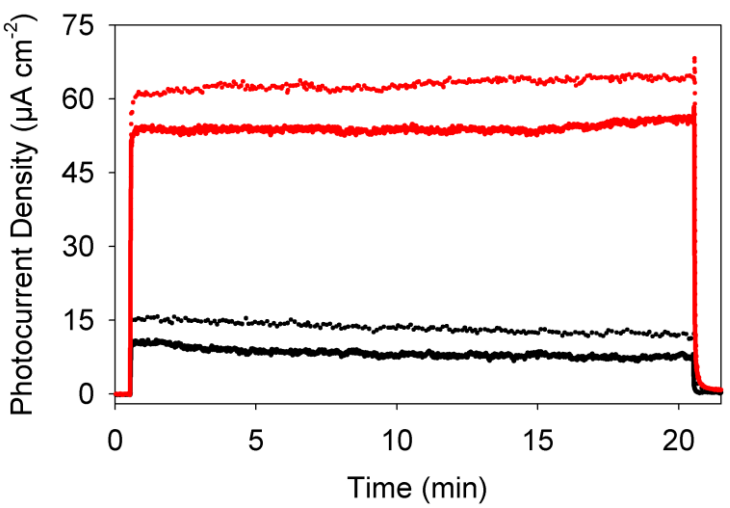

Figure 2.3. Gas phase experiments. Photocurrent density as a function of time obtained for pure water vapour (black) and water-methanol vapour (red) using air (solid lines) or N_2 (dotted lines) as the carrier gas. All experiments were performed without applying any external bias and a N_2-purged cathode. UV on at t = 1 min, UV off at t = 21 min.

The first striking observation is that under inert atmosphere, the photocurrent densities for water vapour as well as methanol vapour are about 30% higher compared to their liquid-phase equivalents (*cf.* Figure 2.2). This could be owed to the absence of diffusion limitations in gas phase.[153] Secondly, the increase in photocurrent in the presence of methanol vapour compared to pure water vapour is again a factor of 4.5, thus similar to the aqueous phase measurements. Finally and more importantly, the effect of oxygen is not as detrimental in gas phase as in aqueous phase. For the methanol-rich vapour feed, a current decrease of only 8% is observed in air instead of inert N_2 as the carrier gas, resulting in a photocurrent that is almost 5 times higher compared to pure water vapour. This is a very encouraging result that spurs further investigation of PEC-based air treatment for energy recovery. In addition, it should be stressed again that all these results are obtained without applying external bias and the electrode materials are not yet fully optimized toward cell performance.[154] This proof of concept is thus an important step in the development of stand-alone PEC cells for simultaneous pollutant abatement and energy recuperation, but still offers ample room for improvement in follow-up studies. For instance, ongoing investigations by our group involve modification of the anode material with plasmonic alloy nanoparticles, of which we have shown they can span the entire UV-VIS spectrum thereby effectively increasing solar photon utilization.[155,156]

As mentioned above, all gaseous species formed during photooxidation at the anode were analysed by infrared spectroscopy. To facilitate the analysis, a representative spectrum of the steady-state gas outlet in dark condition is subtracted from a representative spectrum obtained during illumination (more precisely, after 18 min continuous illumination). These FTIR difference spectra are plotted in Figure 2.4 for both cases in which N_2 (blue) or air (red) was used as the carrier gas. The negative bands in the region 2700 - 3100 cm^{-1} (ν(CH)) corresponding to the C-H stretching vibrations of methanol confirm its disappearance. The mineralization of methanol is furthermore evidenced by the formation of CO_2, as measured in the wavenumber range 2290 - 2390 cm^{-1} (ν_{as}(O=C=O)). This is not attributed to the decomposition of Toray paper, as verified by blank experiments. Comparison of the integrals of the CO_2 bands in this wavenumber region for both carrier gases, reveals 20% more complete

mineralization when air was used. In that case, O_2 was involved directly in the photooxidation process through, for instance, $O_2^{\bullet-}$ radical-initiated pathways after scavenging of photogenerated electrons by O_2 molecules. This is also in line with the observed decrease in photocurrent in the presence of O_2, which clearly exposes a trade-off between more complete pollutant abatement (mineralization to CO_2) *versus* photocurrent generation and consecutive H_2 production.

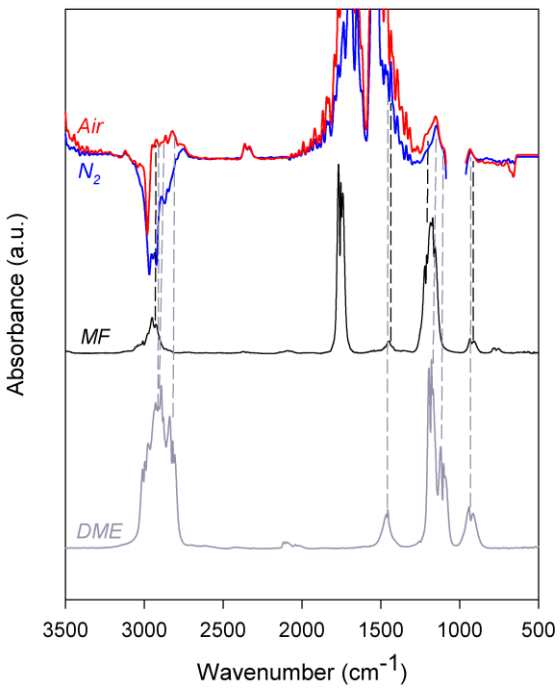

Figure 2.4. Gas phase experiments. FTIR difference spectra of the anode compartment gas outlet obtained by subtracting the spectrum in dark conditions from the one during illumination, for a methanol-rich vapour feed and using air (red) or inert N_2 (blue) as carrier gas at the anode. Reference FTIR absorbance spectra of the formed intermediates MF (black) and DME (grey) as obtained from the NIST database are also shown and the corresponding absorption bands are indicated by dotted lines. Spectra were smoothed for clarity purposes.

The FTIR difference spectra also reveal additional features that are not ascribed to methanol. Prominent bands in the regions 870 - 955 cm^{-1} ($\nu(OCH_3)$) and 1075 - 1245 cm^{-1} ($\nu(CO)$ and $\delta(CH_3)$) are observed for both carrier gases. In the presence of oxygen, additional shoulders are observed in the regions 1195 -

1210 cm^{-1} (ν(CO)) and 1080 - 1130 cm^{-1} ($\delta(CH_3)$), which can be related to C-O stretching and C-H bending (rocking) vibrations. Typical C-H stretching vibration bands between 2780 and 2960 cm^{-1} (ν(CH)) are also observed only when O_2 is present. Considering the possible oxidation pathways for methanol in both anaerobic and aerobic conditions, and comparative analysis of the FTIR difference spectra with spectra of possible gaseous intermediates obtained from the National Institute of Standards and Technology (NIST) database, two stable gaseous intermediate species are identified: methyl formate (MF) and dimethyl ether (DME) (Figure 2.4). MF is formed in both anaerobic and aerobic conditions and is thus encountered in both difference spectra. DME is only formed in the presence of oxygen and is responsible for the remarkable dissimilarities in the FTIR difference spectrum for PEC methanol oxidation in air compared to N_2 carrier gas. Unfortunately the most characteristic infrared bands corresponding to C-O vibrations in the broad region 1250 - 2100 cm^{-1} cannot be used for fingerprint analysis as the difference spectra are dominated by H_2O-related vibrations in this wavenumber range as a result of the high humidity level during the experiments.

Based on the information above, different reaction pathways can be proposed for the PEC treatment of methanol in either absence or presence of oxygen. The formation of MF in anaerobic conditions is assumed to proceed through the formation of methoxy radical species after oxidation by $^{\bullet}OH$ radicals (Eq. 2.2). Consecutive oxidation by $^{\bullet}OH$ radicals will eventually result in the formation of formic acid (Eq. 2.3 – 2.5)[157] and yield MF after reaction with methanol (Eq. 2.6).

$$CH_3OH + {}^{\bullet}OH \text{ (or } h^+) \rightarrow CH_3O^{\bullet} + H_2O \text{ (or } H^+) \quad \text{(Eq. 2.2)}$$

$$CH_3O^{\bullet} + {}^{\bullet}OH \text{ (or } h^+) \rightarrow H_2CO + H_2O \text{ (or } H^+) \quad \text{(Eq. 2.3)}$$

$$H_2CO + {}^{\bullet}OH \text{ (or } h^+) \rightarrow HCO^{\bullet} + H_2O \text{ (or } H^+) \quad \text{(Eq. 2.4)}$$

$$HCO^{\bullet} + {}^{\bullet}OH \rightarrow HCOOH \quad \text{(Eq. 2.5)}$$

$$HCOOH + CH_3OH \rightarrow HCOOCH_3 + H_2O \quad \text{(Eq. 2.6)}$$

Summarizing, the overall anaerobic photooxidation of methanol to methyl formate is given by (Eq. 2.7):

$$2\ CH_3OH + 4\ {}^{\bullet}OH \rightarrow HCOOCH_3 + 4\ H_2O \qquad \text{(Eq. 2.7)}$$

In the presence of O_2, MF formation from methanol can be also be achieved by participation of superoxide anions, after reduction of O_2 by photogenerated electrons with the formation of bidendate-formate bound to the catalyst surface (Eq. 2.8 – 2.10).[158] Ultimately MF is formed by radical attack of a methoxy species (Eq. 2.11).

$$2\ CH_3OH + 2\ {}^{\bullet}OH \rightarrow 2\ CH_3O^{\bullet} + 2\ H_2O \qquad \text{(Eq. 2.8)}$$

$$e^- + O_2 \rightarrow O_2^{\bullet-} \qquad \text{(Eq. 2.9)}$$

$$CH_3O^{\bullet} + O_2^{\bullet-} \rightarrow HCOO_{(ads)} + H_2O + e^- \qquad \text{(Eq. 2.10)}$$

$$HCOO_{(ads)} + CH_3O^{\bullet} \rightarrow HCOOCH_3 + \tfrac{1}{2}\ O_{2(ads)} \qquad \text{(Eq. 2.11)}$$

Overall, MF formation through aerobic photooxidation of methanol is given by (Eq. 2.12):

$$2\ CH_3OH + 2\ {}^{\bullet}OH + \tfrac{1}{2}\ O_2 \rightarrow HCOOCH_3 + 3\ H_2O \qquad \text{(Eq. 2.12)}$$

Next, we suggest a plausible mechanism for the formation of DME from methanol under UV illumination, which can be described as light-induced acid-type catalysed methanol dehydration facilitated by $O_2^{\bullet-}$. As in regular acid-like methanol dehydration to DME,[159] the reaction proceeds in three main steps: (i) protonation, (ii) nucleophilic substitution (with dehydration) and (iii) deprotonation. It is known that UV illumination of a TiO_2 surface induces superhydrophilic properties,[160–162] and entails an increased amount of surface hydroxyl groups that render the surface more acidic. These acidic OH groups can assist in the initial protonation of methanol (Eq. 2.13). The next step is a nucleophilic attack by a second methanol molecule (Eq. 2.14). Finally, deprotonation of the formed intermediate is assumed to be largely facilitated

by superoxide radicals as strong nucleophiles, with the formation of $^{\bullet}OOH$ (Eq. 2.15). The latter can further react to $^{\bullet}OH$ or H_2O for surface re-hydroxylation.

$$CH_3OH + H^+ \rightarrow CH_3OH_2^+ \quad \text{(Eq. 2.13)}$$

$$CH_3OH_2^+ + CH_3OH \rightarrow CH_3\text{-}OH^+\text{-}CH_3 + H_2O \quad \text{(Eq. 2.14)}$$

$$e^- + O_2 \rightarrow O_2^{\bullet-} \quad \text{(Eq. 2.9)}$$

$$CH_3\text{-}OH^+\text{-}CH_3 + O_2^{\bullet-} \rightarrow CH_3\text{-}O\text{-}CH_3 + {}^{\bullet}OOH \quad \text{(Eq. 2.15)}$$

Summarizing, the reaction pathway for the aerobic photodehydration of methanol to DME can be split out into two overall reactions: (i) two molecules of methanol that yield DME and water (Eq. 2.16), and (ii) photocatalytic oxygen radical formation (Eq. 2.17).

$$2\ CH_3OH \rightarrow CH_3\text{-}O\text{-}CH_3 + H_2O \quad \text{(Eq. 2.16)}$$

$$O_2 + e^- + H^+ \rightarrow {}^{\bullet}OOH \quad \text{(Eq. 2.17)}$$

Finally, a very important conclusion can be drawn from this mechanistic analysis. Notably, from (Eq. 2.17) it is clear that in the aerobic pathway both photogenerated electrons and H^+ ions are consumed. This will consequently lower the available photocurrent, which corresponds to what we observe experimentally (Figure 2.3). The same applies to the aerobic photooxidation to MF due to participation of $O_2^{\bullet-}$ that is formed by scavenging photogenerated electrons by O_2. This observation highlights an important trade-off when working with PEC cells for (realistic) air treatment: the presence of oxygen will improve the mineralization efficiency of pollutants to CO_2 at the photocatalytic anode, but at the same time opens gateways for the formation of (stable) intermediate species resulting in a lower photocurrent and thus potential hydrogen yield.

2.3.3 H_2 evolution efficiency and future prospects

In the final part of this chapter the cell's H_2 production efficiency (Faradaic efficiency) is determined. Over a 30 min illumination period 0.41 C of

photogenerated charge was produced when feeding the photoanode with methanol vapour, without applying external bias. This corresponds to a theoretical amount of 0.047 mL H_2 that can potentially be generated. The actual measured amount of H_2 evolution over this 30 min illumination period was 0.044 mL. This results in a Faradaic efficiency of 92%. At this point, it cannot be quantified which fraction of H_2 is originating from methanol or water vapour. Further experiments involving isotope-labelled methanol could enable such relative quantification, but this is outside the scope of this thesis. For pure water vapour, the Faradaic efficiency was determined to be close to 100%.[143] Under the present conditions, an overall energy conversion efficiency of approximately 0.3 % can be estimated based on the lower heating value (LHV) of hydrogen gas (120 MJ kg^{-1}) and the total photon flux incident on the cell. While this value obviously appears quite low, it should be reasoned that (when sunlight would be used) this is still a clear net gain in energy resulting from partial abatement of gaseous pollutants, since no bias was applied. Moreover, it was mentioned before that no cell performance optimization has occurred so far. For instance, the photoanode material currently relies on unmodified TiO_2, which can only interact with a limited number of UV photons emitted from the broadband source used in this experiment, hence resulting in a serious underestimation of the cell's intrinsic efficiency. Altogether, these results are quite encouraging and indicate that even with a rather simple MEA and cell design, non-negligible hydrogen evolution can be obtained at high Faradaic efficiency. The main challenge for the further exploitation of PEC cells for air treatment is scaling up towards hydrogen evolution rates of industrial relevance.

As concluding experiments, the versatility of this application was studied by feeding the anode with air polluted with ethanol and acetic acid, following a similar approach as for methanol. Photocurrent increases of 3.1 and 1.5 were measured with regard to pure water vapour, for ethanol and acetic acid vapours generated from purging aqueous solutions containing 5 wt% of these components, respectively. The order of photocurrent generation for organically contaminated vapour decreases according to methanol $>$ ethanol $>$ acetic acid, for which there are two main explanations. Firstly, the trend follows Henry's law; that is, starting from 5 wt% solutions, more methanol will be

present in the gas phase compared to ethanol or acetic acid and thus a higher partial pressure is achieved. Second, the order of photocurrent generation is inversely related to the PEC VOC oxidation redox potential of these components: CH_3OH/CO_2 (+ 0.03 V) < C_2H_5OH/CO_2 (+ 0.08 V) < CH_3COOH/CO_2 (+ 0.12 V). These results again illustrate the potential of this technology for environmental remediation with simultaneous energy recovery (as current or H_2) with only light as energy input. We are hopeful this research will bring about the further development of stand-alone gas phase PEC devices towards industrial applications.

2.4 Conclusion

In this chapter the use of a photoelectrochemical (PEC) cell for simultaneous pollutant abatement and energy recovery was investigated. An important operating condition is that no external electrical bias was applied in any of the experiments and only light (representative for solar radiation) is used as additional energy input. Using methanol as a model pollutant, the influence of oxygen on the PEC cell performance was investigated for both aqueous solutions and, more importantly, contaminated gas flows. It was confirmed that increasing the concentration of methanol also increases the generated photocurrent, up to the point where an aqueous 5 wt% solution resulted in a 4.5-fold photocurrent increase compared to pure water. When saturating the solutions with oxygen, the photocurrent was reduced by roughly 40%, which is attributed to O_2 acting as an electron scavenger. Upon introducing methanol in a gas flow even higher photocurrents were obtained (30% higher compared to liquid phase) and again a 4.5-fold increase was observed with regard to pure water vapour. When using air as the carrier gas (21% O_2) instead of inert N_2, the photocurrent only dropped by 8%, indicating the suitability of using a PEC cell for waste gas abatement. Preliminary experiments using ethanol and acetic acid also confirm its potential. In the presence of O_2 a more complete mineralization of methanol to CO_2 was observed using infrared spectroscopy, but also the formation of additional intermediates, resulting in the proposition of alternative reaction pathways involving methyl formate and dimethyl ether. This chapter highlights a trade-off when using PEC cells for organic waste gas treatment: the presence of oxygen promotes more complete mineralization to CO_2, but limits the generated photocurrent and consequent H_2 evolution.

Finally, the Faradaic efficiency toward H_2 evolution was determined to be 92% when using a methanol-rich gas flow as the PEC cell feed. This chapter showcases the new application potential of energy-efficient (unbiased) PEC cells for waste gas post-treatment with the attractive advantage of simultaneous energy recovery, additionally delivering increased insights into the ongoing reactions.

Chapter 3

In-depth study of TiO_2- and WO_3-based photofuel cell for simultaneous air purification and electricity generation

Based on:

Myrthe Van Hal, Rui Campos, Silvia Lenaerts, Karolien De Wael, and Sammy W. Verbruggen, *Gas phase photofuel cell consisting of WO_3- and TiO_2-photoanodes and an air-exposed cathode for simultaneous air purification and electricity generation*, Applied Catalysis B: Environmental 292 (2021), 120204. https://doi.org/10.1016/j.apcatb.2021.120204.

with addition of unpublished data in Figure 3.12.

Author contributions:

M.V.H. designed the experiments, performed the material synthesis and characterisation, executed the experiments and wrote the paper.

R.C. assisted in designing the CV measurements and writing the CV part of the paper.

S.L., K.D.W. and S.W.V. supervised the work.

Special thanks to prof. Pascal Van Der Voort and Laurens Bourda for performing additional characterisation measurements.

3.1 Introduction

In Chapter 2, two globally pressing environmental problems were addressed in a single device called a PEC cell. This resulted in a proof of concept of an unbiased all-gas phase PEC cell obtaining simultaneous air purification and H_2 production. Currently, research on PEC cells, both operated in liquid and gas phase, is mainly focussed on H_2 production.[80,87,107,132,140,143] However, when targeting simultaneous energy recovery, several bottlenecks are associated with PEC cells targeting H_2 production. Due to the redox potential of H_2 evolution, an external bias is almost always required for steady operation, thus reducing the net energy gain such a cell can provide. In addition, further H_2-processing infrastructure is required to handle the evolved H_2 gas, while only very small amounts of H_2 can be produced by an autonomous device.[163] As an alternative approach, in 2006 Kaneko presented a photofuel cell (PFC),[43] which is basically a PEC cell with an O_2-reducing cathode, degrading waste products and pollutants acting as the fuel at the anode, while simultaneously recovering part of the energy stored in these compounds as electricity.

While PFCs running on liquid feeds have since become an increasingly studied research area, research on PEC technology using a gas feed and targeting electricity generation (*i.e.* gas phase PFC) is extremely rare, with only a single paper reporting on this topic so far, in which just one type of TiO_2-based photoanode is considered.[116] In this chapter, an in-house engineered low-cost, robust and widely applicable PFC device was used, based on the two-compartment 'reverse fuel cell' concept of Seger and Kamat (2009).[106] Five either TiO_2- or WO_3-based photocatalysts were studied, both from commercially available sources and prepared through established protocols, this way covering a broad range of material properties. In literature, methanol is broadly used as a model VOC and is therefore also used in this chapter.

As photocatalysis is the driving force behind the reactions at the photoanode, and consequently the entire cell operation, the first part of this chapter focusses purely on the photocatalytic behaviour. In the second part, chronoamperometry (CA) and cyclic voltammetry (CV) measurements were combined to characterise the all-gas phase PFC system in more detail. In the final part of this chapter the application range is extended to other common air pollutants/waste gases. Application of the developed PFC on the greenhouse

gas methane (CH_4), the fruit-ripening phytohormone ethylene (C_2H_4) and the ecosystem disturbing ammonia (NH_3) will be briefly studied in this section.

The goal of this chapter is to showcase the potential of a low-cost, autonomous and widely applicable PFC device for waste gas-to-electricity conversion. By doing so, the key performance indicators of the studied PFC systems - unconventionally operated entirely in gas phase - are obtained. The comparison with the direct photocatalytic process enables the identification of the different driving material properties in both processes. Additionally, the applicability towards degradation of a range of air pollutants/waste gases was studied, hence expanding the application range of the presented PFC device.

3.2 Experimental

3.2.1 Material synthesis and characterisation

Five different photocatalysts were studied: commercially available P25 (Evonik), WO_3 nanopowder (Sigma-Aldrich), PC500 (CristalACTiV), and photocatalysts synthesized according to established protocols: TiO_2 according to Qiu *et al.* (2006)[164] and WO_3 after Martínez-de la Cruz *et al.* (2010)[79] further denoted as $TiO_{2\ Qiu}$ and $WO_{3\ Mart.}$ respectively. This set of five materials provides a broad range of varying material properties (surface area, band gap, electronic properties, crystalline composition).

$TiO_{2\ Qiu}$ was synthesized by mixing titanium tetraisopropoxide (TTIP, Acros Organics), isopropanol (Chem-Lab) and deionised water in a respective ratio of 1:2:12. Nitric acid (VWR) was added to obtain a pH of 2 and the resulting solution was left overnight for peptization. The resulting precipitate was filtered, dried at 110°C and calcined at 600°C for 3 hours.

$WO_{3\ Mart.}$ was synthesized using a precipitation method. Ammonium tungstate hydrate (Merck) was dissolved in deionised water at 80°C, after which nitric acid was added. The final tungstate solution was kept at 80°C for 70 minutes. The formed precursors were then decomposed by heating the obtained precipitates 3 hours at 600°C.

A Shimadzu UV-2600 spectrophotometer with integrated sphere was used to obtain UV-VIS absorbance spectra for all studied materials. As reference material bariumsulfate ($BaSO_4$) was used. A Tauc plot was used to obtain the band gap (E_g) of the samples. To determine the specific surface area of the samples N_2-adsorption/desorption measurements were performed using a Micromeritics Tristar 3000 surface area & pore size analyser at -196°C (N_2). Prior to the measurements, the photocatalytic materials were degassed at 200°C for 24 hours using N_2. The crystalline structure of the synthesized photocatalysts was measured with X-ray diffraction (XRD, Bruker D8 Advance diffractometer) using Cu Kα radiation (40 kV, 40 mA) in the range of 20 - 80 degrees. The applied scan rate was 0.5 s $step^{-1}$. The software Diffrac.Eva was used to estimate the amorphous fraction of the studied samples.

Since we rely on materials of which the synthesis and characterisation have already been established in literature, only a brief layout on the synthesis procedures and basic characterisation that validate the syntheses are shown in this chapter (materials synthesis, characterisation, or catalyst optimisation is outside the scope of this chapter).

3.2.2 Photocatalytic measurements

As the photocatalytic reactions occurring at the photoanode of a PFC initiate all further reactions occurring in the PFC system, the photoactive properties of the anode material are crucial for PFC performance and will be studied as such in this first part. Therefore, a custom-made slit-shaped photocatalytic reactor, sealed with a quartz glass on top, with an internal reactor volume of 150 mm x 20 mm x 2.75 mm was used for screening the different photo-catalytic materials. A schematic illustration of the entire setup and reactor geometry is described by Verbruggen and co-workers in 2014.[165] The samples were coated on glass slides and placed in the middle of the reactor bed. First, soda lime glass slides (25 mm x 15 mm, VWR) were washed in Piranha solution (70% sulfuric acid (H_2SO_4, Chem-Lab), 30% hydrogen peroxide (H_2O_2, ChemLab)) for 30 minutes. Application of the coating was performed by drop casting the suspension (the photocatalytic materials were suspended in methanol (Merck) by sonication for 1 hour (16.7 mg mL^{-1})) on a dry glass slide, resulting in a photocatalyst coverage of 0.9 mg cm^{-2}. The glass slides were then dried in air at

room temperature for 2 hours and subsequently overnight at 90°C. Next, the glass slides were placed in a vacuum oven at 35°C for 2 hours and were finally illuminated with UVA for 6 hours in the flat plate reactor under constant flushing (2 L N_2 min^{-1}, Messer) to remove all remaining traces of organic solvent. For each photocatalytic gas phase experiment, six coated glass slides were used.

For the actual photocatalytic test, air (composed of 720 mL N_2 min^{-1} and 190 mL O_2 min^{-1} (Messer)) was bubbled through a gas wash bottle containing an aqueous 5 wt% methanol solution before entering the photocatalytic reactor, resulting in a moist methanol vapour with a methanol vapour concentration of 28 mmol m^{-3}. To reach an adsorption/desorption equilibrium the reactor was closed for 2 hours and subsequently illuminated using a Philips Cleo UVA lamp (25 W) placed longitudinally over the sample area at a distance of 1 cm resulting in an incident intensity of 4.25 mW cm^{-2} with a maximum emission around 370 nm (confirmed using an Avantes AvaSpec-3648 spectrometer). After 24 h of continuous illumination, the reactor was purged with pure nitrogen gas (200 mL min^{-1}) and the composition of the reactor outlet was monitored in-line by FTIR spectroscopy (Thermo Fisher Scientific Nicolet 380 with ZnSe windows and 2 m heated gas cell). A dark control experiment (same setup, 24 h in dark) was performed before each light measurement to account for any intrinsic activity and potential minor leakage. Macros Basic software was used to determine the amount of methanol and CO_2 present in the outlet flow after 24 h of reaction. To that end the C-O stretching vibration bands of methanol (at 1034 cm^{-1}, ν(C-O)) and the O=C=O asymmetrical stretching vibration bands of CO_2 (at 2360 cm^{-1}, ν_{as}(O=C=O)) were recorded over time. These spectral features were selected as they do not interfere with any other species present in the gas mixture. To obtain the conversion efficiency (Eq. 3.1) the amount of methanol present in the outlet flow was expressed as the integrated surface under the IR band (S), both for the dark and light measurement.

$$Conversion\ efficiency\ (\%) = \frac{S_{dark} - S_{light}}{S_{dark}} . 100 \qquad \text{(Eq. 3.1)}$$

3.2.3 Photoelectrochemical measurements

An in-house engineered PFC (50 mm x 50 mm x 30 mm, Figure 3.1) was used for all electrochemical measurements. To obtain an economically viable, competitive technology, a low-cost robust cell design is required. Therefore, for this chapter an inexpensive PFC was designed mainly consisting of chemically resistant poly(methyl methacrylate) (PMMA). The inlet and outlet flow are divided over six different channels (respectively 1.2, 1, 0.8, 0.8, 1 and 1.2 mm internal diameter), that result in a steady laminar flow pattern as verified by means of a computational fluid dynamics (CFD) model in COMSOL multiphysics. A quartz window (13 mm x 13 mm) covers the photoanode to allow UV transparency. The PFC can be used in a two- and a three-electrode configuration. By default, it is equipped with two stainless steel wires, and an additional platinum wire can be added as working electrode at the photoanode of the three-electrode cell to allow voltammetry measurements.

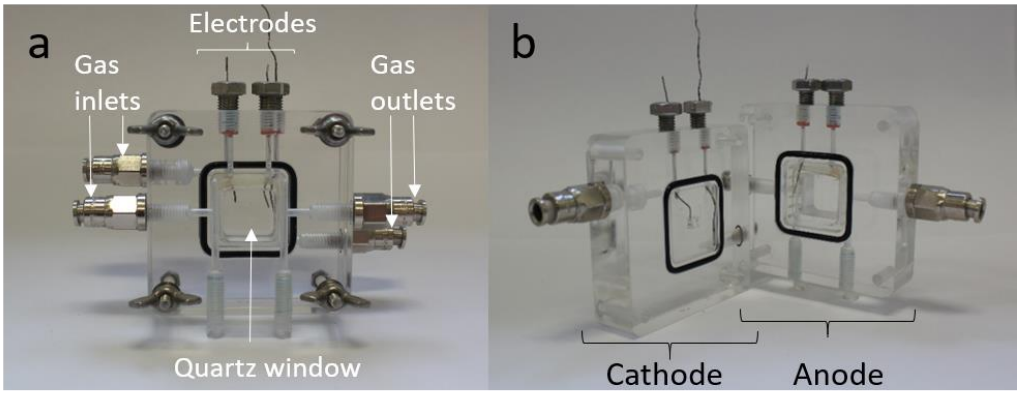

Figure 3.1. Three-electrode PFC employed in this chapter when a) closed and b) open.

For preparing the photoanode, the photocatalyst was suspended in an isopropanol solution (containing 3 wt% Nafion®, Fuel Cell Earth) and drop casted on Toray carbon paper 030 (Fuel Cell Earth), resulting in a photocatalyst loading of 1.6 mg cm^{-2}. For the cathode, platinum nanoparticles on carbon black (10 wt% Pt, Pt-C, Sigma-Aldrich) were suspended in an isopropanol solution (incl. 3 wt% Nafion®) and drop casted on Toray carbon paper 030 resulting in a loading of 0.4 mg Pt-C cm^{-2}. Both anode and cathode were dried overnight at 80°C. A membrane electrode assembly (MEA) was achieved by hot-

pressing (5.5 tons and 135°C for 3 min) both anode and cathode on opposite sides of a preconditioned Nafion® 117 membrane (Fuel Cell Earth) after adding 12 µL Nafion® solution (5 wt%, Fuel Cell Earth) on the anode. Before use, the MEA was illuminated with UV light (Philips Cleo, 25 W), in humid atmosphere, for two days to remove residual traces of solvent. The MEA was subsequently sandwiched between the anode and cathode side of the PFC. A Philips fluorescence S 25 W UVA lamp was positioned 3 cm from the photoanode of the PFC. This resulted in an incident intensity of 2.35 mW cm^{-2} at the photoanode (max. emission (λ_{max}) at 354 nm). The complete PFC setup as used in this chapter is schematically shown in Figure 1.12. Additional experiments were performed using a 300 W Xe source (Oriel Instruments), equipped with an AM1.5g filter to provide simulated solar light adjusted at a total irradiance of 100 mW cm^{-2} (between 300 and 1100 nm). For visible light experiments, a 420 nm cut-on filter was added. The absolute irradiance spectrum of all used lamps is shown in Figure 3.2.

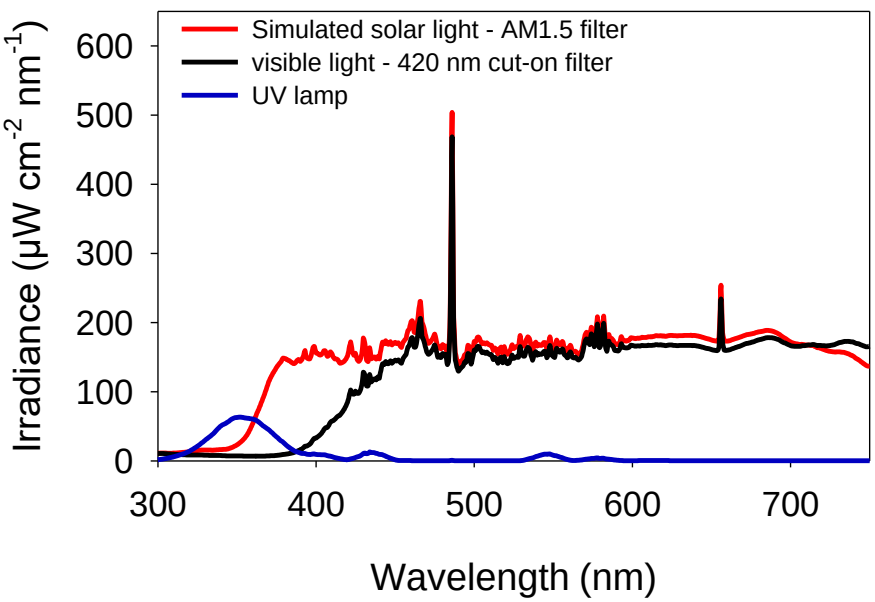

Figure 3.2. Absolute irradiance spectrum of all lamps used in this chapter.

A fully automated, modular test gas setup was used to conduct the gas phase

experiments. Using a gas wash bottle mounted in the gas setup, methanol and water vapour are introduced at the anode. Synthetic air (21 % O_2 in N_2 (Messer)) as carrier gas was sent through the gas wash bottle and fed to the anode inlet at a flow rate of 50 mL min^{-1}. The cathode was not flushed as the final goal is to enable autonomous operation of the PFC (*e.g.* using sunlight, unbiased and without active flushing). All CA and CV measurements were performed using a VersaSTAT 3 potentiostat (Princeton Applied Research). The generated photocurrent density was calculated by dividing the measured photocurrent by the area of the anode surface exposed to the light source (1.8 cm^2). Before each methanol measurement the PFC was flushed with the moist methanol vapour to reach equilibrium (stable photocurrent and IR signal). For the unbiased CA measurements, the photoanode was first illuminated for 6 min, followed by 6 min in dark and finally 20 min of UV illumination while constantly flushing the photoanode with moist methanol vapour. Six different methanol concentrations were studied, corresponding to solutions containing 0, 0.1, 0.5, 1, 3 and 5 wt% of methanol in water, eventually resulting in moist methanol vapours with concentrations of respectively 0, 0.6, 2.8, 5.6, 16.9 and 28.1 mmol m^{-3} in air (0, 86, 429, 858, 2573 and 4288 ppmv). CV was performed for all studied photocatalysts for a methanol concentration of 17 mmol m^{-3} at 10 mV s^{-1} both in dark and under UV illumination. The system was allowed to equilibrate for 5 s at the starting potential prior to each measurement. Each measurement consisted of three cycles in dark and three under UV illumination. The third cycle of each experiment was used for analysis.

To extend the proof of concept beyond methanol vapours, the gas setup was also coupled to gas bottles containing following gases: ammonia (1 vol%, Messer), ethylene (1 mol%, Messer) and methane (1 vol%, Messer). The gases were mixed with moist synthetic air, increasing (and decreasing) the concentration of the gases by increasing (and decreasing) the flow rate of these gases for a constant total flow rate of 50 mL min^{-1}. Following pollutant flow rates were applied: 5, 7, 10, 15, 20, 25 and 40 mL min^{-1}. To prevent dehydration of the Nafion® membrane the photoanode was flushed solely with 'clean' moist air for 20 min in between periods of addition of the pollutant gases (5 min).

3.3 Results and discussion

3.3.1 Characterisation of the photocatalysts

The five photocatalysts selected for this research (P25, $TiO_{2\ Qiu}$, PC500, $WO_{3\ Sigma}$ and $WO_{3\ Mart.}$) have already been extensively described in literature or by the manufacturer.[79,164,166] To confirm correct synthesis of the two photocatalysts prepared in the lab, several standard physico-chemical characterisation experiments (N_2 sorption, UV-VIS spectroscopy, X-ray diffraction and energy dispersive X-ray fluorescence) were performed. An overview of relevant photocatalyst properties is shown in Table 3.1, highlighting the variety in material characteristics that are covered by the different selected photocatalysts. Please note that material optimisation is outside the scope of this chapter.

Table 3.1. Physical characteristics (band gap, BET surface area and crystallite particle size) of commercial and synthesized materials.

Material	Band gap (eV)[3]	BET surface area ($m^2\ g^{-1}$)	Crystallite particle size (nm)[4,5]
$P25_{Evonik}$[1]	3.2	52	19 (A), 32 (R)
$TiO_{2\ Qiu}$[2]	3.1	68	30 (A), 36 (R)
$PC500_{CristalACTiV}$[1]	3.3	295	9.5 (A)[6]
$WO_{3\ Sigma}$[1]	2.6	7	37.5 (W)
$WO_{3\ Mart.}$[2]	2.6	9	32 (W)

1) Commercially available photocatalysts.
2) Photocatalysts synthesized based on literature protocols.
3) Obtained by the Tauc method applied on diffuse reflectance spectra.
4) Estimated from XRD using the Scherrer equation.
5) A = anatase, R = rutile, W = monoclinic polymorph.
6) According to data obtained by Nuño and co-workers in 2016.[167]

An important difference between TiO_2 and WO_3 is of course the band gap. The large band gap of TiO_2 restricts this material to the use of UV light, which is only a small fraction of the solar spectrum ($\sim$ 5%), whereas the somewhat smaller band gap of WO_3 allows this material to also utilise part of the visible fraction of sunlight ($<$ 500 nm, $\sim$ 12% sunlight). On the other hand, the specific surface area of all TiO_2 forms is much higher than that of both WO_3 forms, especially PC500 has a high specific surface area. The N_2 sorption isotherm of $TiO_{2\ Qiu}$ is shown in Figure 3.3.

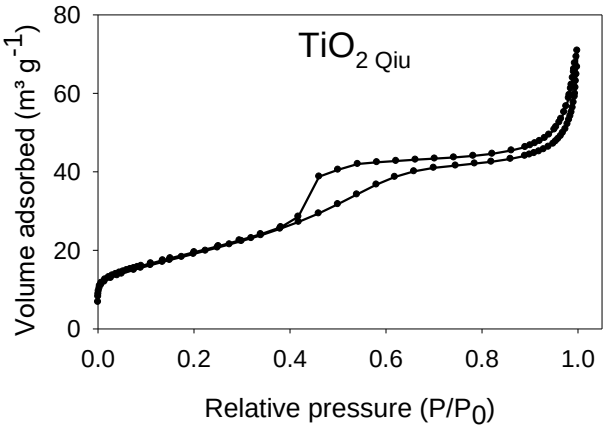

Figure 3.3. N_2 sorption isotherm of TiO_2 synthesized according to Qiu *et al.* (2006).

Based on N_2 sorption isotherms, it can be concluded that only TiO_2 synthesized according to Qiu *et al.* (2006) has a mesoporous structure. WO_3 synthesized according to Martínez-de la Cruz *et al.* (2010) is non-porous, whereas both P25 and the commercial WO_3 show some macroporosity, which can be linked to macroporous interparticle pores due to agglomeration. PC500 is known for its very complex pore channels.[75] The XRD measurements of $TiO_{2\ Qiu}$ and $WO_{3\ Mart.}$ are shown in Figure 3.4 and Figure 3.5, allowing us to determine the crystalline structure of the synthesized photocatalysts.

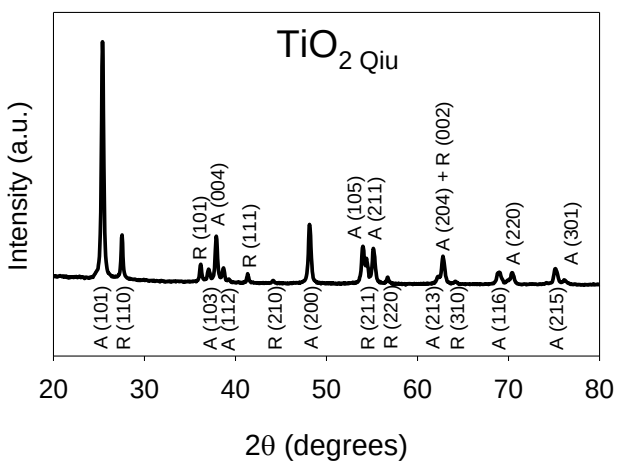

Figure 3.4. XRD pattern of TiO_2 synthesized according to Qiu *et al.* (2006).

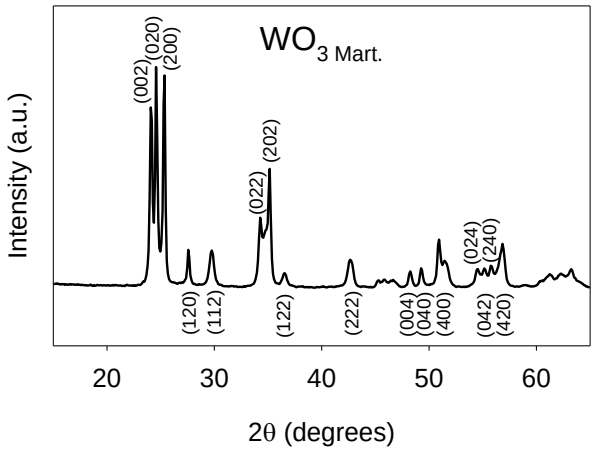

Figure 3.5. XRD pattern of WO_3 synthesized according to Martínez-de la Cruz *et al.* (2010).

The XRD pattern of the synthesized TiO_2 clearly shows the presence of both rutile and anatase (15% amorphous), analogue to P25 (8% amorphous).[168] PC500, on the other hand, is known to be monocrystalline (~ 80% anatase, rest is amorphous).[168] As mentioned in the introduction, the crystal structure(s) present affects a range of properties including activity and stability of the photocatalyst. The WO_3 monoclinic polymorph structure of $WO_{3\ Mart.}$ can be observed in Figure 3.5 (16% amorphous), analogue to $WO_{3\ Sigma}$ (12% amorphous).

3.3.2 Photocatalytic measurements

In a PFC, the photocatalytic reactions occurring at the photoanode are the driving force behind all further reactions, so obtaining a better understanding of gas phase PFC operation implies proper knowledge on the photocatalytic reactions that lie at the base of the PFC operation. In order to do so, the first part of this chapter focuses on the purely photocatalytic degradation of moist methanol vapour by the five selected photocatalysts.

The reaction products (both gaseous and adsorbed on the substrate) were determined by FTIR. After 24 h of reaction (both under UV illumination and in

dark) the content of the slit-shaped reactor was sent to a FTIR spectrometer. The FTIR spectra are shown in Figure 3.6.

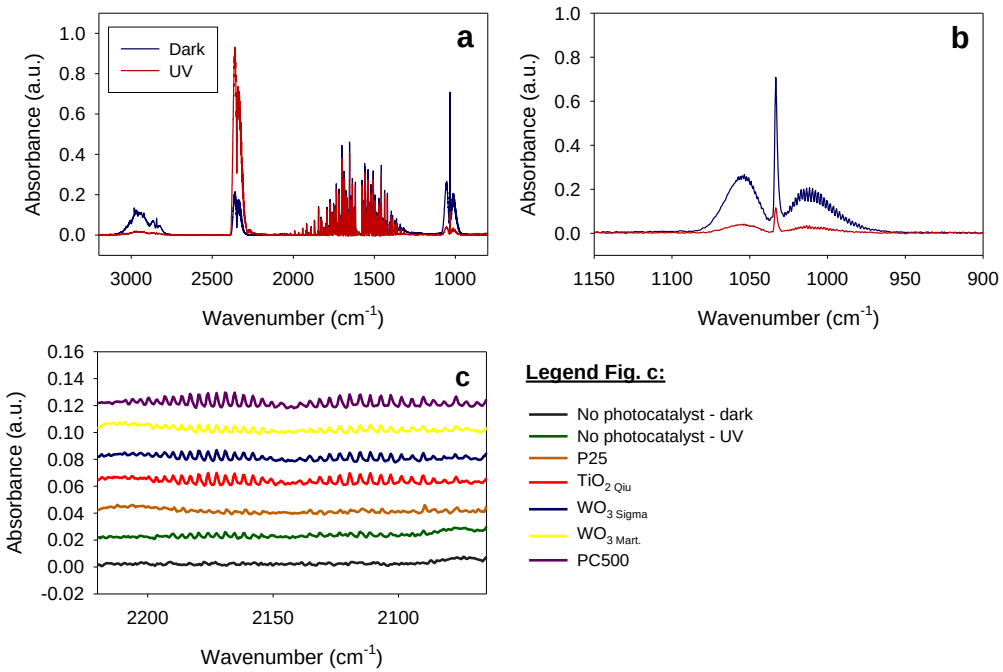

Figure 3.6. Photocatalytic measurements. FTIR spectra of gases flushed out of flat plate reactor filled with a moist methanol vapour (28 mmol m^{-3}): a-b) using glass slides coated with $WO_{3\ Mart.}$, (blue) without and (red) with 24 h of UV illumination and c) using glass slides coated with different photocatalysts (see legend) under UV illumination. A blank measurement with a moist methanol vapour was performed with bare glass slides after 24 h in (black) dark and (green) after 24 h of UV illumination.

Besides CO, CO_2, H_2O and methanol no other stable gaseous intermediates were observed in detectable amounts in the spectra obtained after 24 h UV illumination, pointing at the almost complete oxidation of methanol to CO_2, with formation of small amounts of CO as by-product (not observed for P25). The photocatalytic performance of the different photocatalysts towards methanol degradation, and thus complete conversion to CO_2, was assessed by the ratios of methanol and CO_2 before and after illumination. As expected, for all studied photocatalysts a decrease in the amount of methanol and an increase in the amount of CO_2 can be observed after illumination of the samples.

Figure 3.7 shows that all selected materials present significant methanol conversion ($>$ 64%), with the highest conversion being obtained by $TiO_{2\ Qiu}$ (87%), followed by PC500 (78%) and P25 (76%), while both WO_3-based materials exhibit a slightly lower methanol conversion around 65%. The very small surface area ($<$ 10 $m^2\ g^{-1}$) of both WO_3-based materials can already in part explain their lower methanol conversion efficiencies.[169] Crystal structure and present crystal facets are known to influence photocatalytic methanol oxidation, both due to the effect of ions coordination and the type of adsorption of water and methanol on the photocatalyst surface.[170] Although anatase is known to be more active than rutile, the combination of anatase and rutile, as present in both P25 and $TiO_{2\ Qiu}$, might result in a higher conversion efficiency due to synergistic effects that can be ascribed to enhanced charge separation between the anatase and rutile phases.[171] In addition, faster electron-hole recombination in smaller particles could contribute to the lower methanol conversion presented by P25 and PC500 when compared to $TiO_{2\ Qiu}$.[169] An additional asset of $TiO_{2\ Qiu}$, is its favourable mesoporous structure (Figure 3.3) compared to the other studied photocatalysts. Toledo and co-workers compared pure P25 with a P25-WO_3 photocatalyst and showed that under UV illumination the addition of WO_3 led to a decrease in photocatalytic hydrogen production, which is related to lower methanol conversion. Under UV illumination, TiO_2 outperformed WO_3 for photocatalytic methanol conversion, as is also evidenced by this research. On the other hand, WO_3 can, in contrast to TiO_2, use part of the visible light spectrum and that makes it a promising material for use in sunlight-driven (autonomous) applications, but is not considered here.[172]

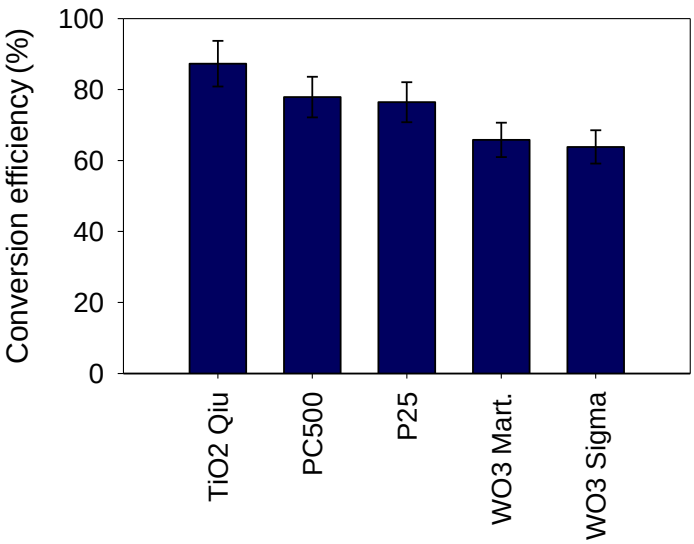

Figure 3.7. Photocatalytic measurements. Results obtained using the flat plate reactor: methanol conversion efficiencies of all studied photocatalysts under UV illumination when saturating the reactor with a moist methanol vapour (28 mmol m^{-3}).

3.3.3 Photoelectrochemical measurements

The combination of unbiased CA with CV measurements (broad potential windows) for the five selected photocatalysts increases the limited knowledge on gas phase PFC operation towards simultaneous waste gas degradation and electricity production. Coupled with results of the photocatalytic methanol oxidation, this will enable the identification of crucial material properties of both processes. The results for different methanol concentrations fed to the PFC device, are presented in Figure 3.8.

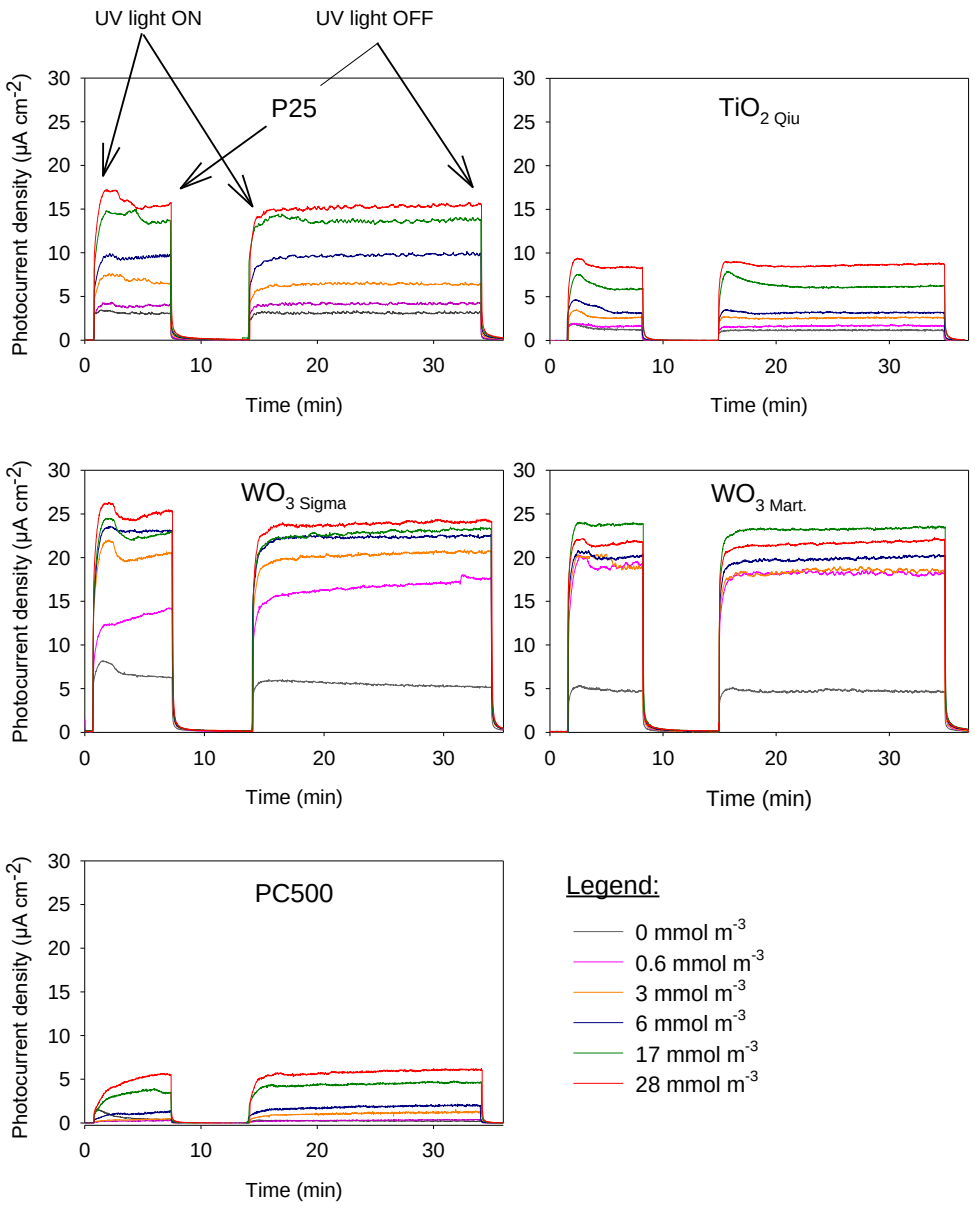

Figure 3.8. Photofuel cell. Photocurrent density as a function of time when feeding the photoanode with moist methanol vapours of different concentrations (see legend, expressed in millimoles of methanol m^{-3}) for different photocatalysts (at photoanode) under UV illumination.

The CA measurements (Figure 3.8) show an increase in generated photocurrent for all studied photocatalysts when methanol vapour was introduced in the photoanode feed, in accordance to what was observed by Kaneko and co-workers for aqueous methanol streams (only for TiO_2).[43] A control experiment

(MEA without photocatalyst) was performed, showing no increase in generated photocurrent upon UV illumination of the cell. The increase in photocurrent upon methanol introduction can be explained by the lower oxidation potential of methanol compared to that of water (0.03 V *vs.* 1.23 V at pH 0 and *vs.* NHE, respectively),[173] which makes it a more efficient hole scavenger and results in less recombination losses. In addition, the current doubling effect is a well-known phenomenon related to increased photocurrent generation upon introduction of methanol. It is associated with the formation of intermediate radicals during oxidation of the hole scavenger, resulting in the injection of an electron into the conduction band of the photocatalyst, obtaining two electrons from one absorbed photon (one photogenerated and one injected).[113] As expected, it can be observed that the increase in generated photocurrent upon methanol introduction is higher at higher methanol concentrations in the moist vapours (Figure 3.8). Also note that, overall, very stable photocurrents are obtained over time, highlighting the robustness of the system used in this chapter.

When considering the first 'light-ON' phase in Figure 3.8, a standard photocurrent profile can be observed, as described in detail by Rongé and co-workers, with an initial anodic overshoot, followed by a steady state current increase and eventually current decay until the light is turned off. The anodic overshoot is absent in almost all of the second 'Light ON' phases, due to repetition of the illumination.[147] The absence of the initial anodic spike for PC500 again reflects the poor electronic properties of this photocatalyst, as hole trapping by surface states at the photoanode surface is known as an important contributor to the generation of an anodic overshoot.[174]

An important performance indicator for future application of gas phase PFC technology is the absolute photocurrent generation. For a pure water vapour feed, the highest photocurrents are obtained using both WO_3-based materials: $WO_{3\ Sigma} > WO_{3\ Mart.} > P25 > TiO_{2\ Qiu} > PC500$. Additionally, strong increases in photocurrent are observed for these WO_3-based photocatalysts when adding methanol vapour to the feed, outperforming the TiO_2-based photocatalysts over the full methanol concentration range. The higher absolute photocurrents generated using WO_3-based photocatalysts can be ascribed to the higher electron mobility ($\sim 5\ cm^2\ V^{-1}\ s^{-1}$) compared to TiO_2 ($\sim 0.2\ cm^2\ V^{-1}\ s^{-1}$).[175] These

results clearly highlight the importance of efficient electron transport in a PFC. To our knowledge, these are the first promising results for application of WO_3-based photocatalysts in a gas phase PFC system. A property known for influencing the electron mobility of a photocatalyst is its crystal structure,[176] which is reflected in the results of the TiO_2-based photocatalysts. While both WO_3-based photocatalysts reach similar absolute photocurrents (both monoclinic crystal structures), distinct differences can be observed between the different TiO_2-based photocatalysts. Polycrystalline photocatalysts (in this case P25 and $TiO_{2\ Qiu}$) are known for their higher electron mobility compared to single-crystal materials,[176] such as PC500 (pure anatase). In addition, the ratio anatase/rutile of the commercially available P25 is close to optimal, while this is presumably not the case for $TiO_{2\ Qiu}$. The degree of crystallinity is also known to affect the photocatalytic activity of a semiconductor. The higher the crystallinity of a material, the lower the amount of non-equilibrium defects in the photocatalysts. This results in overall reduced recombination, improved bulk transport and enhanced activity.[177] $TiO_{2\ Qiu}$ has a lower crystallinity than the better performing commercial TiO_2 P25 (15% *vs.* 8%). PC500 has the highest amorphous fraction (20%),[168] further reducing its performance as photoanode. In addition, smaller crystallite particle sizes - as found in PC500 (Table 3.1) - are also known to reduce electron mobility.[178,179] PC500 is known to have very poor electronic properties, resulting in very low charge carrier stability,[75] explaining the strikingly low absolute photocurrent generation observed for this photocatalyst and thus eliminating this photocatalyst for use in (unbiased) gas phase PFCs, while on the other hand it is known to be an excellent material in pure gas phase photocatalysis.[153]

As the final goal is to obtain an autonomously operating sunlight-driven PFC device solely using polluted air to sustainably generate electricity, additional CA measurements using simulated solar light (and solely visible light) were performed as proof of concept and are shown in Figure 3.9. Autonomous un-biased performance of the PFC was obtained with all studied photocatalysts when feeding the PFC with methanol-rich vapours. These results also underline the suitability of WO_3 as photoanode for this application. The smaller band gap of WO_3 (Table 3.1) enables absorption of visible light besides UV light, thus working with (simulated) solar light instead of solely UV light results in the

generation of higher absolute photocurrents and consequently an even higher photocurrent increase compared to TiO_2-based photocatalysts. Note that the UV measurements were performed with a different lamp as the two other measurements (thus obtaining a different irradiance spectrum as can be seen in Figure 3.2), and consequently the sum of the generated photocurrents obtained under visible and UV light does not equal the photocurrent generated under simulated solar light (AM1.5g).

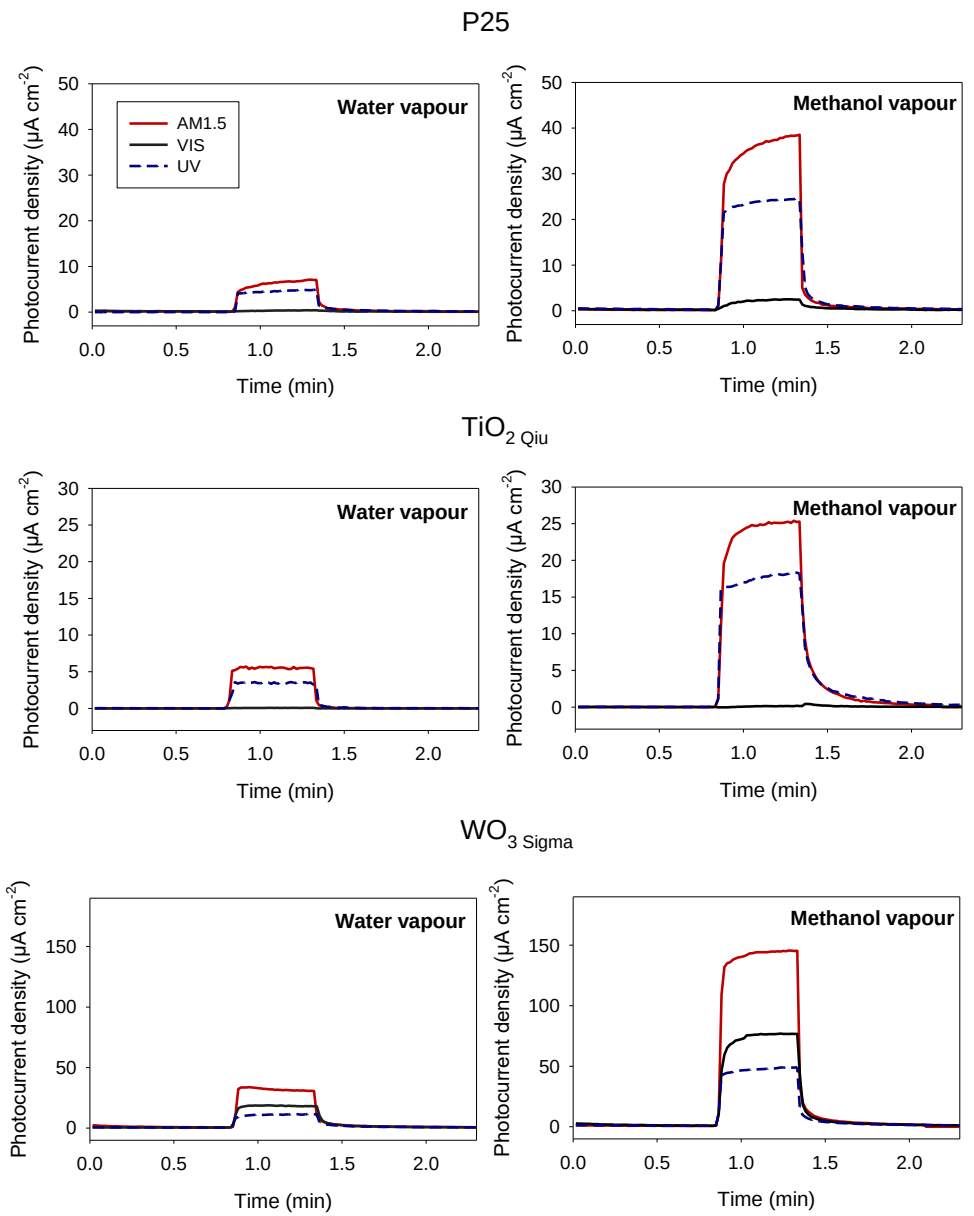

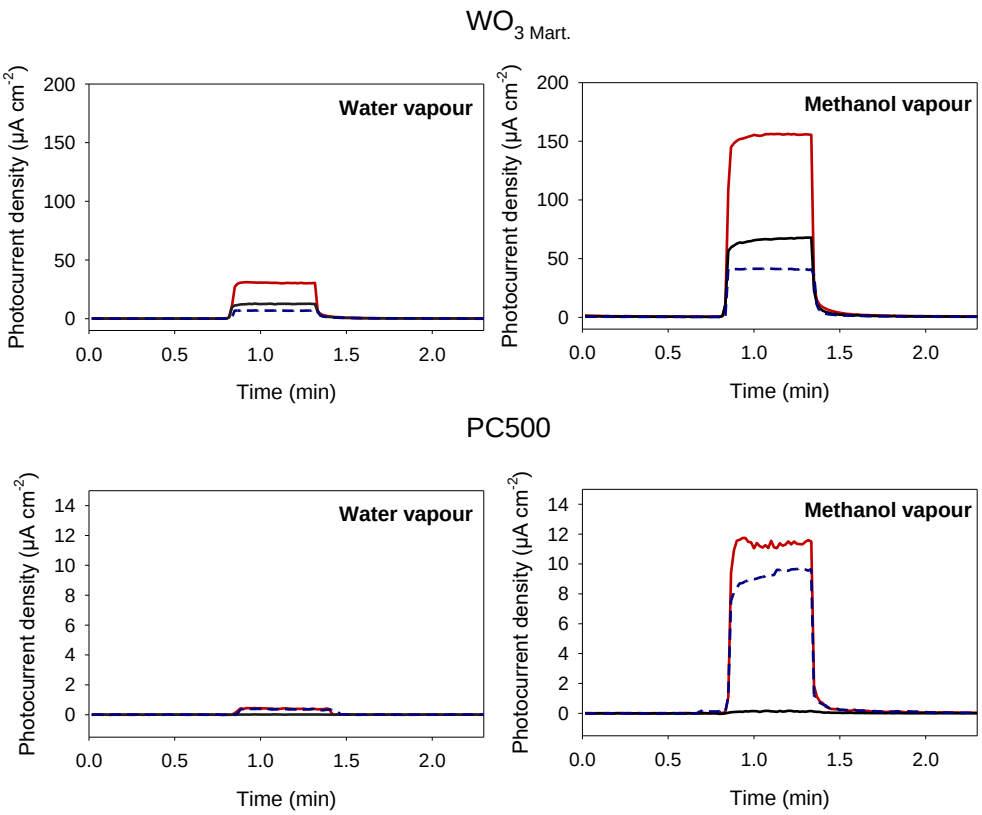

Figure 3.9. Photofuel cell. Solar light response: Photocurrent density as a function of time when using different light sources (simulated sunlight (AM1.5g, 100 mW cm^{-2}), visible light (solar simulator with cut-on filter > 420 nm) and UV light (adjusted to 4 mW cm^{-2})), both when feeding the photoanode with (left) pure water vapour and (right) moist methanol vapour (17 mmol m^{-3}) when using different photocatalysts at the photoanode.

A clear difference in concentration response can be seen between the TiO_2- and WO_3-based photocatalysts (Figure 3.8 and Table 3.2). While both WO_3-based materials follow a similar trend, with a steep increase in generated photocurrent even for low methanol concentrations that levels off at higher methanol concentrations, $TiO_{2\ Qiu}$ and PC500 on the other hand show a distinct proportional increase in generated photocurrent over the entire concentration range, but without reaching the absolute photocurrents generated by the WO_3-based photocatalysts. The concentration response of P25 follows a trend in-between. It is rationalized that decomposition of small quantities of methanol on WO_3 is already very efficient, resulting in only small photocurrent increases at higher methanol concentrations with the same amount of photocatalyst, especially considering the small surface area that eventually results in

saturation or even a drop in photocurrent generation, as seen for $WO_{3\ Mart.}$. Such a decrease in photocurrent upon increasing the concentration of an organic compound might also be ascribed to the formation of intermediates acting as recombination centres, as described by Xie and co-workers.[163] Due to the larger surface area of all TiO_2-based photocatalysts (Table 3.1) saturation of the surface at high methanol concentrations is less likely for these photoanodes, and proportionally increasing photocurrent generation with increasing methanol concentration is expected (Table 3.2), as long as surface saturation is avoided. In addition, the high relative increase in generated photocurrent density upon introduction of high methanol concentrations observed for PC500 might be due to a combination of the favourable morphological characteristics of PC500 and the fact that methanol acts as a hole scavenger that largely reduces the recombination rate. It should be kept in mind though, that PC500 performs very poorly in absolute terms.

Table 3.2. Relative increase in generated photocurrent obtained with a moist methanol vapour relative to the photocurrent generated with pure water vapour ($I_{methanol}/I_{H2O}$).

	$I_{Methanol}$ / I_{H2O}				
Methanol conc. (mmol m^{-3})	**P25**	**$TiO_{2\ Qiu}$**	**$WO_{3\ Sigma}$**	**$WO_{3\ Mart.}$**	**PC500**
0.6	1.3	1.5	3.2	4.0	1.6
2.8	2.0	2.3	3.9	4.0	5.8
5.6	3.2	2.9	4.5	4.4	9.8
16.9	4.3	5.5	4.6	5.1	23.1
28.1	4.9	7.8	4.6	4.8	30.5

Interestingly, the photocatalysts resulting in the lowest direct photocatalytic methanol conversion (Figure 3.7), *i.e.* both types of WO_3, actually lead to the highest absolute photocurrent generation when applying the same methanol vapour concentration (28 mmol m^{-3}) to the photoanode feed (Figure 3.8). In terms of absolute photocurrent increase generated by adding 28 mmol m^{-3} methanol to the photoanode, the following order can be obtained (expressed in µA cm^{-2}): $WO_{3\ Sigma}$ (18.6) > $WO_{3\ Mart.}$ (17.4) > P25 (12.2) > $TiO_{2\ Qiu}$ (7.5) > PC500 (5.9). Thus, a clear difference is observed in the performance of the different photocatalysts when comparing both air remediation technologies (photocatalysis *vs.* PFC). Although photocatalysis is the driving force behind the functional operation of a PFC, large differences are clearly induced by physically

separating the ongoing reactions in two distinct compartments. Therefore, material properties that are beneficial for photocatalytic VOC degradation might be less crucial for photoelectrochemical VOC degradation and *vice versa*. For example, although the high surface area of the studied types of TiO_2 contributed to enhanced direct photocatalytic methanol conversion, this property clearly appears less important for photoelectrochemical VOC oxidation. Good electron mobility on the other hand proves crucial for an efficient PFC system, while of lesser importance for purely gas phase photocatalytic systems. This is clearly evidenced by the fact that the poor electronic properties of PC500 did not result in much lower photocatalytic methanol conversion compared to the other photocatalysts, but did largely decrease the absolute photocurrents that were obtained in the PFC.

In the next section, CV analysis contributes to the understanding of gas phase PFC operation. It should be stressed that this technique has only scarcely been applied in the field of gas phase PFC.[116] CV measurements were performed for all studied photocatalysts, both for pure water vapour and a moist methanol vapour (17 mmol m^{-3}) as photoanode feed. The results are shown in Figure 3.10. The initial CV measurements were performed between -0.2 and 1 V.

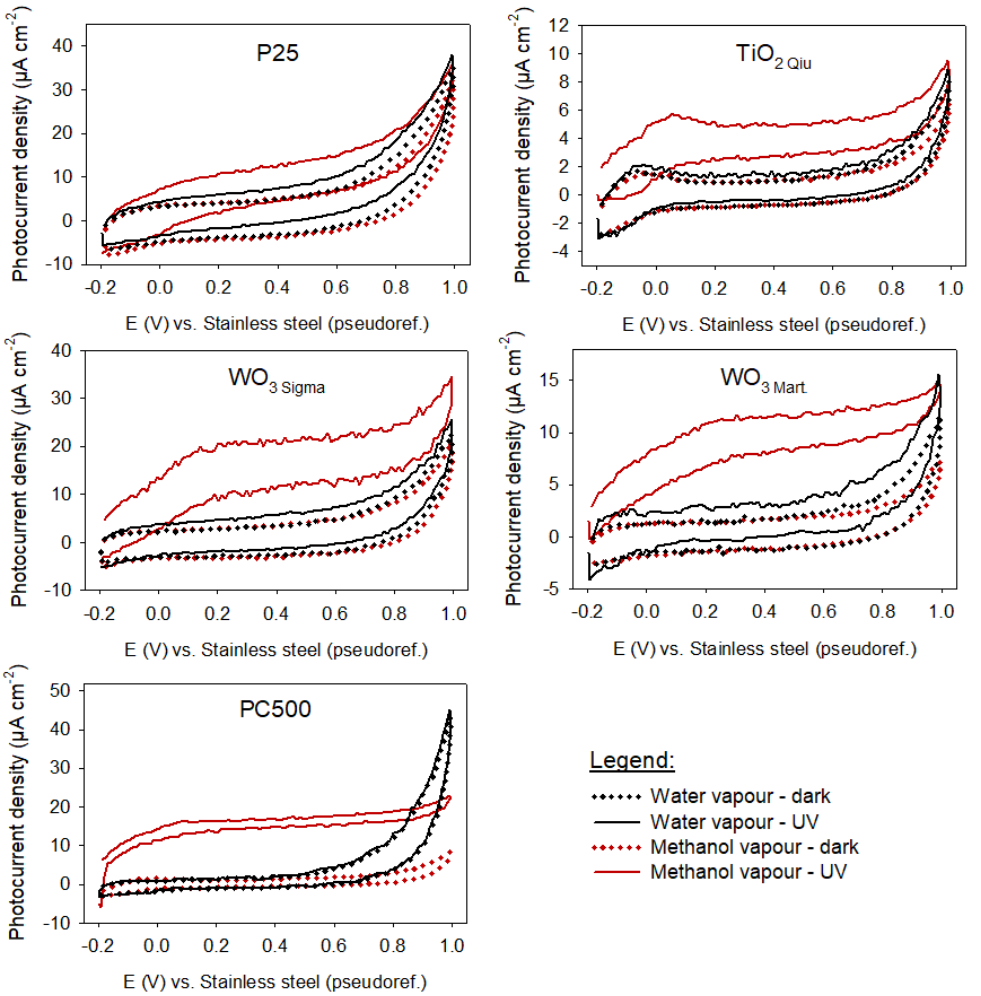

Figure 3.10. Photofuel cell. Cyclic voltammograms (scan rate = 10 mV s^{-1}) obtained for pure water vapour and moist methanol vapour (17 mmol m^{-3}), both in dark and under UV illumination when using different photocatalysts at the photoanode.

The results from Figure 3.10 confirm that upon illumination of the PFC whilst feeding the photoanode with pure water vapour, a small increase in generated current (the photocurrent) can be observed for all materials compared to dark conditions (almost not observable for PC500, which is in agreement with the CA measurements). When adding methanol vapour (17 mmol m^{-3}) to the photoanode feed in dark, no increase in generated current was observed. In fact, the voltammogram nicely coincides with that of pure water vapour for all photocatalysts except at high potentials where a small decrease in generated current can be observed upon introducing methanol. This might be attributed

to the onset of oxygen evolution at this potential, which shall be discussed later. When the PFC is illuminated whilst feeding with methanol vapour, a large increase in generated current can be observed for all studied photocatalysts compared to the dark result. As in the unbiased CA measurements, under illumination an increase in the absolute generated photocurrent is observed when methanol was added to pure water vapour at the photoanode. A control experiment (MEA without photocatalyst) was performed, showing no change in current upon introduction of either UV light or methanol vapour, thus evidencing that the changes in generated photocurrent observed in Figure 3.10 are only due to photoelectrochemical reactions.

Although all studied photocatalysts show photoelectrochemical methanol oxidation, clear differences can be observed amongst the different materials (*e.g.* shape CV, absolute photocurrents). In order to determine the key performance indicators of the studied PFC systems, more extensive CV measurements were performed, scanning to higher (1.5 V) and lower (-1 V) applied potentials. The results for P25 and $WO_{3\ Sigma}$ are shown in Figure 3.11.

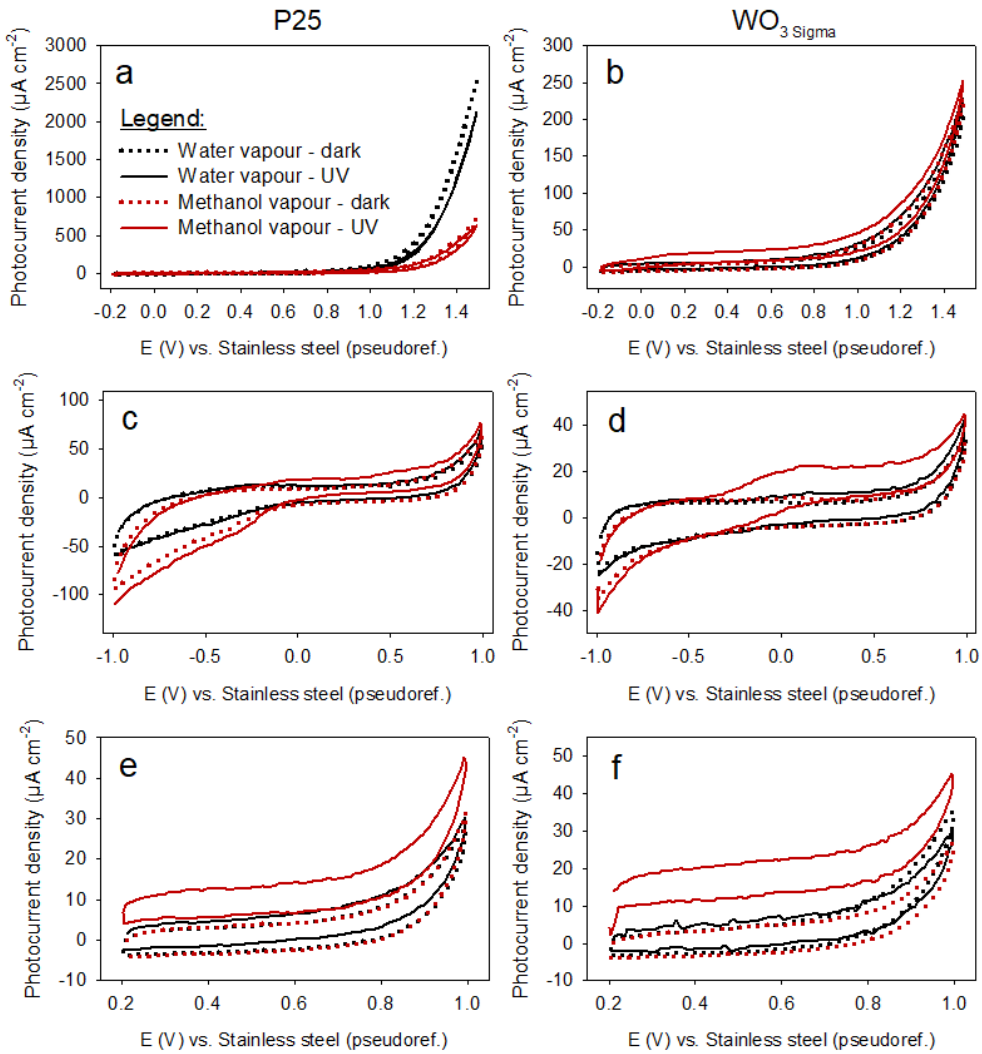

Figure 3.11. Photofuel cell. Cyclic voltammograms showing the effect of the applied potential window (scan rate = 10 mV s^{-1}) obtained for pure water vapour and moist methanol vapour (17 mmol m^{-3}), both in dark and under UV illumination when using (left) P25 and (right) $WO_{3\ Sigma}$ at the photoanode.

Figure 3.11a (CV till 1.5 V) shows that for P25 a steep increase in generated (photo)current is induced around 1.1 V both in dark and under UV, which is less pronounced when feeding the photoanode with a moist methanol vapour (*vs.* pure water vapour). This steep increase in generated current can be attributed to the onset of the oxygen evolution reaction (OER).[180] When studying the CVs ranging till -1 V (Figure 3.11c/d) a clear reaction can also be

observed for all photocatalysts at very low applied potentials. The observed decrease in generated current at these low (negative) potentials can be attributed to the onset of the hydrogen evolution reaction (HER).[181]

When analysing the anodic curve of Figure 3.11c (CVs till -1 V) it can be observed for P25 that at -0.32 V the photocurrents (UV) generated when flushing with a moist methanol vapour no longer coincide with the currents obtained in dark, but are shifted upwards. This sudden upward photocurrent shift can be attributed to the onset of methanol oxidation. To further study this, an additional CV measurement was performed for all photocatalysts initiating the CV measurement at 0.2 V (incl. 5 s equilibration at 0.2 V, Figure 3.11e/f). In this measurement, it could be observed for all photocatalysts that the generated photocurrents obtained when the photoanode was fed with a moist methanol vapour (under UV illumination) were distinctly shifted upwards compared to the currents obtained in dark and with pure water vapour. This distinct upward shift started immediately at the initial applied potential. This indicates that the methanol molecules present in the vicinity of the electrode surface are already oxidised, *i.e.* oxidised at a potential below 0.2 V, hence the initial current is not zero. This distinct upward shift in photocurrent generation directly starting at 0.2 V was present for all studied photocatalysts.

In further characterisation of the PFC system, Table 3.3 summarises the efficiency parameters calculated from the CV measurements. The measured open-circuit voltages (V_{oc}) can be compared to the maximal theoretically expected V_{oc}. The V_{oc} can be regarded as the force driving the electron flow from photoanode to cathode during unbiased PFC operation and is thus determined by the difference between the energy level of the conduction band of the selected photocatalyst and the redox potential of the cathodic reaction. For the theoretical maximal V_{oc}, reduction towards H_2O is assumed at the cathode (1.23 V *vs.* NHE at pH=0), although H_2O_2 formation (0.68 V *vs.* NHE at pH=0) is also technically possible and often favoured due to its lower redox potential. Thus, depending on the exact reaction at the cathode, the measured V_{oc} can deviate largely from the theoretical maximum value. The ratio of the measured V_{oc} to the theoretical maximal V_{oc} was also used by Kaneko and co-workers as a rough estimate for the fuel-to-electricity conversion,[43] and is shown for all studied photocatalysts in Table 3.3 (= fuel-eff. (%)). The WO_3-

based photocatalysts present the highest fuel-to-electricity conversion, associated with the highest V_{oc} values.

Table 3.3. Efficiency parameters of studied photocatalysts when working with a moist methanol feed (17 mmol m^{-3}).

	J_{sc} ($\mu A\ cm^{-2}$)	V_{oc} (V)	P_{max} ($\mu W\ cm^{-2}$)	Fuel-eff. (%)	η (%)	FF (-)
P25	19.9	0.54	3.1	42	0.13	0.29
$TiO_{2\ Qiu}$	6.1	0.78	1.4	60	0.06	0.30
$WO_{3\ Sigma}$	19.4	0.83	4.4	70	0.19	0.27
$WO_{3\ Mart.}$	11.5	0.79	3.5	66	0.15	0.39
PC500	23.4	0.27	1.8	19	0.08	0.28

Polarisation curves (J-V plot), obtained as described by Antoniadou and co-workers,[141] were used to obtain the real maximal electric power output $(J.V)_{max}$ or P_{max}. P_{max} can be used to determine the overall efficiency (η) by dividing P_{max} by the power density of the incident radiation (2.35 mW cm^{-2}). The highest η-values were also found for both WO_3-based photocatalysts, followed by P25, with very low values for both PC500 and $TiO_{2\ Qiu}$. The critical note should be added that the obtained η-values are still quite low, as this is the first study on the application of a PFC for gas phase VOC degradation. This chapter merely aims at showcasing the potential of this technique for the conversion of gaseous pollutants, such as VOCs, serving as fuel for sustainable electricity production. The next step will be to optimise the materials and the process as a whole. Still, the PFC process as used in this chapter already enables to convert large parts of the energy stored in the degraded VOC to electricity, with both WO_3-based photocatalysts exceeding 65% conversion.

The fill factor (FF) was calculated for all photocatalysts by dividing P_{max} by the theoretical maximal power output ($V_{oc}.J_{sc}$). The FFs obtained with both TiO_2 and WO_3-based photocatalysts are significantly higher than those obtained in liquid phase PFC systems working with a methanol solution as reported by Hu and co-workers, showing FFs of 0.17 and 0.11 for TiO_2 and WO_3, respectively,[182] while FFs up to 0.39 are attained in our work. This can be attributed to the cell configuration used in this chapter combining anode, electrolyte and cathode in a MEA, reducing electrolyte resistance and associated current losses due to the reduced distance between the two electrodes. In the study of Hu and co-

workers the TiO_2-photoanode performed better than the WO_3 one.[182] Both the difference in cell configuration (reduced recombination and thus possibly benefiting WO_3), operating phase (drastically lower diffusion limitations could play an important role in gas phase operation, amongst others) and the different nature of the studied photocatalysts can contribute to this difference. Overall, these results illustrate the potential of a PFC, using a WO_3-based photoanode, as waste-to-energy recovering air purification device.

3.3.4 Methane, ethylene and ammonia

To extend the proof of concept of the autonomous and low-cost waste gas-to-electricity PFC device beyond methanol vapour, in the final part of this chapter exploratory experiments were performed using other common air pollutants/waste gases. To this end, the PFC is applied to air contaminated with methane (CH_4), ethylene (C_2H_4) and ammonia (NH_3). The absolute increase in photocurrent generation upon introduction of these pollutants (*vs.* clean moist air) is shown in Figure 3.12 for the five studied TiO_2- and WO_3-based photocatalysts.

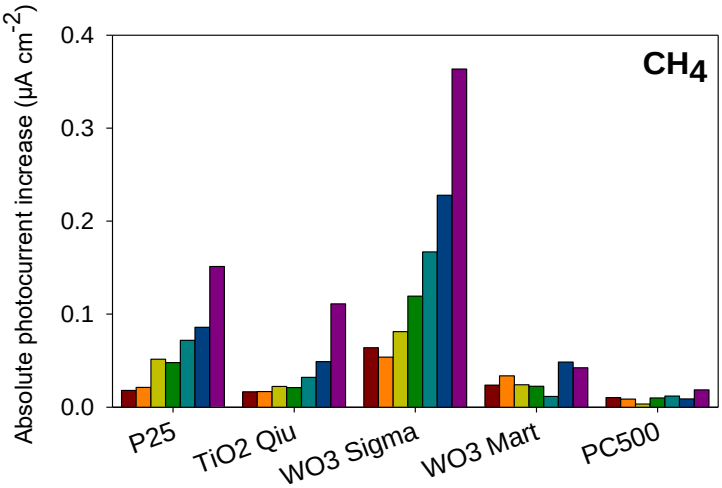

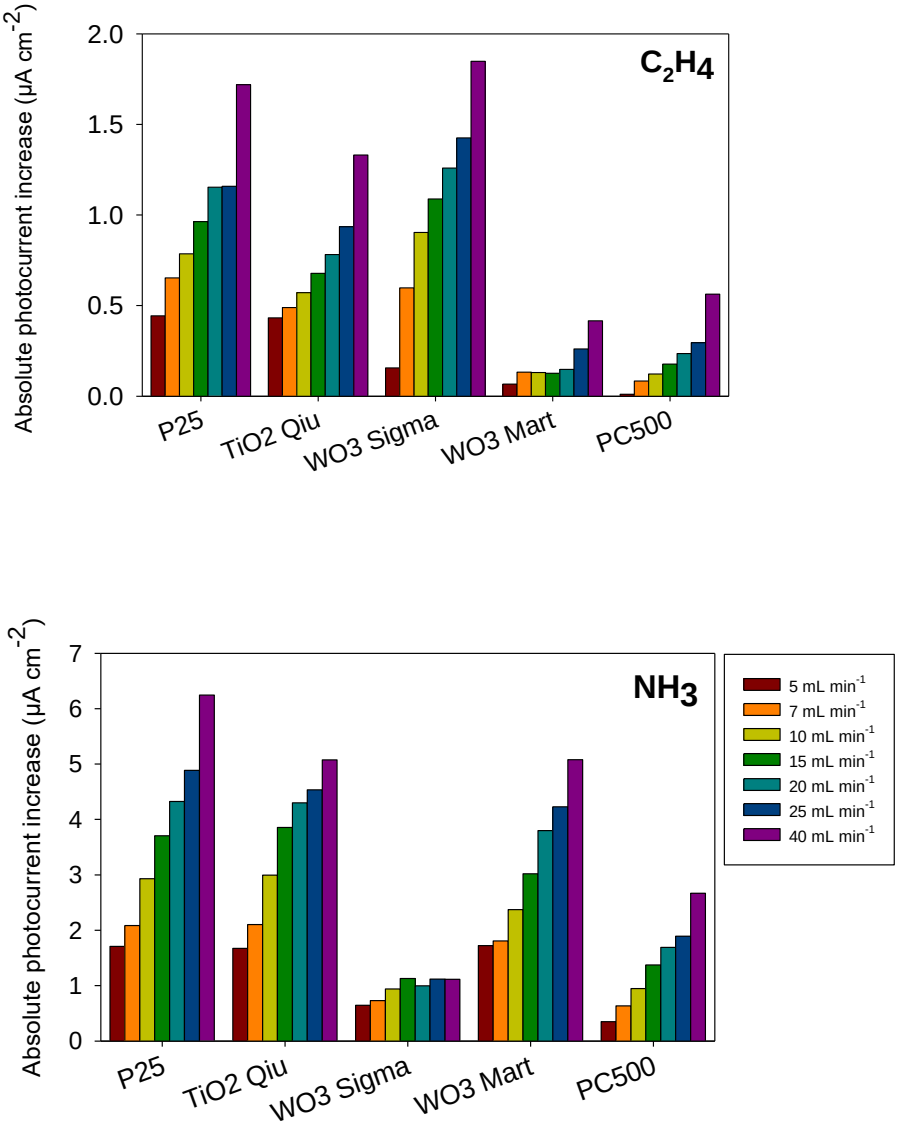

Figure 3.12. Absolute photocurrent increase upon introduction of different gaseous pollutants (CH_4, C_2H_4 and NH_3) at the photoanode compared to photocurrent generation with clean moist air, expressed in µA cm^{-2}, when using different photocatalysts at the photoanode of the PFC.

Figure 3.12 shows that, overall, very low photocurrent increases ($<$ 0.4 µA cm^{-2}) were obtained when working with methane. Methane is known for its high C-H bond energy (413 kJ mol^{-1}) and non-polar nature, making it a much more difficult molecule to degrade than methanol.[33] A clear rise in

photocurrent increase is seen with increasing methane concentration, showing by far the largest photocurrent increase when going from 25 to 40 mL min^{-1} for the three best performing photocatalysts ($WO_{3\ Sigma}$, P25 and $TiO_{2\ Qiu}$). The highest photocurrent increase was obtained for all studied flow rates when using $WO_{3\ Sigma}$. Only negligible increases in photocurrent generation were obtained with PC500. When adding ethylene to the photoanode feed higher photocurrent increases were achieved than for methane. The generated photocurrents increased with increasing ethylene concentration. Overall, again the highest photocurrent increases were reached by $WO_{3\ Sigma.}$ When adding ammonia to the photoanode feed, much higher photocurrent increases were obtained than for the two other studied pollutants, making ammonia an interesting target compound for the presented PFC device. Similar results were obtained for P25 and $TiO_{2\ Qiu}$, with the highest photocurrent increase for P25. Good results were also obtained with $WO_{3\ Mart.}$, only resulting in slightly lower photocurrent increases than both TiO_2-based photocatalysts.

A variety of factors might contribute to the photocurrent generation obtained when introducing a specific gas at the photoanode. An important parameter is the bond energy, which is lowest for a N-H bond as found in NH_3 (391 kJ mol^{-1}), followed by the C-H bond of methane (413 kJ mol^{-1}) and with the highest bond energy for the double C=C bond of ethylene (614 kJ mol^{-1}).[183] Other possible influencing parameters include: polarity of the gas molecule, adsorption characteristics, and selectivity of the reactions.[184] A detailed mechanistic investigation is outside the scope of this thesis.

Overall, using PC500 low absolute photocurrent increases were obtained for all three studied gases, resulting from the poor electronic properties of this photocatalyst.[75] The two other TiO_2-based photocatalysts performed better, and gave similar results, with for all gases slightly better results for P25. This can be attributed to the optimized anatase to rutile ratio (4:1) of this commercial TiO_2-material. With the two studied WO_3-based photocatalysts opposite results were obtained. The commercial WO_3 ($WO_{3\ Sigma}$) performs best for both hydrocarbons, also outperforming all TiO_2-based photocatalysts, while low photocurrent increases are seen with $WO_{3\ Mart.}$ for both hydrocarbons. $WO_{3\ Sigma}$ on the other hand was the worst performing photocatalyst when flushing the photoanode with NH_3, while high photocurrent increases were

obtained with $WO_{3\ Mart.}$ for this gaseous pollutant. A variety of factors (*e.g.* porosity, crystallite particle size) might contribute to these differences, however, more research is required to determine the driving material properties for specific gases.

These results can serve as proof of concept of the applicability of the presented PFC as waste-to-electricity device for a range of gaseous wastes and pollutants. It is clear that the optimal photocatalyst depends on a variety of factors including the type of pollutant(s) and the pollutant concentration.

3.4 Conclusion

In this chapter an autonomous, low-cost, and widely applicable PFC device targeting air pollution was presented. Simultaneous waste gas degradation, using methanol as a model compound, and electricity production were achieved in the absence of an electrical bias. WO_3-based photocatalysts were successfully applied, for the first time, as photoanode material under these conditions. Improved insight into the driving material parameters behind gas phase photofuel cell operation was obtained by comparing direct photocatalytic and photoelectrochemical gas phase experiments for five different materials. The partially visible light active WO_3 photoanodes clearly outperformed the UV-active TiO_2-based electrodes both under pure UV and solar light irradiation. They resulted in the highest steady state photocurrent, fuel-to-electricity conversion ($>$ 65%) and overall efficiency, proving promising candidates as photoanodes for an autonomously operating sunlight-driven PFC device solely using polluted air to sustainably generate electricity. In contrast, both studied WO_3-based photocatalysts resulted in the lowest direct photocatalytic methanol conversion ($\sim$ 65%), highlighting the difference in driving material properties between both processes. While the low surface area of both WO_3-based photocatalysts reduced the direct photocatalytic performance of these materials, this property seemed of lesser importance in a gas phase PFC, which on the other hand largely benefits from the high electron mobility provided by WO_3-based materials.

When broadening the scope to different gaseous wastes/pollutants, simultaneous air purification and electricity generation could also be observed for methane, ethylene and ammonia, with the most promising results for

ammonia. The choice of photocatalyst depends on a variety of factors, including the present gas(es) and their concentration. This chapter aims to serve as proof of concept towards further development of an autonomous, low-cost and widely applicable waste gas-to-electricity PFC device.

Chapter 4

Complete, low-cost and accurate detection methodology for monitoring of (photocatalytic) soot oxidation

Based on:

Myrthe Van Hal, Sammy W. Verbruggen, Xiao-Yu Yang, Silvia Lenaerts, Tom Tytgat, *Image analysis and* in situ *FTIR as complementary detection tools for photocatalytic soot oxidation*. Chemical Engineering Journal. 367 (2019), p.269-277.
https://doi.org/10.1016/j.cej.2019.02.154.

Author contributions:

M.V.H. designed the experiments, performed the material synthesis and characterisation, executed the soot degradation experiments and wrote the paper.

S.W.V, X-Y. Y, S.L. and T.T. supervised the work.

Special thanks to Matthias Minjauw for performing atomic force microscopy measurements.

4.1 Introduction

Air pollution such as particulate matter (PM) is an increasingly urgent problem, especially troubling urban environments. An important component of PM is soot, which is mainly composed of elemental carbon and carbon-based organic matter.[46] It causes both short and long-term health problems, climate interference and aesthetical problems due to fouling of surfaces such as buildings,[46,47] as described in more detail in Chapter 1. To this end, the capacity of semiconductors to cope with deposited soot is crucial for real-life photocatalytic applications. When looking towards application of the in Chapter 2 and 3 studied PEC technology, targeting simultaneous air purification and energy recovery, the soot oxidation capacity of the studied photoanode materials is crucial for long-term and robust operation.

Research has shown the potential of photocatalysis for soot degradation.[88–90,92,94,95,97,185] Photocatalytic soot degradation using TiO_2 has first been shown by Lee and Choi in 2002. They were able to completely oxidize the bulk of a 2 µm layer of soot towards CO_2 after 30 h of irradiation. In this study $OH^{\bullet}$ radicals were assigned as the main oxidant species, however, they also acknowledged the necessity of the presence of oxygen to enable photocatalytic soot oxidation.[88] The limited amount of literature available on the topic of photocatalytic soot oxidation mainly deals with aspects of self-cleaning applications, mechanistic considerations and kinetic modelling of the overall reaction.[88–91,93,97–99] Although photocatalytic soot oxidation is a tough reaction, and involves various practical difficulties, little research has been done on the development and improvement of user-friendly and unambiguous soot oxidation detection methods.[92] This is important to gain better insight into the process of photocatalytic soot degradation, but it also facilitates and improves the photocatalyst screening for a given application (*e.g.* photoanodes). Therefore, in this chapter a low-cost and time-efficient soot oxidation detection methodology was presented, providing a realistic, accurate and all-inclusive description of this process.

The detection method developed by Smits *et al.* (2013) relies on the colour change of a soot-covered photocatalyst layer using digital image analysis.[92] This method has the advantage over the conventionally used quartz crystal

microbalance that it is cheap and less time-consuming since multiple samples can be analysed simultaneously. The method also has some important drawbacks. A first drawback is the use of a threshold value to classify each pixel in the digital image as either fouled with soot or completely clean, without any intermediate classification. This is not a realistic interpretation of the soot degradation process and thus may lead to misinterpretations. As soot is degraded, the colour of each pixel gradually shifts from fouled (black) to clean (original colour), over intermediate (grey) values. In this work the digital analysis method is drastically improved by determining the grade of fouling of each pixel. By doing so, the aforementioned problem is circumvented, and it is now possible to get a more realistic, complete view on the degradation of soot and in addition simultaneously study the degradation of different grades of soot fouling. This improvement was validated by comparison with absorbance measurements. One important drawback of this digital image analysis is that it provides no data whatsoever on the reaction products and thus ongoing reaction pathways. To deal with this limitation an *in situ* FTIR detection method is studied, based on a reaction cell introduced by Hauchecorne *et al.* in 2011.[186] The cell enables to probe the photocatalytic surface as well as the surrounding gas phase simultaneously, while the irradiation process is ongoing. Complementary information on both gaseous reaction products and adsorbed intermediate surface species can thus be obtained in a single measurement. To evaluate the proposed soot oxidation detection methodology the photo-catalytic soot oxidation capacity of common photocatalytic materials (TiO_2, ZnO) was studied, which was to our knowledge the first time for ZnO.

4.2 Experimental

4.2.1 Material synthesis

A sol-gel synthesis method was used to synthesize nano-sized TiO_2 according to Qiu *et al.* (2006),[164] as described in Chapter 3. The ZnO nanoparticles were synthesized according to a precipitation method described by Chen *et al.* (2016).[33] Zinc nitrate (0.005 mol) and oxalic acid (0.005 mol) were each dissolved in 100 mL deionised water. The oxalic acid solution was added dropwise to the zinc nitrate solution, obtaining zinc oxalate precipitates. Subsequently the precipitates were filtered and calcined at 350°C for 6 h.

Commercially available photocatalysts P25 and ZnO nanopowder (< 100 nm) were purchased from Evonik and Sigma Aldrich, respectively, and used as received.

4.2.2 Photocatalyst coating

Soda lime glass slides (2.5 cm x 1.5 cm, VWR) were washed in Piranha solution (70% sulfuric acid (H_2SO_4, Chem-Lab, 95 - 97%), 30% hydrogen peroxide (H_2O_2, ChemLab)) for 30 minutes. The photocatalytic materials were suspended in methanol (Merck) by sonication for 1 hour (66.7 mg mL^{-1}). Application of the coating was performed by drop casting the suspension on a dry glass slide, resulting in a photocatalyst loading of 3.56 mg cm^{-2}. The glass slides were then dried in air at room temperature for 2 hours and subsequently overnight at 80°C. As a model compound for soot, black carbon (Printex-U, Evonik) was suspended in methanol by sonication for 1 hour (1 mg mL^{-1}). This solution was drop casted on the coated glass slides (0.022 mg cm^{-2}). The glass slides were again dried for 2 hours at room temperature and overnight at 80°C. Finally, the glass slides were placed in a vacuum furnace for 2.5 hours at 35°C.

4.2.3 Physical characterisation

A range of physico-chemical characterisation techniques (N_2 sorption, UV-VIS spectroscopy, X-ray diffraction and energy dispersive X-ray fluorescence) were performed to confirm correct synthesis of the synthesized photocatalysts. These methods are described in Chapter 3. Additionally, atomic force microscopy (AFM) measurements (Bruker Dimension Edge) were performed at a scan range of 2 µm and a scan rate of 0.5 Hz to determine the surface morphology of the photocatalysts.

4.2.4 Colour-based monitoring of photocatalytic soot oxidation

A soot-fouled surface obviously darkens when more soot is being deposited. In this way, the result can be directly related to the contemporary problem of fouling of buildings, resulting in aesthetical deterioration. The extent of photocatalytic soot degradation can be monitored by quantifying the discolouration of the surface using digital images, as was suggested by Smits

et al. (2013).[92] In this work this method will be significantly improved towards a more accurate and complete soot oxidation detection method. In addition, a second detection method also based on visual soot degradation will be used for validation purposes. The experiments were all performed by positioning the samples 3 cm under a Philips fluorescence S 25 W UVA lamp, resulting in an incident light intensity of 2.1 mW cm^{-2} in the region of 290 till 400 nm (λ_{max} at 354 nm), as measured by a calibrated spectroradiometer (Avantes Avaspec-3648-USB2).

Pictures were taken in a standardized photobox,[92] excluding external light and direct illumination. A Canon Eos 500D camera was positioned 20 cm above the samples and the digital images were taken in manual mode (iso 200, aperture f8 and focal exposure 1:5) at maximal resolution (5184 x 3456) at 72 dpi. The digital images were processed using the image software ImageJ in the CIELab colour space. For all digital image analysis experiments the entire glass slide sample area (1.5 cm x 2.5 cm) was studied. The L* coordinate (brightness axis) was used as a measure of the amount of soot deposition and ranged between 0 (black) and +100 (white). Rather than pre-defining a threshold value to categorize a pixel as either fouled with soot or completely clean, the adaptation suggested in this chapter is to use the shift of the most frequent L* value (measured in the majority of the pixels) as a measure for soot degradation. In this way, soot degradation can be visualized and observed when the pixels become brighter, resulting in a shift of most frequent L* value towards higher (*i.e.* 'whiter') L* values. This results in a more realistic representation of the cleaning of the surface. An additional advantage of this improved method is that by considering all L* values, a distinction can be made between different grades of soot fouling, thus allowing to simultaneously monitor the degradation of different grades of soot fouling (*e.g.* a shallow soot haze *versus* condensed soot spots).

In Experiment 1 each photocatalyst was applied onto four glass slides. Three glass slides were illuminated, one was kept in the dark as negative control. Photographs were taken from the glass slides before and after soot deposition at specific UV illumination intervals (*e.g.* 0, 0.7, 1, 2, 5, 12, 21, 28, 41 and 65 days). The obtained pictures were processed in ImageJ to determine the

frequency of the L* values. In order to compare the photocatalytic soot degradation of different photocatalytic materials the shift in most frequent L* value was expressed relative to the most frequent L* value of a completely fouled glass slide (L_0). The relative soot degradation efficiency of a uniform soot haze can in this way be expressed as in (Eq. 4.1) and is shown in Figure 4.1a:

$$\textit{Degr. efficiency uniform soot haze (\%)} = \textit{Rel } L^*_{max}\ (\%) = \frac{L_b}{L_a} \cdot 100 = \frac{L_t - L_0}{L_{NS} - L_0} \cdot 100 \qquad \text{(Eq. 4.1)}$$

Where L_t is the position of the most frequent L* value at a specific time of irradiation, L_0 is the position of the most frequent L* value at the beginning of the experiment (no UV illumination = completely fouled glass slide) and L_{NS} is the position of the most frequent L* value when no soot has been deposited on the photocatalyst yet (clean glass slide).

The relative degradation efficiency of concentrated soot spots can be determined by the 'height' (number of pixels) of the peak relative to the peak height of a completely fouled glass slide (NP_0) (eq. 4.2) and is illustrated in Figure 4.1b:

$$\textit{Degr. efficiency conc. soot spots (\%)} = \textit{Rel } NP_{max}\ (\%) = \frac{NP_b}{NP_a} \cdot 100 = \frac{NP_0 - NP_t}{NP_0 - NP_{NS}} \cdot 100 \qquad \text{(Eq. 4.2)}$$

Where NP_t is the height of the concentrated soot peak at a specific time of irradiation, NP_0 is the height of this peak at the beginning of the experiment (no UV illumination = completely fouled glass slide) and NP_{NS} is the height of this peak when no soot has been deposited on the photocatalyst yet (clean glass slide).

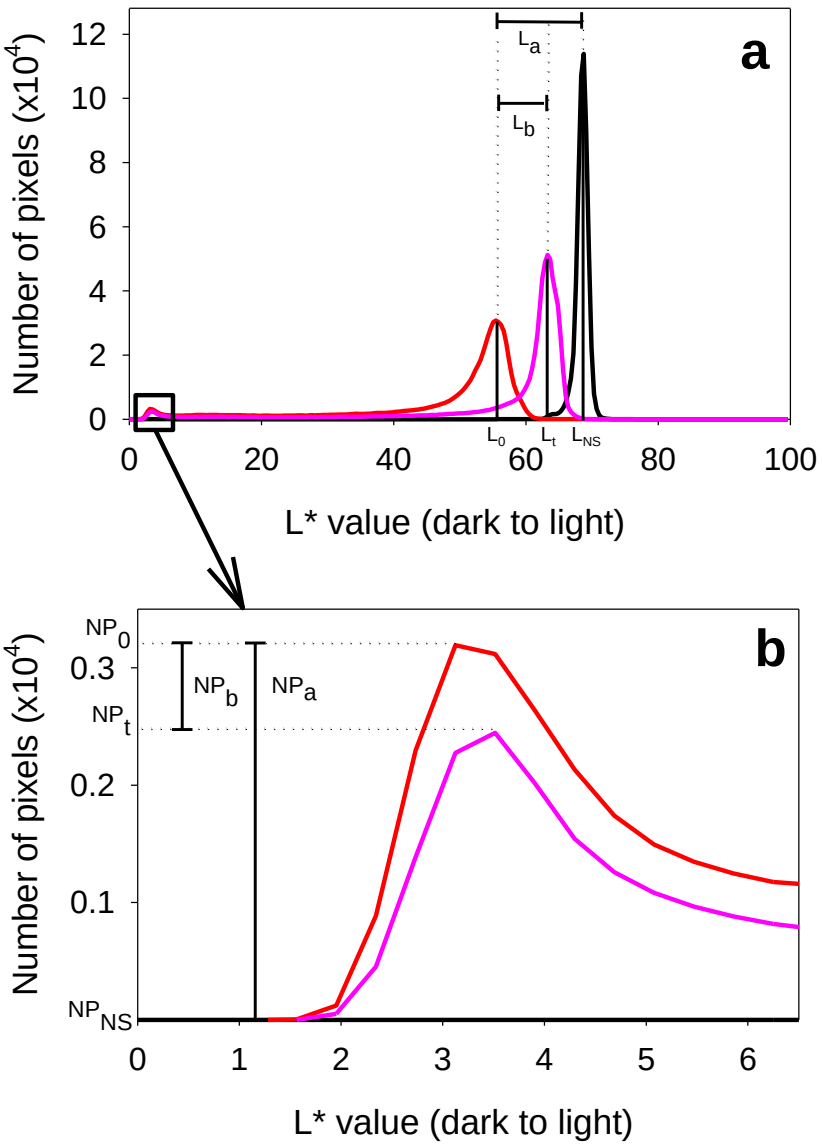

Figure 4.1. a) Illustration of determination of the soot degradation efficiency of a uniform soot haze using the improved digital image analysis with the result before soot deposition (black), before UV illumination (red) and after 120 h of UV illumination (pink). b) Illustration of determination of the soot degradation efficiency of concentrated soot spots using the improved digital image analysis with the results before soot deposition (black), before UV illumination (red) and after 120 h of UV illumination (pink).

Corrections for possible deviations caused by small changes in the background

illumination were made by processing a set area of the background in ImageJ and applying the hereby obtained deviation in L* value to the complete dataset of that time point.

To validate the improvements made to the digital image analysis method suggested by Smits *et al.* (2013),[92] a second optical detection method (absorbance method) was used to measure the photocatalytic soot degradation. The results obtained by this absorbance method could then be compared with the results obtained with both the original and the improved digital image analysis. In Experiment 2 the coated glass slides were again illuminated using a UVA lamp. Photographs were taken at specific UV illumination time intervals (*e.g.* 0, 0.7, 1, 2, 4, 5, 7, 12, 21, 28 and 41 days) and in addition the absorbance of each glass slide was measured each time. This colorimetric method is based on the decrease in absorbance of the samples when soot is being degraded. For this colorimetric analysis an AvaSpec-3648-USB2 spectroradiometer was used. The samples were placed in the standardised photobox during the absorbance measurements.[92] The complete absorbance spectrum in the visible range (400 - 700 nm) was measured, however, since the shape of the absorbance spectra was the same for all measurements, only the absorbance value at 600 nm was used. To quantify the soot degradation using the obtained absorbance values, the absorbance at 600 nm was divided by the initial absorbance at this wavelength, resulting in the value A_t/A_0 representing the amount of fouling on the surface. To compare these results with the results obtained with the digital image analysis, the results were expressed as (Eq. 4.3):

$$\textit{Degr. efficiency uniform soot haze (\%)} = \left(1 - \frac{A_t}{A_0}\right) . 100 \qquad \text{(Eq. 4.3)}$$

4.2.5 *In situ* monitoring of photocatalytic soot oxidation

Insight into the photocatalytic activity at the catalyst surface was gathered using a patented *in situ* Fourier transform infrared (FTIR) reaction cell designed by Hauchecorne *et al.* (2011). The experimental details on the cell design can be retrieved from reference[186]. Printex-U was used as a model compound for soot. To achieve a round flat pellet, 5 mg of a mixture containing the photocatalyst powder and 0.6 wt% soot (Printex-U) was thoroughly mixed with

115 mg KBr (VWR) and pressed for 2 minutes at 5 tons. This pellet was placed in the centre of the *in situ* reaction cell. Before starting the measurement, the reactor was flushed with air at 200 mL min^{-1} until a stable readout was obtained.[149] Next, the reactor was sealed airtight and the batch experiment was started. Over a period of 12 hours, the pellet was illuminated by eight UV LEDs at each side placed in a circular pattern (10 mW each, Roithner LaserTechnik) with an incident intensity of 330 µW cm^{-2} in the region of 350 till 420 nm (λ_{max} at 377 nm). This was followed by a 2 hour control measurement without illumination to confirm the air tightness of the reactor.

4.3 Results and discussion

4.3.1 Characterisation

The obtained characteristics of the photocatalyst powders used in this chapter are summarized in Table 4.1. It is clear that the BET surface area of P25 and the synthesized TiO_2 are similar, however, the synthesized ZnO results in a significant increase in surface area compared to the commercially available form. The adsorption isotherms show that both ZnO materials are non-porous. P25, as also known from literature, is also non-porous,[187] although agglomerates lead to some macroporous interparticle pores. TiO_2 synthesized according to Qiu *et al.* (2006) on the other hand is characterised by a mesoporous structure, as described in Chapter 3 (see Figure 3.3). In addition, it can be seen that the band gaps of the synthesized materials are similar to the commercial ones for both TiO_2 and ZnO. Using AFM measurements, the roughness of the photocatalyst layers was determined. Based on the root mean square values (Table 4.1) both commercial materials (P25 and ZnO_{Sigma}) form a somewhat less rough layer compared to the materials that were synthesized in the lab, with the least rough surface for P25. All four photocatalyst layers can be considered as very rough, as a result of the fact that they are all simple powder films. Overall, it should be clear that such films are not suitable for practical implementation, but in the scope of the present chapter on alternative detection methods this inhomogeneity is not a decisive factor.

Table 4.1. Characteristics of commercial and synthesized materials as powder films on glass.

Material	Band gap (eV)[3]	BET surface area ($m^2 g^{-1}$)	Surface roughness (Rq) (μm)	Crystallite particle size (nm)[4,5]
$P25_{Evonik}$[1]	3.2	52	0.026	19 (A), 32 (R)
$TiO_{2\ Qiu}$[2]	3.1	68	0.128	30 (A), 36 (R)
ZnO_{Sigma}[1]	3.3	11	0.053	< 100[6]
ZnO_{Chen}[2]	3.3	49	0.112	17

1) commercially available photocatalysts.
2) Photocatalysts synthesized based on literature protocols.
3) Obtained by the Tauc method applied on diffuse reflectance spectra.
4) Estimated from XRD using the Scherrer equation.
5) A = anatase, R = rutile.
6) According to manufacturer data (Sigma-Aldrich).

The structure and crystallinity of the synthesized materials was determined using X-ray diffraction (Figure 4.2). The TiO_2 sample was calcined for 3 hours at 600°C to obtain a combination of the crystalline forms anatase and rutile, which is confirmed by the XRD pattern shown in Figure 4.2. In Figure 4.2 the characteristic XRD pattern for the hexagonal wurtzite structure of ZnO can be observed.

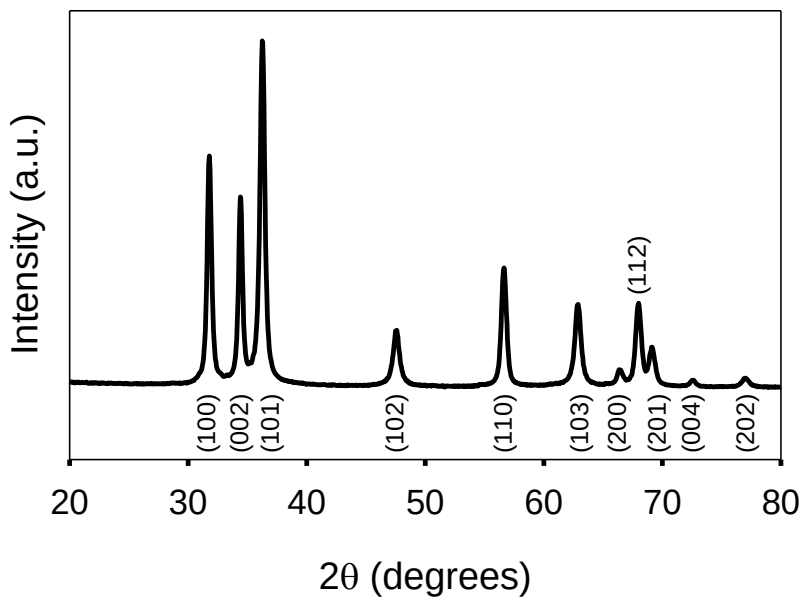

Figure 4.2. XRD pattern of ZnO synthesized according to Chen *et al.* (2016).

4.3.2 Colour-based monitoring of photocatalytic soot oxidation

In the first part of this chapter the original digital image analysis method was drastically improved towards more accurate and detailed monitoring of (photocatalytic) soot degradation. This is done by using the shift of the most frequent L* value (the brightness axis of the CIELab colour space) as a measure for visual soot degradation instead of using a fixed threshold value to categorize each pixel as either fouled or clean. When a soot haze is degraded, the most frequent L* value is expected to shift towards higher and thus brighter L* values.

In Experiment 1 (see Section 4.2.4) the coated glass slides were illuminated with UV light and digital images were taken at specified time intervals. The result for P25 is shown in Figure 4.3. At 0 h the sample is dark grey, which changes over light grey towards the original colour of the coated glass slides (left) when soot is completely photocatalytically degraded. When applying the described improved method, a graph plotting the number of pixels against the L* value can be obtained, resulting in Figure 4.4 for P25. On this graph the photocatalytic soot degradation observed in Figure 4.3 is reflected by the shift of the most frequent L* value towards higher L* values. This shift of the most frequent L* value can then be expressed as a soot degradation efficiency using (Eq. 4.1), resulting in Figure 4.5 for P25. In addition, it can be observed from Figure 4.4 that next to the shift in the peak, also its shape changes when soot is photocatalytically degraded. Initially, a broad low peak is present, reflecting the large amount of different dark grey tones on a completely fouled glass slide. When soot is degraded all pixels shift towards higher ('whiter') L* values and more and more pixels will have similar 'whiter' colours, resulting in more pixels with the same L* value and thus a higher, narrower peak.

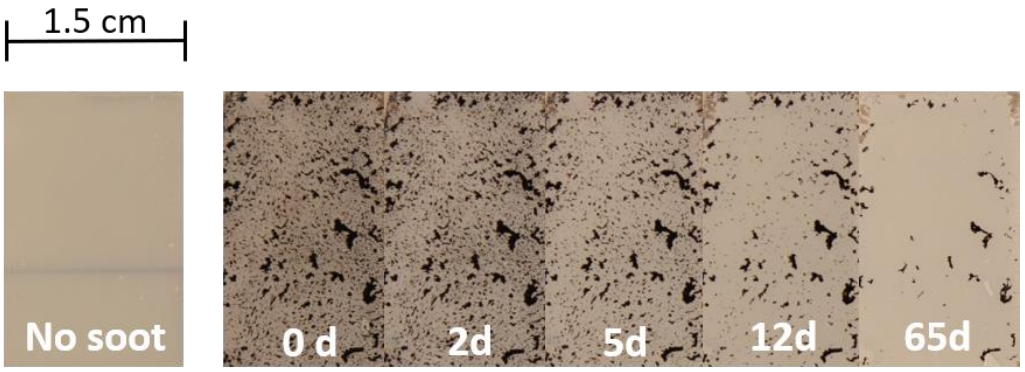

Figure 4.3. Experiment 1. Subsequent digital images of the photocatalytic soot degradation on a glass slide coated with P25 with f.l.t.r. a glass slide without soot, with soot before UV illumination, after 2, 5, 12 and 65 days of illumination.

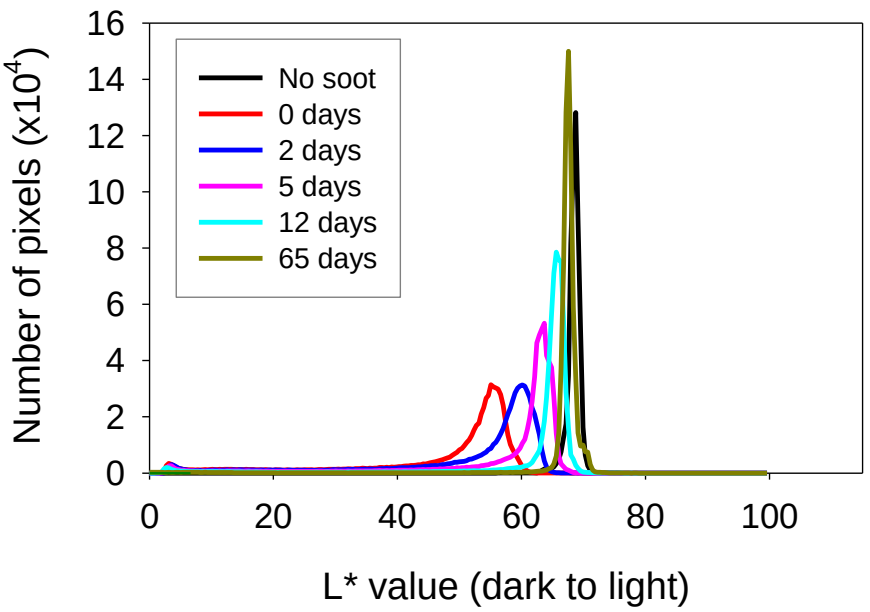

Figure 4.4. Experiment 1. Number of pixels plotted against the L* value, representing the photocatalytic degradation of a uniform soot haze by P25.

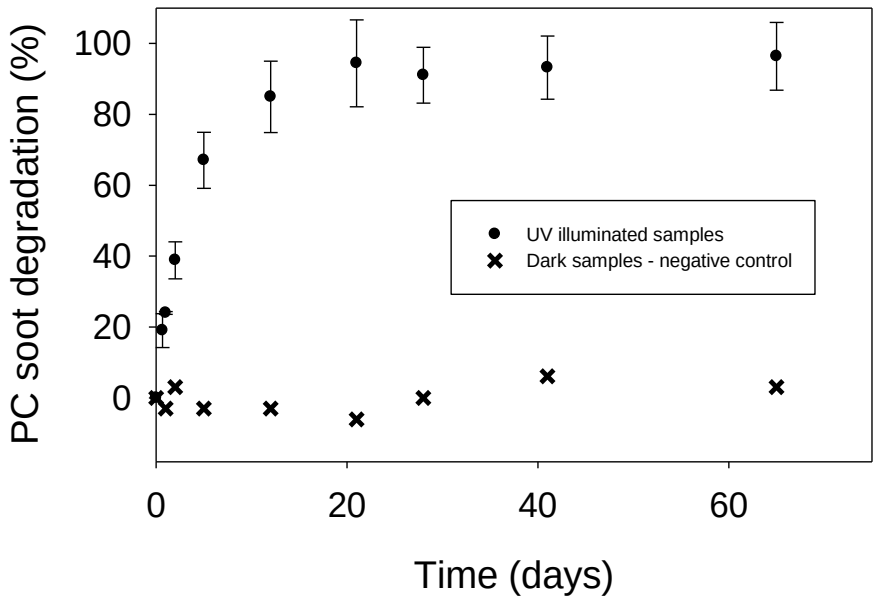

Figure 4.5. Experiment 1. Photocatalytic soot degradation of uniform soot haze (expressed as relative L^*_{max}) by P25, as a function of UV illumination time. The error bars are based on three samples.

The presented improved method allows to visualise the degradation of soot as a shift in most frequent L* value, resulting in a more detailed view on the soot degradation process. It is clear from Figure 4.3 that a distinction can be made between different gradations of soot fouling, that are not all completely degraded at the same time. Figure 4.5 shows that for P25 complete soot degradation is reached after 41 days, however, some concentrated soot spots can still be observed at that time (Figure 4.3). As Figure 4.5 is based on the shift of the peak that is originally present at a L* value of 69 (Figure 4.4), this specifically applies to the 'haze' of soot that is deposited uniformly over the glass slide. However, at the left of Figure 4.4 a second small peak can be observed at low L* values, reflecting the presence of concentrated black soot spots, and is shown in more detail in Figure 4.6. It is clear from Figure 4.6 that these soot spots are also degraded over time, although slower, visualised by the decreasing height of this peak. This illustrates the main limitation of the technique: since it is a visual method, soot oxidation can only be detected when

the colour of the surface changes significantly. Thus, when a very thick layer of soot would be present, it is possible that soot is already being oxidised without any visual colour change at that particular location. When the concentrated soot spots are substantially degraded they will no longer contribute to the presence of concentrated soot spots (*e.g.* disappearance of small L* peak at low L* values) but instead contribute to the haze. The presented adaptation thus enables to separately quantify the degradation of these concentrated soot spots (Eq. 4.2), which was not possible in the original method. It can be concluded that the suggested adaptations thus result in more realistic and detailed data.

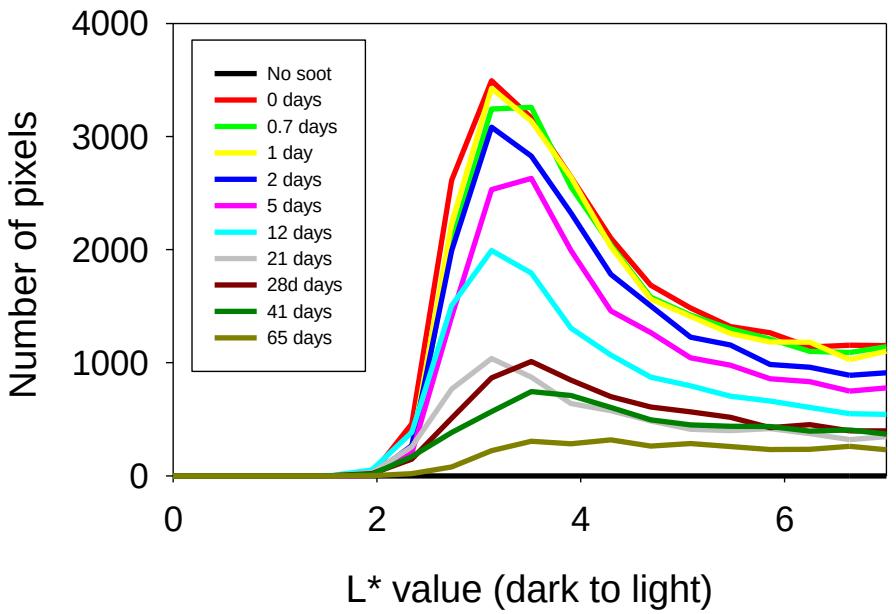

Figure 4.6. Experiment 1. Number of pixels plotted against the L* value, representing the photocatalytic degradation of concentrated soot spots by P25.

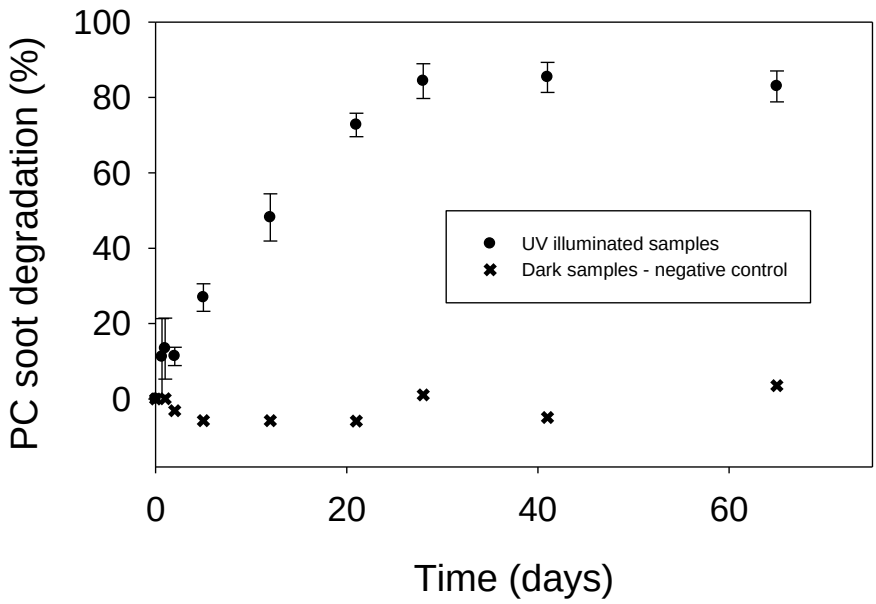

Figure 4.7. Experiment 1. Photocatalytic soot degradation of concentrated soot spots (expressed as relative NP_{max}) by P25, as a function of UV illumination time. The error bars are based on three samples.

The accuracy of the proposed method is validated by comparing the results obtained with both the original and the improved digital image analysis with a second colour-based soot oxidation detection method. This second method is based on the decreasing absorbance of a soot fouled surface when soot is being degraded. This validation experiment (Experiment 2) is presented in Figure 4.8 for P25, demonstrating that the results obtained by the absorbance method and the improved digital image analysis are in good agreement. When applying the method as described by Smits *et al.* using a single fixed threshold value for L*,[92] it can be seen from Figure 4.8 that large differences exist with the results obtained by the absorbance method. Large deviations between the original digital image analysis method and the absorbance method were seen for all four studied photocatalysts. The threshold value depends on a variety of parameters, such as the substrate (*e.g.* mortar samples *versus* glass slides), the colour of the coating, the light source/intensity in the pictures, *etc.* and should

thus be separately determined for each experiment. Thus when using the original digital image analysis a calibration with a different detection method is always needed to determine the threshold value. As the improved digital image analysis directly reflects the actual amount of soot degradation independent of a threshold value this is a much more generic and straightforward method for the detection of soot degradation. Also in the study of Smits *et al.* (2013) a discrepancy between the results obtained with the original digital image analysis and those generated by the absorbance method was present as both methods clearly gave different results for all intermediate time points.[92] This also reflects the unrealistic representation of soot degradation when using a single threshold value, as the colour of a soot fouled surface will not instantly change from black to white when soot is degraded but will rather brighten slowly over time, running over several grey tones.

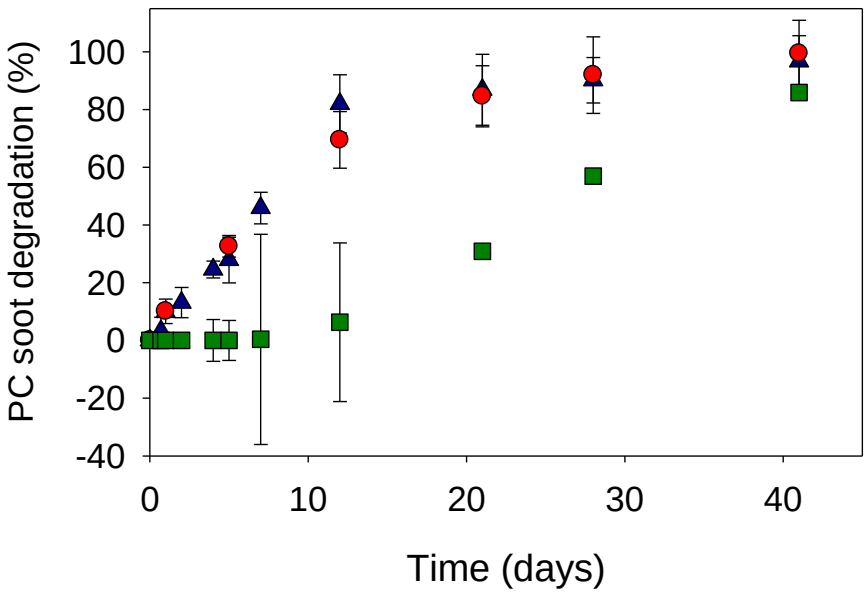

Figure 4.8. Experiment 2. Photocatalytic soot degradation by P25 as a function of UV illumination time: comparison of absorbance method (red ●), the original digital image analysis (green ■) and the improved digital image analysis (blue ▲). The error bars are based on three samples.

Given all the above, it is therefore clear that the suggested adaptations indeed

result in a more accurate, realistic, reliable and straightforward detection tool, that also enables to simultaneously detect the degradation of concentrated soot spots, which was not possible before.

The effect of the studied area on the accuracy of the results was determined by applying the improved digital image analysis on a five times smaller area of the glass slide for P25, as shown in Figure 4.9 for the soot haze and in Figure 4.10 for concentrated soot spots.

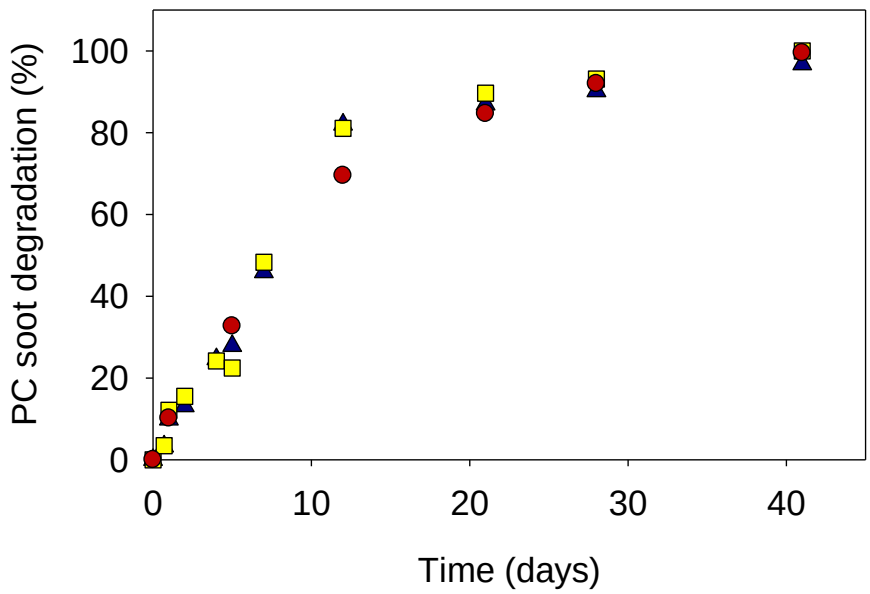

Figure 4.9. Effect of studied area. Photocatalytic degradation of a soot haze by P25: comparison of absorbance method (red ●), the improved digital image analysis applied to the entire glass slide (blue ▲) and the improved digital image analysis applied to a five times smaller selection of the glass slide (yellow ■), as a function of UV illumination time.

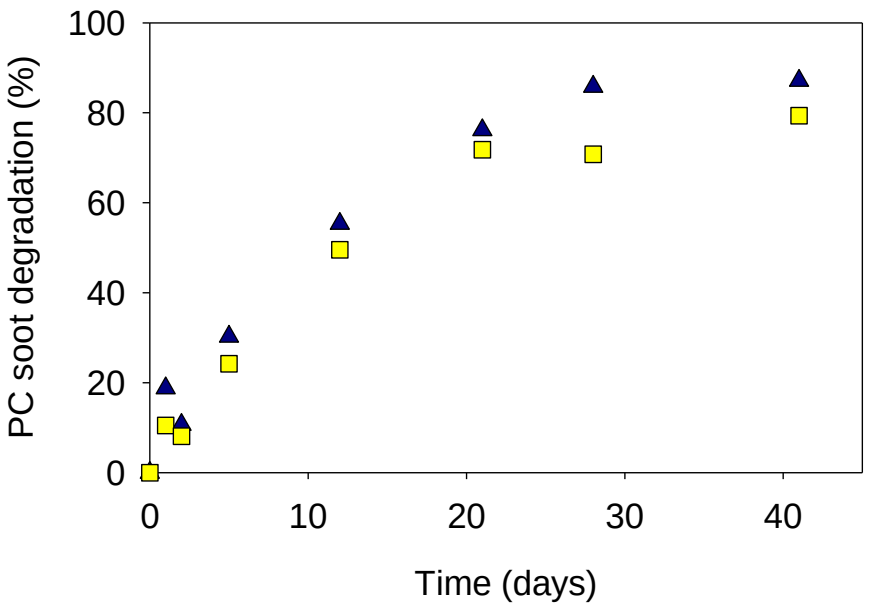

Figure 4.10. Effect of studied area. Photocatalytic degradation of concentrated soot spots by P25: comparison of the improved digital image analysis applied to the entire glass slide (blue ▲) and the improved digital image analysis applied to a five times smaller selection of the glass slide (yellow ■), as a function of UV illumination time.

For a soot haze it is clear from Figure 4.9 that the results obtained by studying a smaller area of the glass slide are very similar to those obtained when analyzing the entire glass slide (average deviation is only 0.8%). For the concentrated soot spots (Figure 4.10) a good agreement between both results can be observed with an average deviation of 6%. Thus, it can be concluded that the improved digital image analysis is not very sensitive to the study area, but to obtain the most accurate results for the degradation of concentrated soot spots it is advised to use a large enough study area (at least 1 cm^2).

As a proof of concept study the adapted digital image analysis is applied to assess the soot degradation capacity (haze) of four photocatalytic materials using the two described colour-based methods (Figure 4.11a). In addition, the photocatalytic degradation of concentrated soot spots was simultaneously monitored with the improved digital image analysis and is presented in Figure 4.11b.

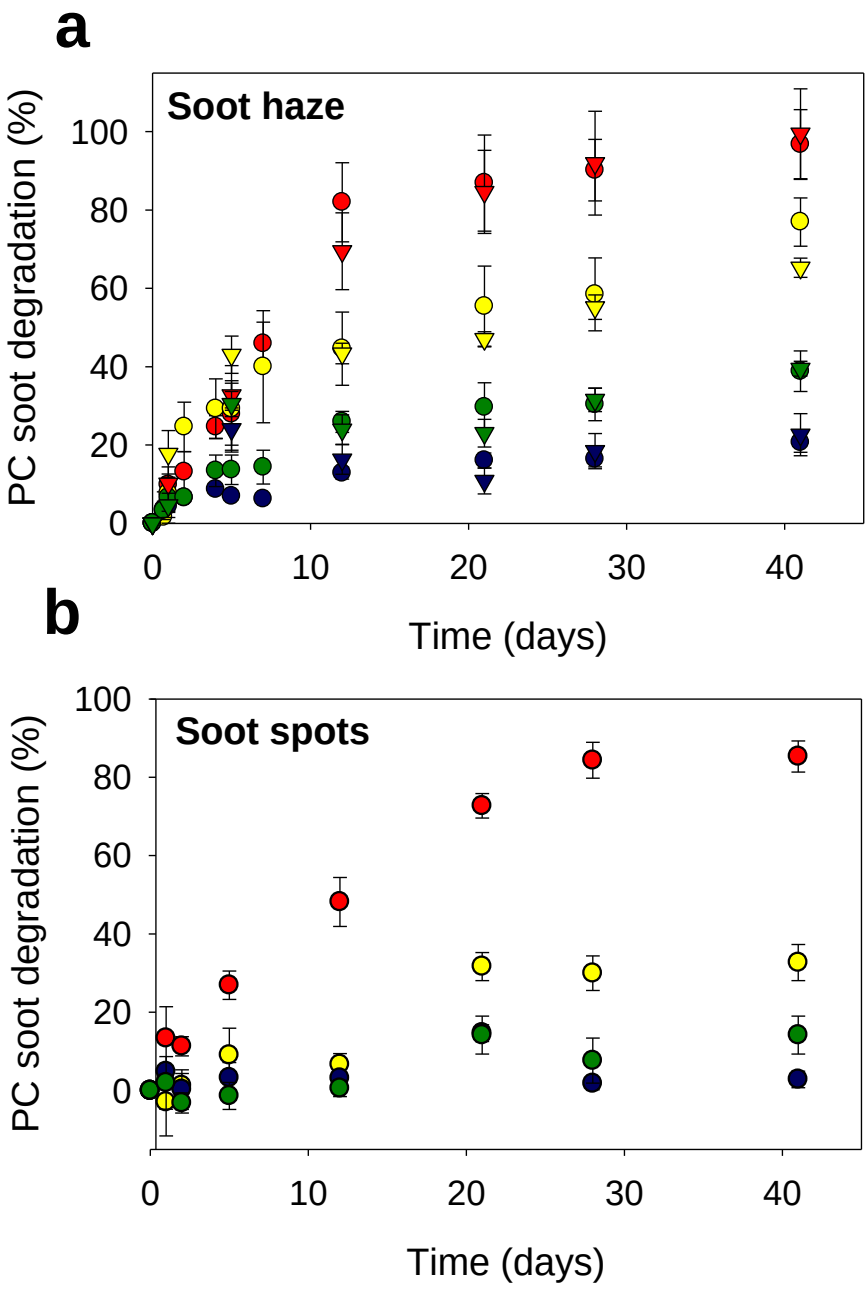

Figure 4.11. Experiment 2. Photocatalytic soot degradation as a function of UV illumination time by following photocatalysts: P25 (red), $TiO_{2\ Qiu}$ (yellow), ZnO_{Chen} (green) and ZnO_{Sigma} (blue) for a) a uniform soot haze: comparison of absorbance (▼) and improved digital image analysis (●) and b) concentrated soot spots determined with the improved digital image analysis.

Figure 4.11a clearly shows that P25 is the fastest photocatalytic soot degrader of all studied materials, resulting in complete soot haze degradation after 41 days (982h) of UV illumination (25 W Philips lamp at 3 cm resulting in an incident irradiance of 2.1 mW cm^{-2}). The TiO_2 synthesized according to Qiu *et al.* (2006) showed a slightly lower soot degradation efficiency, resulting in 65 - 75% degradation after 41 days. The synthesized and commercial ZnO resulted in a soot degradation efficiency of 39 - 39.5% and 20.5 - 22% after 41 days, respectively, illustrating the lower capability of ZnO to degrade soot compared to TiO_2.

Luttrell *et al.* (2014) illustrated the thickness dependency of the photocatalytic soot oxidation reaction up to a thickness in the range of the diffusion length of the excited carriers as there is only negligible penetration of the soot into TiO_2 layers.[188] From the picture without soot deposition in Figure 4.3 it can already be observed that the photocatalyst layers used in these experiments are thicker and differences in the photocatalytic soot oxidation rate between the different materials will likely not originate from different layer thicknesses. As direct oxidation of soot has shown to be the most important oxidation mechanism,[88] all parameters concerning the direct contact area of the photocatalyst with the soot are of key importance for the soot degradation rate. The BET surface area of both TiO_2 forms and ZnO_{Chen} were similar, but the BET surface area of ZnO_{Sigma} was significantly lower (Table 4.1). The low photocatalytic soot oxidation rate of ZnO_{Sigma} might thus be in part be explained by its low surface area.[27] The better performance of both TiO_2 forms might also be partially explained by the fact that TiO_2 synthesized according to Qiu *et al.* (2006) and P25 showed (meso/macro-) porosity, whereas both ZnO materials where non-porous. The porous structure of both materials enables faster diffusion of oxygen species and reaction products. The high performance of P25 can also be attributed to its optimal anatase:rutile ratio. From the AFM surface maps it could already be concluded that all four photocatalyst layers can be considered as rough films, which can be ascribed to the fact that they are simply drop casted powder films. As can be observed in Figure 4.3, the deposited soot layer is also inhomogeneous and rough as soot spots are scattered across the surface of the photocatalyst. Therefore, the surface roughness is not likely to be the

decisive factor for explaining differences in reactivity within this particular sample set.

For P25, the absorbance is halved in the first 7 days (168 h) of illumination, however, complete soot degradation is only reached after 41 days (984 h), illustrating the fast initial soot degradation resembling first order kinetics. This was also observed in previous studies on photocatalytic soot degradation[90,92,93] and kinetic models have been proposed to that end.[91,92] The same can also be observed for all other studied materials, however, no complete soot oxidation was reached after 41 days of illumination for these materials. A dark experiment was simultaneously performed confirming the absence of soot degradation when the glass slides were not illuminated with UV light.

The degradation of concentrated soot spots can only be monitored using the digital image analysis and the result is shown in Figure 4.11b. P25 showed around 85% soot spot degradation after 41 days, $TiO_{2\ Qiu}$ gave 33% degradation, ZnO_{Chen} about 10% and ZnO_{Sigma} resulted in about 3% soot degradation after 41 days. For P25, the degradation of the concentrated soot spots largely corresponds to the degradation of the uniform soot haze, albeit at a lower rate, which corresponds to what can be observed from Figure 4.3. For all the other materials, no to very little soot is being degraded during the first 12 days. Only after 21 days a larger fraction of the soot spots is being visually degraded. This might be explained by the fact that the degradation can initially not be observed on the digital images as the soot spots are still completely black due to the large remaining soot fraction. As P25 has the highest soot degradation capacity of the four studied materials, degradation of the soot spots is visible for P25 earlier.

4.3.3 *In situ* monitoring of photocatalytic soot oxidation

An important limitation of the two previously described colour-based detection methods is that they only represent the visual result of the soot degradation at a specific time but yield no insight into the occurring reactions over time. Therefore, a second soot oxidation detection method is presented in this chapter. With this method soot degradation is studied in an FTIR *in situ* reaction cell. This method enables to determine the degradation of soot by the amount

of CO_2 that is formed in the airtight reactor. In addition, this method also allows detecting all products formed during photocatalytic soot degradation, both gases as well as adsorbed intermediates at the surface.

In the absence of soot, blank tests demonstrated that no CO_2 evolution can be observed when solely irradiating the KBr-photocatalyst pellets. When such pellets also contain soot, a clear signal corresponding to CO_2 evolution can be measured in the wavenumber range 2290 - 2390 cm^{-1} (ν_{as}(O=C=O)), as shown in Figure 4.12a for P25. Initially the height of the CO_2 band increased exponentially, after 10 h this increase started to flatten as illustrated in Figure 4.12b for P25. This flattening was attributed to oxygen depletion in the airtight reaction cell. When the reactor was flushed again with air after CO_2 saturation, the remaining soot could again be further mineralised to CO_2, supporting this hypothesis. In addition, a second important band can be observed in Figure 4.12a in the region 1273 - 1445 cm^{-1} with two maxima at 1360 (ν_s(COO)) and 1380 cm^{-1} (δ(CH)), that can be attributed to adsorbed formate, $CHOO^-_{(ad)}$.[189] Other bands originating from this compound are possibly masked by steric hindrance, as the observed formate is bound to the surface of the pellet. The formation of $CHOO^-_{(ad)}$ supports the theory of Chin *et al.* (2009) that soot can be sequentially oxidized towards CO_2 over several intermediates, next to the possibility of direct oxidation towards CO_2.[97] Using electron paramagnetic resonance (EPR) and FTIR, the reaction mechanisms described by Chin *et al.* have already been elucidated in more detail.[99] A variety of adsorbed intermediates has been determined, possibly containing C-O-C stretching in anhydrides, aryl ether linkages, aromatic rings, C-O bonds and C-H bonds adsorbed on the surface. In addition, in Figure 4.12a two negative bands are observed around 2848 and 2922 cm^{-1}, which can be attributed to the disappearance of C-H stretching vibrations and thus provide clear evidence of soot degradation. This C-H band decreases exponentially, stabilising after ca. 10 hours, in agreement with the CO_2 evolution. Carbon monoxide (CO) could not be detected during the reaction. When analysing the FTIR spectra of the three other studied materials the same bands and trends were observed, pointing at similar reaction mechanisms for photocatalytic soot degradation by TiO_2 and ZnO. The production of CO_2 and formate-related species as a function of UV illumination time for all four studied materials is shown in Figure 4.13.

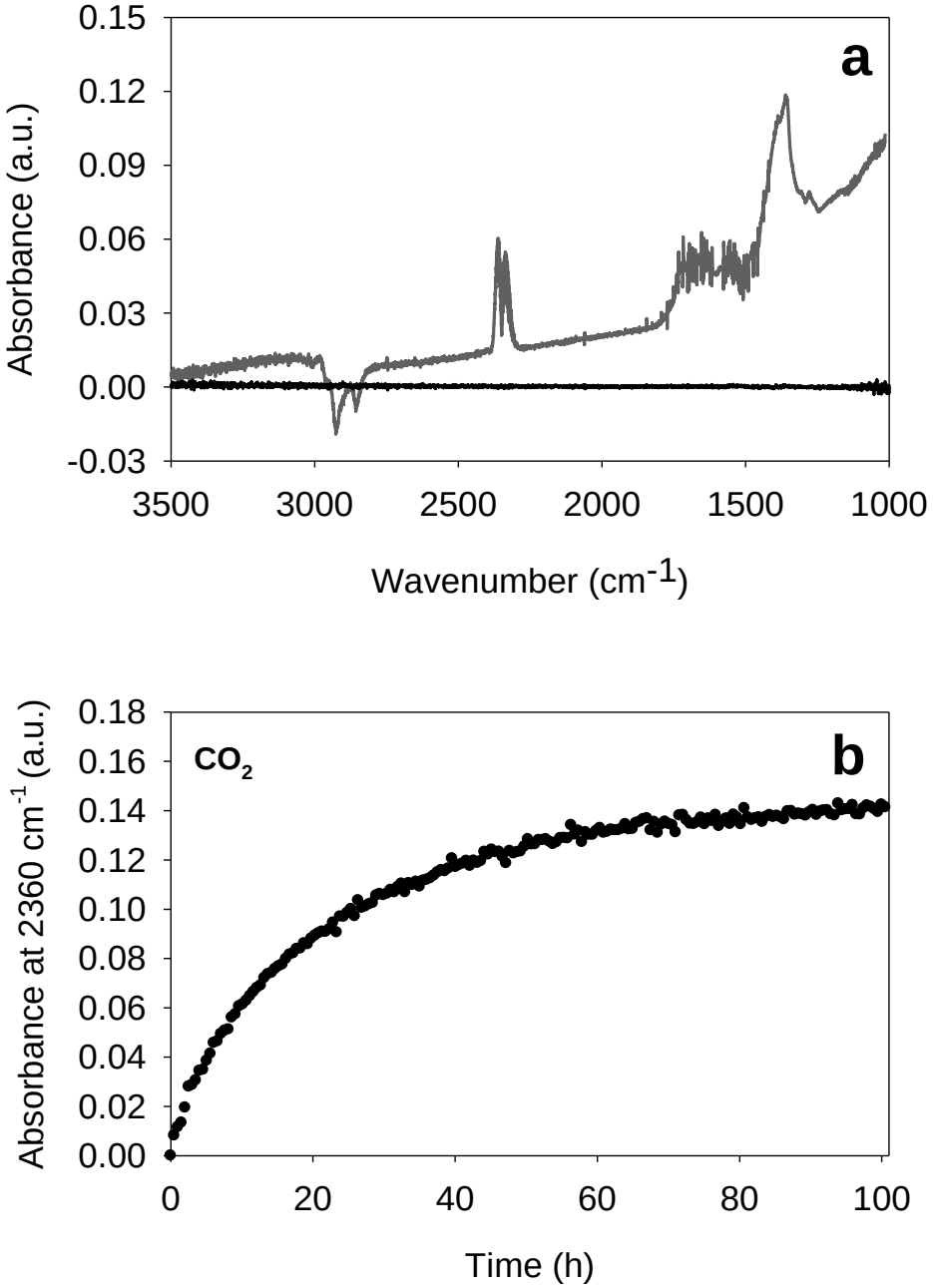

Figure 4.12. a) FTIR spectra of KBr-P25-soot pellet in *in situ* reactor at start experiment (black) and after 10 hours of UV illumination (grey). Positive bands represent formed products, negative bands point at the degradation of products. b) CO_2 (2360 cm^{-1}) production curve of KBr-P25-soot pellet during an *in situ* measurement, as a function of UV illumination time.

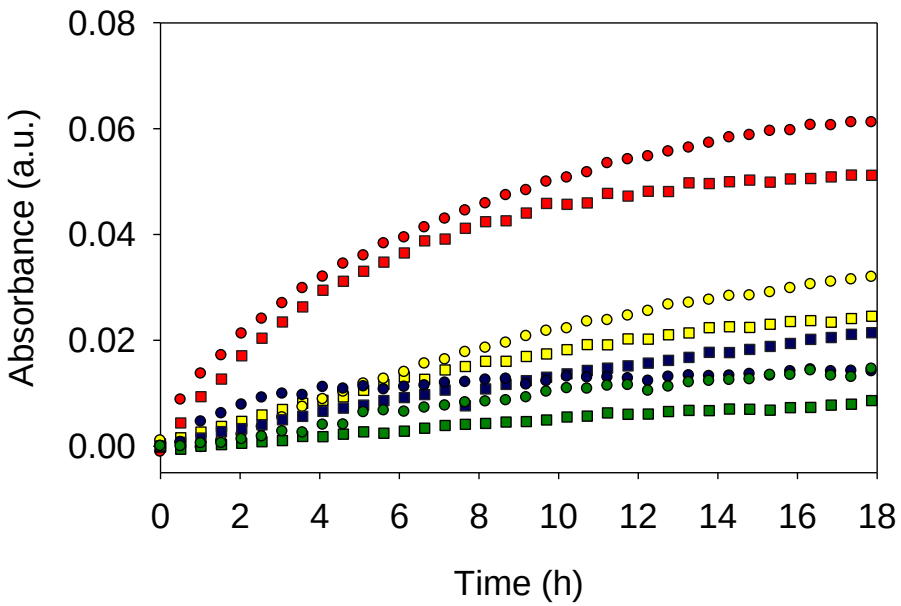

Figure 4.13. Evolution of CO_2 (■) and formate-related species (●) as a function of UV illumination time for a KBr-photocatalyst-soot pellet placed in the *in situ* reactor for following photocatalysts: P25 (red), $TiO_{2\ Qiu}$ (yellow), ZnO_{Sigma} (blue) and ZnO_{Chen} (green).

By monitoring the CO_2 band at 2360 cm^{-1} during photocatalytic soot degradation (every half hour, see Figure 4.12b) the soot mineralisation rate could be determined from the initial slope of the CO_2 evolution curve ($<$ 10 h).

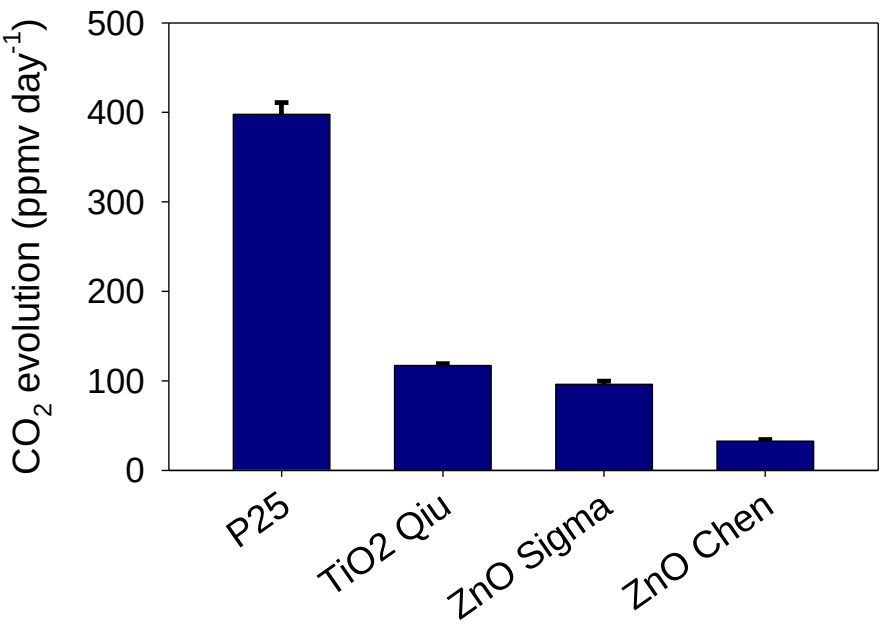

Figure 4.14. CO_2 evolution of studied materials based on the *in situ* soot oxidation detection method. The CO_2 evolution rate is obtained from the slope of the CO_2 evolution curve (see Figure 4.12b) over the first ten hours.

From Figure 4.14 it can be observed that the initial mineralisation rate is by far the highest for P25. The three other materials show drastically lower soot mineralisation rates, with $TiO_{2\ Qiu}$ followed closely by ZnO_{Sigma} and the lowest rate for ZnO_{Chen}. It is hard to directly compare these results with the colour-based methods, as different substrates were used (glass *vs.* KBr pellet) and the colour-based methods reflect a visual change, which might not be directly proportional to CO_2 formation. As is clear from Figure 4.12a, CO_2 is not the only product being formed during photocatalytic soot degradation. Therefore, this *in situ* method allows to assess which materials have a high specificity towards CO_2 and thus result in more complete soot degradation after 10 hours of UV illumination. The ratio of the absorbance of CO_2 (2360 cm^{-1}) to formate (1360 cm^{-1}) (after 10 h) is shown in Table 4.2. These values should solely be used to mutually compare samples, and do not reflect the ratio of actually produced concentrations. From this, ZnO_{Sigma} actually appears to have the

highest specificity towards CO_2, followed by P25, $TiO_{2\ Qiu}$ and finally ZnO_{Chen}. The discrepancy between the low CO_2 production rate of ZnO_{Chen} determined with the *in situ* technique (Figure 4.14) and the relatively higher soot degradation efficiency (compared to ZnO_{Sigma}) measured with the improved digital image analysis (Figure 4.11a) can be explained by Table 4.2. The soot oxidation reaction by ZnO_{Sigma} is more complete than that by ZnO_{Chen} that yields more of the intermediate product formate instead of CO_2.

Table 4.2. Absorbance ratio of CO_2 to formate for the four studied photocatalysts.

	Ratio of absorbance of CO_2 to formate
P25	0.81
$TiO_{2\ Qiu}$	0.71
ZnO_{Sigma}	1.00
ZnO_{Chen}	0.46

Overall, this third *in situ* detection method thus allows monitoring of all formed products, both gases and adsorbed intermediates, in *quasi* real-time, which can be regarded a clear benefit over the colour-based analysis methods described above. An important drawback is that dedicated lab equipment is required to that end, whereas the colorimetric methods are more straightforward and image processing can even be done using digital image analysis freeware.

4.4 Conclusion

In this chapter two complementary detection methods for soot oxidation were studied. First the digital image analysis suggested by Smits *et al.* (2013) was improved towards a more realistic, accurate, and detailed method.[92] This was achieved by using the shift of the most frequent L* value (CIELab colour space) as measure for visual soot degradation instead of using a fixed threshold value to categorize each pixel as either fouled or clean. The improved digital image analysis was validated by comparison with the absorbance method. The adaptation enables simultaneous measurement of the degradation of different grades of soot fouling. By applying this method, we could evidence that P25 is the fastest photocatalytic soot degrader of all studied materials for both a uniform soot haze as well as for concentrated soot spots, followed by $TiO_{2\ Qiu}$, ZnO_{Chen} and finally ZnO_{Sigma}.

In the second part of this chapter, a second detection method was suggested based on *in situ* FTIR measurements. This method delivers additional insight into the products formed during photocatalytic soot degradation by monitoring both gaseous and adsorbed reaction products. Using this method, it was shown that for all studied materials $CHOO^-_{(ad)}$ was formed, supporting the hypothesis of Chin *et al.* (2007) of an indirect soot oxidation pathway via solid intermediates, next to direct soot oxidation to CO_2.[91] Using this method, an initial CO_2 production rate could be determined for the studied materials, which was the highest for P25. In addition, using the ratio CO_2 to formate it could be concluded that ZnO_{Sigma} has the highest specificity towards CO_2, followed by P25, $TiO_{2\ Qiu}$ and finally ZnO_{Chen}. A more in-depth mechanistic study on the photocatalytic soot oxidation pathways is needed to further increase the insight into the process of photocatalytic soot oxidation.

In summary, this chapter results in a complete detection strategy for soot oxidation that provides a realistic, accurate and all-inclusive description of this photocatalytic process.

Chapter 5

In-depth study of photocatalytic soot oxidation capacity of TiO_2- and WO_3-based photocatalysts

Based on:

Myrthe Van Hal, Silvia Lenaerts, Sammy W. Verbruggen, *Photocatalytic soot degradation under UV and visible light*. Submitted to Environmental Science and Pollution Research on the 2nd of July 2021.

Author contributions:

M.V.H. designed the experiments, performed the material synthesis and characterisation, executed the experiments and wrote the manuscript.

S.W.V. and S.L. supervised the work.

5.1 Introduction

Particulate matter (PM) is an important air pollutant, present in high concentrations in cities worldwide, as described in Chapter 1. It is related to a range of problems such as health issues (*e.g.* respiratory and cardiovascular diseases), climate disturbance and fouling of surfaces such as buildings, statues and windows.[46,51] The development of soot degrading technologies is therefore crucial. The possibility of photocatalytic soot oxidation was first evidenced by Lee and Choi in 2002,[88] and has also been shown in Chapter 4. Current research mainly focusses on the large band gap material TiO_2, that exclusively requires UV light,[88–91,93,97,185,190] while visible light active photocatalysts remain largely unstudied in the context of soot degradation. In order to apply photocatalysis as a sustainable, energy-efficient soot abatement technology, the ability of this process to also utilise visible light, and thus a larger fraction of the solar spectrum, should be studied. In addition, as research on the use of visible light active photocatalysts (often WO_3) in other research areas (*e.g.* water and air purification) increases,[163,191,192] the capacity of these materials to cope with deposited soot is an important parameter for the application of these materials in urban (highly soot contaminated) areas.

To ensure long-term operation in urban areas of the in Chapter 3 presented all-gas phase PFC device a 'soot-proof' photoanode material is indispensable. If incapable of soot degradation, the photoanode will become increasingly shielded from incoming light, resulting in reduced performance of the PEC cell. To this end, the photocatalytic soot oxidation capacity of the photocatalysts studied in Chapter 3 is an important parameter determining their application range. In this chapter, the soot degrading properties of both commonly studied TiO_2 and partially visible light active WO_3 are investigated, both using UV, visible and artificial daylight. To the best of our knowledge this is the first time WO_3-based photocatalysts are studied for photocatalytic soot oxidation. The analysis of visible light active photocatalysts for soot degradation is complex, in the sense that typically sensitive and expensive equipment would be required to, for instance, measure weight losses upon degradation.[89] Visible light active photocatalysts are typically coloured materials (*e.g.* WO_3 is green-yellow), which complicates alternative optical detection strategies.

In this chapter we have therefore improved the in Chapter 4 presented low-cost and time-efficient digital image analysis method, by correcting for changes in the intrinsic colour of the catalysts during the degradation experiment. In this way we applied this versatile detection tool for the first time to study coloured samples. Additional information on the ongoing reactions is collected using an *in situ* FTIR reaction cell. Combination of the image analysis method and *in situ* FTIR cell allowed us to easily compare the studied photocatalysts, both considering their short- and long-term soot oxidation capacity, as well as the by-products that were produced (and thus determine the overall mineralisation efficiency). Eventually, the aim of this chapter is four-fold: i) expand the knowledge on photocatalytic soot oxidation using visible light active photocatalysts, ii) expand the knowledge on photocatalytic soot oxidation using visible and daylight, iii) in doing so improve and expand the applicability of a versatile image analysis methodology to coloured samples and iiii) determine the soot oxidation capacity of the photoanodes studied in Chapter 3.

5.2 Experimental

5.2.1 Photocatalyst synthesis, characterisation and coating

TiO_2 was synthesized according to Qiu *et al.* (2006),[164] and will be further denoted as $TiO_{2\ Qiu}$. WO_3 nanopowder (further denoted as $WO_{3\ Mart.}$) was synthesized according to a precipitation method described by Martínez-de la Cruz *et al.* in 2010.[79] Details on the synthesis procedures can be found in Chapter 3. Commercially available P25 was obtained from Evonik, and PC500 and WO_3 nanopowder (further denoted as $WO_{3\ Sigma}$) were obtained from Sigma-Aldrich and used as such in further experiments.

A range of physico-chemical characterisation techniques (N_2 sorption, UV-VIS spectroscopy, X-ray diffraction and energy dispersive X-ray fluorescence) were performed to confirm correct synthesis of the synthesized photocatalysts. These methods are described in Chapter 3.

A detailed description of the photocatalyst coating can be found in Chapter 4.[193] In short, the photocatalysts were drop casted on cleaned glass slides

(3.56 mg cm^{-2}). The coated glass slides were dried to remove residual solvent. Soot (Printex-U) was drop casted on top of the photocatalyst layer (0.022 mg cm^{-2}), and the glass slides were again dried to remove all residual solvent.

5.2.2 Colour-based monitoring of photocatalytic soot oxidation

Soot degradation was monitored using the image analysis method described in chapter 4. In short, this method quantifies the extent of soot degradation by the discolouration of a surface using digital images. For the experiment under UV light, the previously prepared samples were placed 3 cm under a Philips fluorescence S 25 W UVA lamp obtaining an incident light intensity of 2.1 mW cm^{-2} over the wavelength region 290 - 400 nm (λ_{max} at 354 nm), as measured by a calibrated spectroradiometer (Avantes Avaspec-3648-USB2). For the experiment under visible (VIS) light the samples were placed 2.5 cm under a blue LED-array (Roithner LaserTechnik) obtaining an incident light intensity of 14.0 mW cm^{-2} in the wavelength region 390 - 470 nm (λ_{max} at 422 nm). For the experiment under artificial daylight the samples were placed 2.1 cm under a full spectrum daylight lamp (T5 14 W, Philips), obtaining an incident light intensity of 7.2 mW cm^{-2} in the wavelength region 354 - 730 nm. The irradiance spectra are depicted in the Results and discussion section (Figure 5.11).

A standardised custom-made 'photobox' was used to ensure a constant and homogeneous background illumination.[92] Pictures were taken using a Canon Eos 500D camera, positioned 20 cm above the samples, in manual mode (iso 200, aperture f8 and focal exposure 1:5) at maximal resolution (5184 × 3456) at 72 dpi. The free image software ImageJ was used to process the pictures. The L* coordinate of the CIELab colour space (= brightness axis) was used as a measure of the amount of soot deposition and ranged between 0 (black) and 100 (white). The shift of the most frequent L* value was used to quantify the amount of soot degradation of the shallow soot haze that is smeared over the surface of the samples. The degradation of concentrated soot spots was quantified by the decrease of the height of the darkest peak (*i.e.* at low/dark L* values). A more detailed description is given in Chapter 4.

For each experiment, each photocatalyst was applied on five glass slides. Soot was deposited on four of them (samples consisting of both a photocatalyst and a soot layer are further denoted as 'standard' samples), of which three glass slides were illuminated and one was kept in the dark as negative control. The glass slides containing only photocatalyst were illuminated together with the standard samples, in order to correct for colour changes at the level of the catalyst itself. Photographs were taken from the glass slides before and after soot deposition at specific UV illumination intervals (0, 5, 11, 20, 26, 40, 61 and 82 days). Corrections for possible deviations caused by small changes in the background illumination were made by processing a set area of the background in ImageJ and applying the hereby obtained deviation in L* value to the complete dataset of that time point.

A second, additional optical detection method (absorbance method) was performed at the same time points. The decrease in absorbance of the sample surface, as a result of soot degradation, was quantified using a spectroradiometer and converted to a soot haze degradation percentage as described in Chapter 4.

5.2.3 *In situ* monitoring of photocatalytic soot oxidation

Insight into the photocatalytic reactions occurring at the sample surface was gathered using the in Chapter 4 described *in situ* FTIR method. In summary, 5 mg of a 0.6 wt% soot (Printex-U)-photocatalyst mixture was added to 115 mg KBr and pressed for 2 minutes at 5 tons, obtaining a round flat pellet. This pellet was positioned in the centre of the reaction cell. The cell was flushed with air (200 mL min^{-1}) until a stable readout was obtained and sealed airtight. The pellet was illuminated by eight LEDs at each side placed in a circular pattern (10 mW each, Roithner LaserTechnik). The UV-LEDs resulted in an incident intensity of 330 µW cm^{-2} in the wavelength region 350 - 420 nm (λ_{max} at 377 nm), whereas the blue VIS-LEDs reached an incident intensity of 400 µW cm^{-2} in the wavelength region 390 - 470 nm (λ_{max} at 425 nm).

5.3 Results and discussion

5.3.1 Characterisation

In this chapter, the photocatalytic soot oxidation capacity of the photoanode materials studied in Chapter 3 (*i.e.* P25, $TiO_{2\ Qiu}$, PC500, $WO_{3\ Sigma}$ and $WO_{3\ Mart.}$) will be determined. The characterisation of these materials can therefore be found in Chapter 3. An overview of relevant photocatalyst properties is repeated in Table 5.1.

Table 5.1. Physical characteristics (band gap, BET surface area and crystallite particle size) of commercial and synthesized materials.

Material	Band gap (eV)[3]	BET surface area ($m^2\ g^{-1}$)	Crystallite particle size (nm)[4,5]
$P25_{Evonik}$[1]	3.2	52	19 (A), 32 (R)
$TiO_{2\ Qiu}$[2]	3.1	68	30 (A), 36 (R)
$PC500_{CristalACTiV}$[1]	3.3	295	9.5 (A)[6]
$WO_{3\ Sigma}$[1]	2.6	7	37.5 (W)
$WO_{3\ Mart.}$[2]	2.6	9	32 (W)

1) Commercially available photocatalysts.
2) Photocatalysts synthesized based on literature protocols.
3) Obtained by the Tauc method applied on diffuse reflectance spectra.
4) Estimated from XRD using the Scherrer equation.
5) A = anatase, R = rutile, W = monoclinic polymorph.
6) According to data obtained by Nuño and co-workers in 2016.[167]

5.3.2 Colour-based monitoring of photocatalytic soot oxidation

Two optical detection methods (digital image analysis, and the absorbance method) – as applied in Chapter 4 – are in this chapter applied to the in Chapter 3 studied 'white' TiO_2- and (yellow-greenish) coloured WO_3-based photocatalysts. A negative control (*i.e.,* standard sample kept in dark) was added, confirming all changes were induced by illumination. A glass slide coated only with photocatalyst (no soot, 'light-control' sample) was kept under each light source together with the standard samples, to allow for a correction of changes in the intrinsic colours of the photocatalysts themselves throughout the experiments.

Using the digital image analysis method, a graph is obtained showing the number of pixels of each L* coordinate. When applying this to the light-control samples of the UV-experiment for P25, $WO_{3\ Sigma}$ and $WO_{3\ Mart.}$, Figure 5.1 is

obtained, thus reflecting the changes in colour of the photocatalysts themselves, in the absence of soot deposits.

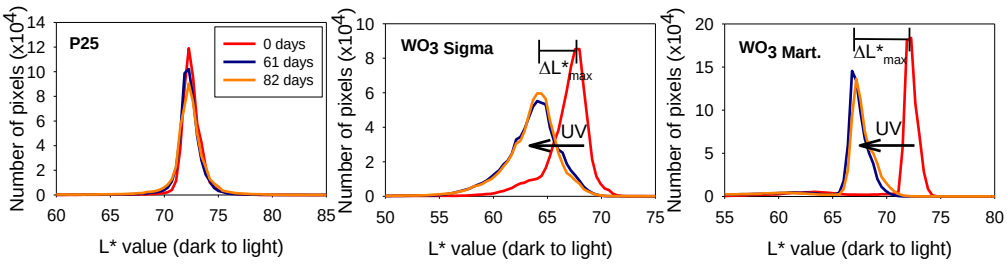

Figure 5.1. UV light experiment. Number of pixels plotted against the L* value of the light-control samples, *i.e.* a glass slide solely coated with (left) P25, (middle) $WO_{3\ Sigma}$ and (right) $WO_{3\ Mart.}$, representing the UV-induced colour change of the photocatalyst surface itself (without soot) upon UV illumination.

A clear colour shift to lower L* values can be observed for both WO_3-based photocatalysts, thus reflecting darkening of the bare photocatalyst surface induced by the UV illumination. This colour change could arise from decreasing amounts of water adsorbed on the (coloured) photocatalyst surface, resulting from a combination of photocatalytic (adsorbed) water oxidation and water evaporation upon illumination of the surface. This was supported by the observation of similar darkening of the photocatalyst surface after drying of the light-control samples, as illustrated in Figure 5.2. As both the digital image analysis and absorbance method are optical detection methods, this photocatalyst colour change will also contribute to the results of the standard samples with soot and might give rise to false interpretations of the degradation efficiency. It is therefore vital to correct for this effect. In contrast, this UV-induced photocatalyst discolouration was not seen for the white photocatalysts (*i.e.* P25, $TiO_{2\ Qiu}$ and PC500, see Figure 5.1).

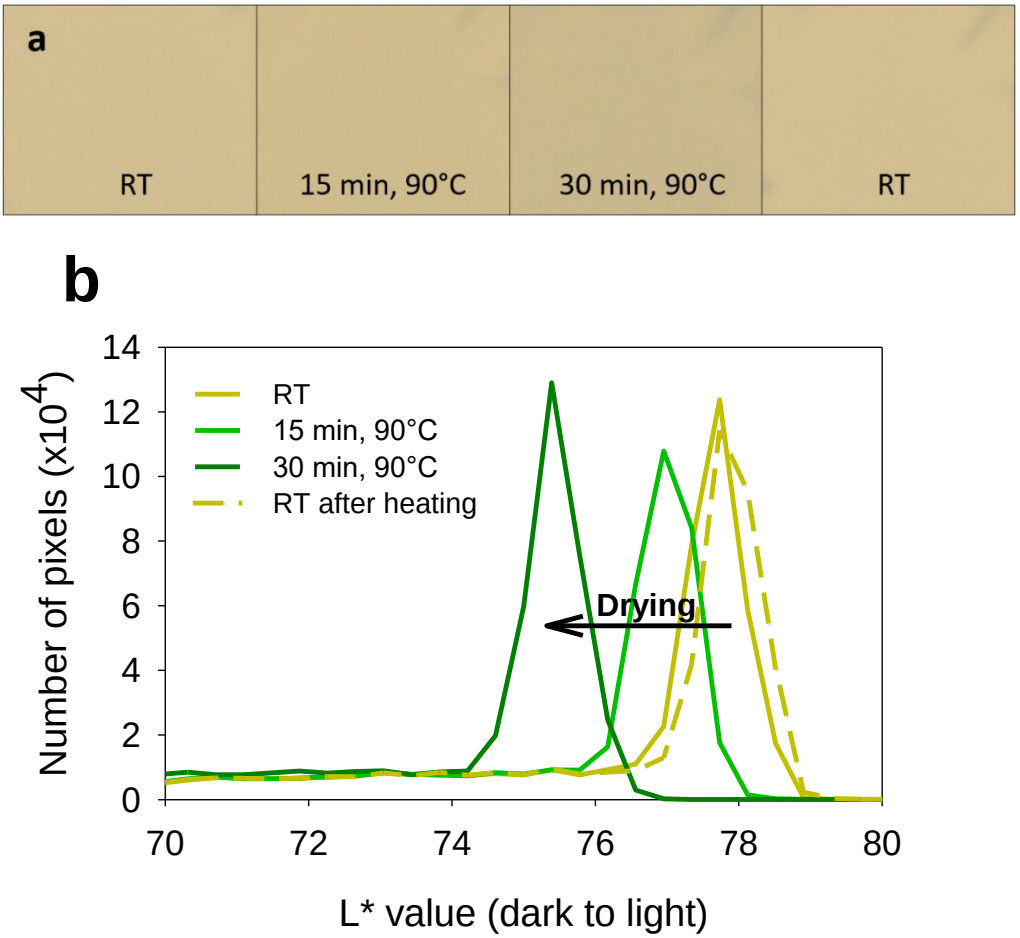

Figure 5.2. a) Subsequent digital images of a glass slide coated with $WO_{3\ Mart.}$ with f.l.t.r. the glass slide kept at room temperature (RT), after 15 and 30 minutes in an oven at 90°C and after cooling down to RT again. b) Number of pixels plotted against the L* value for a glass slide solely coated with $WO_{3\ Mart.}$ when kept at room temperature (RT), after 15 and 30 minutes in an oven at 90°C and after cooling down to RT again. A clear shift to the left is observed after heating, reflecting darkening of the photocatalyst surface. After cooling to RT the curve shifts back to the right.

For the absorbance method, the change in absorbance value attributed to illumination-induced colour changes of the pure photocatalyst can be converted to a theoretical equivalent soot degradation efficiency according to (Eq. 5.1), that can be used to correct the results of the standard samples.

$$\textit{Eq. PC soot degr. efficiency pure photocatalysts (\%)} = \left(\frac{-A_{NS,t}}{A_0}\right) . 100 \qquad \text{(Eq. 5.1)}$$

Where $A_{NS,t}$ represents the absorbance value of the light-control sample (no soot) at a specific time point and A_0 is the absorbance value of a standard sample (photocatalyst with soot on top) at the beginning of the experiment (no illumination = completely fouled glass slide). All absorbance values were taken at 600 nm.

When applying (Eq. 5.1) to the light-control samples of P25, $WO_{3\ Sigma}$ and $WO_{3\ Mart.}$ of the UV light experiment, Figure 5.3 is obtained.

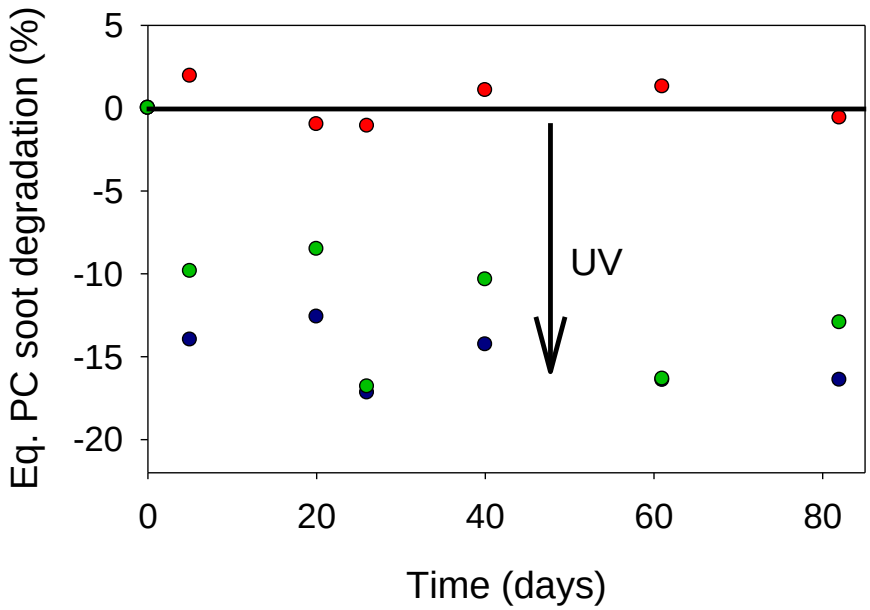

Figure 5.3. UV light experiment. UV-induced darkening of photocatalyst surface expressed as theoretical equivalent soot degradation efficiency for P25 (red), $WO_{3\ Sigma}$ (blue) and $WO_{3\ Mart.}$ (green) determined using the absorbance method, as a function of UV illumination time.

In Figure 5.3 we see that for P25 the theoretical equivalent soot degradation efficiencies fluctuate around 0% soot degradation, again evidencing the absence of colour changes for the 'white' photocatalysts. The slight variation in these data can be ascribed to small variations in the position of the sampling probe, as the same noisiness is encountered for all measured samples (both in dark and under UV illumination). When interpreting the data of WO_3-based photocatalysts, a clear negative theoretical equivalent soot degradation

percentage (ranging between -10% and -17%) is present for all time points after initiation of the UV illumination. This negative equivalent soot degradation again reflects the UV-induced darkening of the photocatalyst surface, thus confirming the results from the digital image analysis method.

A similar illumination-induced photocatalyst discolouration was also observed under visible light and artificial daylight. To correct for this illumination-induced photocatalyst colour change in the image analysis method, an additional processing step should be added to the in Chapter 4 presented methodology. In this case, the 'number of pixels *vs.* L* value' plots of the standard samples need to be shifted an equal distance corresponding to ΔL^*_{max} (see Figure 5.1) in the opposite direction of the discolouration before determining the position of the L^*_{max} value, that corresponds to the final amount of soot. In the absorbance method the soot degradation efficiencies were corrected for the illumination-induced shift by subtracting the negative theoretical equivalent soot degradation efficiencies. The results obtained in the UV light experiment with the original and corrected image analysis and absorbance method are presented in Figure 5.4 and Figure 5.5.

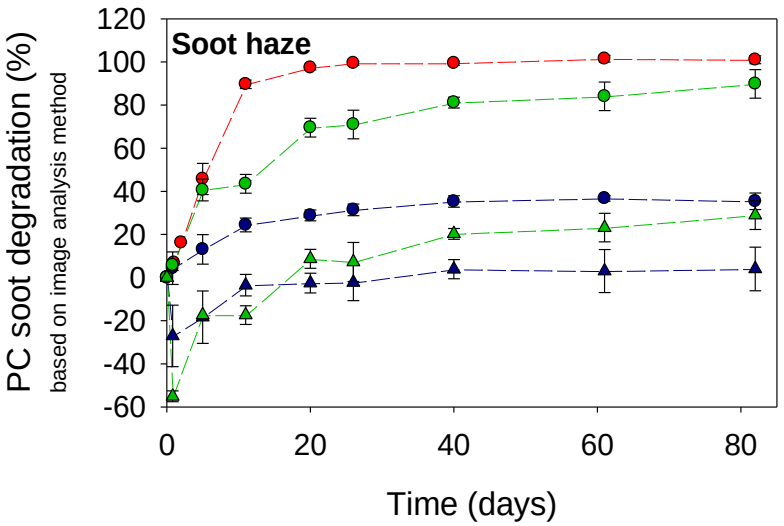

Figure 5.4. UV light experiment. Photocatalytic degradation of uniform soot haze by P25 (red), $WO_{3\ Sigma}$ (blue) and $WO_{3\ Mart.}$ (green), as a function of UV illumination time. Comparison of original (▲) and corrected (●) digital image analysis method. For P25 the original values equal the corrected, as no correction was required (no discolouration of photocatalyst). The error bars are based on standard deviation for three independent samples. Dashed lines are added to guide the reader's eye.

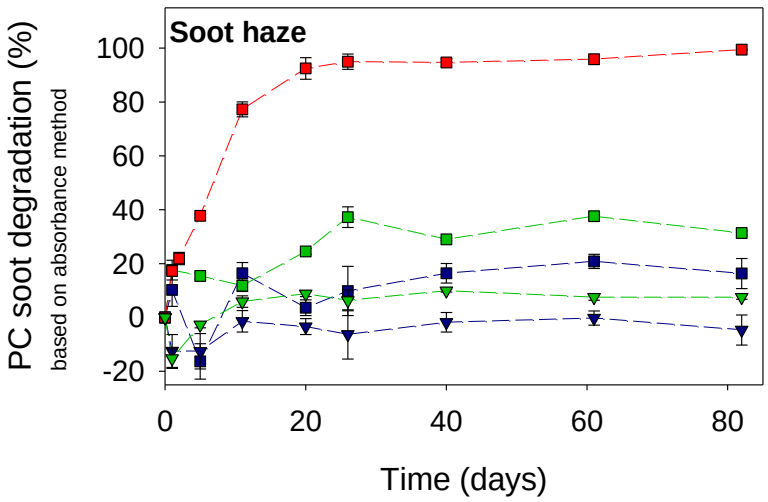

Figure 5.5. UV light experiment. Photocatalytic degradation of uniform soot haze by P25 (red), $WO_{3\ Sigma}$ (blue) and $WO_{3\ Mart.}$ (green), as a function of UV illumination time. Comparison of original (▼) and corrected (■) absorbance method. For P25 the original values equal the corrected, as no correction was required (no discolouration of photocatalyst). The error bars are based on standard deviation for three independent samples. Dashed lines are added to guide the reader's eye.

In Figure 5.4 and Figure 5.5 the UV-induced darkening of the photocatalyst surface is reflected in the (initial) negative photocatalytic soot degradation percentages obtained by both original methods for WO_3-based photocatalysts. An additional data processing step was implemented for both methods correcting for this illumination-induced photocatalyst colour change, as described in the previous paragraph. It can be seen that for WO_3-based photocatalysts (as opposed to the results for P25) large deviations arise between both different (corrected) detection methods. After 82 days almost complete degradation (90%) of the soot haze by $WO_{3\ Mart.}$ was measured using the corrected image analysis method, whereas the corrected absorbance method only appeared to detect 31% degradation. Overall, much lower degradation efficiencies were measured using the corrected absorbance method for WO_3-based photocatalysts compared to the results obtained with the corrected image analysis method. When looking at the actual degradation of the soot haze with $WO_{3\ Mart.}$ (Figure 5.6) almost complete degradation is observed after 82 days as the colour of the surface again equals the colour of the pristine photocatalyst at that UV illumination time (as in the case of

'no soot'), which is not the case at the other time points. Thus, while the absorbance method is able to accurately determine the degradation of the soot haze for non-coloured (*i.e.* white) photocatalysts (*e.g.* P25, $TiO_{2\ Qiu}$, PC500), this is clearly not the case for the studied coloured photocatalysts (WO_3). As the image analysis allows visualization of the complete soot degradation process (over all L* values), the illumination-induced change in colour (in this case darkening) of the photocatalyst can be studied independently from the illumination-induced (photocatalytic) soot degradation (and thus brightening). In the absorbance method, however, all occurring visual changes are contained in a single output value (*i.e.* the absorbance of the entire surface), and as a result both phenomena cannot be disentangled. Therefore, digital image analysis is much more reliable for studying soot degradation over coloured photocatalysts (or by extension, coloured surfaces) compared to the absorbance method. For this reason, only the digital image analysis method will be used further in this study.

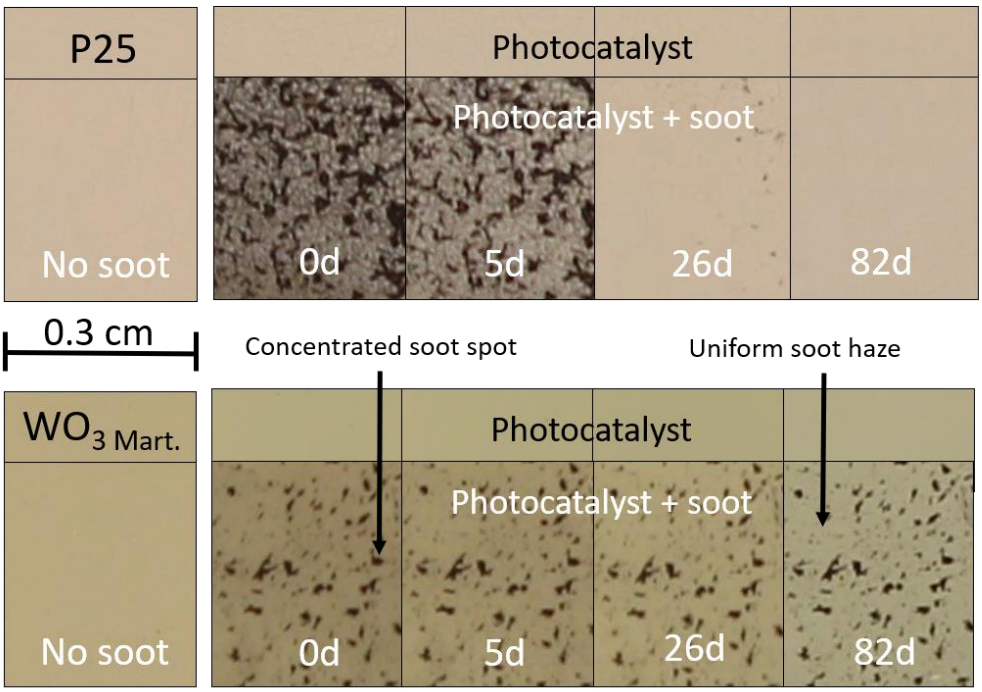

Figure 5.6. UV light experiment. Subsequent digital images of the photocatalytic soot degradation on a glass slide coated with (top) P25 and (bottom) $WO_{3\ Mart.}$ with f.l.t.r. a glass slide without soot, with soot before UV illumination, and after 5, 26 and 82 days of illumination.

The results of the UV light experiment obtained with the corrected digital image analysis method are shown for all photocatalysts and the glass slide containing solely soot in Figure 5.7.

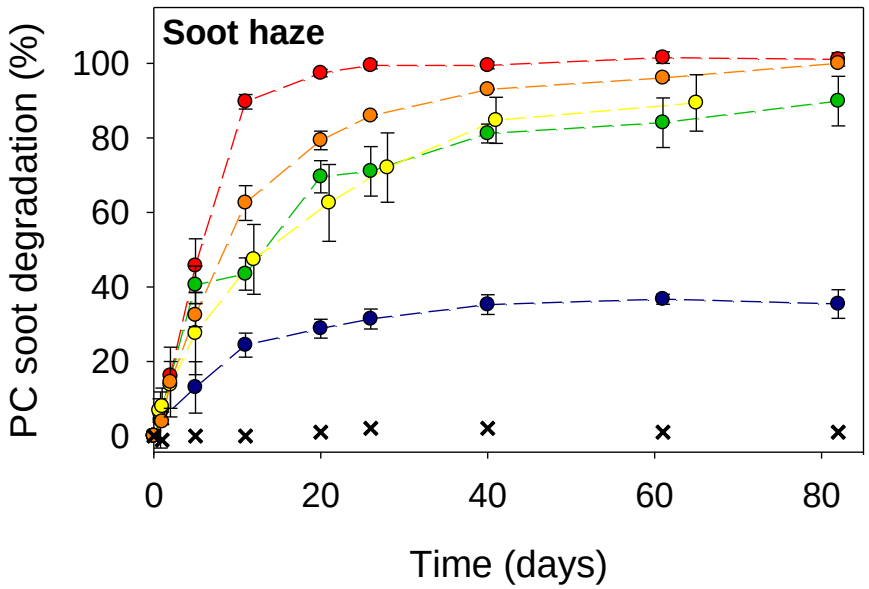

Figure 5.7. UV light experiment. Photocatalytic soot degradation of the soot haze by P25 (red), $TiO_{2\ Qiu}$ (yellow), PC500 (orange), $WO_{3\ Sigma}$ (blue) and $WO_{3\ Mart.}$ (green) determined using the improved digital image analysis method after light-induced colour-change correction, as a function of UV illumination time. The result of $TiO_{2\ Qiu}$ is obtained from Chapter 4. The result of the glass slide solely coated with soot is shown by black crosses (X). The error bars are based on three independent samples. Dashed lines are added to guide the reader's eye.

It is clear that P25 is the fastest photocatalytic soot degrader of all studied materials, achieving complete soot degradation after 40 days of UV illumination. It should be noted that the applied soot quantity (22 µg cm^{-2}) is high compared to outdoor (urban) soot deposition rates (ranging between 0.001 - 0.010 µg cm^{-2} day^{-1}),[93,194,195] thus requiring a much shorter illumination time to obtain complete degradation of real outdoor soot depositions. As soot deposition is a gradual process, soot loadings on existing surfaces reach values as used in this study after many years to decades of exposure.[196] Photocatalytic soot degradation by the other photocatalysts occurred at a more gradual pace.

It took PC500 82 days to completely degrade the soot haze. $TiO_{2\ Qiu}$ reached 89% degradation of the soot haze after 65 days. Around 90% oxidation of the uniform soot haze was obtained by $WO_{3\ Mart.}$ after 82 days, while the commercially available WO_3 nano powder ($WO_{3\ Sigma}$) was only able to degrade around 35% of the soot haze by the end of the experiment. All studied photocatalysts display a fast initial soot degradation rate, slowing down at higher soot degradation percentages, thus resembling first order kinetics as previously described in literature for P25.[90–93]

An interesting additional feature of the image analysis method is that it also enables to separately determine the degradation efficiency of pertinent concentrated soot spots. The degradation of the concentrated soot spots obtained in the UV light experiment is shown in Figure 5.8.

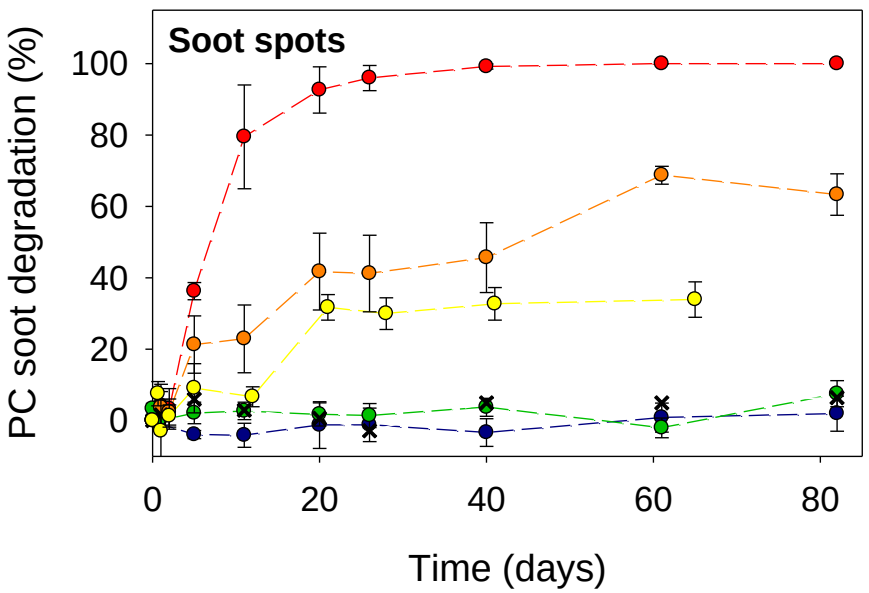

Figure 5.8. UV light experiment. Photocatalytic degradation of concentrated soot spots by P25 (red), $TiO_{2\ Qiu}$ (yellow), PC500 (orange), $WO_{3\ Sigma}$ (blue) and $WO_{3\ Mart.}$ (green) determined by digital image analysis, as a function of UV illumination time. The result of $TiO_{2\ Qiu}$ is obtained from Chapter 4. The result of the glass slide solely coated with soot is shown by black crosses (X). The error bars are based on three independent samples. Dashed lines are added to guide the reader's eye.

When examining the photocatalytic degradation of the concentrated soot spots (Figure 5.8), it can be observed that P25 was able to fully degrade the concentrated soot spots after 61 days, somewhat slower than the uniform soot haze. After 82 days, at the end of the experiment, ca. 65% of the soot spots were degraded by PC500. A slower soot degradation is observed for $TiO_{2\ Qiu}$, obtaining 34% degradation after 65 days. Only very little degradation of the concentrated spots was measured for purely WO_3-based photocatalysts. At the end of the experiment (82 days) only 1.5% of the soot spots were degraded by $WO_{3\ Sigma}$, while $WO_{3\ Mart.}$ reached 7% degradation. A striking difference is thus apparent for WO_3-based photocatalysts when comparing the good degradation capacity for a soot haze *versus* the poor efficiency towards concentrated soot spots.

With direct oxidation being acknowledged as the main photocatalytic soot oxidation mechanism,[88] the characteristics of the photocatalyst-soot surface area are crucial in determining the soot degradation rate. As listed in Table 5.1, both WO_3-based photocatalysts have a very small BET surface area ($< 10\ m^2\ g^{-1}$), PC500 on the other hand is known for its large surface area ($\sim 300\ m^2\ g^{-1}$), and the surface areas of P25 and $TiO_{2\ Qiu}$ lie in-between ($50 – 70\ m^2\ g^{-1}$). The low photocatalytic soot oxidation rate of WO_3-based photocatalysts might thus be related to their low surface area. When considering all TiO_2-based photocatalysts, the best result was obtained with P25, even though it does not possess the largest surface area. The three studied TiO_2-based photocatalysts are characterised by a vastly different crystal structure. PC500 consists of pure anatase, while the two other TiO_2-based photocatalysts both consist of a mixture of anatase and the less active rutile. However, P25 is known to consist of an optimised anatase:rutile ratio (4:1), resulting in enhanced performance compared to pure anatase. Additionally, P25 has the lowest amorphous fraction of the three studied TiO_2-based photocatalysts (8% *vs.* 15% for $TiO_{2\ Qiu}$ and 20% for PC500). As penetration of soot into the photocatalyst layer is negligible, it has been shown that the photocatalytic soot oxidation rate only depends on the thickness of the photocatalyst layer up to a thickness in the range of the diffusion length of the excited carriers.[188] In this study, thick photocatalyst layers were applied ($3.5\ mg\ cm^{-2}$), as also evidenced by Figure 5.6, thus excluding layer thickness as

an influencing factor. In addition, Chapter 4 showed that drop casting of both photocatalyst and soot on glass slides results in rough films, excluding surface roughness as decisive factor for the performed experiments.

Another important difference between the WO_3-based and TiO_2-based photocatalysts is their band gap. The smaller band gap of WO_3 allows at least partial utilisation of visible light and thus a larger fraction of the solar spectrum, making it a promising material for use in energy-efficient environmental remediation processes. To study this effect, the experiments were repeated with a visible light blue LED source. The results of the VIS light experiment are shown in Figure 5.9, Figure 5.10 and Figure 5.12.

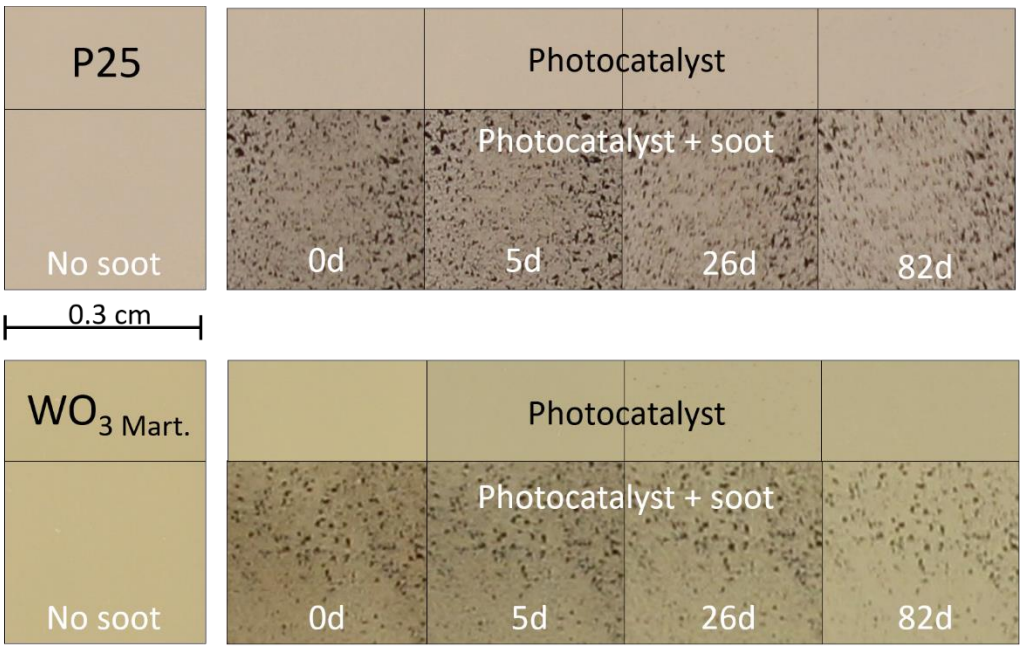

Figure 5.9. VIS light experiment. Subsequent digital images of the photocatalytic soot degradation on a glass slide coated with (top) P25 and (bottom) $WO_{3\ Mart.}$ with f.l.t.r. a glass slide without soot, with soot before VIS light illumination, and after 5, 26 and 82 days of illumination.

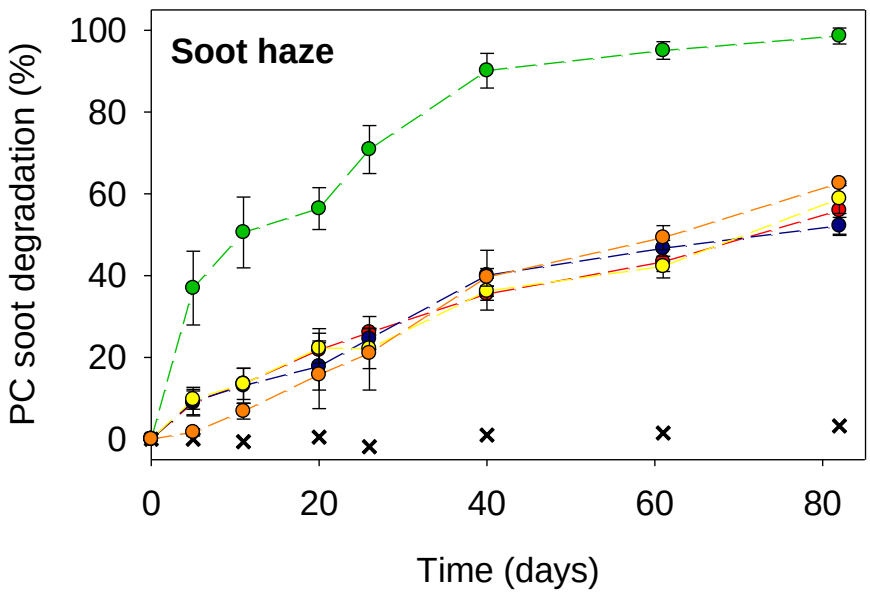

Figure 5.10. VIS light experiment. Photocatalytic soot degradation of a uniform soot haze by P25 (red), $TiO_{2\ Qiu}$ (yellow), PC500 (orange), $WO_{3\ Sigma}$ (blue) and $WO_{3\ Mart.}$ (green) determined using the improved digital image analysis method after light-induced colour-change correction, as a function of visible light illumination time. Using P25 as reference the results of $TiO_{2\ Qiu}$ and PC500 are corrected for differences between the two separate experiments (*i.e.* exp 1 = $WO_{3\ Sigma}$, $WO_{3\ Mart.}$ and P25; exp 2 = $TiO_{2\ Qiu}$, PC500 and P25). The result of the glass slide solely coated with soot is shown by black crosses (X). The error bars are based on three independent samples. Dashed lines are added to guide the reader's eye.

From Figure 5.10 it is clear that under VIS light illumination $WO_{3\ Mart.}$ is the fastest soot degrader, reaching complete oxidation of the uniform soot haze after 82 days. All other photocatalysts degrade the soot haze slower and at a similar rate, resulting in final degradation percentages between 52% and 63% for all other studied photocatalysts.

Despite the large band gap of the studied TiO_2-based photocatalysts (3.1 - 3.3 eV) still significant soot haze degradation is observed under the VIS light lamp, which has also been previously observed in literature.[197,198] This can mainly be attributed to the small, yet existing, overlap of the absorbance band of the TiO_2-based photocatalysts and the irradiance spectrum of the VIS light source, as shown in Figure 5.11. This allows the TiO_2-based photocatalysts to

effectively use a small part of the light emitted by the VIS light lamp over the entire duration of the long-term experiment. For the WO_3-based photocatalysts (band gap = 2.6 eV) a more optimal overlap exists between the photocatalyst absorbance band and the light emission spectrum (Figure 5.11), allowing WO_3-based photocatalysts to potentially use a larger fraction of the light emitted by the VIS light lamp. The advantage of WO_3 when using visible light is clear from Figure 5.10, with $WO_{3\ Mart.}$ clearly outperforming all studied TiO_2-based photocatalysts and reaching complete oxidation after 82 days (*vs.* 90% under UV light), even despite its low surface area. The small differences between the band gaps of the TiO_2-based photocatalysts are not clearly reflected in their soot degradation capacity under visible light, as the VIS LED light has a narrow emission spectrum with a maximum outside the UV range (λ_{max} = 422 nm).

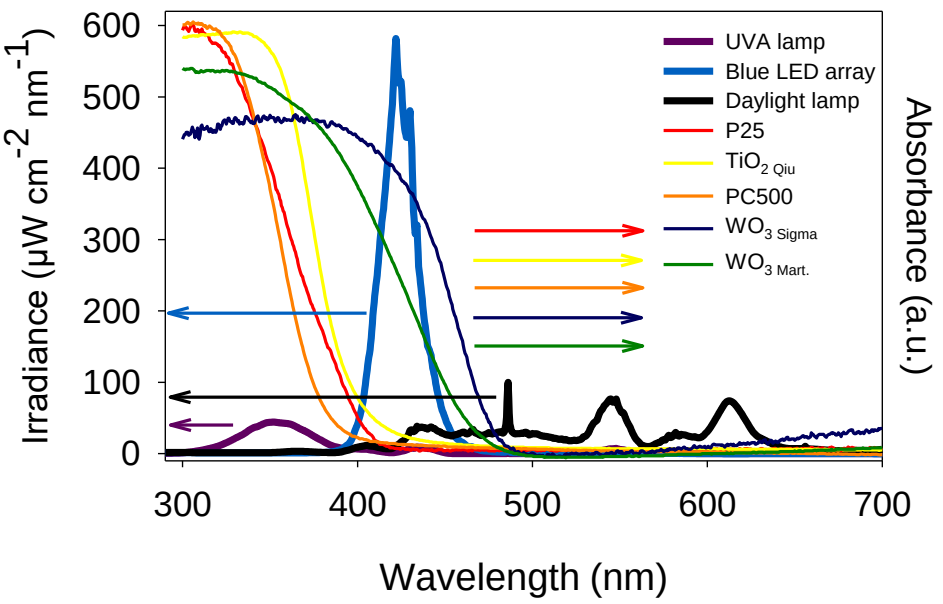

Figure 5.11. Absolute irradiance spectrum of the lamps used in this study combined with the UV-VIS spectra of the studied photocatalysts.

The degradation of the concentrated soot spots under VIS light illumination is shown in Figure 5.12.

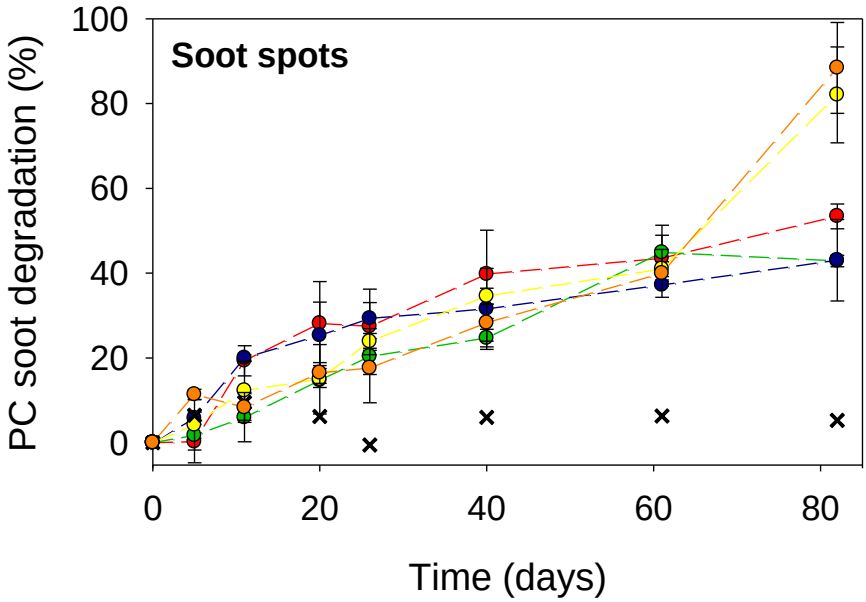

Figure 5.12. VIS light experiment. Photocatalytic degradation of concentrated soot spots by P25 (red), $TiO_{2\ Qiu}$ (yellow), PC500 (orange), $WO_{3\ Sigma}$ (blue) and $WO_{3\ Mart.}$ (green) determined by digital image analysis, as a function of visible light illumination time. The result of the glass slide solely coated with soot is shown by black crosses (X). The error bars are based on three independent samples. Dashed lines are added to guide the reader's eye.

From Figure 5.12 it is clear that all five photocatalysts result in similar degradation of the concentrated soot spots under VIS light over most of the studied time frame. After 82 days the TiO_2-based photocatalysts outperformed the WO_3-based photocatalysts, reaching more than 80% degradation with PC500 and $TiO_{2\ Qiu}$, 53% degradation with P25 and 43% degradation with both WO_3-based photocatalysts. This is in contrast to what was seen in the UV light experiment, where almost no ($< 7\%$) degradation of the soot spots was attained by both WO_3-based photocatalysts. Again, the smaller band gap of WO_3 results in improved performance of these photocatalysts when using VIS light instead of UV light.

As the final goal is to apply photocatalysis as a sustainable and energy-efficient environmental remediation strategy, it should eventually be possible to drive the targeted reactions solely using sunlight. To this end, soot degradation

experiments were repeated using artificial daylight (14 times lower intensity than the standard solar spectrum AM1.5g). The results for the degradation of the uniform soot haze are shown in Figure 5.13.

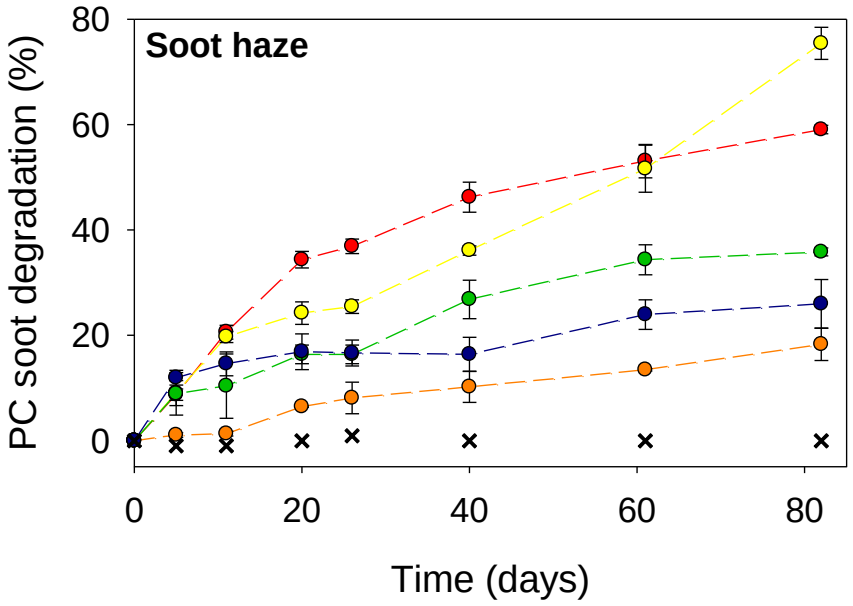

Figure 5.13. Daylight experiment. Photocatalytic soot degradation of the soot haze by P25 (red), $TiO_{2\ Qiu}$ (yellow), PC500 (orange), $WO_{3\ Sigma}$ (blue) and $WO_{3\ Mart.}$ (green) determined using the improved digital image analysis method after light-induced colour-change correction, as a function of illumination time. The result of the glass slide solely coated with soot is shown by black crosses (X). The error bars are based on three independent samples. Dashed lines are added to guide the reader's eye.

Figure 5.13 shows that under low intensity artificial daylight two of the three TiO_2-based photocatalysts perform best, reaching 59% (P25) and 75% ($TiO_{2\ Qiu}$) soot haze degradation after 82 days. PC500 on the other hand resulted in the lowest soot haze degradation (18%). The two WO_3-based photocatalysts lie in-between, with 36% degradation by $WO_{3\ Mart.}$ and 26% by $WO_{3\ Sigma}$ after 82 days. It can be concluded that all studied photocatalysts resulted in significant soot haze degradation under artificial daylight. When considering the high soot loading (22 µg cm^{-2}) and relatively low intensity of the artificial daylight lamp (7.2 mW cm^{-2}) used in this experiment, it is clear that photocatalysis proves

promising as sunlight-driven, and thus energy-efficient, soot degradation technology.

From Figure 5.11 it can be seen that the daylight lamp is characterised by a broad emission spectrum, including even a UVA component that can be used by the TiO_2-based photocatalysts. From the UV light experiment it could be seen that P25 is the fastest soot degrader of these materials, linked to its optimal anatase-rutile ratio. Another important characteristic is the band gap. Table 5.1 shows small differences in the band gaps of the three studied TiO_2-based photocatalysts (PC500 > P25 > $TiO_{2\ Qiu}$), allowing $TiO_{2\ Qiu}$ to use a larger fraction of the light emitted by the daylight lamp than P25, and with the lowest fraction available for PC500. The WO_3-based photocatalysts can use a larger fraction of the light emitted by the daylight lamp, as shown in Figure 5.11. However, as a result of the broader nature of the spectrum of the daylight lamp, the intensity of the visible light that can be used by both WO_3-based photocatalysts is lower than in the case of the visible light lamp. The low surface area of these photocatalysts hinders optimal soot oxidation by these materials, which is not the case for the higher surface area TiO_2-based photocatalysts.

The degradation of the concentrated soot spots under artificial daylight illumination is shown in Figure 5.14.

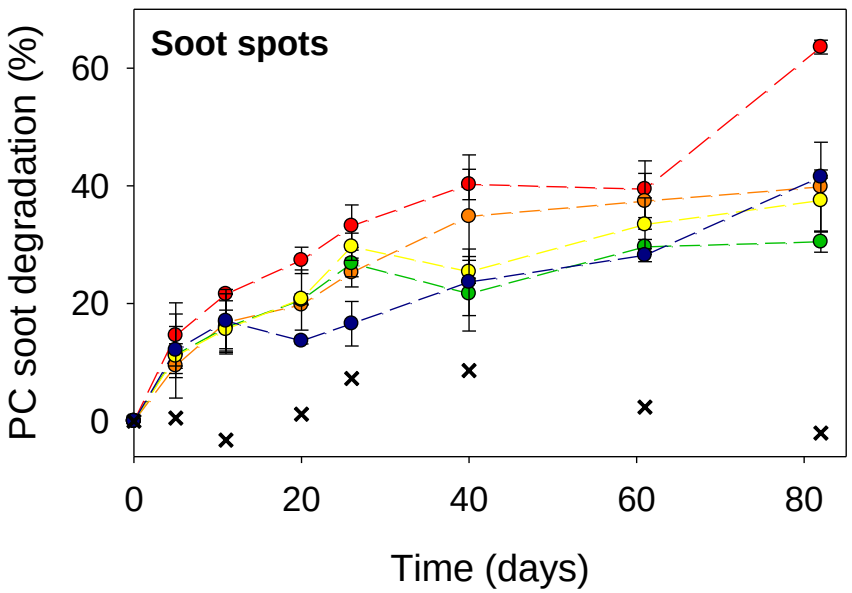

Figure 5.14. Daylight experiment. Photocatalytic degradation of concentrated soot spots by P25 (red), $TiO_{2\ Qiu}$ (yellow), PC500 (orange), $WO_{3\ Sigma}$ (blue) and $WO_{3\ Mart.}$ (green) determined by digital image analysis, as a function of illumination time. The result of the glass slide solely coated with soot is shown by black crosses (X). One sample of each photocatalyst could not be used due to irregular illumination. The error bars are based on two independent samples. Dashed lines are added to guide the reader's eye.

In Figure 5.14 the highest concentrated soot spot degradation after 82 days is reached by P25 (64%), while similar results are seen for all other studied photocatalysts, obtaining between 30% and 41% degradation of the soot spots after 82 days. This result again highlights the outstanding performance of P25 as soot degrader, while also showcasing the potential of sunlight-driven photocatalytic soot degradation.

The short- and long-term performance of the studied photocatalysts using the three different light sources, expressed as photonic efficiency (PE), is summarised in Table 5.2. The PE is defined as the ratio of the photocatalytic reaction rate (degraded carbon molecules s^{-1}) over the incident photon flux (photons s^{-1}).[92,199] The carbon degradation rate was derived from the percentage of soot haze degradation after a certain period of illumination, taking into account the carbon content of Printex-U (95.56%)[92] and the initial

quantity of soot on the sample (22 µg cm^{-2}). In this way, the upper limit of the PE was calculated, as part of the soot is also present in (slower degrading) concentrated soot spots that cannot be accounted for in this calculation. The light intensities were measured with a spectroradiometer, obtaining an incident photon flux of 4.22 x 10^{15} photons s^{-1} cm^{-2} for the UV lamp, of 3.10 x 10^{16} photons s^{-1} cm^{-2} for the VIS light lamp and of 7.95 x 10^{15} photons s^{-1} cm^{-2} for the daylight lamp (between 290 and 800 nm) over an illuminated surface of 3.8 cm^2.

Table 5.2. Upper limit of photonic efficiency - based on the degradation of the soot haze - of the studied photocatalysts after different illumination times for a UV, VIS and artificial daylight lamp. The data of the UV light experiment with $TiO_{2\ Qiu}$ is extracted from Chapter 4 (till 41 days).

	PE after 5 days (x10^{-5})			**PE after 82 days (x10^{-5})**		
	UV light	**VIS light**	**Art. daylight**	**UV light**	**VIS light**	**Art. daylight**
P25	26.6	0.7	2.8	3.4	0.3	1.1
$TiO_{2\ Qiu}$	13.9	0.3	2.8	N.A.	0.3	1.4
PC500	18.5	0.9	0.3	3.5	0.3	0.3
$WO_{3\ Sigma}$	7.5	0.7	3.7	1.2	0.2	0.5
$WO_{3\ Mart.}$	23.7	2.9	2.8	3.2	0.5	0.7

The results again evidence that under UV light the best results are obtained by TiO_2-based photocatalysts, both short- (P25) and long-term (PC500), although closely followed by $WO_{3\ Mart}$. Under VIS light on the other hand, the best results, both short- and long-term, are obtained using $WO_{3\ Mart}$. Using an artificial daylight spectrum lamp a more scattered result is obtained as $WO_{3\ Sigma}$ performs best after five days, while $TiO_{2\ Qiu}$ results in the highest photonic efficiency after 82 days.

The photonic efficiencies obtained with TiO_2-based photocatalysts under UV light are 12 - 44 times higher than those under VIS light, while for the WO_3-based photocatalysts the PEs only dropped by a factor 5 - 11 when using VIS instead of UV light, reflecting the higher capability of WO_3 to utilise VIS light.

5.3.3 *In situ* monitoring of photocatalytic soot oxidation

The image analysis method allows to simultaneously monitor degradation of both soot haze and concentrated soot spots, but provides no information on

the ongoing processes, nor the formation of possible intermediates and end products. To complement the results of the image analysis method, an *in situ* FTIR reaction cell was used in this second part of the study.

Blank tests (no soot) were performed as negative control, showing no CO_2 evolution in the absence of soot under UV illumination. Experiments with soot-photocatalyst-KBr pellets under UV light clearly revealed CO_2 evolution for all studied photocatalysts, evidenced by the signal in the wavenumber range 2290 - 2390 cm^{-1} (ν_{as}(O=C=O)). The IR spectra after 10 hours of UV illumination are presented in Figure 5.15a for PC500, $WO_{3\ Sigma}$ and $WO_{3\ Mart}$. Oxygen depletion in the airtight reaction cell results in saturation of soot oxidation after ca. 10 h, resulting in flattening of the CO_2 evolution curve after this time point (see Figure 4.12b). A second significant band can be observed in the wavenumber range 1273 - 1445 cm^{-1} with two maxima at 1360 (ν_s(COO)) and 1380 cm^{-1} (δ(CH)). This band can be ascribed to formate adsorbed on the photocatalyst surface, $CHOO^-_{(ad)}$,[189] and was observed for all studied materials. Steric hindrance possibly masks other bands attributed to this compound as it is adsorbed to the surface. These results suggest that the hypothesis of Chin and co-workers from 2009,[97] originally presented for TiO_2, is also valid for WO_3-based photocatalysts. This hypothesis states that soot can be photocatalytically oxidised via two soot oxidation pathways, either through direct oxidation to CO_2, or via a sequential mechanism involving a variety of intermediates. The IR spectrum of PC500 contained an additional band that was not detected for the other photocatalysts, located between 1483 and 1783 cm^{-1} with a maximum near 1665 cm^{-1} (ν(C=O)). This band can be ascribed to adsorbed formate-related products such as formaldehyde ($HCHO_{(ad)}$) and methyl formate ($CH_3OOCH_{(ad)}$),[189] evidencing the largely incomplete oxidation of soot when using PC500. The degradation of soot can be monitored by the generation of two negative bands centred around 2848 and 2922 cm^{-1}, reflecting the disappearance of C-H stretching vibrations. The production of both CO_2 and adsorbed formate as a function of UV illumination time are shown in Figure 5.15b.

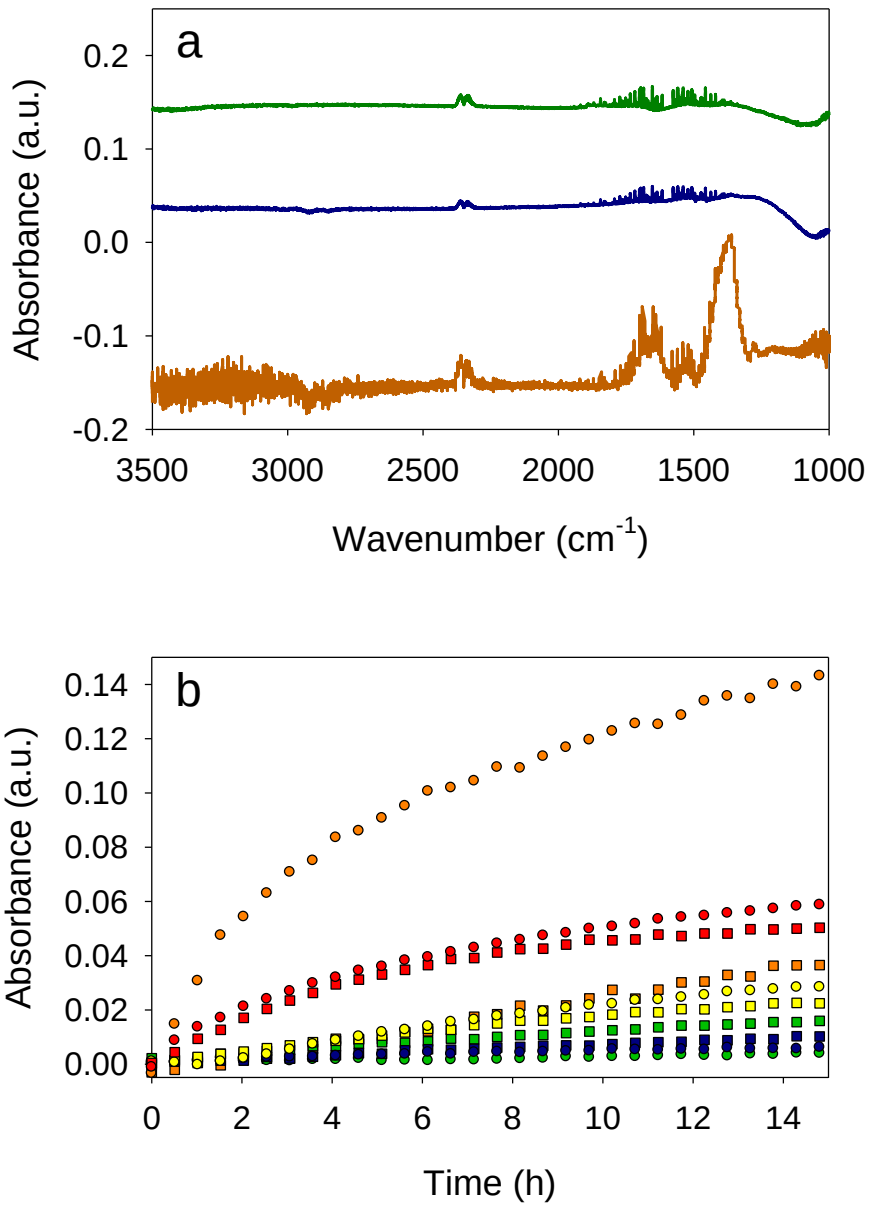

Figure 5.15. UV light experiment. a) FTIR spectra of soot-photocatalyst-KBr pellet in *in situ* reaction cell after 10 hours of UV illumination for PC500 (orange), $WO_{3\ Sigma}$ (blue) and $WO_{3\ Mart.}$ (green). Positive bands represent product formation, negative bands point at the degradation of soot. b) Evolution of CO_2 (■) and formate (●) as a function of UV illumination time for a soot-photocatalyst-KBr pellet placed in the *in situ* reaction cell for following photocatalysts: P25 (red), $TiO_{2\ Qiu}$ (yellow), PC500 (orange), $WO_{3\ Sigma}$ (blue) and $WO_{3\ Mart.}$ (green). The result of $TiO_{2\ Qiu}$ is obtained from Chapter 4.

The *in situ* experiment was repeated using visible light LEDs. Under these conditions, the same bands were observed as with UV light for P25 and $WO_{3\ Mart.}$ (positive: CO_2 and $CHOO^-_{(ad)}$; negative: C-H), but for $TiO_{2\ Qiu}$, PC500 and $WO_{3\ Sigma}$ no bands could be observed after 10 hours of illumination. The slope of the CO_2 evolution curve ($<$ 10h, at 2360 cm^{-1}) was extracted, reflecting the short-term soot mineralization rate of the photocatalysts and is shown in Figure 5.16 for both UV and VIS light.

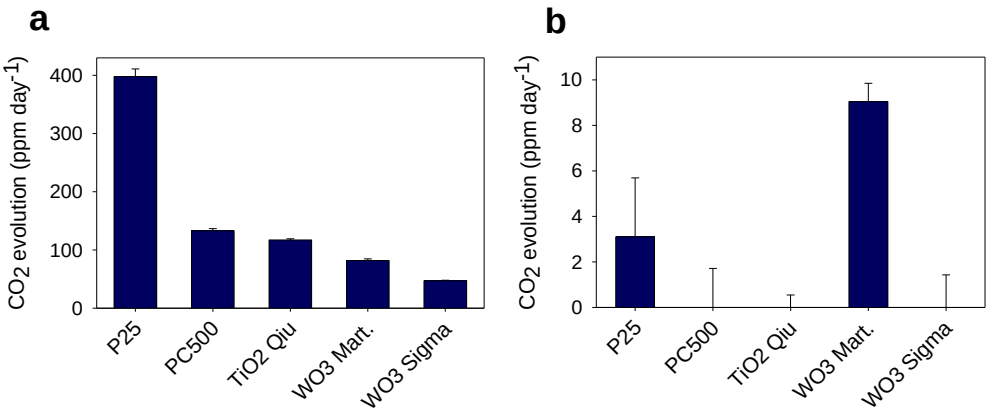

Figure 5.16. CO_2 evolution of studied photocatalysts based on the *in situ* soot oxidation detection method when using a) UV and b) VIS light. The result of $TiO_{2\ Qiu}$ under UV light is obtained from Chapter 4.

When looking at Figure 5.16a it is clear that the short-term or initial soot mineralization rate under UV light is highest for P25. PC500 has the second highest initial mineralization rate, 3 times lower than that of P25, closely followed by $TiO_{2\ Qiu}$. A lower short-term soot degradation rate is seen for $WO_{3\ Mart.}$, with the lowest initial mineralisation rate obtained with $WO_{3\ Sigma}$. From Figure 5.16b a different order can be seen under VIS light, with the highest initial mineralisation rate for $WO_{3\ Mart.}$, followed by P25 and without quantifiable CO_2 formation obtained for the other studied photocatalysts.

It is important to note that it is not possible to directly correlate these results to those obtained in the (long-term) digital image analysis experiments above. Both methodologies differ in many ways (*e.g.* substrate, duration, measured parameter). Nevertheless, largely similar trends can still be observed. In the digital image analysis experiments P25 also achieved complete fast soot

oxidation under UV light, while $WO_{3\ Mart.}$ was also the fastest soot degrader under VIS light.

Besides the initial mineralisation rate, the *in situ* experiments can also be used to assess the specificity of the photocatalytic materials towards full mineralisation of soot into CO_2. This specificity is expressed as the ratio of the absorbance of CO_2 (at 2360 cm^{-1}) to that of formate (at 1360 cm^{-1}) after 10 h of illumination. The result is shown in Table 5.3 for both UV and VIS light.

Table 5.3. Absorbance ratio of CO_2 to formate for the studied photocatalysts when using UV and VIS light. The result of $TiO_{2\ Qiu}$ under UV light is obtained from Chapter 4.

	UV light	**VIS light**
P25	0.81	0.50
$TiO_{2\ Qiu}$	0.71	N.A.
PC500	0.22	N.A.
$WO_{3\ Sigma}$	1.36	N.A.
$WO_{3\ Mart.}$	4.46	2.64

Under both light sources $WO_{3\ Mart.}$ has by far the highest specificity towards CO_2 production, thus resulting in the most complete mineralization after 10 h of UV illumination. In contrast, PC500 has a very low specificity towards full mineralisation, which can be rationalised given its large available surface area but poor electronic properties, that can accommodate a large fraction of less reactive intermediates, without the required photocatalytic power for their fast further degradation.

To summarise, the *in situ* method - just as the image analysis method - showed that under UV light P25 results in the fastest (short-term) soot degradation, and under VIS light $WO_{3\ Mart.}$ was the fastest soot degrader, while in terms of specificity $WO_{3\ Mart.}$ performed best under both light sources. When considering real-life applications, the eventual purpose will determine which characteristics are decisive (*e.g.* fast surface cleaning, prevention of release of toxic compounds).

5.4 Conclusion

Existing studies on photocatalytic soot degradation focus on TiO_2-based photocatalysts under UV light, which accounts for only ~ 5% of the solar spectrum. In this study the photocatalytic soot oxidation capacity of WO_3-based

photocatalysts was studied for the first time, along with TiO_2-based benchmark materials, using UV, visible and artificial daylight. The use of WO_3-based photocatalysts proved to be challenging due to their intrinsic yellow-greenish appearance, that furthermore changed upon progressive illumination. The latter impeded straightforward use of a previously introduced digital image analysis technique for quantifying the degree of soot degradation in a fast and cost-effective manner. As a solution, an additional data processing step is presented, correcting for intrinsic photocatalyst colour changes. This way, the application range of this versatile and accurate detection method has now also been broadened to coloured samples.

Our results have shown that under pure UV light TiO_2-based photocatalysts still outperform WO_3-based materials, both for the degradation of a uniform soot haze as well as for concentrated soot spots, which was further supported by *in situ* experiments. However, under visible light, the lab-synthesized WO_3 was more than two times faster in completely degrading a uniform soot haze, compared to all studied TiO_2-based photocatalysts, which was also supported by the *in situ* experiments. Similar results were detected for all photocatalysts for the degradation of concentrated soot spots under visible light during most of the experiment. After 82 days the TiO_2-based photocatalysts outperformed the WO_3-based photocatalysts. Under artificial daylight significant soot degradation - ranging between 18% and 75% - was obtained by all studied photocatalysts, both for the haze and spots, showcasing the potential of photocatalysis as sustainable and energy-efficient soot degradation technology. Two of the three studied TiO_2-based photocatalysts outperformed both WO_3-based photocatalysts for the degradation of the soot haze, while similar results were seen for all photocatalysts for the soot spots, with the best results for P25. When considering the specificity of all materials towards full soot mineralisation into CO_2, the lab-synthesized WO_3 showed the best performance under both UV and visible light, only generating very small amounts of undesired intermediates.

The obtained results highlight the potential of photocatalysis as a sunlight-driven, and thus energy-efficient, soot degradation technology, and in doing so a low-cost and time-efficient soot detection method was improved, allowing

accurate monitoring of this process, even for inherently coloured, and thus visible light active materials.

Chapter 6

Proof of concept of an autonomous and robust TiO_2/WO_3-based waste gas-to-electricity PFC device

Myrthe Van Hal, Rajeshreddy Ninakanti, Karthick Raj Ag, Silvia Lenaerts, Sammy W. Verbruggen, *TiO_2/WO_3-based waste gas-to-electricity device for application in soot contaminated environments.* In preparation.

Author contributions:

M.V.H. designed the experiments, performed the material synthesis, executed the experiments and is drafting the first paper.

R.N. performed XRD and SEM-EDX measurements.

K.R.A. performed additional characterisation measurements.

S.W.V. and S.L. supervised the work.

6.1 Introduction

Chapter 2 and 3 showed that a photoelectrochemical (PEC) cell is capable of addressing both air pollution, more specifically VOC emissions, and sustainable energy production, generating either H_2 gas or electricity, in a single device. The PEC cell uses (sun)light to oxidise VOCs at the photoanode and simultaneously recover part of the energy of these degraded compounds at the cathode. As high soot concentrations are a globally encountered problem, especially in urban areas,[48] soot is likely to be deposited on the photoanode of a MEA during operation. A first effect of a soot layer covering the photoanode surface, resulting in a decreased amount of light reaching the photoanode, could thus be a reduced PEC cell performance. A second effect could result from interaction between the deposited soot and holes or other reactive oxidants that can compete with ongoing reactions at the anode (*e.g.* H_2O and VOC oxidation). Therefore, the ability of a photoanode of a PEC cell to cope with soot is crucial to obtain stable and long-term operation in soot contaminated (*i.e.* urban) environments. To this end, the results of the previous chapters will be combined in this chapter.

In Chapter 3 it was shown that WO_3-based photocatalysts outperform TiO_2-based photocatalysts as photoanodes of an all-gas phase PFC device targeting VOC degradation. An additional advantage of WO_3 when targeting autonomous, and thus sunlight-driven, PFC operation is the ability of WO_3-based photocatalysts to utilise part of the visible fraction of the solar spectrum. In Chapter 5, the photocatalytic soot oxidation capacity of the photoanodes studied in Chapter 3 was determined with the soot oxidation detection methodology presented in Chapter 4. It was shown that TiO_2-based photocatalysts in general have a higher soot oxidation capacity than WO_3-based photocatalysts. As the final goal of this thesis is to obtain efficient, long-term and robust PFC operation both excellent photoanode performance and a high soot oxidation capacity are required. Therefore, in this chapter both types of photocatalysts are combined, striving for the best of both worlds, *i.e.* an efficient, sunlight-driven and soot-degrading waste gas-to-electricity PFC device.

In this chapter, the most promising TiO_2- and WO_3-based photocatalysts were selected based on the soot oxidation capacity and photoanode performance

obtained in previous chapters. Next, these photocatalysts were combined, both by physical mixing and layering. Subsequently, the performance of the obtained photocatalyst combinations, both as photoanode and soot degrader, were studied. The soot oxidation detection methodology presented in Chapter 4 was applied to the best performing materials – both pure photocatalysts and combinations - to monitor soot degradation during PFC operation. In the final part of this chapter the in-house engineered PFC device was applied outdoors serving as proof of concept of a PFC system operating autonomously, solely using sunlight and outdoor air to sustainably generate electricity.

6.2 Experimental

6.2.1 Material synthesis and characterisation

The two best performing photocatalysts were further studied in this final experimental chapter: commercially available P25 (Evonik) and WO_3 synthesized according to Martínez-de la Cruz *et al.* (2010)[79], further denoted as $WO_{3\ Mart.}$. In Chapter 3, the synthesis procedure of $WO_{3\ Mart.}$ can be found.

The two best performing photocatalysts (P25 and $WO_{3\ Mart.}$) were combined. The first combination method was to mix both photocatalyst powders. The photocatalysts were mixed in two different ratios. P25-$WO_{3\ Mart.,\ mass}$ was obtained by using equal masses of both photocatalyst, and P25-$WO_{3\ Mart.,\ mol}$ was obtained by mixing both photocatalysts in an equal molar ratio. A second combination strategy was to combine both photocatalysts in a layered configuration. After drop casting (see section 6.2.2 and 6.2.3) and drying (80°C, overnight) of the first photocatalyst layer, the second layer was drop casted on top of this layer, again followed by overnight drying at 80°C. Different amounts of photocatalyst were applied, starting from the standard loading used in PFC experiments (= 1.6 mg cm^{-2}). The photocatalyst combination is denoted by the photocatalyst loading of each material involved, top to bottom, expressed in mg cm^{-2}. For example the photocatalyst denoted by 'P25 on $WO_{3\ Mart}$ (0.8/0.8)' is obtained by adding a layer of 0.8 mg P25 cm^{-2} on top of a layer of 0.8 mg $WO_{3\ Mart.}$ cm^{-2}.

A range of physico-chemical characterisation techniques (N_2 sorption, UV-VIS spectroscopy, X-ray diffraction and energy dispersive X-ray fluorescence) were performed and are described in Chapter 3.

6.2.2 PFC experiments

The membrane electrode assemblies (MEA) were produced as described in detail in Chapter 3. In brief, for a standard MEA the photoanode consists of photocatalyst (1.6 mg cm^{-2}) embedded in Nafion® (Sigma-Aldrich) and drop casted on Toray paper 030 (Fuel Cell Earth). The cathode consisted of 0.4 mg cm^{-2} platinum nanoparticles on carbon black (Sigma-Aldrich) embedded in Nafion® and drop casted on Toray paper 030. Both were dried overnight at 80°C. A MEA was obtained by hot-pressing both photoanode and cathode on opposite sides of a preconditioned Nafion® 117 membrane (Fuel Cell Earth) after addition of 12 µL of a 5 wt% Nafion® solution (Fuel Cell Earth) on the anode. The hot-pressing conditions were 5.5 tons at 135°C for 3 minutes. Residual solvent was removed by overnight illumination (UVA) in humid atmosphere.

The PFC design is described in detail in Chapter 3. The MEA is placed in the centre of the PFC device, between the anode and cathode compartment. For the UV measurements, a Philips fluorescence S 25 W UVA lamp was placed 3 cm from the photoanode, reaching an incident intensity of 2.35 mW cm^{-2} in the region of 290 - 400 nm (λ_{max} at 354 nm), as measured with an Avantes Avaspec-3648-USB2 spectroradiometer. The simulated solar light measurements were performed using a 300 W Xe source (Oriel Instruments), equipped with an AM1.5g filter to provide simulated solar light adjusted to a total irradiance of 100 mW cm^{-2} (between 300 and 1100 nm). For visible light measurements, a 420 nm cut-on filter was added. The absolute irradiance spectrum of all used lamps can be obtained from Chapter 3 in Figure 3.2.

All gas phase experiments were performed using a fully automated gas test setup developed in our group.[149] Water and methanol vapour were introduced in the gas flow by a gas wash bottle. Synthetic air (Messer) was bubbled through the bottle at a flow rate of 50 mL min^{-1}. The gas wash bottle was either filled with pure deionized water, obtaining moist air, or a 3 wt% methanol (Merck)

aqueous solution, resulting in a moist vapour with a methanol concentration of 17 mmol m^{-3} (2573 ppmv). To obtain stable photocurrent generation, the photoanode compartment of the PFC was flushed for 30 minutes with the vapour under study prior to each measurement. The cathode was not flushed, but kept exposed to air, targeting electricity production (PFC operation). A VersaSTAT 3 potentiostat (Princeton Applied Research) was used for all chronoamperometric (CA) measurements. The generated photocurrent density was calculated by dividing the measured photocurrent by the area of the anode surface exposed to the light source (1.8 cm^2).

6.2.3 Photocatalytic soot oxidation experiments

A detailed description of the coating procedure can be found in Chapter 4. In short, the photocatalysts were drop casted on cleaned glass slides (standard loading = 1.6 mg cm^{-2}). The coated glass slides were dried to remove residual solvent. Soot (Printex-U) was drop casted on top of the photocatalyst layer (22 µg cm^{-2}), and the glass slides were again dried to remove all residual solvent. The photocatalyst combination P25 on $WO_{3\ Mart.}$ (1.6/1.6) was excluded from the experiments due to large cracks in the P25 layer.

Soot degradation was monitored using the image analysis method as presented and described in detail in Chapter 4 and 5. In brief the samples were placed 3 cm under a Philips fluorescence S 25 W UVA lamp obtaining an incident light intensity of 2.1 mW cm^{-2} in the region of 290 - 400 nm (λ_{max} at 354 nm). The irradiance spectra can be obtained from Chapter 5 in Figure 5.11.

A standardised photobox was used to ensure repeatability.[92] A Canon Eos 500D camera was used, positioned 20 cm above the samples, in manual mode (iso 200, aperture f8 and focal exposure 1:5) at maximal resolution (5184 × 3456) at 72 dpi. To process the images, the free image software ImageJ was used. The brightness axis of the CIELab colour space (= L* coordinate) was used as a measure of the amount of soot deposition. The extent of the shift of the most frequent L* value quantifies the degree of degradation of the uniform soot haze. The decrease in height of the concentrated soot peak of the L* curve (at low L* values) represents the amount of degradation of the concentrated soot spots. A more detailed description can be found in Chapter 4.

Each photocatalyst was applied on five glass slides and soot was deposited on four of them (*i.e.* standard samples). Three standard samples were illuminated and one was kept in the dark as negative control. The glass slides containing only photocatalyst were illuminated together with the standard samples (*i.e.* light-control samples). Pictures were taken from the glass slides before and after soot deposition at specific UV illumination intervals (0, 5, 11, 20, 26, 40, 61 and 82 days). Corrections for possible deviations caused by small changes in the background illumination were made by processing a set area of the background in ImageJ and applying the hereby obtained deviation in L* value to the complete dataset of that time point.

6.2.4 Combined PFC-soot experiments

In this section the soot oxidation capacity of fully assembled PFC systems was studied. MEA's were first produced according to the description in Section 6.2.2. For the soot deposition, a Printex-U suspension (in methanol) was ultrasonicated for 1 hour and drop casted (40 µL) on the photoanode, obtaining a soot coverage of 22 µg cm^{-2}. Methanol was eliminated from the surface by heating the MEA in a vacuum oven (50°C) for 2 hours.

A Philips fluorescence S 25 W UVA lamp was placed 3 cm from the photoanode, reaching an incident intensity of 2.35 mW cm^{-2} in the region of 290 - 400 nm (λ_{max} at 354 nm). The soot detection method applied to monitor the degradation of soot during PFC operation is summarised in section 6.2.3 and described in more detail in Chapter 4. No concentrated soot spots were observed when depositing soot on the photoanode of a MEA, hence only the degradation of a uniform soot haze was determined. Photographs were taken from the photoanode side of the MEA before and after soot deposition at specific UV illumination intervals (0, 1, 3, 7, 10 and 14 days). Possible changes in background illumination were cancelled by processing a set area of the background analogue to the pictures of the MEA and correcting for the obtained deviation in maximal L* value. Long CA measurements were performed continuously flushing the anode with the vapour under study and illuminating the photoanode.

6.2.5 Outdoor application

In the last part of this chapter the in-house engineered PFC device was tested in a real-life application, aiming at autonomous PFC operation purely using sunlight and outdoor air to sustainably generate electricity. P25, $WO_{3\ Mart.}$ and P25 on $WO_{3\ Mart.}$ (0.4/1.6) were used as photoanode materials. An ampere meter (Kopp, Pan multimeter) was connected to the stainless steel electrodes of the PFC device. The results were collected after a short equilibration period ($\pm$ 1 minute after exposure to sunlight). The generated photocurrent density was calculated by dividing the measured photocurrent by the area of the anode surface exposed to light (1.8 cm^2). The intensity of the sunlight was measured using a calibrated spectroradiometer.

6.3 Results and discussion

6.3.1 Pure photocatalysts: photoanode performance *vs.* soot oxidation capacity

In Chapter 3, the performance of a range of TiO_2- and WO_3-based photocatalysts as photoanode materials was studied. In Chapter 4 and 5 the photocatalytic soot oxidation capacity of these photocatalysts was studied. When looking towards outdoor application of a PFC, the ability of the photoanode to degrade soot will be crucial to achieve robust and long-term operation of the device. To this end, the results of the previous chapters are visually summarised in Figure 6.1.

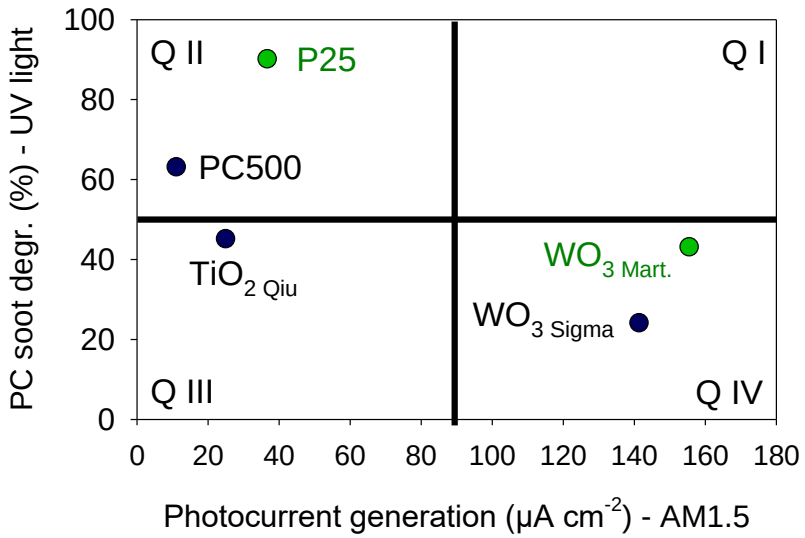

Figure 6.1. Comparison of studied photocatalysts, plotting the photocatalytic soot degradation after 11 days under UV light (2.1 mW cm^{-2}) against the instant photocurrent generation (extracted from CA measurements) under simulated solar light (100 mW cm^{-2}) when flushing the PFC device with a moist methanol vapour (17 mmol m^{-3}). Q = quadrant.

Figure 6.1 gives an overview of the photocatalytic soot oxidation capacity and photoanode performance of the five TiO_2- and WO_3-based photocatalysts studied in this thesis. As the final goal is to autonomously operate a PFC using sunlight the results from the previous chapters that are closest to the absolute values that will be attained under actual sunlight are combined in Figure 6.1. No photocatalysts are present in quadrant I (QI) of Figure 6.1. As shown in Figure 6.1, previous chapters evidenced that in general TiO_2-based photocatalysts are the fastest soot degraders, but poor photoanodes (quadrant II and top of quadrant III), while WO_3-based photocatalysts performed best as photoanodes in a gas phase PFC device, but are less efficient soot degraders (quadrant IV). Therefore, in this chapter the best performing TiO_2- and WO_3-based photocatalysts will be combined, aiming to combine the beneficial properties of both pure photocatalysts thus synthesizing a photocatalyst that lies in quadrant I. Figure 6.1 shows that of the three studied TiO_2-based photocatalysts, P25 is the most efficient soot degrader. As a result P25 is the TiO_2-based photocatalyst selected for further study. A slightly better performance was seen in the all-gas phase PFC when using $WO_{3\ Mart.}$ as

photoanode, thus selecting this as the WO_3-based photocatalyst used in further experiments. Thus, P25, $WO_{3\ Mart.}$ and combinations based on both photocatalysts will be further studied in the rest of this chapter.

6.3.2 Screening of TiO_2-WO_3 combined photocatalysts

6.3.2.1 Characterisation

The two pure photocatalysts selected for further study in this chapter (P25 and $WO_{3\ Mart.}$) are extensively described in literature or by the manufacturer.[79] The characterisation of these materials can be found in Chapter 3. An overview of relevant photocatalyst properties is shown in Table 6.1. For the combined materials after physical mixing, intermediate surface areas were measured, as expected, yielding a higher surface area for samples with a higher P25 content (*i.e.* P25-$WO_{3\ Mart,\ mass}$). XRD measurements confirmed the presence of both anatase, rutile and the WO_3 monoclinic polymorph.

Table 6.1. Physical characteristics (band gap, BET surface area and crystallite particle size) of commercial and synthesized materials.

Material	Band gap (eV)[4]	BET surface area ($m^2\ g^{-1}$)	Crystallite particle size (nm)[5,6]
$P25_{Evonik}$[1]	3.2	52	19 (A), 32 (R)
$WO_{3\ Mart.}$[2]	2.6	9	32 (W)
P25-$WO_{3\ Mart,\ mass}$[3]	2.6/3.2	31	19 (A), 32 (R), 32 (W)
P25-$WO_{3\ Mart,\ mol}$[3]	2.6/3.2	24	19 (A), 32 (R), 32 (W)

1) Commercially available photocatalyst.
2) Photocatalyst synthesized based on literature protocols.
3) Photocatalyst synthesized by mixing two pure photocatalysts.
4) Obtained by the Tauc method applied on diffuse reflectance spectra.
5) Estimated from XRD using the Scherrer equation.
6) A = anatase, R = rutile, W = monoclinic polymorph.

6.3.2.2 PFC experiments

The performance of the combined TiO_2-WO_3 photocatalysts as photoanode in the PFC device is studied in this section. The best performing material under simulated solar light when flushing with methanol vapour is shown in Figure 6.2.

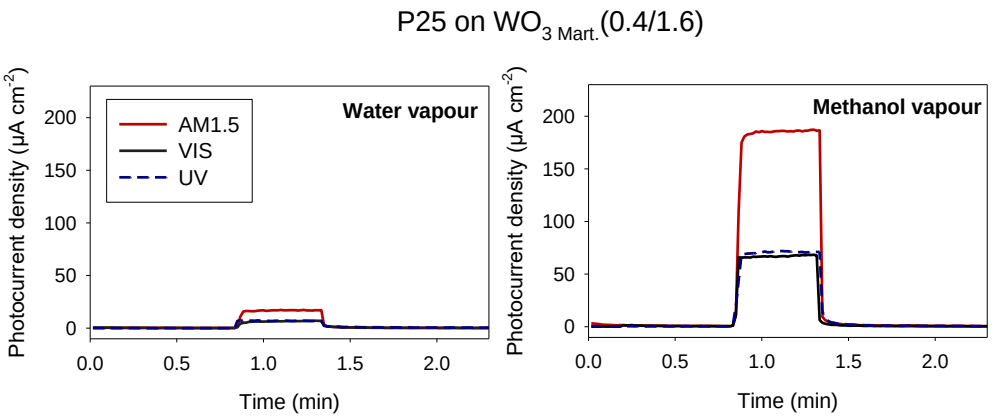

Figure 6.2. Photocurrent density as a function of time when using different light sources (simulated solar light (AM1.5g, 100 mW cm^{-2}), visible light (> 420 nm, 96 mW cm^{-2}) and UV light (4 mW cm^{-2})), both when feeding the photoanode with (left) pure water vapour and (right) moist methanol vapour (17 mmol m^{-3}) when using P25 on $WO_{3\ Mart.}$ (0.4/1.6) as photoanode.

The results of the other studied combinations are summarised in Figure 6.3. These results show that when flushing with methanol vapour the photocurrent generated with the best performing layered combination (P25 on $WO_{3\ Mart.}$ (0.4/1.6)) is around twice as high as that obtained with the best performing mixed combination (P25-$WO_{3\ Mart,\ mol}$).

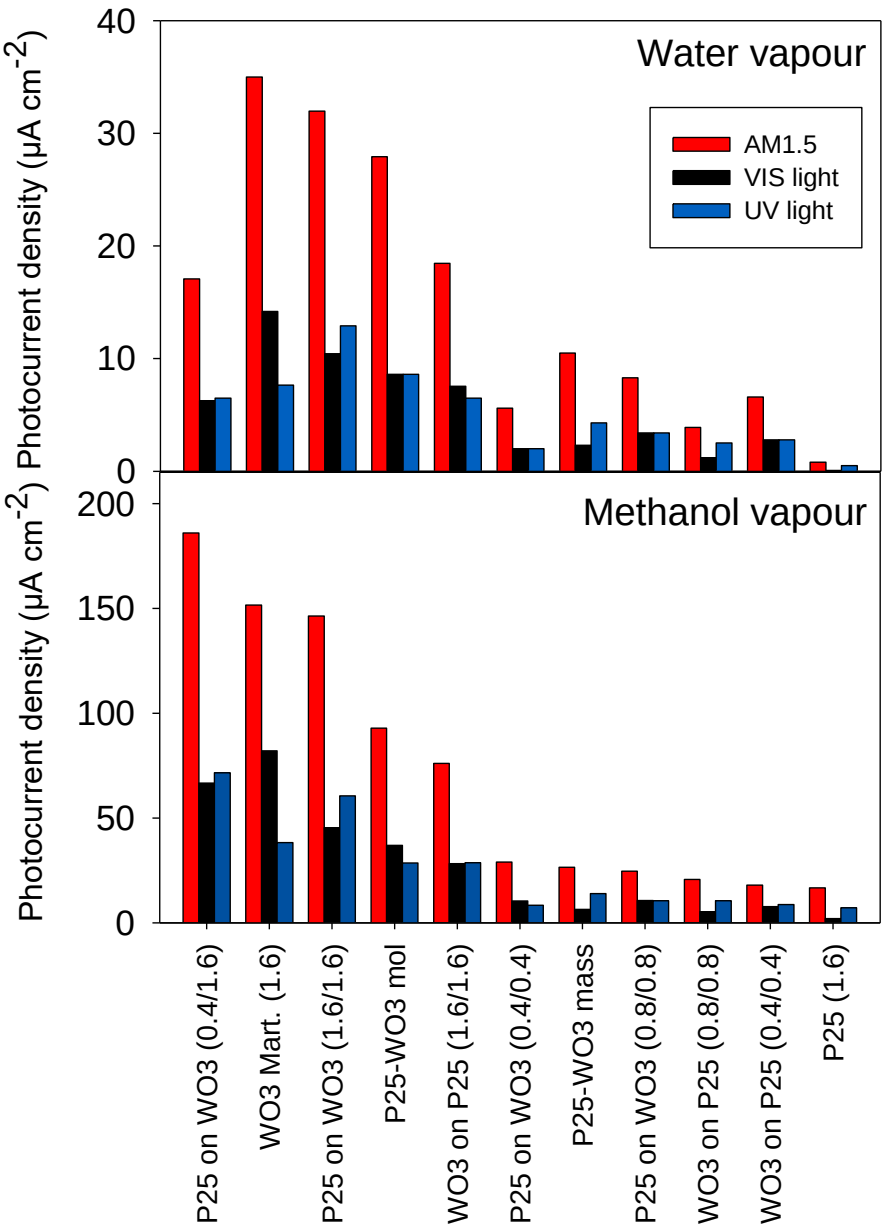

Figure 6.3. Photocurrent densities generated by different TiO_2-WO_3 combinations using different illumination sources, both when flushing the PFC with (top) water vapour and (bottom) moist methanol vapour (17 mmol m^{-3}).

Examining Figure 6.3 it is clear that under simulated solar light, overall, a layer

of P25 on a layer of WO_3 performs better than a layer of WO_3 on a layer of P25. This can be explained by the lower band gap of WO_3, allowing it to also use the visible fraction of the solar light, which is largely unused by the wider band gap material P25 on top. Transmittance data through all layers is provided in Figure 6.4, evidencing the larger fraction of solar and VIS light available after passing a layer of P25 compared to $WO_{3\ Mart}$. When flushing with methanol vapour a similar result is seen for P25 on $WO_{3\ Mart.}$ (1.6/1.6) and pure $WO_{3\ Mart.}$ under simulated solar light. The higher photocurrent generation under VIS light for pure $WO_{3\ Mart.}$ is almost completely outweighed by the increase in photocurrent generation under UV light when adding a layer of P25 on top. Note that still significant photocurrent generation is obtained with P25 on $WO_{3\ Mart.}$ (1.6/1.6) under purely VIS light. Lowering the amount of P25 of the top layer (P25 on $WO_{3\ Mart.}$ (0.4/1.6)) increases the generated photocurrent under simulated solar light and thus results in the highest photocurrent generation when flushing with methanol vapour. This can be attributed to the increased transmittance of light through a thinner upper P25 layer (see Figure 6.4), resulting in more light that can be used by the bottom (= more active) WO_3 layer. Compared to a standard layer of pure $WO_{3\ Mart.}$ (= 1.6 mg cm^{-2}) the photocurrent generation increased with respectively 87% and 22% under UV and simulated solar light by the addition of a thinner P25 layer (= 0.4 mg cm^{-2}) on top. The solar light response lies between that of pure P25 and $WO_{3\ Mart.}$, resulting in a 2.6 times higher photocurrent generation under simulated solar light compared to pure UV light (*vs.* a factor of resp. 1.5 and 4.0 for pure P25 and $WO_{3\ Mart}$).

The best performing mixed TiO_2-WO_3 combination - P25-$WO_{3\ Mart,\ mol}$ - results in a 5.2 times higher generated photocurrent compared to pure P25 under solar light and when flushing with methanol vapour, while attaining 62% of the generated photocurrent of pure $WO_{3\ Mart}$. When simply mixing both photocatalysts intermediate results were obtained. When lowering the amount of $WO_{3\ Mart}$, as is the case for P25-$WO_{3\ Mart,\ mass}$ (ca. $\frac{1}{4}$ mol% WO_3 *vs.* $\frac{1}{2}$ mol% WO_3 for P25-$WO_{3\ Mart,\ mol}$), lower photocurrents were generated.

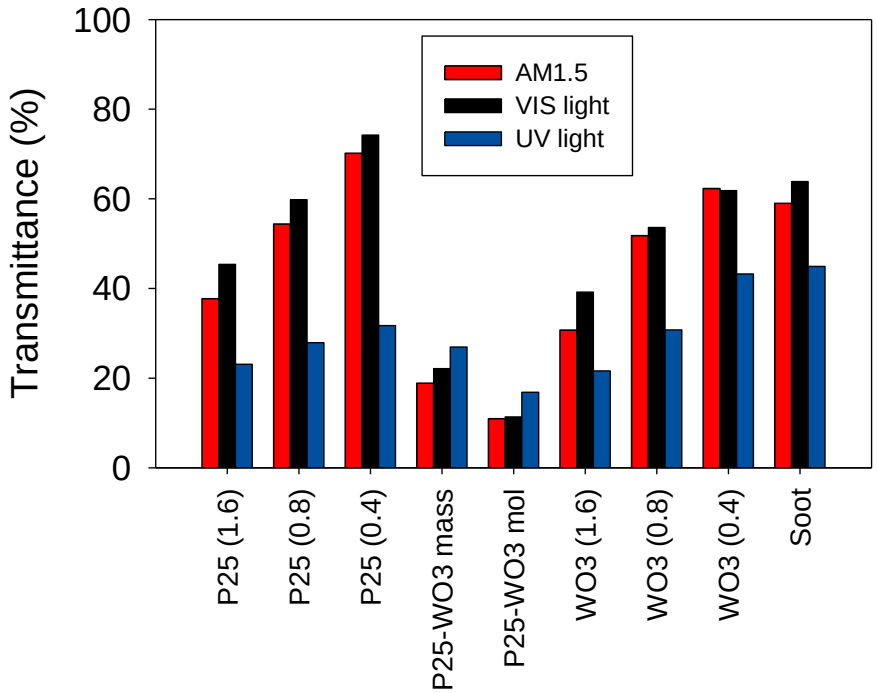

Figure 6.4. Transmittance (%) of simulated solar light (AM1.5g, 100 mW cm^{-2}), visible light (> 420 nm, 96 mW cm^{-2}) and UVA light (4 mW cm^{-2}) through a glass slide coated with a photocatalyst or a soot layer (22 µg cm^{-2}). The photocatalyst loading is shown between brackets (in mg cm^{-2}). The lamp was positioned 4 cm from the spectroradiometer, the glass slide was placed in the middle.

6.3.2.3 Photocatalytic soot oxidation experiments

In the previous paragraph the performance of a range of TiO_2-WO_3 combined photocatalysts as photoanode of a (sun)light driven waste gas-to-electricity PFC was studied. In this section the soot oxidation capacity of these photocatalysts is studied. The results are shown in Figure 6.5.

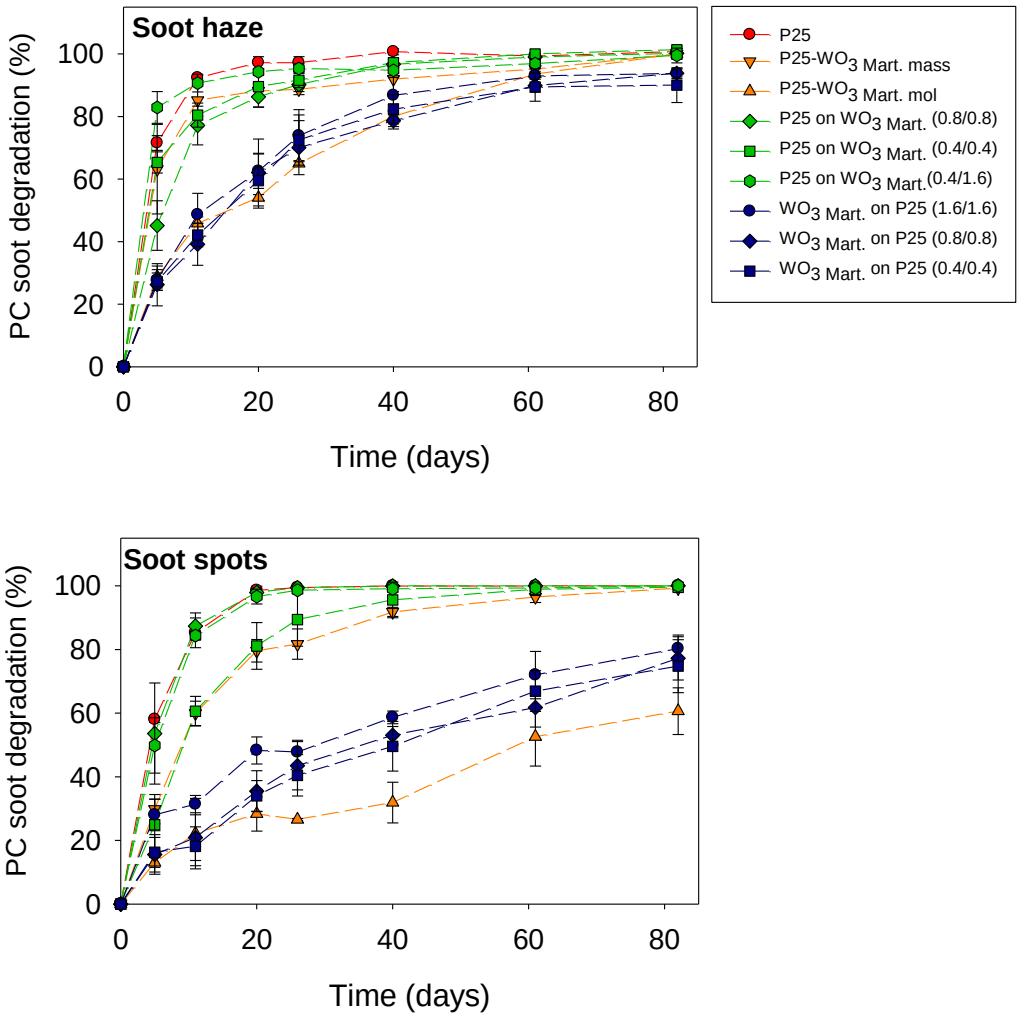

Figure 6.5. Photocatalytic soot degradation of the (top) soot haze and (bottom) concentrated soot spots by a range of photocatalysts determined by digital image analysis after light-induced colour-change correction, as a function of UV illumination time. The error bars are based on three independent samples. Dashed lines are added to guide the reader's eye.

Figure 6.5 shows that for the soot haze P25 is the fastest soot degrader, reaching complete oxidation after 40 days, closely followed by all combinations of P25 on $WO_{3\ Mart.}$ (all reaching > 95% degradation after 40 days). After 40 days, P25-$WO_{3\ Mart.\ mass}$ reached 92% degradation, $WO_{3\ Mart.}$ on P25 (1.6/1.6) 87%, and all other studied photocatalysts reached circa 80% degradation of the soot haze. It is clear that the photocatalyst used for the top layer is decisive for the soot oxidation capacity of the layered configuration. As a result,

combinations of P25 on top of $WO_{3\ Mart.}$ all result in similar soot degradation percentages, close to that of pure P25. In accordance, the soot haze degradation rates obtained by the layered combinations with $WO_{3\ Mart.}$ on top of P25 are also all very similar, but significantly lower than those obtained with P25 as top layer. The results are alike those obtained with pure $WO_{3\ Mart.}$ in Chapter 5 (Figure 5.7). As there is only negligible penetration of the soot into the photocatalyst layer, the photocatalytic soot oxidation reaction only depends on the thickness of the photocatalyst layer in the range of the diffusion length of the excited carriers.[188] Even when decreasing the photocatalyst loading four times, the top photocatalyst layer remains thick enough to rule out the effect of the bottom layer. When taking into account the coated photoanode surface and the densities of the photocatalyst powders, the thickness of the layers is estimated to be of the order of 0.5 – 4.5 µm, as confirmed by scanning electron microscopy (SEM) measurements, whereas the diffusion length of charge carriers is in the order of nanometres.[109,188] When mixing the photocatalysts, a better result was obtained with a higher ratio of P25 to $WO_{3\ Mart}$, as expected since under UV light P25 is the better soot degrader of both photocatalysts.

When considering the degradation of the concentrated soot spots, the best performing photocatalyst combinations were again all combinations of P25 on $WO_{3\ Mart}$, almost coinciding with the results of pure P25. The layered combinations with $WO_{3\ Mart.}$ as top layer also all reached similar results, as for the soot haze obtaining lower degradation rates than the combinations with P25 as top layer. Of the two studied mixed photocatalyst combinations, again P25-$WO_{3\ Mart.\ mass}$ performs best.

As these UV experiments support the previously in literature described limitation of the photocatalytic soot oxidation reaction to the thin upper photocatalyst layer, no soot experiments were performed under artificial daylight and visible light.

6.3.2.4 Photoanode performance *vs.* soot oxidation capacity

The performance of the TiO_2-WO_3 combined photocatalysts as photoanodes of a gas phase PFC and as photocatalytic soot degraders was studied separately in previous paragraphs. To obtain an efficient and soot-degrading waste gas-to-

electricity PFC device both good photoanode performance and a high soot oxidation capacity are crucial. To this end, the results of previous paragraphs are visually summarised in Figure 6.6.

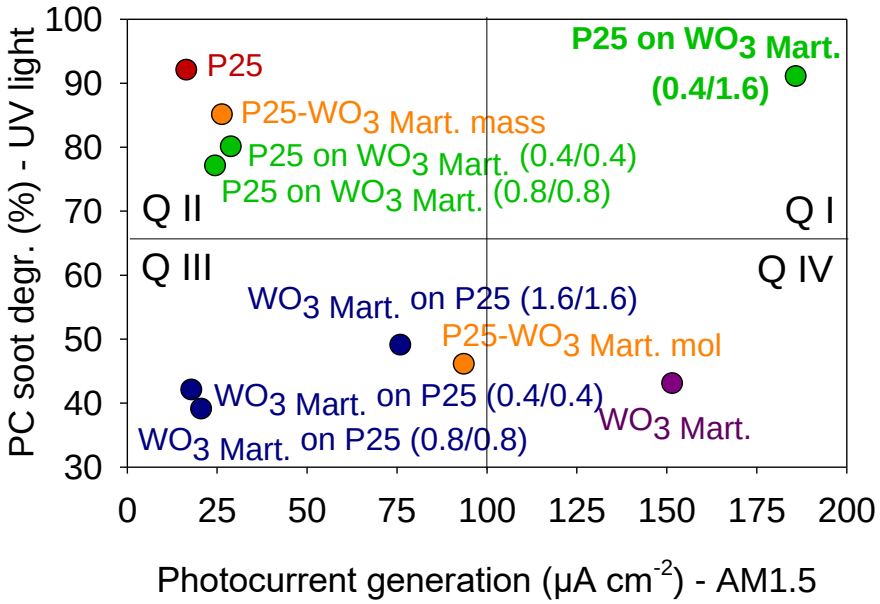

Figure 6.6. Comparison of studied photocatalysts, plotting the photocatalytic soot degradation after 11 days under UV light (2.1 mW cm^{-2}) against the instant photocurrent generation (extracted from CA measurements) under simulated solar light (100 mW cm^{-2}), when flushing the PFC device with a moist methanol vapour (17 mmol m^{-3}). Following photocatalysts are studied: (red) pure P25, (purple) pure $WO_{3\ Mart.}$, (green) layered P25 on $WO_{3\ Mart.}$ combinations, (blue) layered $WO_{3\ Mart.}$ on P25 combinations, and (orange) mixed P25-$WO_{3\ Mart.}$ combinations. Q = quadrant.

Figure 6.6 shows that a four times less dense P25 layer (0.4 mg cm^{-2}) on top of a standard layer of $WO_{3\ Mart.}$ (1.6 mg cm^{-2}) outperformed all other studied photocatalysts. It is the only photocatalyst located in quadrant I, thus achieving the targeted combination of excellent photoanode performance with efficient photocatalytic soot degradation. The photocatalysts with P25 on top or with a large amount of P25 (*i.e.* pure P25, or P25-$WO_{3\ Mart.\ mass}$) are situated in quadrant II, and thus perform very well towards photocatalytic soot oxidation, but act poorly as photoanodes. On the other hand, photocatalysts containing a large amount of $WO_{3\ Mart.}$ (*i.e.* pure $WO_{3\ Mart.}$, and P25-$WO_{3\ Mart.\ mol}$), or with

$WO_{3\ Mart.}$ on top of P25, all show to be less efficient photocatalytic soot degraders (quadrants III and IV). While the photocatalysts with a less dense top layer of $WO_{3\ Mart.}$ also perform bad as photoanodes (located in the left corner of quadrant III), the other materials did show better results in the gas phase PFC device. The addition of a four times less dense P25 layer (0.4 mg cm^{-2}) on top of a standard layer of $WO_{3\ Mart.}$ (1.6 mg cm^{-2}) thus results in 'the best of both worlds', combining the high soot oxidation capacity of P25 with the excellent photoanode properties of the underlying $WO_{3\ Mart.}$ layer. This configuration results in the highest PFC performance (23% better than pure $WO_{3\ Mart.}$), while maintaining a good photocatalytic soot oxidation capacity (only 1% drop compared to pure P25). These results evidence the suitability of this photoanode for application in a sunlight-driven gas phase PFC device operating in soot contaminated (*e.g.* urban) environments.

6.3.3 Combined PFC-soot experiments

During operation of a gas phase PFC device in soot contaminated environments, soot will be continuously deposited on the photoanode. With increasing thickness of the soot layer, the photoanode will become shielded from incoming light, hence reducing the performance of the PFC device. This section will study the ability of the PFC device to cope with soot during PFC operation. To this end, the digital image analysis method as presented in Chapter 4 is applied to quantify the degradation of soot on the photoanode during PFC operation. For this, pure P25, pure $WO_{3\ Mart.}$ and P25 on $WO_{3\ Mart.}$ (0.4/1.6) will be used as photoanodes. The results are shown in Figure 6.7 and Figure 6.8.

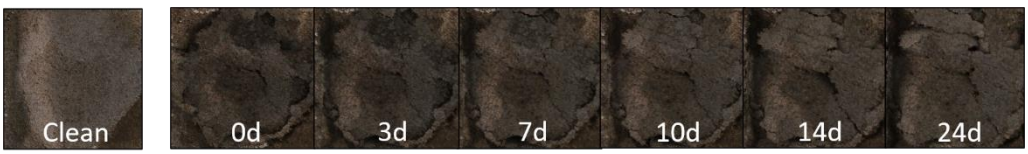

Figure 6.7. Subsequent digital images of soot degradation on a PFC photoanode coated with P25 when flushed with water vapour with f.l.t.r. a photoanode without soot, with soot before UV illumination, after 3, 7, 10, 14 and 24 days of UV illumination.

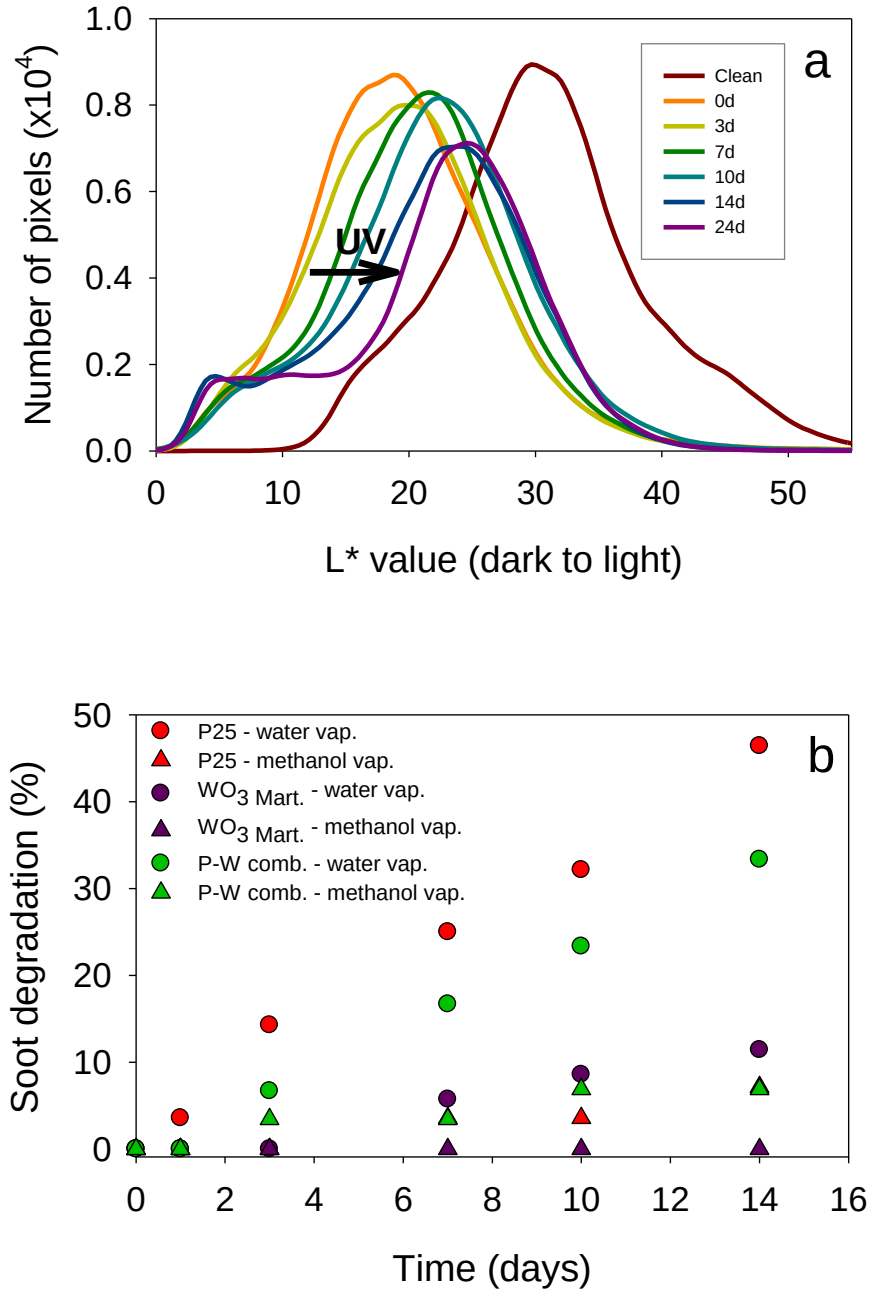

Figure 6.8. a) Number of pixels plotted against the L* value, representing the degradation of soot on a P25 photoanode during PFC operation when using water vapour as photoanode feed. The data was smoothed 10 times. b) Soot degradation, determined by digital image analysis, as a function of UV illumination time. P25 on $WO_{3\ Mart.}$ (0.4/1.6) is denoted as 'P-W comb'.

In Figure 6.7 the degradation of soot during PFC operation is clearly visible as brightening of the photoanode surface. In Figure 6.8a this brightening is reflected in the shift of the graph (and thus most frequent L* value) to higher (and thus brighter) L* values. The digital image analysis method, as presented in Chapter 4 to monitor photocatalytic soot degradation, can thus also be applied to quantify soot degradation on a photoanode surface during PFC operation. No colour correction was required as the photoanode compartment of the PFC device was constantly flushed with either water vapour or moist methanol vapour, preventing dehydration, and thus subsequent discolouration, of the photoanode surface. The soot degradation results obtained by the three studied photocatalysts are shown in Figure 6.8b and summarised in Table 6.2.

Table 6.2. Percentage of soot degradation during PFC operation under UV illumination, determined by digital image analysis, obtained with the studied photoanodes using either water vapour or methanol vapour (17 mmol m^{-3}) as photoanode feed.

	P25		P25 on $WO_{3\ Mart.}$ (0.4/1.6)		$WO_{3\ Mart.}$	
Days	**Water**	**Methanol**	**Water**	**Methanol**	**Water**	**Methanol**
0	0	0	0	0	0	0
1	4	0	0	0	0	0
3	14	0	7	3	0	0
7	25	4	17	3	6	0
10	32	4	23	7	9	0
14	46	7	33	7	11	0

When comparing these results to those obtained in the purely photocatalytic soot degradation experiments (Figure 6.5), it can be seen that P25 was able to degrade over 90% of the uniform soot haze after 11 days in the direct photocatalytic experiments (ambient air, RH ~ 33%), while only 32% of the soot haze was degraded after ten days during PFC operation (moist synthetic air, RH ~ 65%). A similar trend was also established for the two other photo-catalysts with respectively 43% *vs.* 9% degradation for $WO_{3\ Mart.}$ and 91% *vs.* 23% for P25 on $WO_{3\ Mart.}$ (0.4/1.6). The two experiments differ in many ways, including substrate, setup and RH, and are thus not directly comparable. The lower RH in the photocatalytic soot experiments may at least in part explain the

observed differences. Such conditions are thought to decrease both competition between soot and water for oxidants and blocking of active reaction sites, thus enhancing the soot degradation rate. Additionally, as evidenced in Chapter 3, large differences are induced by physically separating the ongoing reactions in two distinct compartments.

It can be noticed from Figure 6.8b that all obtained results follow a clear linear trend, *i.e.* zero-order kinetics, up until 14 days. The soot degradation rate during PFC operation of the three studied photoanodes is shown in Table 6.3.

Table 6.3. Soot degradation rate of studied photoanodes in PFC flushed with water vapour or methanol vapour (17 mmol m^{-3}) under UV illumination.

	Soot degradation rate (µg cm^{-2} day^{-1})	
	Water	**Methanol**
P25	0.75 ± 0.02	0.10 ± 0.01
P25 on $WO_{3\ Mart.}$ (0.4/1.6)	0.52 ± 0.01	0.12 ± 0.01
$WO_{3\ Mart.}$	0.18 ± 0.01	0 ± 0

Table 6.3 shows that for all three studied photocatalysts the soot degradation rate obtained when flushing with water vapour is much higher than that obtained with methanol vapour. As methanol is a much more efficient hole scavenger than water (0.03 V *vs.* 1.23 V at pH = 0 and *vs.* NHE),[173] the addition of methanol to the photoanode feed will decrease the amount of oxidants available for soot degradation. When comparing the different photoanodes, it can be observed that when flushing with water vapour P25 still results in the highest soot degradation rate, followed by P25 on $WO_{3\ Mart.}$ (0.4/1.6) and $WO_{3\ Mart}$. These results are in line with the direct photocatalytic soot experiments, with both P25-based photocatalysts clearly outperforming pure $WO_{3\ Mart}$. When using moist methanol vapours as photoanode feed, no soot degradation was obtained by pure $WO_{3\ Mart}$ after 14 days, while similar results were attained for P25 and P25 on $WO_{3\ Mart.}$ (0.4/1.6). The soot degradation rates obtained in the PFC device (see Table 6.3) evidence the applicability of this technology for tackling urban soot depositions (ranging between 0.001 - 0.010 µg cm^{-2} day^{-1}).[93,194,195]

To summarise, by adding a four times less dense P25 layer (0.4 mg cm^{-2}) on top of a standard $WO_{3\ Mart.}$ layer (1.6 mg cm^{-2}) the soot oxidation capacity during PFC operation was largely increased compared to that of pure $WO_{3\ Mart}$. This is

a result of the limitation of the (photocatalytic) soot oxidation reaction to the top photocatalyst layer. Additionally, this combined photocatalyst performs well as photoanode of an all-gas phase PFC, exploiting the high electron mobility of the thick WO_3-layer for efficient PFC operation. A final important advantage of this combined photocatalyst is the ability to use the visible light activity of $WO_{3\ Mart.}$, resulting in increased performance of the PFC device under sunlight. Thus, a four times less dense P25 layer on top of a standard $WO_{3\ Mart.}$ layer combines the high soot degradation capacity of P25 with the excellent photoanode performance of $WO_{3\ Mart}$, obtaining the 'best of both worlds'. Additionally, this conclusion can be extrapolated to other photocatalyst materials in the quest for an efficient and robust PFC device, applying a small amount of an efficient soot degrader on a standard layer of an excellent photoanode material.

6.3.4 Outdoor application

In this final part, outdoor measurements were performed studying the potential of the in-house developed PFC device and selected photoanodes for autonomous PFC operation. This measurement was performed on the 14th of June 2021 (2 p.m.). The standard measurements were performed at the University of Antwerp (CGB, Antwerp, in front of the V-building). An absolute sunlight irradiance of 57 mW cm^{-2} was measured between 280 and 1100 nm (280 - 400 nm: 2 mW/cm^{-2}; 400 - 800 nm: 35 mW cm^{-2}). Figure 6.9b shows the autonomously operating PFC device, solely driven by sunlight and outdoor air. As shown in Figure 6.9a, the highest photocurrent density was generated using $WO_{3\ Mart.}$ (26 µA cm^{-2}), closely followed by P25 on $WO_{3\ Mart.}$ (0.4/1.6) (23 µA cm^{-2}) and with very low photocurrents generated by P25 (2 µA cm^{-2}). A large range of pollutants might be present in outdoor air serving – just as methanol – as hole scavengers.

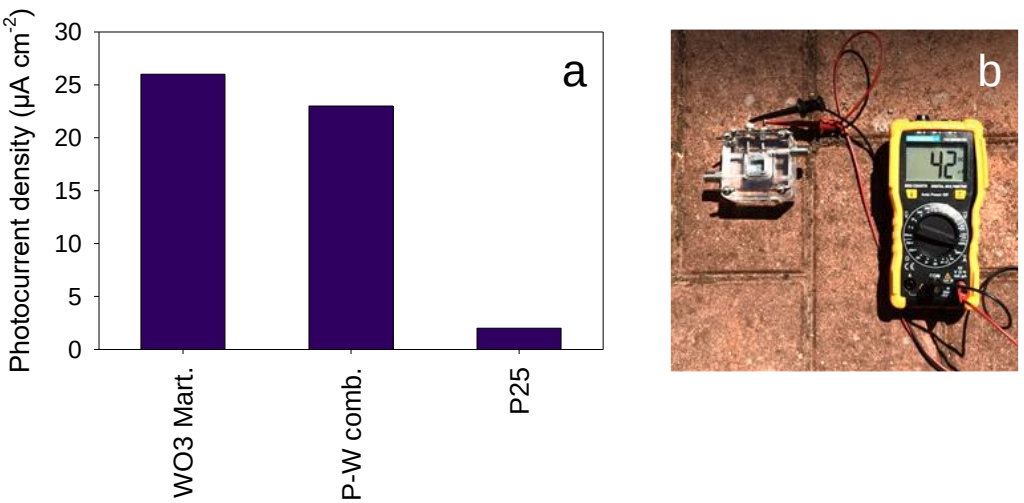

Figure 6.9. a) Photocurrent density as a function of time when autonomously applying the PFC device outside (CGB, Antwerp), when using following photocatalysts at the photoanode: $WO_{3\ Mart.}$, P25 on $WO_{3\ Mart.}$ (0.4/1.6) - denoted as 'P-W comb' - and P25. The measurement was performed on the 14th of June 2021 at 2 p.m., b) Picture of outdoor application of PFC device, using P25 on $WO_{3\ Mart.}$ (0.4/1.6) as photoanode.

The best performing PFC configuration (with $WO_{3\ Mart.}$) was also applied the same day in a 'polluted' area. A measurement was performed on a bridge over a busy highway (Floraliënlaan over E19, Antwerp), resulting in a 28% increase in generated photocurrent compared to the 'standard' site (CGB). Cars emit a broad range of pollutants, including VOCs, NO_x and PM (*e.g.* soot),[200] resulting in increased presence of hole scavengers. In contrast to the easily degradable methanol, most compounds present will be more stable and/or complex, resulting in a lower instant photocurrent increase (see also Chapter 3: CH_4, C_2H_4 and NH_3). More research is required to get more insight into the effect of common waste gases/pollutants on PFC operation, eventually linking outdoor air sampling with on-site photocurrent measurements. However, this first proof of concept experiment already demonstrates the feasibility of our proposed technology.

When combining the results of the outdoor measurements with those of the combined PFC-soot experiments, it can be concluded that a four times less dense P25 layer (0.4 mg cm^{-2}) on top of a standard layer of $WO_{3\ Mart.}$

(1.6 mg cm^{-2}) largely increased the soot oxidation capacity compared to pure $WO_{3\ Mart.}$ ($\geq$ factor 3 increase) during PFC operation, while still retaining most of its photoanode performance when applied outdoor (only 12% photocurrent drop compared to pure $WO_{3\ Mart.}$). It thus proves promising for application as photoanode in an efficient, autonomous and soot-degrading waste gas-to-electricity PFC device.

It should be noted that the produced photocurrents are still quite low in absolute terms, as only limited research has been performed on all-gas phase PFC operation. This chapter aimed at improving the photoanode material towards application in a VOC-degrading PFC device operating in soot contaminated (*e.g.* urban) environments. Overall, these are first promising results striving towards an efficient and robust PFC device. We are hopeful that the described proof of concept can serve further development of an autonomous, low-cost and widely applicable gas phase PFC system.

6.4 Conclusion

Previous chapters showed that while the partially visible light active WO_3-based photocatalysts were more efficient photoanodes for use in gas phase PFCs, TiO_2-based photocatalysts proved to have the highest photocatalytic soot oxidation capacity. In this chapter both types of photocatalysts are combined, striving towards an efficient, sunlight-driven and soot-degrading waste gas-to-electricity PFC device. To this end, P25 and $WO_{3\ Mart.}$ were selected based on the results of the previous chapters. Addition of a four times less dense P25 layer (0.4 mg cm^{-2}) on top of standard $WO_{3\ Mart.}$ layer (1.6 mg cm^{-2}) resulted in a 22% increase in solar-driven photocurrent generation compared to pure $WO_{3\ Mart.}$ when flushing the PFC with methanol-rich vapours. When targeting photocatalytic soot degradation all layered combinations with P25 on top showed good results - similar to those of pure P25 - since the soot oxidation process is limited to the top photocatalyst layer in contact with the soot. When combining the results obtained in both experiments, a four times less dense P25 layer on top of standard $WO_{3\ Mart.}$ layer proved to be the 'best of both worlds', combining excellent photoanode performance with efficient soot degradation.

In the final part of this thesis, soot degradation during PFC operation was measured for the most promising materials from the previous experiments. A drastic decrease in soot degradation rate was seen for all studied photocatalysts when adding methanol to the photoanode feed, as a result of the excellent hole-scavenging properties of methanol. In the presence of methanol a similar result was obtained by P25 and P25 on $WO_{3\ Mart.}$ (0.4/1.6), while no soot degradation was seen for $WO_{3\ Mart}$. Finally, the in-house engineered PFC device was applied outside, evidencing autonomous PFC operation solely using sunlight and outdoor air. The best results were obtained by $WO_{3\ Mart.}$, closely followed by P25 on $WO_{3\ Mart.}$ (0.4/1.6), and with very low photocurrent generation obtained by P25. The application of a four times less dense P25 layer (0.4 mg cm^{-2}) on top of a standard $WO_{3\ Mart.}$ layer (1.6 mg cm^{-2}) thus proves promising for application in an efficient, sunlight-driven and soot-degrading waste gas-to-electricity PFC device. By extension, the configuration of a thinner layer of an efficient soot degrader on top of an excellent photoanode material offers a wide range of opportunities for future research.

Chapter 7

General conclusions and future perspective

7.1 General conclusions

Society nowadays faces a range of challenging environmental problems, including air pollution and the quest for sustainable energy sources.

The goal of this thesis was to study autonomous, all-gas phase PEC cell operation simultaneously degrading air pollution (*e.g.* VOCs, soot) and producing energy (*i.e.* H_2 gas or electricity) using (sun)light.

PEC cells have been widely studied for the purpose of wastewater treatment and water splitting, but research on gas phase operation of PEC cells is limited. Moreover, for the scarce accounts available external electrical bias is always applied. In **Chapter 2**, for the first time a proof of concept of a completely bias-free and all-gas phase PEC cell was presented, targeting simultaneous VOC degradation and H_2 gas production. Besides the commonly studied PEC cell configuration targeting H_2 gas production, PEC cells can also produce energy by generating electricity. When a PEC cell targets the degradation of waste products and pollutants at the anode (= 'fuel'), while generating electricity at the (aerobic) cathode, the PEC cell is called a photofuel cell (PFC). PFC operation is a relatively new research area and barely studied for gas phase applications. In **Chapter 3** an in-house developed low-cost waste gas-to-electricity PFC device was studied. The performance of a range of TiO_2- and WO_3-based photocatalytic photoanodes was compared. As high PM - and thus soot - concentrations are a worldwide problem, especially troubling urban areas, the ability of these studied photoanodes to cope with soot is crucial to obtain robust and long-term PFC operation. However, the limited soot oxidation detection methods present are either expensive to carry out, time-consuming and/or incomplete. To this end, in **Chapter 4** a low-cost, time-efficient, accurate and realistic soot detection methodology was presented and validated. In **Chapter 5** this methodology was applied to study the soot oxidation capacity of the in Chapter 3 studied photoanode materials. In doing so, the method presented in Chapter 4 was adapted, expanding the application range to inherently coloured (visible light active) photocatalysts. In **Chapter 6** the results of the previous chapters were combined to obtain an improved photoanode, targeting efficient, soot-degrading and sunlight-driven waste gas-to-electricity PFC operation. The following paragraphs list the most important conclusions of each chapter.

Chapter 2 served as proof of concept of an all-gas phase PEC cell simultaneously degrading VOCs at the anode and producing H_2 gas at the cathode. To achieve energy-efficient and autonomous PEC cell operation, all experiments were performed in the absence of an external bias. In liquid phase, increasing photocurrent generation was observed when increasing the methanol content of the photoanode feed, up to a 4.5-fold increase with a 5 wt% solution. When working in gas phase instead of liquid phase a further 30% increase in photocurrent generation was achieved, evidencing the potential of gas phase PEC cell operation. In gas phase the increase of the methanol content of the photoanode feed also resulted in increasing photocurrent generation, reaching a 4.5-fold increase with the highest studied methanol concentration (28 mmol m^{-3}) compared to pure water vapour. In the next part, the effect of oxygen on the PEC cell performance was studied both in aqueous and gas phase. In liquid phase, a 40% photocurrent reduction was observed when completely saturating the photoanode feed with O_2, which was attributed to the electron scavenging properties of O_2. In gas phase an important trade-off was observed when working with air instead of pure N_2. While the presence of O_2 resulted in a slight photocurrent drop (8%), infrared spectroscopy evidenced a more complete mineralisation towards CO_2 under aerobic conditions. These results again supported the suitability of PEC cells for air purification purposes. In the presence of O_2, methyl formate and dimethyl ether were detected as important intermediates. Possible reaction pathways, both under anaerobic and aerobic conditions, were proposed in this chapter. A Faradaic efficiency of 92% was determined for the studied system when working with methanol-rich gas flows. In the final part, gas phase PEC cell operation was also evidenced with ethanol and acetic acid.

In Chapter 2 the potential of an unbiased all-gas phase PEC cell, combining air purification and energy production (as H_2), was evidenced, additionally delivering increased insights into the ongoing reactions. H_2-producing PEC cells face a range of bottlenecks hindering large-scale application such as the limited H_2 infrastructure and often required additional bias to produce H_2 gas. Many of these limitations can be overcome when targeting electricity generation instead of H_2 production at the cathode, as is done in so-called photofuel cells. In **Chapter 3** the goal was to study an autonomously (*i.e.* unbiased, sunlight-

driven) operating waste gas-to-electricity PFC device, comparing TiO_2- and WO_3-based photoanode materials. The in-house engineered PFC largely consisted of the low-cost poly(methyl methacrylate) (PMMA) and was equipped with six flow channels in the anode compartment obtaining a uniform flow pattern. The partially visible light active WO_3-based photocatalysts clearly outperformed the studied TiO_2-based photocatalysts in the gas phase PFC, both under UV and simulated solar light. Both WO_3-based photocatalysts produced the highest steady state photocurrent, fuel-to-electricity conversion ($>$ 65%) and overall efficiency. The combination of the high electron mobility and visible light activity of WO_3 makes this a promising candidate for use in a sunlight-driven gas phase photofuel cell. Additionally, gas phase photocatalytic experiments were performed to allow comparison with the gas phase PFC experiments. In the direct photocatalytic experiments WO_3-based photo-catalysts were outperformed by all studied TiO_2-based photocatalysts, highlighting the difference in driving material properties between both processes. While the low surface area of WO_3 largely hindered its direct photocatalytic performance, this property seemed of lesser importance in the gas phase PFC. The high electron mobility of WO_3 on the other hand largely benefited its photoanode performance. In the final part of this chapter the scope was broadened, applying the gas phase PFC to degrade methane, ethylene and ammonia, showing the most promising results for ammonia.

Whereas Chapter 2 and 3 evidenced the potential of a PEC cell as VOC degrading device, the following two chapters focussed on another important air pollutant, namely soot. High PM, and thus soot, concentrations are a worldwide problem, especially troubling urban areas. The ability of photocatalysts to cope with soot is thus crucial when targeting robust air purifying technologies, avoiding shielding of incoming (sun)light. However, the currently available soot detection methods are either expensive, time-consuming and/or incomplete, hindering straightforward and accurate soot detection. To this end, in **Chapter 4** a low-cost, time-efficient and versatile soot detection methodology was presented, combining two complementary detection strategies. The first was obtained by improving the digital image analysis method as presented by Smits *et al.* in 2013, which uses the L* coordinate (*i.e.* brightness axis) of the CIELab colour space. In the original

method, soot degradation was quantified by the decrease of fouled pixels, categorising each pixel as either completely fouled or clean based on a single L* threshold value. As photocatalytic soot oxidation is a gradual process, the improved method used the extent of the shift of the most frequent L* value as a measure of soot degradation. The absorbance method was used to validate the improved method. An additional advantage resulting from this adaptation was the possibility to monitor different grades of soot fouling simultaneously. A more realistic, accurate and detailed method was hence obtained. The second detection strategy consisted of an *in situ* FTIR reaction cell, allowing detection of both gaseous and adsorbed reaction products during photocatalytic soot oxidation. The presented methodology was applied to a range of TiO_2- and ZnO-based photocatalysts. All studied photocatalysts produced formate-related intermediates ($CHOO^-_{(ad)}$), supporting the hypothesis of Chin *et al.* (2007) stating that soot can be oxidised either directly to CO_2 or indirect via solid intermediates. P25 (commercial TiO_2) showed to be the fastest soot degrader, both for a uniform soot haze and concentrated soot spots. The highest specificity towards complete mineralisation into CO_2 on the other hand was seen for commercial ZnO nano powder.

In Chapter 4 a realistic, accurate and all-inclusive soot detection methodology was presented and validated. In **Chapter 5** the soot oxidation capacity of the TiO_2- and WO_3-based photoanodes studied in Chapter 3 was determined using this methodology. To allow accurate detection of soot degradation when using coloured (visible light active) photocatalysts such as WO_3, an additional data processing step was added to the optical image analysis method, correcting for intrinsic photocatalyst colour changes. This allowed accurate detection of soot degradation by both TiO_2- and WO_3-based photocatalysts, hence expanding the application range of this method to inherently coloured materials. The soot oxidation capacity of the photocatalysts was studied using a range of light sources. In the UV light experiment the TiO_2-based photocatalysts clearly outperformed the WO_3-based photocatalysts, while under the visible light lamp the lab-synthesized WO_3 was more than two times faster in completely degrading a uniform soot haze compared to all studied TiO_2-based photocatalysts. Under an artificial daylight lamp two of the three studied TiO_2-based photocatalysts outperformed both WO_3-based photocatalysts for the

degradation of the soot haze, while similar results were seen for degradation of the soot spots. Interestingly, after 82 days of illumination with the low-intensity daylight lamp all studied photocatalysts achieved soot degradation, ranging between 18% and 75%, highlighting the potential of photocatalysis as energy-efficient soot abatement strategy. In the last part of this chapter the in Chapter 4 presented *in situ* FTIR reaction cell was used to determine the specificity of the studied photocatalysts towards full soot mineralisation into CO_2. It was seen that the lab-synthesized WO_3 had the highest specificity, both under UV and visible light, thus producing the least amount of (undesired) intermediates.

In the last experimental chapter of this thesis, **Chapter 6**, the results of all previous chapters were combined to produce an improved photoanode material, striving towards an efficient, soot-degrading and sunlight-driven waste gas-to-electricity PFC device. From previous chapters it could be concluded that while the partially visible light active WO_3-based photocatalysts proved efficient photoanodes for use in an all-gas phase PFC (Chapter 3), TiO_2-based photocatalysts in general had the highest soot oxidation capacity (Chapter 5). As a result, the best performing TiO_2- and WO_3-based photo-catalysts from previous chapters were selected to be combined, either by physical mixing or by layering of both photocatalysts. To this end, the commercial TiO_2 P25 and the WO_3 synthesized according to Martinez *et al.* were further used in this chapter. The soot oxidation capacity and photoanode performance of a range of combinations were determined. A four times less dense P25 layer (0.4 mg cm^{-2}) on top of standard layer of the lab-synthesized WO_3 (1.6 mg cm^{-2}) proved to be 'the best of both worlds', as it expressed the beneficial properties of both photocatalysts. In this way, the high soot oxidation capacity of P25 was combined with the excellent photoanode performance and visible light activity of the lab-synthesized WO_3. Next, the ability of this combined photocatalyst and both pure photocatalysts to degrade soot during PFC operation was studied. In the presence of a hole scavenger such as methanol a drastic decrease in the soot oxidation rate was seen for all studied photocatalysts. Pure P25 and the combined photocatalyst showed similar soot degradation rates in the PFC device when flushed with methanol-rich vapours, while no soot degradation was achieved by pure WO_3. In the last part of this

thesis the in-house engineered PFC device was applied outside, evidencing autonomous operation using solely sunlight and outdoor air to sustainably generate electricity. The highest photocurrents were generated by pure WO_3, closely followed by the combined photocatalyst, and with only very low photocurrent generation obtained by pure P25. To summarise, Chapter 6 showed that when applying a photoanode consisting of a thinner P25 layer on top of a standard WO_3 layer in an all-gas phase PFC device, it retains the excellent photoanode properties of WO_3 - even when using outdoor air - additionally exploiting its visible light activity, while also achieving the high soot oxidation capacity of P25.

In short, to ensure long-term and sustainable operation of an all-gas phase PEC device, the ability of the photoanode material to cope with soot is crucial as high soot concentrations are encountered worldwide. Therefore, this thesis focussed on two different research areas, studying both gas phase PEC cell operation and photocatalytic soot degradation. This has led to important practical results in each of the respective research fields, with the development of a low-cost and widely applicable PEC cell on one hand and the presentation of an accurate, versatile and complete soot detection methodology on the other hand. In addition, for both processes insight into the reaction pathways and key material properties was gained. In the quest for an efficient, soot-degrading and sunlight-driven waste gas-to-electricity PFC device a four times less dense P25 layer (0.4 mg cm^{-2}) on top of standard $WO_{3\ Mart.}$ layer (1.6 mg cm^{-2}) was able to combine the high soot oxidation capacity of TiO_2 with the excellent photoanode properties of WO_3. By extension, this configuration - adding a thinner layer of an efficient soot degrader on top of an excellent photoanode material - opens a range of possibilities for future research.

7.2 Future perspective

Along with the results and insights that are obtained in over four years of research on this thesis, a lot of additional questions and new research opportunities arose. Therefore, the most interesting opportunities will briefly be discussed here.

7.2.1 Photoanode optimisation

In this work TiO_2- and WO_3-based photocatalysts were thoroughly investigated in both the context of gas phase PEC cell operation and photocatalytic soot oxidation, resulting in the presentation of a promising photoanode material in Chapter 6. This configuration of a thinner layer of an efficient soot degrader (*i.e.* TiO_2) on top of an excellent photoanode material (*i.e.* WO_3) can be extended to other photocatalysts. To this end, the experiments as presented in Chapter 3 and 5 of this thesis can be repeated with a range of promising photocatalysts (*e.g.* SnO_2, Fe_2O_3, $BiVO_4$),[119] targeting further enhanced photoanode performance. Additionally, a more in-depth characterisation of the studied materials would be interesting (*e.g.* electron mobility, exact position of conduction and valence band). This would allow further optimisation of the selected photoanodes as the materials could be altered aiming at enhancement of specific properties.

As the final goal is to autonomously operate the PEC cell, the ability of the photocatalysts to operate under sunlight is crucial. Promising results were already observed in this thesis under artificial daylight, simulated solar light and actual sunlight, but the fraction of sunlight that can be used by both TiO_2 and WO_3 is limited by their relatively large band gaps. In our research group a possible solution for this limitation is studied, using a phenomenon called surface plasmon resonance (SPR). Gold and silver can for example be added to TiO_2, allowing it to use a larger fraction of the solar spectrum. Promising results were already obtained in preliminary experiments performed by Fons Dingenen as part of a master thesis. In these experiments enhanced visible light activity was observed when adding a gold-silver mixture to a P25 photoanode. It would be interesting to further study the possibilities of combining these two research areas, applying the in our research group obtained fundamental insights on SPR to achieve enhanced sunlight-driven PEC cell performance in real-life applications.

In Chapter 3 the performance of the PEC cell was studied using a range of methanol concentrations. Additionally, in subsequent experiments the soot loading could be altered, ranging between values encountered in real-life applications. The experiments could also be extended to other waste gases and

pollutants, as briefly done in Chapter 2 and 3, eventually allowing to select the optimal photoanode material for each specific situation (*e.g.* low VOC concentration and high soot loading).

7.2.2 Recirculation setup

In Chapter 2 possible reaction pathways were proposed, both for aerobic and anaerobic conditions, by coupling the anode compartment of a PEC cell to an FTIR detection cell. The low volume of the anode compartment (0.4 cm^3), however, results in fast transport of the inlet gases through the photoanode compartment. Using a CFD model made with COMSOL Multiphysics (by Jelle Roegiers) the residence time of the gases in the anode compartment was estimated to be 0.4 s, largely hindering accurate detection and quantification of reaction products formed during PEC cell operation. To allow detailed monitoring of the ongoing reactions during PEC cell operation, a recirculation setup was built during this thesis, with the help of a master student, Thomas Theys, as shown in Figure 7.1. Two buffer volumes were added (35.5 cm^3 each) to ensure a uniform composition of the inlet feed before sending it through the anode compartment of the PEC cell. To this end, the setup can be operated in bypass mode. VOCs or other targeted compounds can be added either through a septum in the buffer volume or via the gas setup present in our lab. Detection can be performed by either sampling from a buffer volume (*i.e.* GC) or by sending the gases to an FTIR detector. Currently the setup is not operational yet, as the purchased diaphragm pump (NMP03KPDC-M, KNF Verder) is not sufficiently airtight. A possible solution could be to confine the pump in an airtight casing.

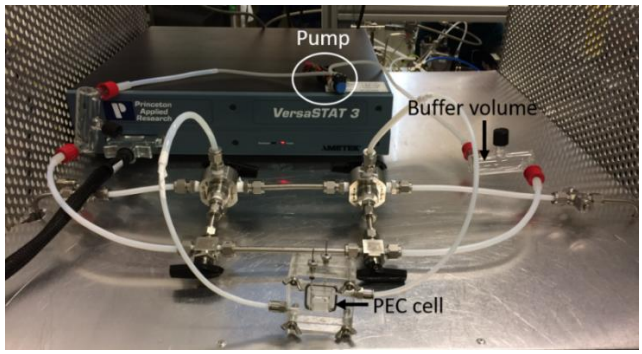

Figure 7.1. Preliminary recirculation setup.

When operational, the recirculation setup allows to greatly increase the residence time of the gases in the PEC cell by pumping the gases through the cell for a prolonged period of time before sending them to a detection unit. This is crucial to further elucidate the reaction pathways occurring during PEC cell operation. To the best of our knowledge, no research has been performed on the effect of soot on PEC cell performance. A recirculation setup might provide insight on the soot degradation pathways in a PEC cell, and on the other hand the effect of the presence of soot on the VOC mineralisation pathway. Additionally, in view of specific applications, this setup can be used to study a wide range of waste gases/pollutants and gas mixtures.

7.2.3 Upscaling

In the final part of this thesis the autonomous operation of the in-house engineered PFC device was evidenced, achieving electricity generation solely using sunlight and outdoor air as energy input. The photocurrents that were generated are still quite low. Optimisation of the different materials used for the production of the MEA (*e.g.* Nafion®, carbon paper) was outside the scope of this thesis but is indispensable when targeting large-scale application. It should be highlighted that photofuel cells are still a relatively new research area and barely studied in gas phase. As upscaling of the PEC cell technology remains a challenging topic, persistent research is required before large-scale applications can become widespread.

7.2.4 Towards application

7.2.4.1 NH_3 reduction: agriculture

This work could serve as the base for application of a solar driven PFC device for the abatement of NH_3 emissions in agriculture. Section 3.3.4 presented the first promising results for application of the in-house engineered PFC device on ammonia contaminated waste streams. All over Europe nitrogen emissions caused by agricultural activities create a huge challenge for the Natura 2000 habitat guidelines.[201] Application of the device on the exhaust of stables housing pigs could remove the on-site generated NH_3 emissions and simultaneously generate a small amount of electricity, for instance to drive the ventilation system. The low-cost and autonomous nature of the device make it

an easy and widely applicable technology. The previously described experiments can be applied to increase insights into the performance of the technology for NH_3-contaminated feed prior to large-scale application.

7.2.4.2 CH_4 reduction: methane slip and agriculture

Methane is an important greenhouse gas, with a 28 times higher global warming potential than CO_2. It accounts for 16% of the enhanced greenhouse effect, which emphasizes the need to control methane emissions.[202]

Due to increasing emission regulations, a shift is being made towards cleaner fossil fuels, resulting in the implementation of liquefied natural gas (LNG) in a range of highly polluting sectors such as the shipping industry. Utilisation, transport, and storage of LNG are accompanied by significant methane leakages, called 'methane slip'.[17] The autonomous nature of the PEC cell makes it a suitable technology for application on board of large vessels. As seen in Section 3.3.4, the current PEC cell is not yet optimised towards methane degradation and further research is required, studying other photocatalysts and operating conditions, to increase the performance of the PEC cell towards methane conversion.

In addition, the livestock farming sector is responsible for around 35% of the anthropogenic methane emissions, thus also providing large opportunities for methane reduction.[202] By implementing PEC cells to treat the exhaust gases of livestock housing, NH_3 and CH_4 emissions could simultaneously be targeted (see Section 7.2.4.1).

7.2.4.3 Pollution sensors

Another interesting opportunity could be to operate autonomous PFCs to drive pollution sensors. It is known that we spend most of our time indoor ($\sim$ 90%), where VOC concentrations often (greatly) exceed outdoor concentrations. High indoor VOC concentrations are known to cause a range of detrimental health effects, gathered under the sick building syndrome (SBS).[6,7] It would therefore be useful to implement a PFC that allows simultaneous degradation and monitoring of these compounds. The electricity produced by degradation of indoor VOCs could be used to drive a range of coloured LED lamps, indicating the level of pollution. This technology could be broadly applied (*e.g.* class rooms, office spaces, living spaces) simultaneously purifying indoor air and

raising awareness regarding indoor air quality, for example suggesting ventilation when exceeding a certain pollution level. To apply the PFC for indoor applications it is crucial that the photoanode is active under the present indoor light source. To this end, light utilisation by the PFC should first be optimised to obtain efficient visible light absorption (*e.g.* efficient small band gap photocatalyst (combinations), SPR).

Appendix – curriculum vitae

PERSONAL INFORMATION

Name	Myrthe Van Hal
Date of birth	August 27th, 1993
Place of birth	Edegem
Nationality	Belgian
e-mail (private)	myrthe_vanhal@hotmail.com
Mobile phone	+32479/31.95.12

EDUCATION

2016 - 2021	PhD in Bioscience Engineering (UAntwerp) "Photo(electro)catalytic air purification and soot degradation with simultaneous energy recovery"
2014 - 2016	Master in Bioscience Engineering: Environmental Technology (UGent) Minor: Environmental Co-ordination
2011 - 2014	Bachelor in Bioscience Engineering: Environmental Technology (UAntwerp)

PUBLICATIONS

- Fons Dingenen, Natan Blommaerts, **Myrthe Van Hal**, Rituraj Borah, Daniel Arenas Esteban, Silvia Lenaerts, Sara Bals, Sammy W. Verbruggen, *Layer-by-Layer stabilized plasmonic gold-silver nanoparticles on TiO_2: towards stable solar active photocatalysts*, Nanomaterials 11 (2021), 2624. https://doi.org/10.3390/nano11102624.

- **Myrthe Van Hal**, Rui Campos, Silvia Lenaerts, Karolien De Wael, and Sammy W. Verbruggen, *Gas phase photofuel cell consisting of WO_3- and TiO_2-photoanodes and an air-exposed cathode for simultaneous air purification and electricity generation*, Applied Catalysis B: Environmental 292 (2021), 120204. https://doi.org/10.1016/j.apcatb.2021.120204.

- **Myrthe Van Hal**, Sammy W. Verbruggen, Xiao-Yu Yang, Silvia Lenaerts, Tom Tytgat, *Image analysis and in situ FTIR as complementary detection tools for photocatalytic soot oxidation*. Chemical Engineering Journal. 367 (2019), p. 269-277. https://doi.org/10.1016/j.cej.2019.02.154.

- Sammy W. Verbruggen, **Myrthe Van Hal**, Tom Bosserez, Jan Rongé, Birger Hauchecorne, Johan A. Martens, and Silvia Lenaerts, *Harvesting hydrogen gas from air pollutants with an unbiased gas phase photoelectrochemical cell*, ChemSusChem. 10 (2017), p. 1413-1418. http://doi.org/10.1002/cssc.201601806.

SUBMITTED PUBLICATIONS

- **Myrthe Van Hal**, Silvia Lenaerts, Sammy W. Verbruggen, *Photocatalytic soot degradation under UV and visible light.* Submitted to Environmental Science and Pollution Research on the 2nd of July 2021.

CONFERENCE CONTRIBUTIONS

Oral presentations

- M. Van Hal, R. Campos, K. De Wael, S. Lenaerts, S. W. Verbruggen. *Waste gas-to-electricity conversion using a robust and low-cost photofuel cell*. 22th Netherlands Catalysis and Chemistry Conference (NCCC), online conference (01/03/2021)

- M. Van Hal, S. W. Verbruggen, X-Y. Yang, S. Lenaerts, T. Tytgat. *Soot oxidation detection methods: presentation of two complementary straighforward techniques.* The 4th International Conference on New Photocatalytic Materials for Environment, Energy and Sustainability (NPM-4), Antwerp- Belgium, (23/04/201 – 25/04/2019)

- M. Van Hal, T. Bosserez, J. Rongé, J.A. Martens, S. Lenaerts, S.W. Verbruggen. *Harvesting energy from air pollution with an un-biased gas phase photoelectrochemical cell.* Chemistry Conference for Young Scientists (Chemcys), Blankeberge, België (21/02/2018 – 23/02/2018)

- M. Van Hal, T. Bosserez, J. Rongé, J. A. Martens, S. Lenaerts, S. W. Verbruggen. *Harvesting energy from air pollution with an un-biased gas phase photo-electrochemical cell.* 5th European Conference on Environmental Applications of Advanced Oxidation Processes (EAAOP5), Prague - Czech Republic (25/6/2017 – 29/6/2017). **Top 12 finalist**

Poster presentations

- M. Van Hal, S. W. Verbruggen, X-Y. Yang, S. Lenaerts, T. Tytgat. *Soot oxidation detection methods: presentation of two complementary straightforward techniques.* 21th Netherlands Catalysis and Chemistry Conference (NCCC), Noordwijkerhout - the Netherlands (02/03/2020 – 04/03/2020)

- M. Van Hal, S. W. Verbruggen, X-Y. Yang, S. Lenaerts, T. Tytgat. *Soot oxidation detection methods: presentation of two complementary straighforward techniques.* 23nd National Symposium on Applied Biological Sciences (NSABS). Ghent, Belgium (04/02/2019)

- M. Van Hal, T. Bosserez, J. Rongé, J.A. Martens, S. Lenaerts, S. W. Verbruggen. *Harvesting energy from air pollution with an un-biased gas phase photoelectrochemical cell.* 19th Netherlands Catalysis and Chemistry Conference (NCCC), Noordwijkerhout - the Netherlands (05/03/2018 – 07/03/2018)

- M. Van Hal, T. Bosserez, J. Rongé, J. A. Martens, S. Lenaerts, S. W. Verbruggen. *Harvesting energy from air pollution with an un-biased gas phase photo-electrochemical cell.* 5th European Conference on Environmental Applications of Advanced Oxidation Processes (EAAOP5), Prague - Czech Republic (25/6/2017 – 29/6/2017)

- M. Van Hal, T. Bosserez, J. Rongé, J. A. Martens, S. Lenaerts, S. W. Verbruggen. *Harvesting energy from air pollution with an un-biased gas phase photo-electrochemical cell.* MELiSSA mini-symposium & master class, Antwerp - Belgium (30/03/2017)

- M. Van Hal, T. Bosserez, J. Rongé, J. A. Martens, S. Lenaerts, S. W. Verbruggen. *Harvesting energy from air pollution with an un-biased gas phase photo-electrochemical cell.* 18th Netherlands Catalysis and Chemistry Conference (NCCC), Noordwijkerhout - the Netherlands (06/03/2017 – 08/03/2017)

- M. Van Hal, T. Bosserez, J. Rongé, J. A. Martens, S. Lenaerts, S. W. Verbruggen. *Harvesting energy from air pollution with an un-biased gas phase photo-electrochemical cell.* 22nd National Symposium on Applied Biological Sciences (NSABS). Leuven, Belgium (07/02/2017)

RESERACH VISIT

One-month research stay (30/07/2018 – 24/08/2018) at Wuhan University of Technology (China) at the lab of professor Xiao-Yu Yang (State Key Lab of Advanced Technology for Materials Synthesis and Processing) based on the FWO-NSFC international cooperation project "*Hierarchically fractal photocatalysts for indoor VOCs elimination*" (Project No. 21711530705)

SUPERVISION OF BACHELOR PROJECTS

- Ruben Lemmens, Sam Vermeiren, University of Antwerp (2019-2020) *Vergelijking tussen fotokatalytische roetafbraak door TiO_2 en WO_3 met behulp van digital image analyse en in situ FTIR*

- Stefaan Borghgraef, Joppe Brosens, Marine Van der Voordt, University of Antwerp (2018-2019)

Simultane foto-elektrochemische luchtzuivering en waterstofproductie

- Robbe Elzas, University of Antwerp: cooperation Bioscience engineering and Applied engineering (2017-2018)
  Exploring the Use of a Photo-Electrochemical Cell as an Energy Source for Wireless Sensor Nodes

- Daan Van Havere, Sophie De Ridder, Cedric De Coninck, University of Antwerp (2017-2018)
  Foto-anode materiaalselectie voor foto-elektrochemische luchtzuivering en waterstofproductie

- Robin Lowet, IMDO - University of Antwerp: Bridging programme Environmental science (2016-2017)
  Antropogene methaanemissies in de Europese Unie en in Vlaanderen

- Jeroen Pattyn, Mussie Zewede, Erdem Ince, University of Antwerp (2016-2017)
  Waterstofproductie door foto-elektrochemische afbraak van methaanafval

SUPERVISION OF MASTER THESES

- Thomas Theys, KU Leuven (2019-2020)
  Photo-electrochemical energy recovery out of polluted air - a model approach

- Fons Dingenen, KU Leuven (2018-2019)
  Plasmon-versterkte foto-elektrochemische cellen voor luchtzuivering en simultane energierecuperatie

- Yanaika Denoyelle, KU Leuven (2017-2018)
  Energie uit methaanafval: parameterstudie van een foto-elektrochemische cel

Bibliography

1. WHO. *Economic cost of the health impact of air pollution in Europe*. (2015).

2. World Health Organisation. *Ambient air pollution: a global assessment of exposure and burden of disease*. (2016).

3. United Nations. *Transforming our world: the 2030 agenda for sustainable development*. (2015).

4. Jones, A. P. Indoor air quality and health. *Atmospheric Environment* **33**, 4535–4564 (1999).

5. Jia, C., Stuart, B. & Godwin, C. VOCs in industrial, urban and suburban neighborhoods — Part 2 : Factors affecting indoor and outdoor concentrations. *Atmospheric Environment* **42**, 2101–2116 (2008).

6. Jia, C., Stuart, B. & Godwin, C. VOCs in industrial, urban and suburban neighborhoods , Part 1 : Indoor and outdoor concentrations, variation, and risk drivers. *Atmospheric Environment* **42**, 2083–2100 (2008).

7. U.S. Environmental Protection Agency. *Exposure Factors Handbook 2011 Edition (Final Report)*. (2011).

8. Nakaoka, H. *et al.* Correlating the symptoms of sick-building syndrome to indoor VOCs concentration levels and odour. *Indoor and Built Environment* **23**, 804–813 (2014).

9. EPA. *Photochemical smog: what it means for us*. (2004).

10. Vogiatzis, K. Environmental noise and air pollution monitoring in the athens ring road ('attiki odos') an important parameter for a sustainable urban development. *International Journal of Sustainable Development and Planning* **10**, 528–543 (2015).

11. Saltveit, M. E. Effect of ethylene on quality of fresh fruits and vegetables. *Postharvest biology and technology* **15**, 279–292 (1999).

12. Basso, A., Fátima, R. De, Muniz, P. & José, H. J. Effect of operational conditions on photocatalytic ethylene degradation applied to control tomato ripening. *Journal of Photochemistry & Photobiology A: Chemistry* **367**, 294–301 (2018).

13. Liu, X. *et al.* Synthesis of a WO3 photocatalyst with high photocatalytic activity and stability using synergetic internal Fe 3+ doping and superficial Pt loading for ethylene degradation under visible-light irradiation. *Catalysis Science and Technology* **9**, 652–658 (2019).

14. European Environment Agency (EEA). *Atmospheric greenhouse gas concentrations*. (2019).

15. Wuebbles, D. J. & Hayhoe, K. Atmospheric methane and global change. *earth-science reviews* **57**, 177–210 (2002).

16. Saunois, M. *et al.* The Global Methane Budget: 2000-2012. *Earth System Science Data Discussions* **8**, 1–79 (2016).

17. European Commission DG. *Science for environmental policy: environment news alert service*. vol. 49 (2015).

18. Behera, S. N., Sharma, M., Aneja, V. P. & Balasubramanian, R. Ammonia in the atmosphere: A review on emission sources, atmospheric chemistry and deposition on terrestrial bodies. *Environmental Science and Pollution Research* **20**, 8092–8131 (2013).

19. Trierweiler, J. F. & Bishop, B. L. Estimated NH3-volatilization losses from surface-applied urea on a wet calcareous Vertisol. *Fertilizer Research* **4**, 271–280 (1983).

20. Sutton, M. A., Willem, J., Dentener, F. & Mo, D. Ammonia in the environment: From ancient times to the present. *Environmental pollution* **156**, 583–604 (2008).

21. EU. *Richtlijn 1999/13/EG*. (1999).

22. Blommaerts, N. *et al.* Ultrafast screening of commercial sorbent materials for VOC adsorption using real-time FTIR spectroscopy. *Separation and Purification Technology* **207**, 284–290 (2018).

23. Detchanamurthy, S. & Gostomski, P. A. Biofiltration for treating VOCs: an overview. *Reviews in Environmental Science and Bio/Technology* **11**, 231–241 (2012).

24. Twigg, M. V. Catalytic control of emissions from cars. *Catalysis Today* **163**, 33–41 (2011).

25. Batuira, M. *et al.* Science of the Total Environment Ozonation and ozone-enhanced photocatalysis for VOC removal from air streams : Process optimization , synergy and mechanism assessment. *Science of the Total Environment* **687**, 1357–1368 (2019).

26. Blommaerts, N. *et al.* Gas phase photocatalytic spiral reactor for fast and efficient pollutant degradation. *Chemical Engineering Journal* **316**, 850–856 (2017).

27. Verbruggen, S. W. TiO2 photocatalysis for the degradation of pollutants in gas phase: From morphological design to plasmonic enhancement. *Journal of Photochemistry and Photobiology C: Photochemistry Reviews* **24**, 64–82 (2015).

28. Verbruggen, S. W. *et al.* Harvesting hydrogen gas from air pollutants with an un-biased gas phase photo-electrochemical cell. *ChemSusChem* **10**, 1413–1418 (2017).

29. Arseneault, M. H. & Cline, J. A. A review of apple preharvest fruit drop and practices for horticultural management. *Scientia Horticulturae* **211**, 40–52 (2016).

30. Tytgat, T. *et al.* Photocatalytic process optimisation for ethylene oxidation. *Chemical Engineering Journal* **209**, 494–500 (2012).

31. Ye, S. ying, Tian, Q. mei, Song, X. liang & Luo, S. can. Photoelectrocatalytic degradation of ethylene by a combination of TiO2 and activated carbon felts. *Journal of Photochemistry and Photobiology A: Chemistry* **208**, 27–35 (2010).

32. Ye, S. Y., Zheng, S. H., Song, X. L. & Luo, S. C. Photoelectrocatalytic decomposition of ethylene using TiO2/activated carbon fiber electrode with applied pulsed direct current square-wave potential. *Applied Surface Science* **341**, 61–68 (2015).

33. Chen, X. *et al.* Photocatalytic oxidation of methane over silver decorated zinc oxide nanocatalysts. *Nature Communications* **7**, 12273 (2016).

34. Li, W. *et al.* Selective CO Production by Photoelectrochemical Methane Oxidation on TiO2. *ACS Central Science* **4**, 631–637 (2018).

35. Rockafellow, E. M., Koziel, J. A. & Jenks, W. S. Laboratory-scale investigation of UV treatment of ammonia for livestock and poultry barn exhaust applications. *Journal of Environmental Quality* **41**, 281–288 (2012).

36. Hadlocon, L. J. S., Manuzon, R. B. & Zhao, L. Development and evaluation of a full-scale spray scrubber for ammonia recovery and production of nitrogen fertilizer at poultry facilities. *Environmental Technology (United Kingdom)* **36**, 405–416 (2015).

37. van der Heyden, C., Solon, K., Demeyer, P. & Volcke, E. I. P. Model-based evaluation of ammonia removal in biological air scrubbers. *Biosystems Engineering* **191**, 85–95 (2020).

38. Geng, Q., Guo, Q., Cao, C., Zhang, Y. & Wang, L. Investigation into Photocatalytic Degradation of Gaseous Ammonia in CPCR. *Ind. Eng. Chem. Res.* **47**, 4363–4368 (2008).

39. Yamazoe, S., Okumura, T. & Tanaka, T. Photo-oxidation of NH3 over various TiO2. *Catalysis Today* **120**, 220–225 (2007).

40. Zhang, S., Liang, K. & Tan, Y. Dynamics study of TiO2 semiconductor photoelectrode by EIS in the ammonia degradation. *Advanced Materials Research* **183–185**, 2192–2196 (2011).

41. Xiao, S., Qu, J., Zhao, X., Liu, H. & Wan, D. Electrochemical process combined with UV light irradiation for synergistic degradation of ammonia in chloride-containing solutions. *Water Research* **43**, 1432–1440 (2009).

42. Kropp, R. *et al.* A device that converts aqueous ammonia into nitrogen gas. *Aquacultural Engineering* **41**, 28–34 (2009).

43. Kaneko, M. *et al.* Photoelectrochemical reaction of biomass and bio-related compounds with nanoporous TiO2 film photoanode and O2-reducing cathode. *Electrochemistry Communications* **8**, 336–340 (2006).

44. Ji, Y. *et al.* Highly selective transformation of ammonia nitrogen to N2 based on a novel solar-driven photoelectrocatalytic-chlorine radical reactions system. *Water Research* **125**, 512–519 (2017).

45. Antoniadou, M. & Lianos, P. Photoelectrochemical oxidation of organic substances over nanocrystalline titania: Optimization of the photoelectrochemical cell. *Catalysis today* **144**, 166–171 (2009).

46. EEA. *Air quality in Europe — 2016 report*. (2016).

47. van Donkelaar, A. *et al.* Global estimates of ambient fine particulate matter concentrations from satellite-based aerosol optical depth: Development and application. *Environmental Health Perspectives* **118**, 847–855 (2010).

48. Mukherjee, A. & Agrawal, M. World air particulate matter: sources, distribution and health effects. *Environmental Chemistry Letters* **15**, 283–309 (2017).

49. Kennedy, I. M. The health effects of combustion-generated aerosols. *Proceedings of the Combustion Institute* **31 II**, 2757–2770 (2007).

50. Kampa, M. & Castanas, E. Health effects of air pollution. *Environmental pollution* **151**, 362–367 (2008).

51. Maury, A. & De Belie, N. State of the art of TiO2 containing cementitious materials: self-cleaning properties. *Materiales de Construcción* **60**, 33–50 (2010).

52. Lighty, J. S. *et al.* Combustion Aerosols: Factors Governing Their Size and Composition and Implications to Human Health Combustion. *Journal of the air and waste management association* **50**, 1565–1618 (2000).

53. EU. Richtlijn 2008/50/EG. 1–44 (2008).

54. Weinbruch, S. *et al.* Source identification of individual soot agglomerates in Arctic air by transmission electron microscopy. *Atmospheric Environment* **172**, 47–54 (2018).

55. The European Commission. *Commission regulation (EU) 2018/1832*. (2018).

56. IPCC Panel. Climate Change 2014: Synthesis Report. 1–151 (2014).

57. Brussels. Affected vehicles. https://www.lez.brussels/en/content/affected-vehicles.

58. Kousoulidou, M., Ntziachristos, L., Mellios, G. & Samaras, Z. Road-transport emission projections to 2020 in European urban environments. *Atmospheric Environment* **42**, 7465–7475 (2008).

59. Dhal, G. C., Mohan, D. & Prasad, R. Preparation and application of effective different catalysts for simultaneous control of diesel soot and NOx emissions: an overview. *Catalysis science & technology* **7**, 1803–1825 (2017).

60. Duprez, L. *EVALUATION DE LA ZONE DE BASSES EMISSIONS RAPPORT 2018*. (2018).

61. Peeters, H. *et al.* Plasmonic gold-embedded TiO2 thin films as photocatalytic self-cleaning coatings. *Applied Catalysis B: Environmental* **267**, (2020).

62. Segundo, I. G. da R. *et al.* Photocatalytic asphalt pavement: the physicochemical and rheological impact of TiO2 nano / microparticles and ZnO microparticles onto the bitumen. *Road material and pavement design* **20**, 1452–1467 (2018).

63. International Energy Agency. Key World Statistic 2017. 97 (2017).

64. United Nations. Energy Statistics Pocketbook. (2015).

65. E3MLab/ICCS National Technical University of Athens. *PRIMES model*. (2014).

66. BP. *BP Report*. *Statistical Review of World Energy* vol. 4 (2019).

67. Ehsan, S. & Wahid, M. A. Hydrogen production from renewable and sustainable energy resources: Promising green energy carrier for clean development. *Renewable and Sustainable Energy Reviews* **57**, 850–866 (2016).

68. Rocheleau, R. E. & Miller, E. L. Engineering production of hydrogen: loss analysis. *Int. J. Hydrogen Energy* **22**, 771–782 (1997).

69. Carp, O., Huisman, C. L. & Reller, A. Photoinduced reactivity of titanium dioxide. *Progress in solid state chemistry* **32**, 33–177 (2004).

70. Nakata, K. & Fujishima, A. TiO 2 photocatalysis: Design and applications. *Journal of Photochemistry and Photobiology C: Photochemistry Reviews* **13**, 169–189 (2012).

71. Jenkin, E. & Pilling, J. The tropospheric degradation of volatile organic compounds: a protocol for mechanism development. *Atmospheric environment* **31**, 81–104 (1997).

72. Jarandehei, A., Golpayegani, M. K. & Visscher, A. De. Kinetic modeling of photocatalytic degradation reactions : Effect of charge trapping. *Applied Catalysis B, Environmental* **84**, 65–74 (2008).

73. Serpone, N. Relative photonic efficiencies and quantum yields in heterogeneous photocatalysis. *Journal of Photochemistry and Photobiology, A: Chemistry* **104**, 1–12 (1997).

74. Nandjou, F. & Haussener, S. Degradation in photoelectrochemical devices: Review with an illustrative case study. *Journal of Physics D: Applied Physics* **50**, (2017).

75. Keulemans, M., Verbruggen, S. W., Hauchecorne, B., Martens, J. A. & Lenaerts, S. Activity versus selectivity in photocatalysis: Morphological or electronic properties tipping the scale. *Journal of Catalysis* **344**, 221–228 (2016).

76. Shakeel, M. *et al.* Toxicity of Nano-Titanium Dioxide (TiO2-NP) Through Various Routes of Exposure: a Review. *Biological Trace Element Research* **172**, 1–36 (2016).

77. European food safety authority. Titanium dioxide: E171 no longer considered safe when used as a food additive. https://www.efsa.europa.eu/en/news/titanium-dioxide-e171-no-longer-considered-safe-when-used-food-additive.

78. Dong, P., Hou, G., Xi, X., Shao, R. & Dong, F. WO3-based photocatalysts: morphology control, activity enhancement and multifunctional applications. *Environmental Science: Nano* **4**, 539–557 (2017).

79. Martínez, D. S. & Cuéllar, E. L. Synthesis and characterization of WO3 nanoparticles prepared by the precipitation method: Evaluation of photocatalytic activity under vis-irradiation. *Solid State Sciences* **12**, 88–94 (2010).

80. Georgieva, J. TiO2/WO3 photoanodes with enhanced photocatalytic activity for air treatment in a polymer electrolyte cell. *Journal of Solid State Electrochemistry* **16**, 1111–1119 (2012).

81. Alberici, R. M., Mendes, M. A., Jardim, W. F. & Eberlin, M. N. Mass spectrometry on-line monitoring and MS2 product characterization of TiO2/UV photocatalytic degradation of chlorinated volatile organic compounds. *Journal of the American Society for Mass Spectrometry* **9**, 1321–1327 (1998).

82. Dibble, L. A. & Raupp, G. B. Kinetics of the gas-solid heterogeneous photocatalytic oxidation of trichloroethylene by near UV illuminated titanium dioxide. *Catalysis Letters* **4**, 345–354 (1990).

83. Shah, K. W. & Li, W. A review on catalytic nanomaterials for volatile organic compounds VOC removal and their applications for healthy buildings. *Nanomaterials* **9**, (2019).

84. Boonen, E. & Beeldens, A. Recent photocatalytic applications for air purification in Belgium. *Coatings* **4**, 553–573 (2014).

85. Li, L. *et al.* Novel Synthesis of a High-Performance Pt/ZnO/SiC Filter for the Oxidation of Toluene. *Industrial and Engineering Chemistry Research* **56**, 13857–13865 (2017).

86. van Walsem, J., Roegiers, J., Modde, B., Lenaerts, S. & Denys, S. Integration of a photocatalytic multi-tube reactor for indoor air purification in HVAC systems: a feasibility study. *Environmental Science and Pollution Research* **25**, 18015–18026 (2018).

87. Georgieva, J., Armyanov, S., Poulios, I. & Sotiropoulos, S. An all-solid photoelectrochemical cell for the photooxidation of organic vapours under ultraviolet and visible light illumination. *Electrochemistry Communications* **11**, 1643–1646 (2009).

88. Lee, M. C. & Choi, W. Solid phase photocatalytic reaction on the Soot/TiO2 interface: The role of migrating OH radicals. *Journal of Physical Chemistry B* **106**, 11818–11822 (2002).

89. Lee, S. K., McIntyre, S. & Mills, A. Visible illustration of the direct, lateral and remote photocatalytic destruction of soot by titania. *Journal of Photochemistry and Photobiology A: Chemistry* **162**, 203–206 (2004).

90. Mills, A., Wang, J. & Crow, M. Photocatalytic oxidation of soot by P25 TiO2 films. *Chemosphere* **64**, 1032–1035 (2006).

91. Chin, P., Roberts, G. W. & Ollis, D. F. Kinetic Modeling of Photocatalyzed Soot Oxidation on Titanium Dioxide Thin Films. *Industrial & Engineering Chemistry Research* **46**, 7598–7604 (2007).

92. Smits, M. *et al.* Photocatalytic degradation of soot deposition: Self-cleaning effect on titanium dioxide coated cementitious materials. *Chemical Engineering Journal* **222**, 411–418 (2013).

93. Smits, M., Huygh, D., Craeye, B. & Lenaerts, S. Effect of process parameters on the photocatalytic soot degradation on self-cleaning cementitious materials. *Catalysis Today* **230**, 250–255 (2014).

94. Liao, L. *et al.* Photocatalytic carbon oxidation with nitric oxide. *Applied Catalysis B: Environmental* **166–167**, 374–380 (2015).

95. Liao, L. *et al.* Photocatalysis assisted simultaneous carbon oxidation and NOx reduction. *Applied Catalysis B: Environmental* **202**, 381–387 (2017).

96. Pacheco-Torgal, F. *et al.* Photocatalytic applications. in *Nanotechnology in eco-efficient construction: materials, processes and applications* 525–703.

97. Chin, P., Grant, C. S. & Ollis, D. F. Quantitative photocatalyzed soot oxidation on titanium dioxide. *Applied Catalysis B: Environmental* **87**, 220–229 (2009).

98. Bassou, B., Guilhaume, N., Lombaert, K., Mirodatos, C. & Bianchi, D. Experimental microkinetic approach of the catalytic oxidation of diesel soot by ceria using temperature-programmed experiments. Part 2: Kinetic modeling of the impact of the ceria/soot contacts on the rate of oxidation. *Energy and Fuels* **24**, 4781–4792 (2010).

99. Smits, M., Ling, Y., Lenaerts, S. & Van Doorslaer, S. Photocatalytic removal of soot: Unravelling of the reaction mechanism by EPR and in situ FTIR spectroscopy. *ChemPhysChem* **13**, 4251–4257 (2012).

100. Ruot, B., Plassais, A., Olive, F., Guillot, L. & Bonafous, L. TiO2-containing cement pastes and mortars: Measurements of the photocatalytic efficiency using a rhodamine B-based colourimetric test. *Solar Energy* **83**, 1794–1801 (2009).

101. Li, R. & Li, C. *Photocatalytic Water Splitting on Semiconductor-Based Photocatalysts*. *Advances in Catalysis* vol. 60 (Elsevier Inc., 2017).

102. Fujishima, A., & Honda, K. Electrochemical Photolysis of Water at a Semiconductor Electrode. *Nature* **238**, 37–38 (1972).

103. Kawai, T. & Sakata, T. Conversion of carbohydrate into hydrogen fuel by a photocatalytic process. *Nature* **286**, 474–476 (1980).

104. Hashimoto, K., Irie, H. & Fujishima, A. Invited Review Paper TiO 2 Photocatalysis: A Historical Overview and Future Prospects. *Japanese Journal of Applied Physics* **44**, 8269–8285 (2005).

105. Liao, C. H., Huang, C. W. & Wu, J. C. S. Hydrogen production from semiconductor-based photocatalysis via water splitting. *Catalysts* **2**, 490–516 (2012).

106. Seger, B. & Kamat, P. V. Fuel cell geared in reverse: Photocatalytic hydrogen production using a TiO2/Nafion/Pt membrane assembly with no applied bias. *Journal of Physical Chemistry C* **113**, 18946–18952 (2009).

107. Georgieva, J., Armyanov, S., Poulios, I., Jannakoudakis, a. D. & Sotiropoulos, S. Gas Phase Photoelectrochemistry in a Polymer Electrolyte Cell with a Titanium Dioxide/Carbon/Nafion Photoanode. *Electrochemical and Solid-State Letters* **13**, 11–13 (2010).

108. Iwu, K. O., Galeckas, A., Kuznetsov, A. Y. & Norby, T. Solid-state photoelectrochemical H2 generation with gaseous reactants. *Electrochimica Acta* **97**, 320–325 (2013).

109. Lianos, P. Environmental Review of recent trends in photoelectrocatalytic conversion of solar energy to electricity and hydrogen. *Applied Catalysis B, Environmental* **210**, 235–254 (2017).

110. Kalamaras, E. & Lianos, P. Current Doubling effect revisited: Current multiplication in a PhotoFuelCell. *Journal of Electroanalytical Chemistry* **751**, 37–42 (2015).

111. Kaneko, M., Ueno, H. & Nemoto, J. Direct biomass fuel cell (BMFC) with anode/catalyst comprising a nanocomposite of a mesoporous n-semiconductor film and a metal thin layer: A new concept of catalyst design. *Catalysis Letters* **142**, 469–479 (2012).

112. Kaneko, M. *et al.* Direct electrical power generation from urine, wastes and biomass with simultaneous photodecomposition and cleaning. *Biosensors and Bioelectronics* **23**, 140–143 (2007).

113. Antoniadou, M. & Lianos, P. Production of electricity by photoelectrochemical oxidation of ethanol in a PhotoFuelCell. *Applied Catalysis B: Environmental* **99**, 307–313 (2010).

114. Sfaelou, S., Zhuang, X., Feng, X. & Lianos, P. Sulfur-doped porous carbon nanosheets as high performance electrocatalysts for PhotoFuelCells. *RSC Advances* **5**, 27953–27963 (2015).

115. Lianos, P. Production of electricity and hydrogen by photocatalytic degradation of organic wastes in a photoelectrochemical cell. The concept of the Photofuelcell: A review of a re-emerging research field. *Journal of Hazardous Materials* **185**, 575–590 (2011).

116. Yang, Z. *et al.* A Graphene-Based Coaxial Fibrous Photofuel Cell Powered by Mine Gas. *Advanced Functional Materials* **29**, (2019).

117. Brian O'Regan & Michael Grätzel. A low-cost, high-efficiency solar cell based on dye-sensitized colloidal TiO2 films. *Nature* **354**, 737–740 (1991).

118. Ahmed, M. & Dincer, I. A review on photoelectrochemical hydrogen production systems: Challenges and future directions. *International Journal of Hydrogen Energy* **44**, 2474–2507 (2019).

119. Lu, X., Xie, S., Yang, H., Tong, Y. & Ji, H. Photoelectrochemical hydrogen production from biomass derivatives and water. *Chemical Society Reviews* **43**, 7581–7593 (2014).

120. Kumar, P. Photoelectrochemical splitting of water to produce a power appetizer hydrogen: A green system for future (A short review). *Oriental Journal of Chemistry* **32**, 1473–1483 (2016).

121. Leisch, J. E., Abushama, J. & Turner, J. A. Investigation of CuGaSe2 Thin Films for Photoelectrochemical Water Splitting Devices. *ECS Abstract* (2006).

122. Marsen, B., Cole, B. & Miller, E. L. Photoelectrolysis of water using thin copper gallium diselenide electrodes. *Solar Energy Materials and Solar Cells* **92**, 1054–1058 (2008).

123. Hensel, J., Wang, G., Li, Y. & Zhang, J. Z. Synergistic Effect of CdSe Quantum Dot Sensitization and Nitrogen Doping of TiO2 Nanostructures for Photoelectrochemical Solar Hydrogen Generation. *Nano Letters* **10**, 478–483 (2010).

124. Sfaelou, S. *et al.* Buckypaper as Pt-free cathode electrode in photoactivated fuel cells. *Electrochimica Acta* **80**, 399–404 (2012).

125. Holmes-Gentle, I., Alhersh, F., Bedoya-Lora, F. & Hellgardt, K. Photoelectrochemical reaction engineering for solar fuels production. in *Photoelectrochemical solar cell* 1–43 (2019).

126. Heremans, G. *et al.* vapor-fed solar hydrogen production exceeding 15 % efficiency using earth abundant catalysts and anion exchange membrane. *Sustainable Energy & Fuels* **1**, 2061–2065 (2017).

127. Kraytsberg, A. & Ein-eli, Y. A Review of Advanced Materials for Proton Exchange Membrane Fuel Cells. *Energy Fuels* **28**, 7303–7330 (2014).

128. Paidar, M., Fateev, V. & Bouzek, K. Membrane electrolysis — History, current status and perspective. *Electrochimica Acta* **209**, 737–756 (2016).

129. De Bruijn, F. A., Dam, V. A. T. & Janssen, G. J. M. Review: Durability and degradation issues of PEM fuel cell components. *Fuel Cells* **8**, 3–22 (2008).

130. Shi, W. & Baker, L. A. Imaging heterogeneity and transport of degraded Nafion membranes. *RSC Advances* **5**, 99284–99290 (2015).

131. Bosserez, T. *et al.* Minimization of Ionic Transport Resistance in Porous Monoliths for Application in Integrated Solar Water Splitting Devices. *The Journal of Physical Chemistry C* **120**, 21242–21247 (2016).

132. Lianos, P., Strataki, N. & Antoniadou, M. Photocatalytic and photoelectrochemical hydrogen production by photodegradation of organic substances. *Pure and Applied Chemistry* **81**, 1441–1448 (2009).

133. Antoniadou, M. & Lianos, P. Near Ultraviolet and Visible light photoelectrochemical degradation of organic substances producing electricity and hydrogen. *Journal of Photochemistry and Photobiology A: Chemistry* **204**, 69–74 (2009).

134. Zhou, Z., Wu, Z., Xu, Q. & Zhao, G. A solar-charged photoelectrochemical wastewater fuel cell for efficient and sustainable hydrogen production. *Journal of Materials Chemistry A* **5**, 25450–25459 (2017).

135. Rongé, J. *et al.* Air-based photoelectrochemical cell capturing water molecules from ambient air for hydrogen production. *RSC Advances* **4**, 29286 (2014).

136. Rongé, J. *et al.* Solar hydrogen reaching maturity. *Oil & gas science and technology* **70**, 863–876 (2015).

137. Iwu, K. O. *et al.* Effects of temperature, triazole and hot-pressing on the performance of TiO2 photoanode in a solid-state photoelectrochemical cell. *Electrochimica Acta* **115**, 66–74 (2014).

138. Kudo, A. & Miseki, Y. Heterogeneous photocatalyst materials for water splitting. *Chemical Society Reviews* **38**, 253–278 (2009).

139. Maeda, K. *et al.* Photocatalyst releasing hydrogen from water. *Nature* **440**, 295–295 (2006).

140. Antoniadou, M., Kondarides, D. I. & Lianos, P. Photooxidation products of ethanol during photoelectrochemical operation using a nanocrystalline titania anode and a two compartment chemically biased cell. *Catalysis Letters* **129**, 344–349 (2009).

141. Antoniadou, M., Bouras, P., Strataki, N. & Lianos, P. Hydrogen and electricity generation by photoelectrochemical decomposition of ethanol over nanocrystalline titania. *International Journal of Hydrogen Energy* **33**, 5045–5051 (2008).

142. Seger, B., (Max) Lu, G. Q. & Wang, L. Electrical power and hydrogen production from a photo-fuel cell using formic acid and other single-carbon organics. *Journal of Materials Chemistry* **22**, 10709 (2012).

143. Rongé, J. *et al.* Air-based photoelectrochemical cell capturing water molecules from ambient air for hydrogen production. *RSC Advances* **4**, 29286–29290 (2014).

144. Seger, B. & Kamat, P. V. Fuel Cell Geared in Reverse: Photocatalytic Hydrogen Production Using a TiO2/Nafion/Pt Membrane Assembly with No Applied Bias. *Journal of Physical Chemistry C* **113**, 18946–18952 (2009).

145. Rongé, J. *et al.* Air-based photoelectrochemical cell capturing water molecules from ambient air for hydrogen production. *RSC Advances* **4**, 29286–29290 (2014).

146. Georgieva, J., Armyanov, S., Poulios, I. & Sotiropoulos, S. An all-solid photoelectrochemical cell for the photooxidation of organic vapours under ultraviolet and visible light illumination. *Electrochemistry Communications* **11**, 1643–1646 (2009).

147. Rongé, J., Nijs, D., Kerkhofs, S., Masschaele, K. & Martens, J. a. Chronoamperometric study of membrane electrode assembly operation in continuous flow photoelectrochemical water splitting. *Physical chemistry chemical physics : PCCP* **15**, 9315–25 (2013).

148. Ampelli, C., Centi, G., Passalacqua, R. & Perathoner, S. Synthesis of solar fuels by a novel photoelectrocatalytic approach. *Energy & Environmental Science* **3**, 292 (2010).

149. Tytgat, T., Hauchecorne, B., Smits, M., Verbruggen, S. W. & Lenaerts, S. Concept and validation of a fully automated photocatalytic test setup. *Journal of Laboratory Automation* **17**, 134–143 (2012).

150. Ampelli, C., Centi, G., Passalacqua, R. & Perathoner, S. Synthesis of solar fuels by a novel photoelectrocatalytic approach. *Energy & Environmental Science* **3**, 292 (2010).

151. Seger, B. & Kamat, P. V. Fuel Cell Geared in Reverse: Photocatalytic Hydrogen Production Using a TiO2/Nafion/Pt Membrane Assembly with No Applied Bias. *Journal of Physical Chemistry C* **113**, 18946–18952 (2009).

152. Chen, J. *et al.* Role of One-Dimensional Ribbonlike Nanostructures in Dye-Sensitized TiO2-Based Solar Cells. *The Journal of Physical Chemistry C* **115**, 7104–7113 (2011).

153. Verbruggen, S. W. *et al.* Factors driving the activity of commercial titanium dioxide powders towards gas phase photocatalytic oxidation of acetaldehyde. *Catalysis Science and Technology* **2**, 2311–2318 (2012).

154. Dumortier, M., Bosserez, T., Rongé, J., Martens, J. A. & Haussener, S. Combined Experimental-Numerical Analysis of Transient Phenomena in a Photoelectrochemical Water Splitting Cell. *Journal of Physical Chemistry C* **120**, 3705–3714 (2016).

155. Verbruggen, S. W. *et al.* Plasmonic gold–silver alloy on TiO2 photocatalysts with tunable visible light activity. *Applied Catalysis B: Environmental* **156–157**, 116–121 (2014).

156. Verbruggen, S. W. *et al.* Plasmonic 'rainbow' photocatalyst with broadband solar light response for environmental applications. *Applied Catalysis B: Environmental* **188**, 147–153 (2016).

157. Chiarello, G. L., Aguirre, M. H. & Selli, E. Hydrogen production by photocatalytic steam reforming of methanol on noble metal-modified TiO2. *Journal of Catalysis* **273**, 182–190 (2010).

158. El-Roz, M., Bazin, P. & Thibault-Starzyk, F. An operando-IR study of photocatalytic reaction of methanol on new *BEA supported TiO2 catalyst. *Catalysis Today* **205**, 111–119 (2013).

159. Carr, R. T., Neurock, M. & Iglesia, E. Catalytic consequences of acid strength in the conversion of methanol to dimethyl ether. *Journal of Catalysis* **278**, 78–93 (2011).

160. Wang, R. *et al.* Light-induced amphiphilic surfaces. *Nature* **388**, 431–432 (1997).

161. Feng, X., Zhai, J. & Jiang, L. The Fabrication and Switchable Superhydrophobicity of TiO2 Nanorod Films. *Angewandte Chemie International Edition* **44**, 5115–5118 (2005).

162. N. Stevens, C. I. Priest, R. Sedev & J. Ralston. Wettability of Photoresponsive Titanium Dioxide Surfaces. *Langmuir* **19**, 3272–3275 (2003).

163. Xie, S. & Ouyang, K. Degradation of refractory organic compounds by photocatalytic fuel cell with solar responsive WO3/FTO photoanode and air-breathing cathode. *Journal of Colloid and Interface Science* **500**, 220–227 (2017).

164. Qiu, S. & Kalita, S. J. Synthesis, processing and characterization of nanocrystalline titanium dioxide. *Materials Science and Engineering A* **435–436**, 327–332 (2006).

165. Verbruggen, S. W. *et al.* Photocatalytic acetaldehyde oxidation in air using spacious TiO2films prepared by atomic layer deposition on supported carbonaceous sacrificial templates. *Applied Catalysis B: Environmental* **160–161**, 204–210 (2014).

166. Sanchez-Martinez, D., Martinez-De La Cruz, A. & Lopez-Cuellar, E. Synthesis of WO3 nanoparticles by citric acid-assisted precipitation and evaluation of their photocatalytic properties. *Materials Research Bulletin* **48**, 691–697 (2013).

167. Nuno, M., Ball, R. J. & Bowen, C. R. Photocatalytic Properties of Commercially Available TiO2 Powders for Pollution Control. in *Semiconductor Photocatalysis - Materials, Mechanisms and Applications Anatase* vol. Chapter 22 614–634 (2016).

168. Šuligoj, A. *et al.* TiO2-SiO2 films from organic-free colloidal TiO2 anatase nanoparticles as photocatalyst for removal of volatile organic compounds from indoor air. *Applied Catalysis B: Environmental* **184**, 119–131 (2016).

169. Deng, X., Yue, Y. & Gao, Z. Gas-phase photo-oxidation of organic compounds over nanosized TiO2 photocatalysts by various preparations. *Applied Catalysis B: Environmental* **39**, 135–147 (2002).

170. Günnemann, C. *et al.* Insights into Different Photocatalytic Oxidation Activities of Anatase, Brookite, and Rutile Single-Crystal Facets. *ACS Catalysis* **9**, 1001–1012 (2019).

171. Ohno, T., Sarukawa, K., Tokieda, K. & Matsumura, M. Morphology of a TiO2 photocatalyst (Degussa, P-25) consisting of anatase and rutile crystalline phases. *Journal of Catalysis* **203**, 82–86 (2001).

172. Toledo Camacho, S. Y. *et al.* Pd/TiO2 -WO3 photocatalysts for hydrogen generation from water-methanol mixtures. *Applied Surface Science* **455**, 570–580 (2018).

173. Zhang, W. *et al.* Progress and Perspective of Electrocatalytic CO2 Reduction for Renewable Carbonaceous Fuels and Chemicals. *Advanced Science* **5**, (2018).

174. Verbruggen, S. W., Dirckx, J. J. J., Martens, J. A. & Lenaerts, S. Surface photovoltage measurements: A quick assessment of the photocatalytic activity? *Catalysis Today* **209**, 215–220 (2013).

175. Liu, Y., Xie, C., Li, J., Zou, T. & Zeng, D. New insights into the relationship between photocatalytic activity and photocurrent of TiO2/WO3 nanocomposite. *Applied Catalysis A: General* **433–434**, 81–87 (2012).

176. Bak, T., Nowotny, M. K., Sheppard, L. R. & Nowotny, J. Mobility of electronic charge carriers in titanium dioxide. *Journal of Physical Chemistry C* **112**, 12981–12987 (2008).

177. Li, L., Salvador, P. A. & Rohrer, G. S. Photocatalysts with internal electric fields. *Nanoscale* **6**, 24–42 (2014).

178. Rey, G. *et al.* Electron scattering mechanisms in fluorine-doped SnO2 thin films. *Journal of Applied Physics* **114**, (2013).

179. Ohtomo, A. *et al.* Lateral grain size and electron mobility in ZnO epitaxial films grown on sapphire substrates. *Journal of Crystal Growth* **214/215**, 284–288 (2000).

180. Martinez-Huitle, C. A., Rodrigo, M. A. & Scialdone, O. *Electrochemical water and Wastewater Treatment*. *Elsevier* (Elsevier Inc., 2018).

181. Dubouis, N. & Grimaud, A. The hydrogen evolution reaction: From material to interfacial descriptors. *Chemical Science* **10**, 9165–9181 (2019).

182. Hu, C. *et al.* Designing Photoelectrodes for Photocatalytic Fuel Cells and Elucidating the Effects of Organic Substrates. *ChemSusChem* **8**, 4005–4015 (2015).

183. Benson, S. W. Papers — III Bond Energies. *Journal of Chemical Education* **42**, 502–518 (1965).

184. Kumaravel, V. *et al.* Photocatalytic hydrogen production: Role of sacrificial reagents on the activity of oxide, carbon, and sulfide catalysts. *Catalysts* **9**, (2019).

185. Kameya, Y., Torii, K., Hirai, S. & Kaviany, M. Photocatalytic soot oxidation on TiO 2 microstructured substrate. *Chemical Engineering Journal* **327**, 831–837 (2017).

186. Hauchecorne, B. M. J., Terrens, D. G. M., Vanpachtenbeke, F. J. G., Lenaerts, S. K. & Tytgat, T. Reaction chamber for studying a solid-gas interaction. (2011).

187. Raj, K. J. A. & Viswanathan, B. Effect of surface area , pore volume and particle size of P25 titania on the phase transformation of anatase to rutile. **48**, 1378–1382 (2009).

188. Luttrell, T. *et al.* Why is anatase a better photocatalyst TiO 2 films. *Scientific Reports* **4**, 1–8 (2014).

189. Hauchecorne, B. *et al.* Elucidating the photocatalytic degradation pathway of acetaldehyde: An FTIR in situ study under atmospheric conditions. *Applied Catalysis B: Environmental* **106**, 630–638 (2011).

190. Pozo-Antonio, J. S., Noya-Pintos, D. & Sanmartín, P. Moving toward smart cities: Evaluation of the self-cleaning properties of si-based consolidants containing

nanocrystalline tio2 activated by either uv-a or uv-b radiation. *Polymers* **12**, 1–20 (2020).

191. Chen, Q. *et al.* Visible-light responsive photocatalytic fuel cell based on WO3/W photoanode and Cu2O/Cu photocathode for simultaneous wastewater treatment and electricity generation. *Environmental Science and Technology* **46**, 11451–11458 (2012).

192. Fukumura, T., Sambandan, E. & Yamashita, H. Synthesis and VOC degradation ability of a CeO2/WO3 thin-layer visible-light photocatalyst. *Materials Research Bulletin* **94**, 493–499 (2017).

193. Van Hal, M., Verbruggen, S. W., Yang, X., Lenaerts, S. & Tytgat, T. Image analysis and in situ FTIR as complementary detection tools for photocatalytic soot oxidation. *Chemical Engineering Journal* **367**, 269–277 (2019).

194. Chabas, A. *et al.* Behaviour of self-cleaning glass in urban atmosphere. *Building and Environment* **43**, 2124–2131 (2008).

195. Ferm, M., Watt, J., O'Hanlon, S., De Santis, F. & Varotsos, C. Deposition measurement of particulate matter in connection with corrosion studies. *Analytical and Bioanalytical Chemistry* **384**, 1320–1330 (2006).

196. Ferrero, L. *et al.* On the synergy between elemental carbon and inorganic ions in the determination of the electrical conductance properties of deposited aerosols: Implications for energy applications. *Applied Sciences* **10**, 5559 (2020).

197. Rosli, N. S., Abdullah, C. A. C. & Hazan, R. Synthesis, characterization and investigation of photocatalytic activity of nano-titania from natural ilmenite with graphite for cigarette smoke degradation. *Results in Physics* **11**, 72–78 (2018).

198. Verbruggen, S. W. *et al.* Plasmonic 'rainbow' photocatalyst with broadband solar light response for environmental applications. *Applied Catalysis B: Environmental* **188**, 147–153 (2016).

199. Braslavsky, S. E. *et al.* Glossary of terms used in photocatalysis and radiation catalysis (IUPAC recommendations 2011). *Pure and Applied Chemistry* **83**, 931–1014 (2011).

200. Clairotte, M. *et al.* Exhaust emission factors of greenhouse gases (GHGs) from European road vehicles. *Environmental Sciences Europe* **32**, 20 (2020).

201. European commission. Natura 2000. https://ec.europa.eu/environment/nature/natura2000/index_en.htm.

202. de Richter, R. & Caillol, S. Fighting global warming: The potential of photocatalysis against CO2, CH4, N2O, CFCs, tropospheric O3, BC and other major contributors to climate change. *Journal of Photochemistry and Photobiology C: Photochemistry Reviews* **12**, 1–19 (2011).